Digital Micromirror Devices and Femtosecond Laser Pulses for Rapid Laser Micromachining

by

Daniel Heath

Supervisor: Robert W. Eason

Co-Supervisor: Ben Mills

in the

Optoelectronics Research Centre

July 5, 2017

Declaration of Authorship

I, Daniel Heath, declare that this thesis titled, 'Digital Micromirror Devices and Femtosecond Laser Pulses for Rapid Laser Micromachining' and the work presented in it are my own. I confirm that:

- This work was done wholly or mainly while in candidature for a research degree at this University.

- Where any part of this thesis has previously been submitted for a degree or any other qualification at this University or any other institution, this has been clearly stated.

- Where I have consulted the published work of others, this is always clearly attributed.

- Where I have quoted from the work of others, the source is always given. With the exception of such quotations, this thesis is entirely my own work.

- I have acknowledged all main sources of help.

- Where the thesis is based on work done by myself jointly with others, I have made clear exactly what was done by others and what I have contributed myself.

Signed:

Date:

"Step 1: Write thesis

Step 2: See Step 1

Step 0: Could you come and help in the lab tomorrow?"

- Ben Mills, on how to get a thesis finished.

Abstract

Laser machining techniques are almost ubiquitous in industry for micro- to nanoscale fabrication. It is essential for the advancement of the field that faster, cheaper processes be developed. Enhancements in speed and fidelity of production can be made to both additive and subtractive writing techniques by using Digital Micromirror Devices (DMD), particularly when coupled with femtosecond laser pulses. The objective of this thesis is the demonstration of DMDs used in conjunction with ultrafast laser pulses for both novel and rapid machining applications; primarily image-projection based techniques, using DMDs as dynamic intensity masks, will be used for subtractive patterning, laser-induced transfer, multi-photon polymerisation and centimetre-scale micro-machining. The dynamic nature of the DMD enables its application to the field of multiple exposures, and the centimetre-scale machining is applied to functional biological assays. Adaptive mask techniques are used to enhance the image reproduction achieved, correct for positional errors introduced by translation stages, as well as to attain greyscale intensity control with a DMD in single ultrashort pulses. A new technique for producing digital holograms is developed, and will form the basis of future work.

Image projection-based patterning using DMDs as dynamic intensity masks is shown via ablation, multiphoton polymerisation and Laser-Induced Transfer (LIT). Ablation was achieved in a range of materials (including, but not limited to: gold, graphite, diamond, bismuth telluride and antimony telluride, glass, nickel, glucose, and gelatin), with 2 micron resolutions in samples and overall sizes of $\approx 1 \text{cm}^2$. A multiple exposure technique reduced final structure resolution by $\approx 2.7\times$ compared to the diffraction limit possible in a single exposure – from 1μm to 370nm on one experimental setup, and from 727nm to 270nm on a second setup. The first demonstration of shaped, solid-phase LIT deposits has been made, both in forward and backward directions of transfer.

Adaptive optics techniques have been developed for DMD mask corrections, and have reduced the positional error of samples introduced by translation stages. Greyscale intensity patterns have been projected at samples using the strictly binary-style DMD display technology, and the loss of intensity in high spatial frequencies at the sample has been addressed. A novel method for the generation of binary holograms is introduced, which allows for several additional degrees of control over spatial intensity patterns when using DMDs, such as the effective mask position relative to imaging optics, greyscale control, the formation of images at multiple planes, phase control, and overall lateral shifts of the intensity distribution below a single DMD pixel width.

Acknowledgements

First of all, my thanks go to Rob for taking me on as his final student. Your positive energy and enthusiasm were clear since my first year in undergrad, where you somehow explained wave physics with the use of 'virtual strings' by waving your arms around at the front of the lecture theatre, and I consider myself very lucky to have had you as my PhD supervisor. I hope I've managed to adopt some fraction of your attitude into my presentation style, you've made it very easy to get excited about new work over the years.

Ben, you've been an enormous help both in the lab and during outside discussions. I hope I've been a satisfactory first student – can't have been too bad, if we're going to co-supervise someone else soon! You've been a great support throughout the entire PhD, always ready to help with some new experiment. I'm just about set to get into areas of research I've been fascinated by for over ten years, and of course that wouldn't have been possible without all that you've done.

To past group members, Matthias Feinauegle and James Grant-Jacob, I couldn't have gotten up to speed on half the equipment I did without you showing me the ropes. Matthias, you were always ready with an insight into how to tweak things for an improvement, and the entire 'laser-induced transfer' section of this thesis wouldn't have happened without the basis of your work. James, you're an endless source of new project ideas, even after leaving the group, and of course it would have been quite a different PhD without you...

Contents

Chapter 1

Introduction

1.1 Motivation

Fabrication processes at the micro- and nano-scale are essential for emerging technologies which rely on ever-smaller feature sizes. Gordon Moore famously predicted in 1965 that the number of components on an integrated circuit board per unit cost would roughly double every two years [1], with much of this exponential improvement relying on the reduction of individual component sizes. Originally foreseen as likely to continue for at least ten years, Moore's law has held (up to some fluctuation) for the past five decades, meaning a vast improvement has been made within computer science over the last half-century, enabling any scientific endeavours capable of taking advantage of enhanced processing power.

The production steps involved in creating state-of-the-art integrated circuit boards, however, are somewhat restrictive. Clean-room environments, bespoke lithography masks, and multiple exposure steps, often involving the use of complex chemicals, are typically required. Processes are also often optimised for a narrow range of materials, with silicon being of particular importance in the semi-conductor industry, for example. The industry is, to an extent, focused on high throughput of identical devices, such that a great deal of cost can be afforded to the initial preparation of sample production. This approach is less conducive to fast prototyping of micro-scale features, especially in novel materials, or using novel processes; a high cost associated with each iteration of a prototype device is difficult to maintain. For this reason, alternative methods must be developed for the rapid fabrication of samples with micro-scale features with bespoke designs and material requirements.

While such techniques exist that produce nanoscale resolutions, with features as small as 2nm reported via electron-beam lithography for example [2], or greater material removal speed, such as laser galvo-scanning ($\approx 10 \mathrm{ms}^{-1}$ line-patterning speed [3]), there is usually a trade off between the two. The objective of this work, therefore, will be to demonstrate machining at a resolution comparable to other optical methods via femtosecond laser pulses and DMDs, in a wide variety of materials – enabling a wide range of fast

prototyping applications. These materials will include metals, ceramics, glasses, and photo-sensitive polymers, among others. While the overall volume of material removed per exposure when using a DMD as an intensity mask is unlikely to reach that attainable with a focused spot (as some intensity is lost at the point of masking), the complexity of each feature per exposure may mean that the line-patterning speed possible via DMD exposure is greatly enhanced in comparison to galvo-scanning. Machining a serpentine path via galvo-scanning would require many overlapping exposures, for instance, while the entire path (or section of path) could be exposed simultaneously via DMD image-projection based machining. Some processes, of course, are not amenable to focused spot machining, and require a mask – one such example being the shaped laser-induced transfer in Chapter 4. The demonstration of the use of a DMD in any such process will be of interest, as a result of the inherently rapid nature of mask generation using a DMD.

The following work is based on novel microfabrication techniques that combine the inherent speed and machining accuracy (in terms of feature size and disruption to adjacent features) of femtosecond laser pulses [4] with Digital Micromirror Devices (DMDs). The goal of this research is to enhance the use of DMDs as a manufacturing tool for fast prototyping, by characterising the fidelity of machining possible in a range of materials, developing automation incorporating DMDs to demonstrate centimetre-scale patterning with micro-scale features, and by extending the understanding of a DMD as an optical element.

1.2   Thesis Outline

As a range of micro-fabrication techniques are explored in the thesis, each chapter will begin with a literature review on the respective process.

A brief outline of ultrafast pulse generation and their interactions with matter are given in Chapter 2. A mechanical and optical description of DMDs is also given, as well as details of the experimental setups and control software used during this thesis. A review of alternative optical micro-processing techniques is also given in this chapter.

The potential of DMD image projection-based subtractive patterning with ultrafast laser pulses is demonstrated in a range of materials in Chapter 3. The ablative patterning of areas of $\approx 100mm^2$ with feature sizes on the order of $\approx 1\mu$m is shown, which took a matter of hours and could be scaled up to faster speeds. Such large area patterns have been used for the production of novel cell growth arrays with applications in regenerative medicine.

Laser-induced forward transfer (LIFT) of shaped, solid-phase materials is shown in Chapter 4. Additionally, deposits created via laser-induced backward transfer (LIBT) are shown, including examples with nano-scale imprinted surface. Shadowgraphy has been used to determine the dynamics of LIBT, and modelling efforts have recreated

some features of the observed results.

Chapter 5 explores a method for producing reduced feature sizes, and patterns in multiple pulses with final resolutions which would be below the diffraction limit of the used optical setup for features produced via ablation in a single pulse. Multiphoton polymerisation (MPP) of similar compound structures fabricated in multiple pulses using a DMD are also shown.

Adaptive mask techniques are introduced in Chapter 6, which allow the usually binary-value projected intensity patterns from a DMD mask to reach greyscale values, and correct for positional errors introduced by translation stages. A method of automating optical proximity corrections is presented, and theoretical work is introduced for the production of binary holograms, which could greatly enhance the potential of DMDs as an optical elements.

Finally, results will be summarised in Chapter 7. Appendices containing work published in the course of this PhD, as well as code used to model LIBT dynamics and extended discussions on the theoretical work in Chapter 6 will follow.

Chapter 2

Experimental equipment and setup

2.1 Introduction

In this chapter the working principle of the DMD is explained, as well as a brief summary of ultrashort laser pulse generation by mode-locking. The advantages and mechanisms of ultrashort pulse ablation are given, as well as the optical behaviour of a DMD under femtosecond illumination. The chapter then details the specifics of the experimental setups used in this thesis, including a description on the software automation control and limitations encountered.

2.2 Femtosecond laser pulses

The formation of ultrashort laser pulses can be understood from the Fourier transforms between a function of time $f(t)$ and frequency $\mathcal{F}(\omega)$, given in equations 2.1 and 2.2.

$$\mathcal{F}(\omega) = \int f(t) \exp(-i\omega t) dt \tag{2.1}$$

$$f(t) = \frac{1}{2\pi} \int \mathcal{F}(\omega) \exp(i\omega t) d\omega \tag{2.2}$$

The orthonormal basis of plane wave solutions to Maxwell's equations which govern the time-dependent behaviour of electronmagnetism can then be combined analogously to Fourier synthesis in order to construct any wave-form of light. The necessary control of relative amplitudes and phases of monochromatic plane waves is described in this section, with particular detail given on the method used in the ultrafast laser system used throughout experiments in this thesis.

4

2.2.1 Mode-locking

A laser cavity of length L and refractive index n with the speed of light in vacuum being c, can support multiple modes of frequencies v_q, where the separation between adjacent frequencies is given by equation 2.3, given enough gain at each frequency. Using a broadband laser source (for example our 12nm bandwidth 150fs Ti:sapphire amplifier), one can support, in principle, many ($\approx 10^6$) modes.

$$v_{q+1} - v_q = \frac{c}{2nL} \tag{2.3}$$

It is possible to couple these modes together such that they are in phase, so that the electric (and magnetic) fields sum to a high value for a short period of time and are near zero elsewhere, as illustrated in Figure 2.1.
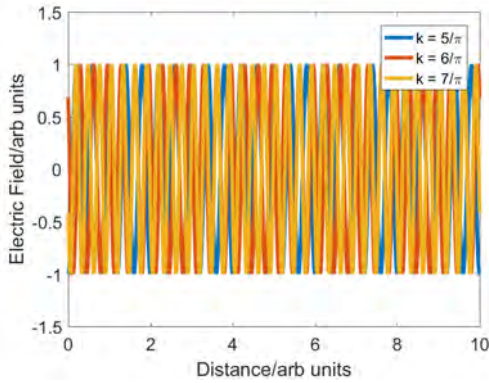
(a) Three modes output from a resonator of length 1 of equally spaced wavenumbers k
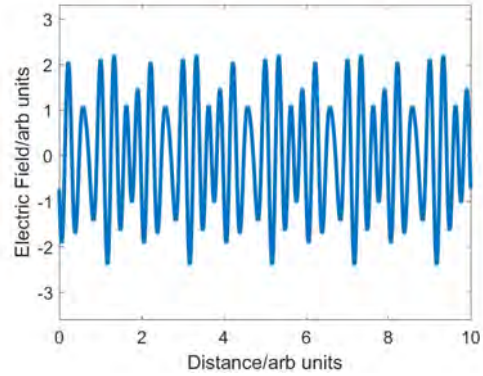
(b) Three modes combined with random relative phases
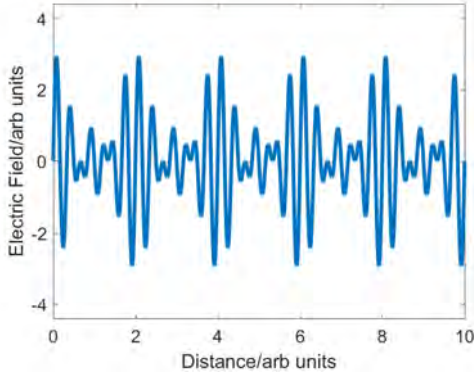
(c) Three modes combined in phase
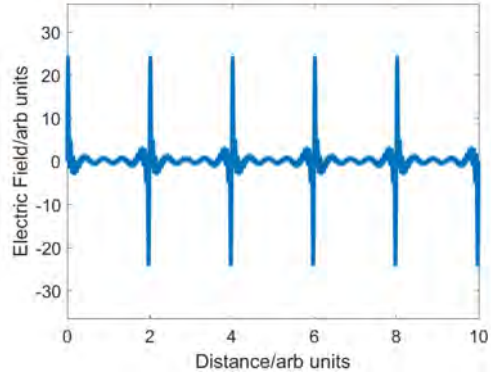
(d) Thirty modes combined in phase

Figure 2.1: A demonstration of the short pulse generation possible by summing separate laser modes in phase. (a) shows three distinct modes with equally spaced wavenumbers. (b) shows the summation of these three modes with random relative phases, (c) shows the summation of the three modes when in phase, while (d) shows the high peak field possible with an example of 30 modes oscillating in phase.

There are various methods to ensure that the modes oscillate in phase [5, pp. 257–273] which are beyond the scope of this thesis; briefly however, they rely on "survival of the fittest" mechanisms, wherein a short, intense pulse is more likely to propagate, experiencing higher gain and/or lower loss, in the laser cavity than many modes out of phase. The Ti:sapphire (Ti:Al_2O_3) source stage of the laser system used here relies on Kerr lens mode-locking [6]; the non-linear refractive index n as a function of intensity I with constants n_0 and n_2 is given in equation 2.4.

$$n = n_0 + n_2I \tag{2.4}$$

The beam mode used here was TEM$_{00}$, a Gaussian spatial intensity distribution transverse to the beam path, and thus experienced a greater refractive index at the centre of the beam than at the 'wings'. This led to a focusing of the beam, the basis of Kerr lens mode-locking. A small aperture is placed in the beam path at the focus within the optical cavity such that an intense pulse will self-focus to the aperture size and pass through almost unattenuated, while many modes out of phase would not focus strongly enough to survive round-trips inside the cavity. This stage of the laser, a 1.0W *Coherent Mira 900*, was pumped using a *Verdi 10* 532nm, 10W semiconductor diode pumped laser to provide 150fs pulses at a repetition rate of 76MHz [7], but required a second stage of amplification to reach the ≈ 2mJ, 1kHz repetition rate before being fed to later points in the experimental setup [8].

In order to amplify femtosecond pulses to the millijoule per pulse range, Chirped Pulse Amplification (CPA) is used here [5, pp. 277–281]. The high peak powers of ≈50GW of a 150fs 2mJ pulse may cause damage to the Ti:sapphire gain medium, and hence the pulses are stretched in time before entering an *Evolution* 527nm pumped Ti:sapphire crystal. In the system used here, a grating pair is used to introduce the dispersion necessary to stretch the pulse, before a Pockels cell allows one pulse per millisecond into the CPA cavity. The stretched pulse typically made 20 passes through the gain medium before being switched out of the cavity by a second Pockels cell – a value where saturation of the gain medium was reached. After exiting the CPA cavity, a grating pair is used to recompress the pulse, achieving the final output of 150fs pulses with ≈2mJ energy, which would be fed to experiments.

2.2.2 Femtosecond laser-material interactions

The time-scale and intensity of a laser pulse lead to different possible absorption mechanisms in a target sample. The first reported implementation of 'ablative photodecomposition', wherein a nanosecond UV excimer source was used to break interatomic bonds reported absorption depths following Beer's law [9], where absorption cross-section is a material constant at a particular wavelength. In this case the removal of material may occur either through a photochemical reaction, where molecular species are converted through the breaking of bonds into species which would naturally dissipate (gaseous molecules, for example), or through thermal decomposition – UV photons are absorbed and coverted to heat, and chemical decomposition or vaporisation occurs as in thermal

processes.

The time period over which ionised electrons reach thermal equilibrium with the material lattice is on the scale of picoseconds [10], and is thus short compared to nanosecond pulses. For sub-picosecond pulses, the interaction of free electrons generated by the leading edge of a pulse with the remaining pulse must be considered. As charged particles in an electric field, the free electrons are accelerated and may collide with ions or atoms via the inverse Bremsstrahlung effect [11] – in a strong electric field, this collision may provide enough kinetic energy to liberate another electron, and lead to 'avalanche ionisation' [12]. The efficiency of ionisation decreases with increased loss of energy through electron-phonon coupling, and can be approximately considered linear with laser intensity [13]. At a critical density of free electrons of $\approx 10^{29} \mathrm{m}^{-3}$, the electrons act as a plasma which is naturally resonant to the laser frequency, greatly increasing absorption [14]. This phenomenon is known as optical breakdown. The electron plasma created during the process may then leave a charged layer of material in dielectrics with low charge carrier mobility, which leads to material removal via 'Coulomb explosion' [15]. In materials with faster charge carrier mobility, electron-phonon collisions heat the lattice and lead to thermal vaporisation [16]. Avalanche ionisation is the dominant ionisation mechanism when using ultrashort pulses of intensities below $10^{12} \mathrm{W/cm}^2$.

With the intensities afforded by ultrashort pulses ($\approx 10^{14} \mathrm{W/cm}^2$ [4]), multiphoton effects become practicable – energy levels being excited by the absorption of two or more quanta of light equalling the separation between energy levels, rather than a single photon [17]. This multiphoton excitation can liberate an initial 'seed' of free electrons to initiate avalanche ionisation, however multiphoton ionisation alone is the dominant ionisation mechanism between $10^{12} - 10^{14} \mathrm{W/cm}^2$. Effectively, this means there is a threshold intensity at which excitation begins if the material is transparent at the central wavelength of the pulse. As two photon absorption is proportional to the square of intensity (and n-photon absorption proportional to the nth power of intensity), finer features can be written than with single photon effects [18]. Considering a focused beam, this means that excitation can begin deep within a transparent material, where the focused spot is at its most intense, rather than throughout the path of the beam; or, for example with a Gaussian beam, excitation could be thresholded only to occur within a region of width well below the full-width half-maximum (FWHM) – 20nm features using a 527nm wavelength source in Corning 0211 glass, for instance [19]. This is discussed further in Chapter 5.

A further possible ionisation mechanism occurs when the electric field of the pulse is comparable to that between electron and nucleus – above $\approx 10^{14} \mathrm{W/cm}^2$ *tunnelling ionisation* may occur [16]. The incident laser field effectively lowers the energy barrier of a nucleus' potential well, such that the probability of an electron escaping and hence ionising via quantum tunnelling becomes non-negligible.

While a range of possible excitation mechanisms exist, energy from femtosecond pulses is transferred to electrons on a timescale short compared to the thermal relaxation time of the electrons within the lattice. If material removal occurs, this then means that minimal heat transfer can occur between ablated material and surrounding regions when compared with ablation via longer pulses. The ablation threshold will vary depending upon the target material, however typical values observed in this work were tens of mJ/cm^2 for opaque materials, and between 1–12J/cm^2 for transparent materials. The idealised differences in damage between femtosecond and longer pulses are shown in Figure 2.2, where in the figure zero transfer of heat or pressure occurs between the intended material removal region and surrounding material.
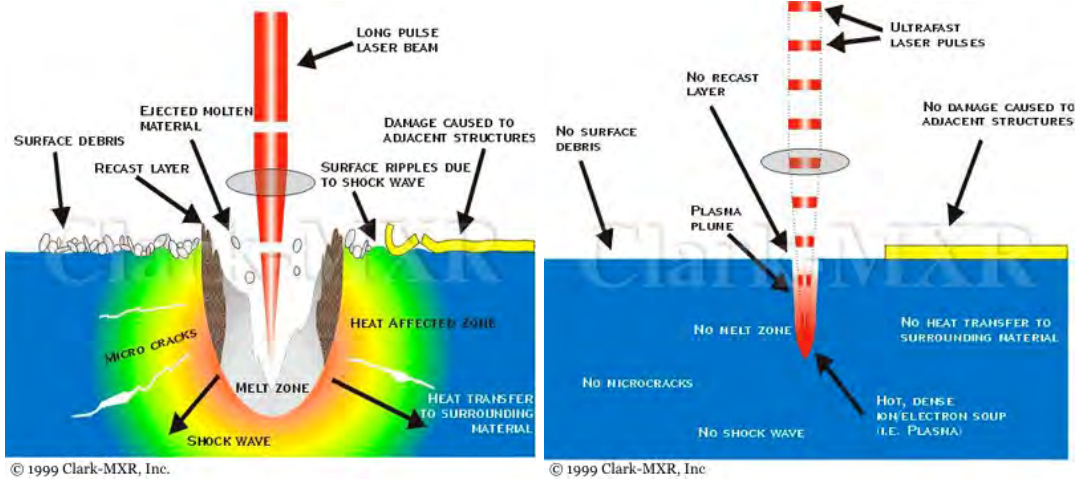
(a) A long pulse results in heat transfer to surrounding material, damaging the substrate and deposited features

(b) A femtosecond pulse occurs on a shorter timescale than the picoseconds typical of Coulomb collisions [4], meaning that heat transfer is limited and hence there is less damage to the surrounding substrate

Figure 2.2: Idealised effects present in long (nano/picosecond) vs. short (femtosecond) laser ablation (after [20]).

2.3 Digital micromirror devices

The work in this thesis will focus on the use of a digital micromirror device (DMD), a type of spatial light modulator (SLM), as a variable illumination mask. This section will describe the mechanical and operational specifications of DMDs and micro-electromechanical systems (MEMS), before discussing their optical behaviour under continuous wave (cw) and femtosecond illumination.

2.3.1 Mechanical description

A DMD has on its surface an array of square mirrors, often on the order of 1000×1000, each of which is $\approx 10\mu m$ on a side with similar centre-to-centre separations (depending on make/model and accounting for a small gap between adjacent mirrors). Figure 2.3
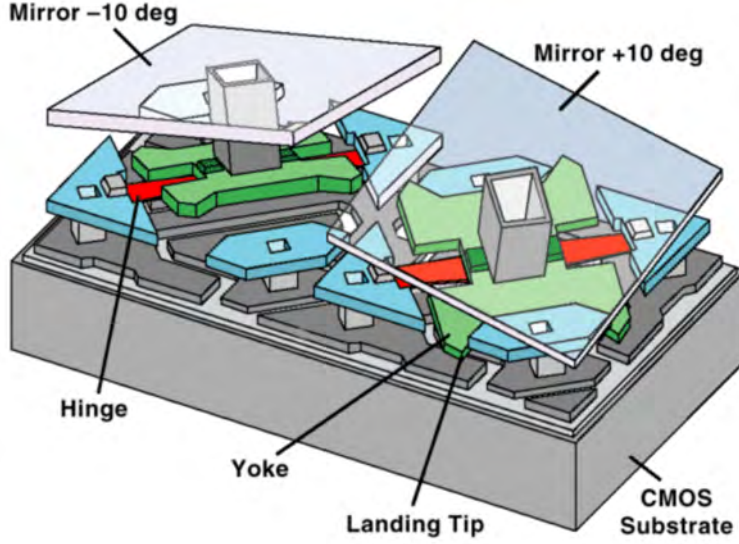
Figure 2.3: A diagram of two pixels in a DMD [after [22]]. The tilt angles in this case are $\pm 10°$, but DMDs with mirror tilts of $\pm 12°$ were used for the work in this thesis.

describes the MEMS employed in each DMD pixel, which usually have switching speeds of $\approx$1kHz, with >30kHz possible in some models [21]. DMDs can be used commercially to reproduce RGB colour levels in projectors, and so are a cheap, mature technology (around £200 for 1kHz models). Owing to their low price and rapid switching speeds, DMDs are attractive as dynamic intensity masks.

Each pixel is a microelectromechanical system (MEMS) capable of tilting a mirror on a diagonal axis either at some negative angle relative to the normal to the plane of the DMD chip, which directs light into an internal beam dump and will be referred to as "off", or a positive angle which directs an incident beam outwards and will be referred to as "on". The time taken for a mirror to reposition between 'off' and 'on' positions is referred to as 'crossover time', and is on the order of a few microseconds typically.

The $TexasInstruments$ DMDs used in this work were either the DLP3000 [23] or the DLP7000 [24]. Both used aluminium mirrors protected by an anti-reflection coated window [25], however the DLP3000 mirrors were arranged in a diamond lattice as in Figure 2.4(a) with 684 zig-zagging columns by 608 rows for a final aspect ratio of 854:480 [23], while the DLP7000 mirrors were arranged in a square lattice as in Figure 2.4(b) with 1024 columns by 768 rows.

9
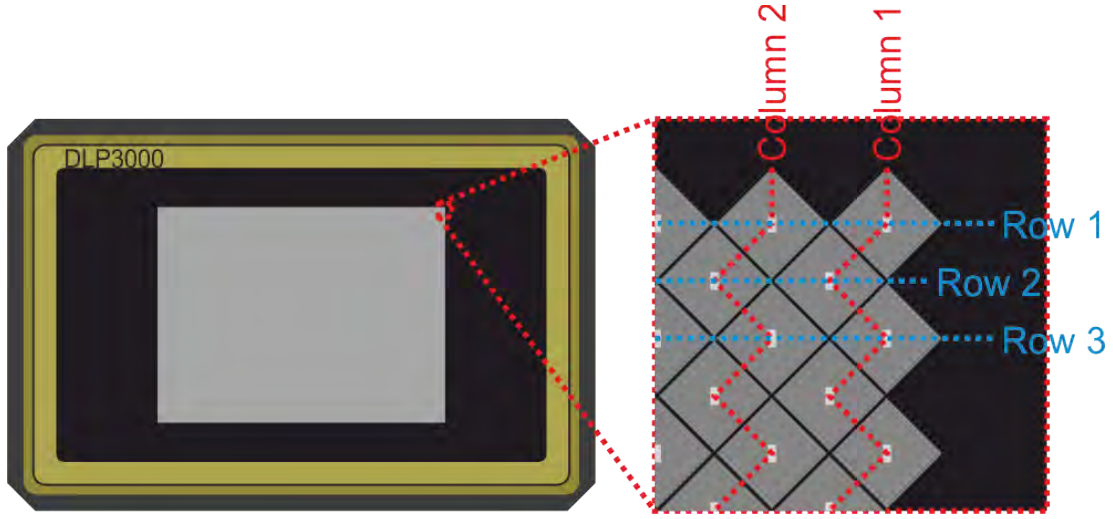
(a) The MEMS mirrors of the DLP3000 DMD arranged in a diamond lattice
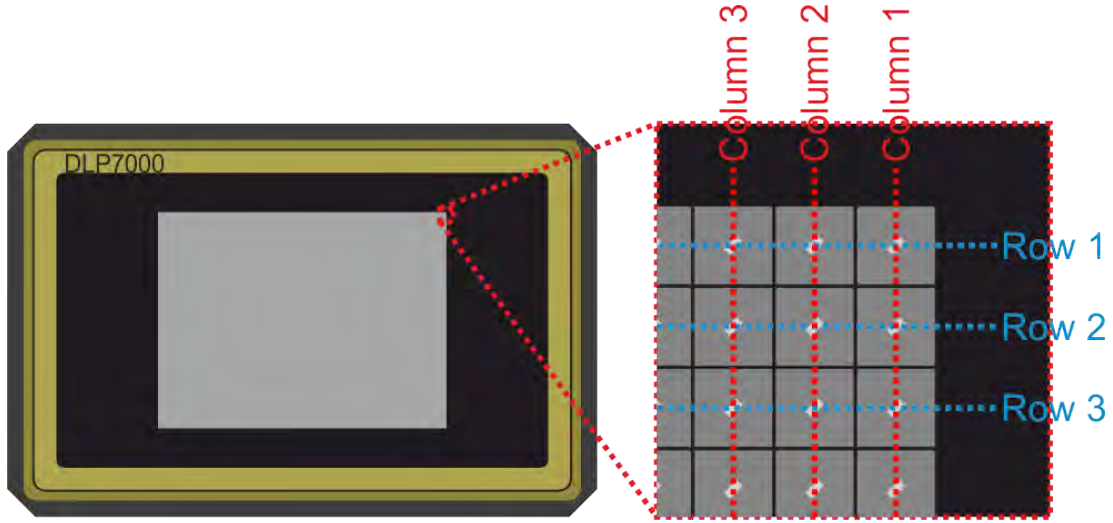
(b) The MEMS mirrors of the DLP7000 DMD arranged in a square lattice

Figure 2.4: The relative arrangements of MEMS mirrors for the two DMD chips.

In both cases, the square mirrors tilt along their diagonals at $\pm 12°$. The side length of each mirror in the DLP3000 was 7.64μm [23] including a small gap between mirrors, for a pitch along the axis orthogonal to the tilt axis of 10.8μm. The crossover time was $\approx 5\mu$s, though there would be some delay between the end of a single mirror crossing over and being ready for a second crossover, such that the maximum refresh frequency of 4kHz. The DLP7000 mirrors had a side length of 13.68μm [24], for a pitch orthogonal to the tilt axis of 19.35μm. The crossover time was 16μs, with a maximum possible refresh frequency of 32kHz.

2.3.2 Optical description

The MEMS mirrors of the DMD were aluminium-coated silicon, with a reflectance at 800nm of $\approx 87\%$ [26], while a protective window placed in front of the MEMS mirror
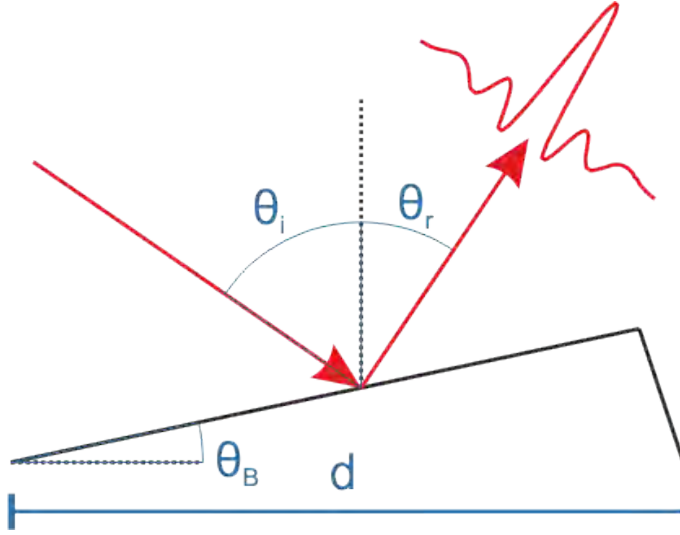
Figure 2.5: The angular shift of a single-mirror diffraction pattern at a blaze angle θ_B and AOI θ_i.

surface has a transmission of $\approx 88\%$ at an angle of incidence (AOI) of $30°$ and $\approx 90\%$ at an AOI of $0°$ [25]. The group has been implementing DMDs as intensity spatial light modulators (SLMs) [27], as well as other researchers [28–30]. In order to properly design a beam-line to make use of a DMD, its diffractive properties must be considered.

An important consequence of the periodicity of the DMD mirrors is that, when using a spatially coherent incident beam, the DMDs behave as 2D gratings and hence produced a 2D array of diffraction peaks. In order to image the surface of the DMD on the sample, which was perpendicular to the path of the pulse, the output direction of the pulse from the DMD is required to be normal to the DMD surface. The DMD mirror tilt of $\pm 12°$ enabled its operation as a blazed grating, and a geometry enhancing the diffraction efficiency into a single peak (known as *blazing*), in this case near-normal to the DMD surface, can be calculated by modelling the 1D case. A single mirror with incident illumination at an AOI of θ_i, output angle of θ_r, mirror tilt (or *blaze angle*) of θ_B, with width at $0°$ tilt of d, will have a far-field behaviour according to single-slit diffraction as in Equation 2.5.

$$I(\theta_r) = I_0 \operatorname{sinc}^2(\frac{d\pi}{\lambda}\cos(2\theta_B - \theta_i)\sin(\theta_r + 2\theta_B - \theta_i)) \tag{2.5}$$

$I(\theta_r)$ is the intensity at the output angle, while I_0 is the peak output intensity. All angles are taken to be positive in the clockwise direction. The factors of $\cos(2\theta_B - \theta_i)$ and $2\theta_B - \theta_i$ are the only differences to the standard single-slit far-field diffraction result known from standard optics theory. These factors reflect the *effective* mirror width at a tilt under non-normal illumination – the single-slit pattern is angled and spread/narrowed according to the relative angles, with the change in direction given in Figure 2.5.
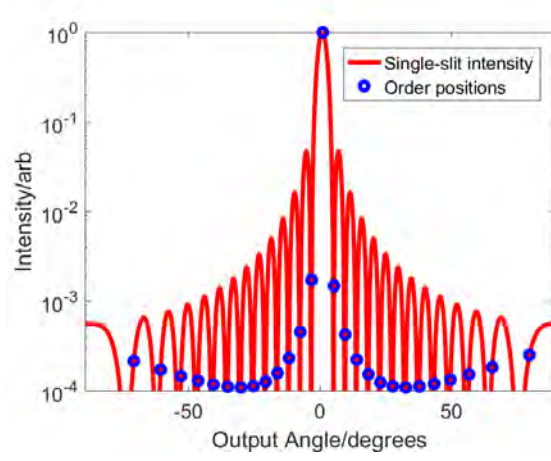
Figure 2.6: The relative intensities of diffraction orders in a 1D approximation to the DMD surface for the DLP3000 with $\theta_i = -23°$.

The DMD surface can then be considered as a convolution of a single mirror profile with a periodic array of dirac delta functions (or *Dirac comb*). The angular positions of diffraction maxima from a Dirac comb at non-normal incidence follow the Bragg Equation 2.6, with θ_m being the angular position of diffraction order m, θ_i the angle of incidence, λ the wavelength and d the array period.

$$\sin(\theta_i) + \sin(\theta_m) = \frac{m\lambda}{d} \tag{2.6}$$

By the convolution theorem, given in Equation 2.7 (convolution denoted by $*$), the relative intensities of these diffraction orders can be calculated by the relative intensities of the single-mirror pattern at positions θ_m.

$$\mathcal{F}(f * g) = \mathcal{F}(f) \times \mathcal{F}(g) \tag{2.7}$$

Figure 2.6 shows a semi-logarithmic plot of the intensities at diffraction orders between $m = -8$ to $m = +18$ with variables chosen to reflect the DLP3000.

Recalling that a near-normal output direction to the DMD surface was required for imaging, and that the single-mirror angular output with a fixed $\theta_B = -12°$ would only be centred on $0°$ when $\theta_i = -24°$, only input angles close to this value were searched. Figure 2.6 shows blazing for the $m = +5$ order with an input angle of $-23°$. The same method when using the tilt-orthogonal pitch of $19.68\mu m$ for the DLP7000 found that blazing into the $m = +1$ order at a near-normal output was achieved with an input angle of $-23°$. Note that for a full prediction of relative intensities for diffraction orders from a 2D grating, the model would require extension; this simplified version serves as a rapid approximation to aid experimental setup design. In practice, both DMDs achieved an efficiency of $\approx 30\%$ into single orders, as measured by a photodiode.
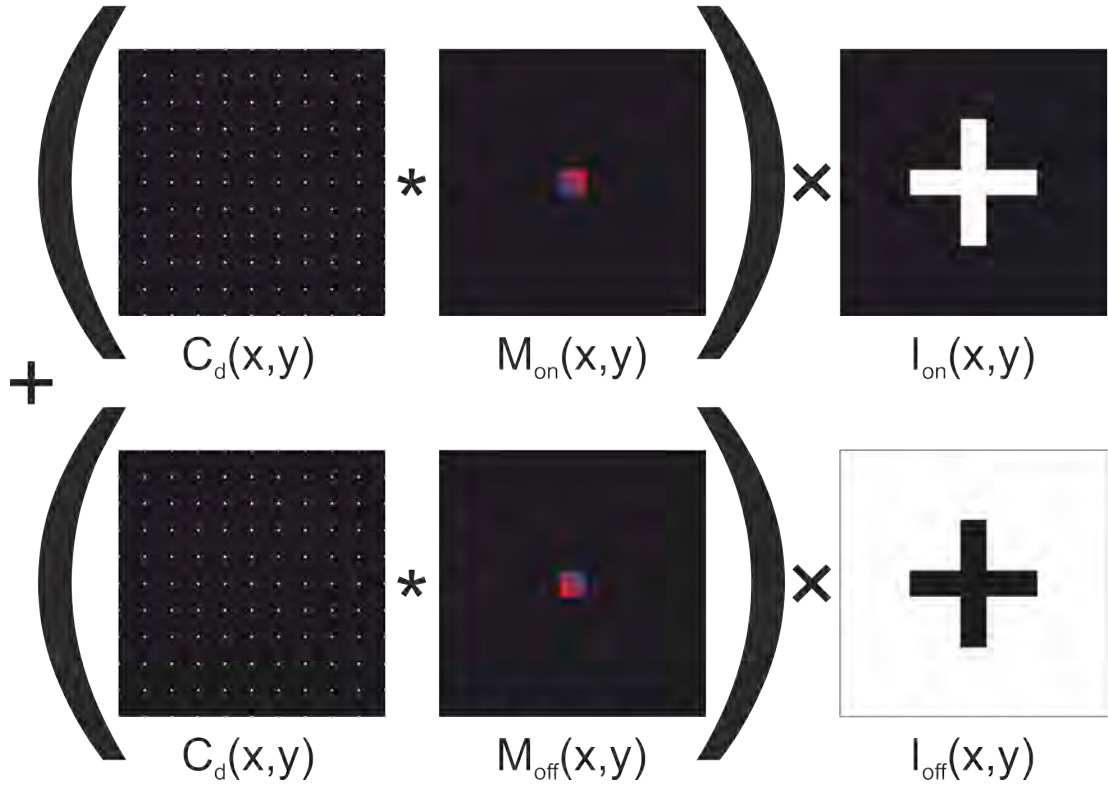
Figure 2.7: Pictorial form of the terms in Equation 2.8 showing the mathematical components considered when forming a 'cross' of 'on' mirrors on a DMD. A blue-red gradient highlights different phase behaviours, M_{on} and M_{off}, across on/off mirrors, while a larger-scale phase dependence due to non-normal incidence is not shown in the Dirac combs C_d. The $I_{on/off}$ profiles are binary functions, white when equal to 1, black when equal to 0.

Thus far, the DMD surface has been modelled as an infinite array with all mirrors in the on position, however for the purposes of beam-shaping via the DMD as a dynamic intensity mask, the far-field diffraction effects must be considered for a finite DMD where some arrangement of mirrors may be off. Let $C_d(x, y)$ denote the Dirac comb of period d over spatial coordinates parallel to the DMD surface x and y with appropriate phase dependence to account for non-normal incidence be denoted, and the profile of a single 'on' or 'off' mirror be $M_{on}(x, y)$ or $M_{off}(x, y)$ respectively. A final pair of 'mask' functions, $I_{on}(x, y)$, $I_{off}(x, y)$ will then define where mirrors are on or off in the final mask, with I_{on} equalling 1 in regions intended in a given intensity mask and 0 elsewhere, and $I_{off} = (1 - I_{on})$ within the borders of the DMD surface, and $I_{off} = 0$ elsewhere. The full description of a DMD surface illuminated at non-normal incidence can then be given by $\text{DMD}_{surf}(x, y)$ in Equation 2.8, where dependence on x and y has been dropped for brevity, with a pictographic form given in Figure 2.7.

$$DMD_{surf} = (C_d * M_{on}) \times I_{on} + (C_d * M_{off}) \times I_{off} \tag{2.8}$$

In order to obtain the far-field diffraction pattern from an arbitrary image displayed on a DMD then, we once more take the Fourier transform. As the transform is distributive, contributions from 'on' and 'off' mirrors can be considered separately to start

13

with. By the convolution theorem in equation 2.7, and the fact that the transform of a Dirac comb is a Dirac comb (analagously to the diffraction order positions given by equation 2.6), we find that the transform of 'on' mirrors is the convolution of the mask function I_{on} with a Dirac comb which has been weighted by a sinc profile. This is a highly important result for the purposes of beam shaping – in the far-field diffraction pattern, each diffraction order associated with mirrors in the 'on' position will contain all information necessary to image I_{on}; a single order can then be considered 'the beam line' at later points in the imaging setup, and is easily focussed/redirected. The only remaining concern is interference from orders associated with 'off' mirrors, however it is quickly seen that there will be negligible interference between the two sets of orders. Note that there is a 24° difference in blaze angle between 'on' and 'off' mirrors, and hence a 48° shift in single-mirror diffraction pattern peak intensities. At this separation in Figure 2.6, there is a factor of ≈1000 reduction in intensity compared to the peak; any diffraction orders associated with 'off' mirrors coinciding with the angular direction of the blazed order from 'on' mirrors will then have little effect. As discussed in Chapter 6, the spectral dispersion across the bandwidth of frequencies in ultrashort pulses was not observed to have a significant effect when imaging the DMD surface, though it did impact the viability of 'binary holograms'.

The above theoretical considerations have worked with 800nm illumination, which of course is a simplification for femtosecond pulsed sources. An angular shift of approximately $\pm0.16°$ is seen for a ±6nm wavelength for the blazed order for the DLP3000, with around 1% difference in efficiency of blazing (though of course this value is based on the 1D model and is only meant for demonstrative purposes). While these disparities over the bandwidth of the Ti:sapphire source did not lead to significant difficulties when the DMD surface was imaged at the sample, they are of greater concern when highly complex patterns are to be displayed as intensity masks, as in digital holography. The phenomenon has been dealt with by others by using gratings prior to the DMD to apply an appropriate dispersion of opposite sign [31], but has not been addressed further in this thesis.

2.4   Experimental Setup

This section will describe the experimental setups used throughout this the work in this thesis. Two beam lines have been employed, both using the 150fs pulse duration, 1kHz repetition rate, 800nm wavelength, Ti:sapphire amplifier described in section 2.2.1, with pulses energies deliberately attenuated to ≈1mJ to avoid damage to the DMD chips. The major difference between the two lines was the DMD used in each and the spatial intensity homogenisation – a Texas Instruments DLP3000 [21] was used in the majority of work, while work which required single-pixel control was carried out on a Texas Instruments DLP7000 in Chapter 5. The two lines shall be referred to as the 'DLP3000 line' and 'DLP7000' line respectively.

2.4.1   Beam lines

The two beam lines were maintained in parallel, with the DLP7000 line constructed during the course of the PhD and the DLP3000 present at its commencement, with a few modifications made. An approximately spatially Gaussian intensity 150fs 800nm pulse is incident on a continuous-gradient variable neutral density (ND) filter before being directed via flip mirror (FM) to either beam line. The variable ND was mounted on a 50mm total travel distance, $\approx 1\mu$m positional accuracy translation stage so that pulse energy could be computer-controlled. The variable ND was a metallic reflective continuous gradient between 0.04-4.0 optical densities, of length 100mm. The filter was positioned such that the regions of optical density between 0.04 and 2.0 were able to be positioned in the beam path via the 50mm translation stage. A second, static identical filter was sometimes placed immediately after the first, with the direction of increasing gradient reversed, to correct for the necessarily different attenuations applied across a beam spot of finite width, however little improvement was observed over the beam homogeneity achieved after the homogenisers in each setup when using a single filter. In practice, the gradient in intensity on the input Gaussian distribution introduced by a single variable ND filter was corrected for via realignment at the entrance to the homogenisers.
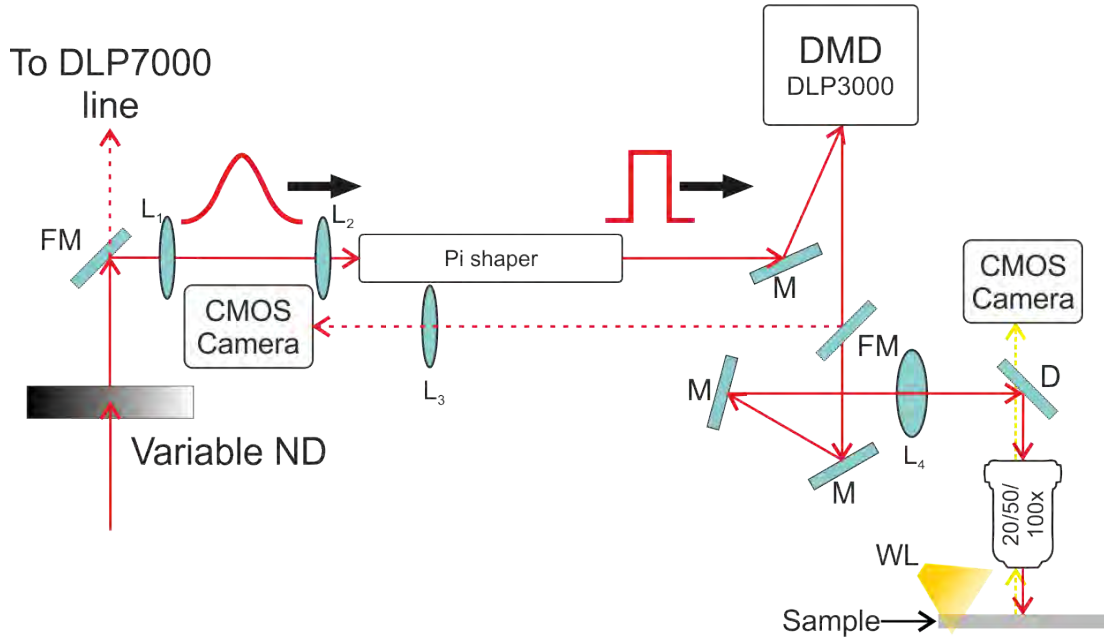
Figure 2.8: The DLP3000 line. Focal lengths and diameters of lenses used are detailed in Table 2.1.

Figure 2.8 shows the DLP3000 line. The pulse was directed through a lens pair which acted as both telescope and collimator, to reach the required 6mm diameter collimated profile required for the input to an AdlOptica 6_6 pi-shaper, a refractive beam shaper which redistributes the transverse intensity distribution across the beam to form a circular top-hat function. Issues concerning the use of this beam shaping element are

addressed after the description of the second experimental setup. The spatial homogeni-
sation was necessary to ensure that all mirrors to be exposed in a DMD mask were
illuminated with approximately equal intensity. The pulse is then incident on the DMD
at 23° and reflected from two metallic mirrors (M) through a collimating lens (L), onto
a dichroic mirror (D) and through a 100x/50x/20x microscope objective onto the sam-
ple. The sample is illuminated by a white light (WL) source, which is observed by a
CMOS camera through the dichroic mirror. An optional flip mirror (FM) can be raised
in order to test beam quality and alignment on a second CMOS camera.

A difficulty with loading images onto the DLP3000 prevented the use of binary images
with features below a few DMD pixels wide. The images were uploaded to the DLP3000
via an HDMI cable, enabling the DMD as a 'second screen' on a personal computer.
The binary images sent to this second screen were intended for a square grid of pixels,
however the DLP3000's pixels are in fact laid out in a diagonal pattern. This presents
a problem in displaying fine features, as shown in Figure 2.9.

Intended 'second screen' square
pixel layout

Mapping on a diagonal layout of
pixels
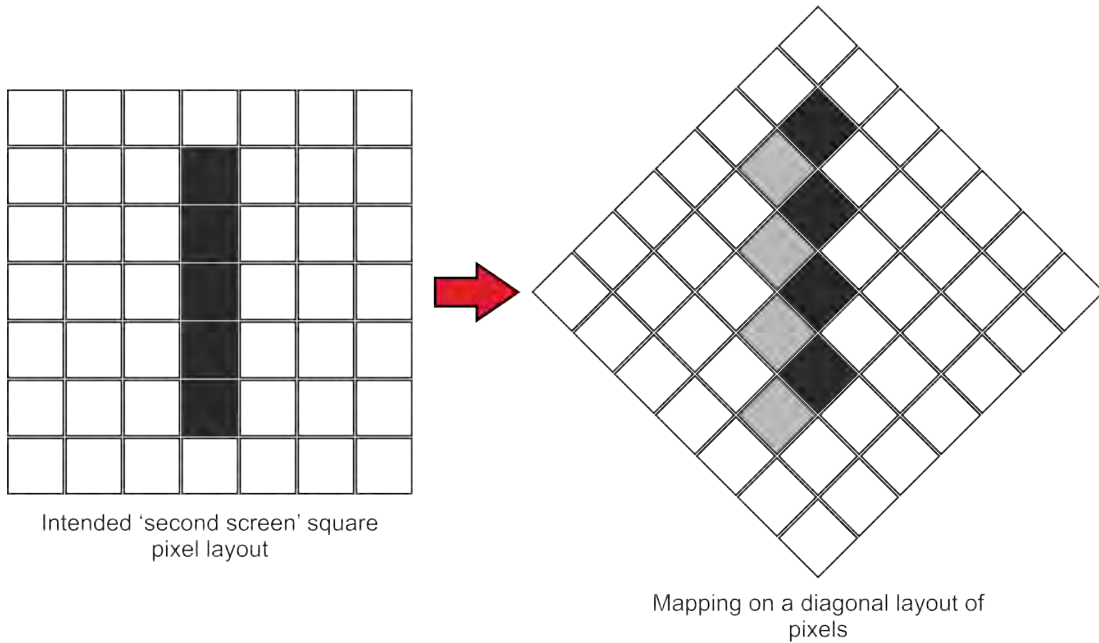
Figure 2.9: Problem displaying features on the DLP3000, translating from a square to
a diamond grid. White pixels are off, black are on, and gray are dithering between on
and off to recreate the intended line pattern on a diagonal grid.

Rather than map each pixel in the intended square grid to a corresponding pixel in the
diamond grid, which would mean the image was displayed at 45° for a straight vertical
line, the DLP3000 attempts to preserve the orientation of the feature (straight vertical
line of black pixels in the Figure), while 'dithering' some pixels on and off (shown in gray)
to maintain an average output intensity that well-approximates the intended pattern.
This dithering is fast enough for the intended projector display usage of commercial
DMDs, but slow compared to an ultrafast laser pulse – this means that different pulses
arriving at the DLP3000 while some pixels are dithering will likely have different spatial
intensity profiles (some pixels may be on where they were off during the previous pulse

arrival, and vice versa). For large displayed images, with only some dithering at borders, this is not a concern. For fine features, of only a few pixels, it is a limit of the setup, and so the Discovery 4100 Development Kit with ViALUX ALP-4 Controller Suite was purchased from Texas instruments; a controller capable of addressing individual pixels, and a DLP7000 DMD chip. The DLP7000 setup is shown in Figure 2.10, and has a few key differences to the DLP3000 line.
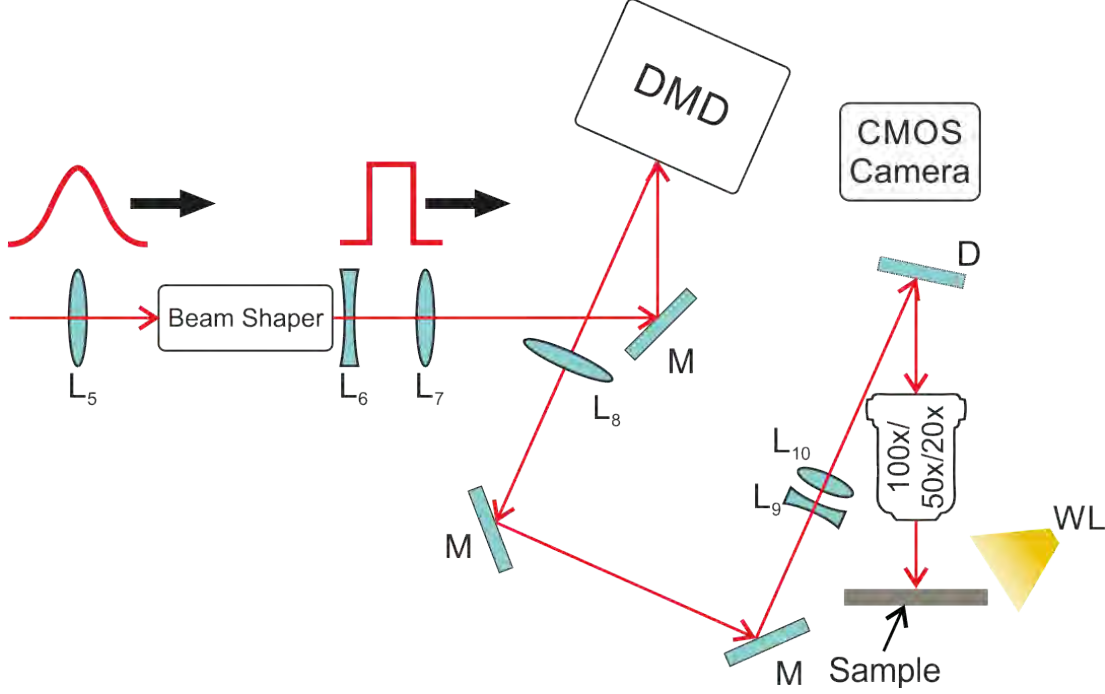
Figure 2.10: The DLP7000 line. Focal lengths and diameters of lenses used are detailed in Table 2.1.

All mirrors used in the DLP7000 line were dielectric, rather than metallic as in the DLP3000 line, with peak efficiency at 45° AOI, requiring a different geometry. The two lenses prior to the DLP7000 chip, and the one immediately after it were of 2 inch diameter, in order to minimise spherical aberrations inherent to 1 inch lenses when working with a DMD surface of greater dimensions (14×10.5mm for the DLP7000 vs 6.6×3.7mm for the DLP3000). Details of lenses for both experimental setups are given in Table 2.1.

Currently, the collimating 1 inch diameter lens pair immediately before the dichroic mirror are positioned to achieve a spot size of appropriate diameter for entrance into the aperture at the entrance of the 20x microscope objective; the 50x and 100x objectives' smaller apertures would require minor reconfiguration for use. The refractive beamshaper used to homogenise the pulses for the DLP7000 line was a TOPAG GTH-5-250/4 lens [32]. While the pi-shaper used on the DLP3000 line redistributed Gaussian input pulses to circular top-hat output pulses, the TOPAG beam shaper gave an output of square top-hat pulses. A circular input to the DLP3000 DMD surface meant that in order to expose all mirrors, some portion of energy would be wasted in order to cover all points of the square DMD surface. In practice, a central region of the DLP3000 was usually exposed, as seen in the CMOS camera image in Figure 2.11.

Table 2.1: Focal lengths and diameters of lenses used in experimental setups shown in Figures 2.8 and 2.10.

Lens	Focal length (mm)	Diameter (mm)
L_1	-100	25.4
L_2	150	25.4
L_3	100	25.4
L_4	100	25.4
L_5	1000	50.8
L_6	-150	50.8
L_7	250	50.8
L_8	500	50.8
L_9	-200	25.4
$L_1$0	150	25.4
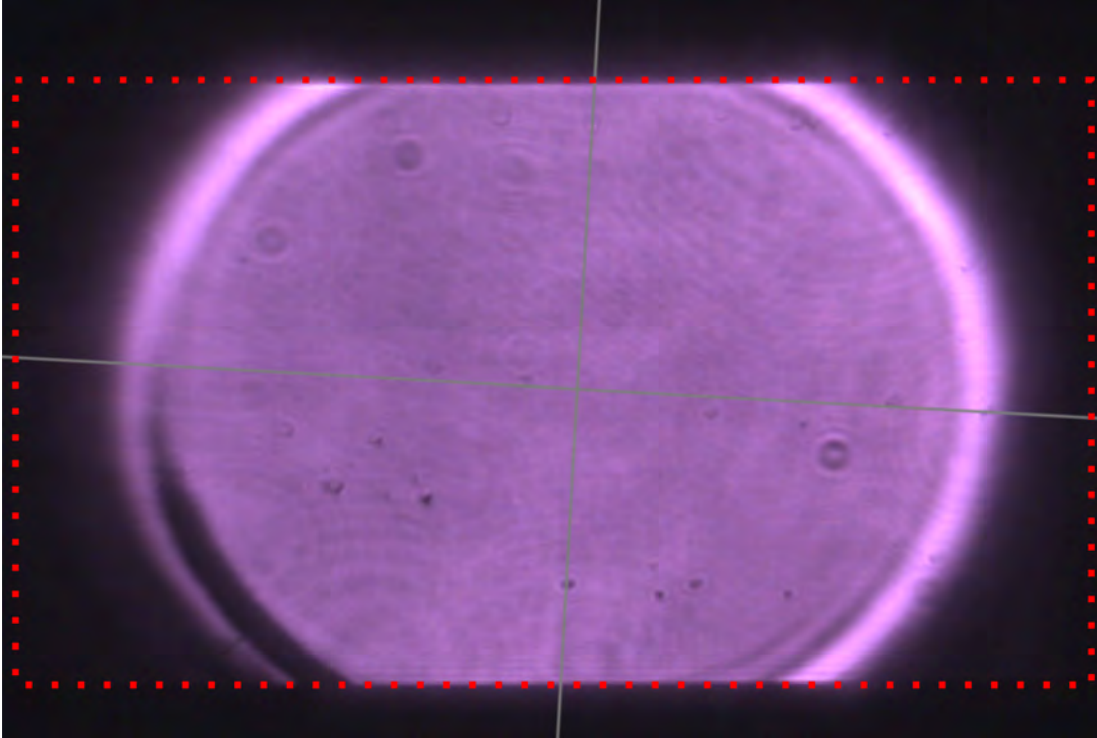
Figure 2.11: CMOS camera image of the intensity distribution on the DLP3000 DMD surface, underfilled by the circular top-hat output of a pi-shaper. The red dotted outline shows the relative position of the DMD chip surface. A high-intensity ring was present around an otherwise near-homogenised intensity distribution.

A high-intensity ring was present around the circular top-hat output of the pi-shaper, and was seen whenever the DLP3000 surface was deliberately underfilled by reducing the input spot size to the pi-shaper. Even when repositioned to minimise the strength of this high-intensity ring however, an ideal flat-top was not achieved – this may have been due to non-Gaussian input. While the output of the Ti:sapphire was close to TEM_{00}, unavoidable clipping occurred as a result of the beam containment system around the grating compressor stage; in addition to other imperfections of the optics used later in the beam line, this led to only near-Gaussian input to beam shapers in both lines. By

using a square top-hat output beam shaper, the entire DMD surface could be illuminated with less overlap, and hence wasted energy. During design of the DLP7000 line, it was expected that a deliberate overlapping of the DMD surface would avoid damage from any high intensity perimeter square analogue to the ring seen in Figure 2.11, however in practice no high intensity edges were observed from the TOPAG beam shaper.

Samples were typically mounted on a *Thorlabs TravelMax* 3 axis stage, individual stage model numbers LNR50P1, P2 and P3, stacked for 3-axis movement. The stages had a minimum $\approx 1\mu$m incremental movement, and 50mm total travel distance in each direction. The stages were motorized-screw-driven, with a backlash of $\approx 6\mu$m and a repeatability of $\approx 10\mu$m. Samples were either fixed in place with screws, putty or tape, or expected to remain immobile with respect to the stage surface due to friction. Stage position, velocity and acceleration, as well as displayed DMD mask and variable ND position, were controlled digitally, with some details given in the next section.

2.4.2 Software

Over the course of the PhD, several elements of the experimental setups were altered for improved computer control. These included the triggering and mode (single pulse vs continuous train of pulses) of the laser, pulse energy attenuation, DMD image loading and sample stage repositioning. Initially, a LabVIEW$^{\text{TM}}$ interface allowed for repositioning of the sample, while triggering of the laser, as well as mode switching, required manual control on separate hardware. DMD images were loaded via USB on a standalone device (a *Texas Instruments DLP LightCrafter Display 2010 EVM*) connected to the DLP3000 chip and pulse energy was attenuated manually with a continuous reflection ND filter (*Thorlabs part number NDL-10C-2*). The camera (*Thorlabs DCC1645C CMOS*) used for live viewing of the sample during machining was connected to a separate computer than that which ran the LabVIEW interface, and hence no image recognition-based logic was possible. Each repositioning and triggering command was entered at the time of execution and required user input on several pieces of separate hardware, requiring many seconds even for a simple command such as 'fire additional pulse at this location'.

Control of each component was centralised to a single computer (*Windows 7, 64-bit, Intel Core i5 processor, 12GB RAM*). The LabVIEW interface was expanded and linked to a MATLAB$^{\text{TM}}$ kernel, so that a series of commands incorporating adaptive logic would control the setup continuously for several hours with little oversight, including the triggering of laser pulses and switching laser modes. While an exhaustive list of utilised functions is impractical, a description of the most commonly used automation is given here.

A typical experiment would require between tens and tens of thousands of exposures of different DMD masks at different positions on a sample, with different pulse energies and repetitions of exposures at single points. The sample would be translated in the x- and y-directions (perpendicular to the beam line) over several mm, and the z-direction

(parallel to the beam line) only to maintain image position at the sample, typically not more than 100μm. A *sample map* detailing relative positions in x and y of exposure points, DMD masks to be displayed at each position, pulse energy, number of pulses at each position, and points at which to switch laser mode (between a continuous train of pulses at integer repetition rates between 1 and 1000Hz, and individually triggered pulses) would be generated in preparation of an experiment. Points at which to perform additional logic, such as refocusing, would also be set. The sample map was converted to sequential instructions readable by LabVIEW, with steps involving complex operations (for instance image recognition) being parsed by the MATLAB kernel.

Power calibration of the beam was performed with a thermal power meter (*Coherent, FieldMax power meter and EnergyMax sensor*) placed immediately after the variable ND filter, with the amplifier set to 1kHz mode and the beam spot size of ≈4mm diameter at the 10mm diameter sensor active area. The ND filter was repositioned typically ≈30 times, evenly spaced over a range input by the user, with power readings input by the user at each position. Though the filter would produce approximately logarithmic attenuation along its length, with 30 readings a linear fit between known data points was found to be ±1% accurate to thermal power readings. These calibration values would be saved, and only the minimum and maximum values regularly required calibration to provide an offset for the overall curve. Any desired power values dictated by the sample map outside the available range would be set to the nearest possible value and return an error.

While a z-repositioning was possible via the initial sample map instructions, all results shown in this thesis were produced on planar samples. Ideally, any sample would lie in a plane orthogonal to the beam path, such that z-repositioning after x or y translation was not necessary, however it was not possible to ensure that the surface of the translation stages were perfectly 'flat', or that there was zero debris between the stage surface and the sample which would introduce a small tilt. A priori knowledge of the tilt of the sample when generating the sample map was not possible, and so a plane of points 'in focus' was defined by moving to three positions which would define three of four corners of a square large enough to encompass the machining region for the experiment. The z-positions of these points were rarely separated by more than 100μm, and typically took a few minutes to determine. A 2D linear interpolation at each x- and y-position in the sample map then determined the required z-offset in order to maintain the correct imaging position at the sample.

Over the course of many bidirectional z-repositioning steps, the finite repeatability of the stages meant that a gradual drift from the true imaging plane would occur. The direction and magnitude of this drift could not be predicted in the sample map, and so additional instructions at predefined points during machining were added where either a manual refocusing or an autofocus step would occur. A global offset to expected image z-positions would then be added based on the difference between predicted and actual imaging positions. The autofocus algorithm began by positioning the stages below the expected z-position, and making small steps over a defined range until the stages were

an equal distance above the expected z-position. All results which relied on the aut-ofocus function in this thesis used 11 steps of 2μm in the z-direction, meaning that the image plane was maintained to 2μm accuracy during machining. When in focus, a 'sharp' image contains a higher proportion of high spatial frequencies – an image was recorded in RAM at each step and the absolute sum of spatial frequencies above a user-defined value was recorded, to be compared to the sum of spatial frequencies at other z-positions. In fact, a user-defined number of sub-regions of each image were taken, and the median absolute sum of high spatial frequencies recorded, to avoid the possible impact of large (greater than $\approx5\mu$m tall) debris on a sample skewing the imaging posi-tion. The stages then return to the z-position maximising high spatial frequencies, and apply an appropriate offset to future z-positions. The range over which the autofocus tests is set to a large value compared to expected drift between autofocus steps, such that it is unlikely the stages can drift to a value outside of this range. If the autofocus determines the imaging to be optimal at either extreme of positions tested, an error is given and the central z-position is used, to avoid runaway repositioning. In practice, such runaway repositioning was not observed after the subset of images and median sum method were applied.

2.4.3 Limitations and future upgrades

The experimental setup has been automated to a degree which has greatly enhanced the scale, speed and accuracy of DMD-enabled femtosecond laser machining. However, several known issues remain to be solved, which shall be addressed in this section.

Four major problems have arisen from the expansion in scale of machined structures during a single experiment. These are power stability over a several-hour interval, build up of redeposited material ejected from kerf, adjusting for stage drift, and quality con-trol for failed pulses.

The power variation for the *Mira* Kerr lens mode-locked source was $< 3\%$ after warm-up over a 2 hour period [7], while the *Legend* CPA stage had a root-mean-squared pulse energy variation of $< 0.75\%$ over 8 hours [8], both at stable environmental conditions, these variations were consistent with observed variations in this work between the be-ginning and end of experiments; fluences and intensities used are stated as measured immediately prior to the beginning of experiments. The longest experiments carried out during this PhD from a single sample map were on the order of ≈6 hours, and hence power stability, particularly for multi-photon effects, became a concern. Though it did not lead to the failure of any particular experiment, control of pulse energies is criti-cal for the control of laser-matter interactions, and hence machining quality. A trivial solution would be to add a permanent high-ratio beamsplitter or computer-controlled flip-mirror in the beam path, to produce a secondary diagnostic line focused at a power meter, for regular power monitoring and adjustment throughout any experiment lasting on the order of 2 hours or greater. While most commercial power meters would not be capable of measuring individual pulse energies, additional breaks in code generated from the sample map could be added to periodically switch the laser mode to 1kHz and

record an average power (as was usually done before starting experiments), and adjust the variable ND filter accordingly. Though the per-pulse energy is expected to remain constant regardless of the repetition rate of the laser (which could be set at any integer repetition rate between 1–1000), it is possible that measuring the power at 1kHz and dividing by 1000 is not an exact solution for calculating the power when single pulses are triggered. With the addition of automated power monitoring, an initial calibration step before each experiment would be to measure the power at many repetition rates, provided the measured power were high compared to background, and extrapolate down to 1Hz; a closer approximation to individually triggered pulses, which may have several-second periods between triggerings.

The build up of redeposited material during some experiments (typically from ablation), would be solved by the addition of a nitrogen assist, or vacuum pump near the point of machining. While the involved air currents could potentially reduce imaging fidelity, no observable loss of quality has been observed when using the current solution of a semi-regular (every $\approx$30 minutes) air hand-pump gas assist. If the air currents were found to be negatively affecting any experiment, the gas assist could be activated only during known periods when no machining is taking place (while repositioning the sample between pulses, for instance).

Stage drift in the z direction has already been corrected for (as with the autofocus algorithm in the previous section). A suite of image-recognition algorithms under development will also address drift in x and y. While these algorithms may correct the problem, stages which interferometrically track their positions to 0.1μm with 3μm full travel and return accuracy have been purchased in order to reduce the frequency of algorithmic corrections [33] (Thorlabs 50mm TravelMax Translation Stage with Optical Encoder), however an apparent fault/reverse-compatibility issue has limited their integration into the setup.

A failure to receive a pulse from the CPA stage has been observed, though the rate of failure has not been measured accurately – an estimated $1/100-1/1000$ triggered pulses fail, both when pulses are requested individually or during a train of regular pulses while the CPA system is set to 'continuous' mode. Some failure rate may be inherent to the Synchronization and Delay Generator (Coherent SDG) [34] for the Pockels cells, where the control voltage rise time of < 2ns and < 250ps timing jitter may fail to allow entry/exit of pulses to/from the CPA cavity of length $\approx$60cm [8] and hence round-trip time of $\approx$4ns. Random fluctuations in the Kerr lens mode-locking system may cause momentary loss of bandwidth, which in turn would disallow pulses from entering the CPA system (a permanent grating/photodetector-pair electronically shutters the system when appropriate bandwidth for ultrashort pulses is lost). In the case of single pulse triggering failures, the USB-RS-232 converter used to comminucate between computer and SDG may contribute; USB signals require conversion by the CPU, and are given some priority in a queue of operations rather than being transmitted immediately upon request. Internal electronics of the converter are unknown, and may also suffer from

some failure rate.

While suspected sources of this fault require testing, image recognition algorithms under development may ameliorate the problem. Detection of a bright flash, or change to the surface structure in the expected location viewed in real-time via CMOS camera, will mark the arrival of an expected pulse. Failure to detect such an event could be used to immediately request additional pulses, or mark the location for later inspection.

The current data communication methods introduce additional concerns for the setup. The computer operating system's internal prioritisation of USB-signalling as mentioned above introduces unknown time lags between each sent command. The delay is on the order of milliseconds, and causes little concern when a sample is stationary during exposures. For the machining of large areas, however, the sample is often kept in constant motion during the arrival of a train of pulses, and hence the exact positioning of machined points, and the upload times of new DMD masks to the DLP7000 are uncertain. The DMD mask upload method is a particular problem. The DLP3000 is enabled via HMDI cable as a second screen on the PC used for all controls, and is hence limited to $\approx$60 frames per second – i.e. a maximum of 60 unique masks per second, as opposed to the design maximum of 4kHz. Alternatively, loading each image via USB to the DLP7000 is limited via data-rate, in addition to USB-prioritisation; at $\approx$100kB per monochrome bitmap file readable by the Discovery 4100 Development Kit, it would not be possible to upload unique images at the maximum design refresh rate of 32kHz. In both cases, to achieve unique images at the maximum possible rate, it is necessary to upload all desired images, display sequence and switching times ahead of other experimental procedures. A trigger signal can then be sent to begin the display sequence – the exact timings to display each image would be impossible to know a priori to any acceptable degree of accuracy with the current translation stages, and synchronisation would be much more difficult with the inclusion of corrective logic, such as the autofocus algorithm.

Finally, the refresh behaviour of the DMDs can impact the mask displayed at the time of pulse exposure. Typically, a binary image file will correspond to the charge uploaded to a CMOS cell beneath each DMD mirror, before a 'clocking pulse' triggers the mirrors to change position depending on the CMOS cell charge [23, 24]. This triggering to reset is explicitly performed in controllable blocks of columns sequentially for the DLP7000 (up to resetting the entire chip in response to a single clocking pulse), while the DLP3000 should by default update all mirrors at once. It has been observed at a rate of $< 1/1000$ exposures when using the DLP3000 line that DMD masks contain a band of 'off' mirrors where 'on' mirrors are expected. This may be a result of obfuscated internal electronics updating blocks of columns in the DLP3000 rather than all columns simultaneously as expected, or an unexpected result of the HDMI connection causing a band of 'off' charges being applied to underlying CMOS cells before a clocking pulse arrives..

2.5 Competing beam shaping technologies

The work in this thesis aims to extend the functionality of DMDs in laser machining, however there are, of course, alternative SLMs available for the purpose of beam shaping. While SLMs such as acoustic optical modulators [35, 36] and liquid crystal spatial light modulators (LC SLMs) [37] have been used for femtosecond pulse shaping in the *frequency* domain, this thesis focuses on the use of beam shaping in the *spatial* domain, i.e. using DMDs as dynamic intensity masks. The discussion will thus be limited to SLM technologies used for beam shaping in this domain.

2.5.1 Liquid crystal SLMs

Perhaps the best known alternative to DMDs within the field of beam-shaping, LC SLMs cover a wide variety of different implementations [38]. LC SLMs (also referred to as liquid crystal on silicon, LCOS, when a silicon backing plane is used) can achieve both amplitude and phase modulation [39], depending on the particular implementation, but the principle underlying each is similar; the transmission of polarised light through an LC layer, comprised of molecules in an intermediate state between a liquid and a solid exhibiting birefringence and self-alignment of orientation. Typically, the LC layer will be placed between two alignment layers, as in Figure 2.12, and the orientation of the LC molecules during transmission will have some effect on the polarisation or phase of the incident light.

(a) A LC cell in the 'off' state   (b) A LC cell in the 'on' state
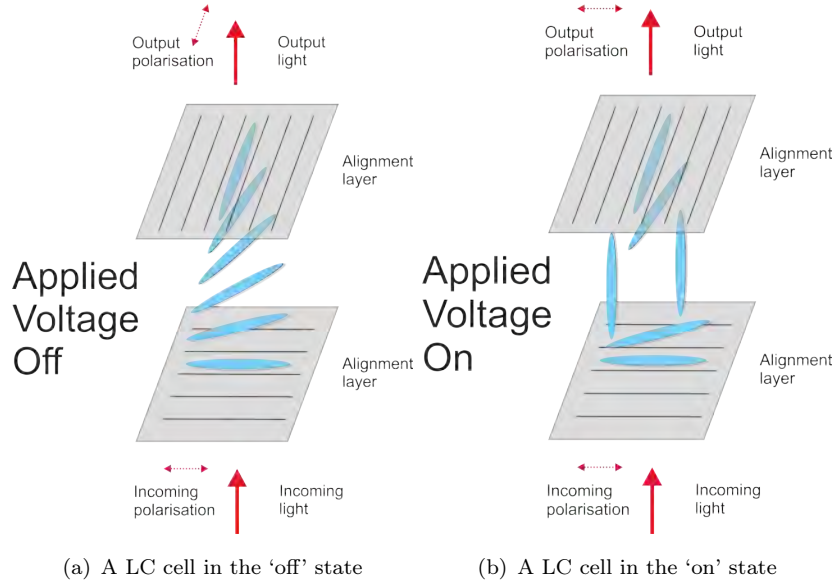
Figure 2.12: An example LC cell in (a) 'off' state and (b) 'on' state. In this case, the directions of the alignment layers are orthogonal. Additional polarisers and electrode layers have been omitted.

In the absence of an external electric field, LC molecules will align with grooves on the alignment layers, with a gradual mutual rotation between layers of the LC molecules themselves between the two alignment layers if the alignment directions are not parallel, as in Figure 2.12(a). The birefringence along the different axes of the LC molecules results in a rotation of the polarisation of incoming light [38]. In the presence of an electric field, as in Figure 2.12(b), most of the LC molecules align instead with the field direction, and do not cause a significant change to the direction of polarisation of light. Polarisation filters can be placed before and after the elements shown in Figure 2.12, and if the filter is orthogonal to the alignment layer at the output position then this form of LC cell acts as an amplitude modulator. The applied voltage, and hence polarisation rotation, can be varied continuously, for continuous amplitude modulation.

An alternative, phase-only LC SLM, may take a similar form to that shown in Figure 2.12, but with parallel alignment layers. The applied voltage then purely determines the phase lag experienced by light transmitting through the LC cell. LC SLMs exist in both transmissive and reflective implementations, with the latter making the addition of a reflective coating after one of the two alignment layers. By arranging many of these LC cells in a 2D array, an SLM with continuous amplitude and phase control is feasible. As LC SLMs are comprised of regular 2D arrays of these cells, or pixels, intensity is distributed among various diffraction orders as with DMDs. The diffraction efficiency into each order is affected by the particular choice of phase pattern across the LC SLM [40, 41], and the particular application will determine which order, or selection of orders, is desired for high efficiency. Efficiency into the first order may be as low as 30% if the phase alternates by $\pi/2$ between each pixel [42], or above 90% when the phase shift between adjacent pixels is lower, or optimisation algorithms are used to design a phase distribution [41].

LC SLMs have been used with femtosecond illumination for micro-machining applications [43], with illumination fluences similar to those used in this thesis. The overall size of the active surfaces and the individual cell pitches are also similar to the dimensions available in DMDs, $\approx$1cm and $\approx$10μm respectively. The major advantage of DMD technology over LC SLMs is the refresh rate; a typical LC SLM will refresh at $\approx$100Hz, with a maximum available in the low kHz range [38]. DMDs, however, boast refresh rates >1kHz refresh rates commonly, with a maximum available rate of 32kHz [21]. A second advantage of DMDs is their price; a LC SLM typically will cost >\$10,000 [44], while a DMD chip can cost as little as \$100 [23].

Though continuous intensity control would clearly be of benefit for laser micro-machining applications, it will be shown in Chapter 6 that DMDs can also be used for continuous intensity control of ultrashort pulse exposure. While the phase control offered by LC SLMs is of great benefit to wavefront correction and hologram generation, typically the work undertaken during this PhD relied on image projection-based techniques, and thus the phase of light was not a concern.

2.5.2 Other MEMS devices

Several microelectromechanical systems can be used other than DMDs for beam shaping applications, and to address them all here would be impractical. A review of some such devices by Liao et al. is available [45]; notable examples include deformable mirrors [46], an interferometric modulator (IMod) based on a Fabry-Perot etalon [47], and the Grating Light Valve [48]. Deformable mirrors consist of a reflective layer distorted by an array of MEMS actuators, and typically only allow phase control. The principle of operation of an IMod is somewhat similar to a deformable mirror, in that a flexible surface is displaced continuously over a 2D array of points. While the front layer of a deformable mirror is highly reflective, and driven by actuators, the front layer in an IMod is a partially-reflecting polymer suspended above an air gap, driven by electrostatic attraction, and then a highly reflective surface. The depth of the air gap is on the order of the visible wavelengths of light (600nm), and the deformation leads to differing levels of interference between light reflected from the front and highly reflective surfaces. The device is intended as 'electronic paper' for rewritable colour posters and other displays, however, and has not been demonstrated within laser machining applications.

The mode of operation of GLV also relies on the electrostatic deformation of material, though in this case the material is silicon nitride coated in aluminium. A single GLV pixel is shown in Figure 2.13; typically a GLV pixel will be comprised of six silicon nitride ribbons, three of which will be stationary, and three of which will deform in response to a voltage being applied across their surface and the underlying electrode layer. The displacement of the deformable ribbons towards the electrode layer alters the efficiency of diffraction into different orders; when no voltage is applied, there will be high efficiency into the zeroth order, when voltage is applied there will typically be low efficiency into the zeroth order, and high efficiency into the first order. The first order is captured for light modulation applications, and due to the low thickness and hence mass of the silicon nitride ribbons, refresh rates as high as 500kHz are achievable.
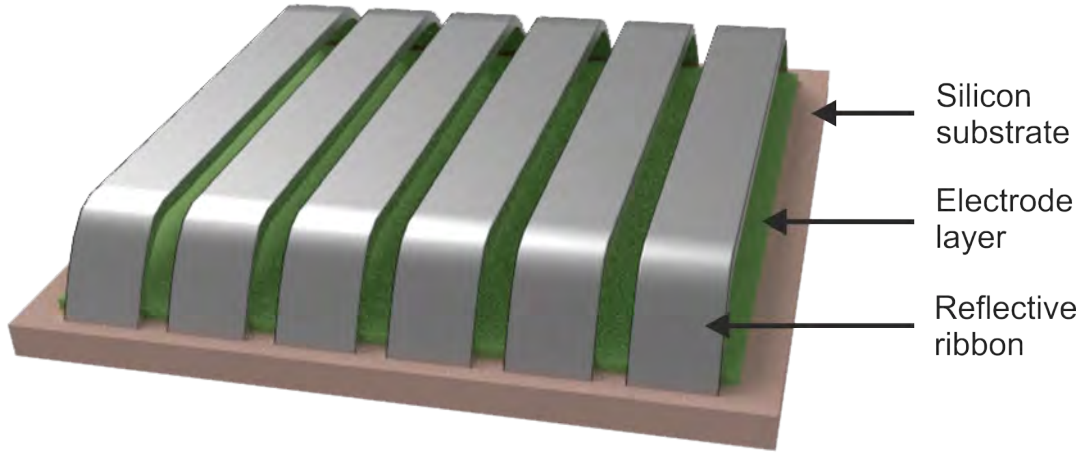
(a) A GLV pixel in the 'off' state
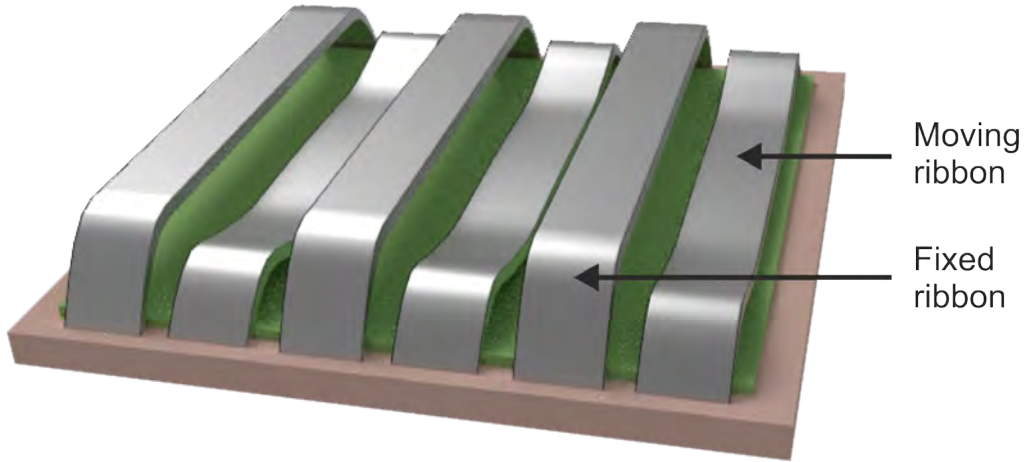
(b) A GLV pixell in the 'on' state

Figure 2.13: An example GLV pixell. (a) in the 'off' state, all reflective ribbons' top layers maintain the same height, diffracting light efficiently into the zeroth order. (b) in the 'on' state, half of the ribbons are deflected downwards, altering the diffraction efficiency into various orders.

Diffraction efficiencies of over 95% have been demonstrated with GLVs [49], with stable operation after ≈5 trillion ribbon cycles. Requiring only 7 mask exposure steps to create the devices [50], their fabrication is quite simple. GLVs have been demonstrated for the purposes of laser micro-machining [51] using UV sources, and while their application to femtosecond laser machining was not found in the literature, their similar constituent material layers to DMDs means that they would likely be a viable option. The major disadvantage of GLVs compared to DMDs is the necessary length of the moving micro-ribbons; in order to flex without breaking, while achieving a displacement comparable to the wavelength of illumination, the lengths of these ribbons are typically between 100–1000μm [49]. The width of the ribbons is not of as great a concern, with dimensions of ≈10μm being typical. This disparity between length and width means that GLVs are more practically used as 1D, rather than 2D, spatial light modulators.

Emerging new technologies for DMDs offer enhanced functionality, with MHz refresh rates and analogue mirror tilt angles being available in some models [52, 53], though these are typically produced as quai-1D arrays of MEMS mirrors, with a few rows by many thousands of columns of pixels in a 2D array. DMDs offer a promising combination of refresh rate and resolution within available SLM technologies, and as the underlying MEMS systems are enhanced, they will no doubt continue to be applied to ever-more advanced laser machining applications.

2.6 Conclusions

The light-matter interactions that occur when ultrafast laser pulses are used mean that there are distinct advantages to working with this type of laser source for micro-machining over longer pulsed sources. The high peak intensities available allow for multi-photon effects, making absorption in a wide variety of materials possible with a single central wavelength of light. The ultrafast timescale also means limited damage to non-exposed regions of a given sample, making ultrafast laser pulses an attractive option for high-fidelity laser machining.

DMDs are to be used as dynamic intensity masks throughout this thesis. A single DMD mirror of $\approx 10\mu$m to a side scales down geometrically on the described beam lines to below the diffraction limit, and hence the entire $\approx 1000 \times 1000$ array of mirrors can be used for the imaging of patterns of resolution at the diffraction limits of the systems. The behaviour of a DMD surface as a blazed grating means that high efficiency output is possible when using DMDs as intensity masks.

Various levels of software automation have been added to enhance experimental capability and fabrication speed during the PhD, some of which have been described in this chapter. This automation has aided experimental throughput in the current work, with such forms of automation being vital for the adoption of DMD-based laser fabrication methods by industry.

Chapter 3

Image projection-based subtractive patterning

A broad range of techniques, which will be referred to as 'subtractive patterning', focus on the targeted removal of material from a sample in order to produce a final structure. Typical examples include chemical etching, Focused Ion Beam (FIB) machining, and laser ablation. While FIB offers feature sizes down to a few nanometres [2], over large areas it becomes impractically slow, with typical removal rates in the μm^3/minute range [54]. The high peak intensities available in an ultrashort pulse ($\approx 10^{14} W/cm^2$ [4]) allow for the machining of a wide range of materials, as multi-photon effects enable absorption in materials which are transparent at low intensities for a particular wavelength. As the timescale of thermal conduction is long compared to the duration of femtosecond pulses, highly targeted material removal with minimal damage to adjacent regions is possible, as explained in section 2.2.2. Typical lateral dimensions of features produced via subtractive patterning with a single femtosecond laser pulse in this chapter range between ≈ 1–$100\mu m$, with depths on the order of ≈ 10–200nm. With a maximum repetition rate of 1kHz on the Ti:sapphire amplifier, this translates to a $\approx 10^7$ factor material removal rate improvement over FIB albeit at a much greater minimum feature size). Despite produced resolutions being diffraction-limited, this speed advantage makes laser ablation an attractive option for subtractive machining.

The method by which laser intensity is delivered to the desired region of a sample for targeted material removal must then be decided. A point-wise approach, such as galvanometer scanning [55], wherein a focused laser spot directed between points on a sample via the angular deflections of a small, light mirror, ensures a high optical transfer efficiency for material removal. Additionally, by translating the beam rather than the sample, faster relative repositioning of the beam spot to the sample is achieved than by translating the sample itself, for instance using relatively massive translation stages. The surfaces of samples will often not be suitable for large-area machining using galvonometer scanning however, as the focal positions of the beam for different angular deflections will describe a curved 2D surface; additional focussing optics, such as an f-theta lens, can be used in order to achieve foci over some extended region of a plane. In order to build up a continuous line, for example, or other pattern of removed material,

many focused pulses must be overlapped in galvonometer scanning, which may result in unintended structuring – one such result of which is exploited in Chapter 5.

An optical element may be used to split the intensity into multiple identical foci or images [56, 57], patterning many points on a sample simultaneously. The interference of multiple beams may also be used to produce periodic structures [58]. These techniques are useful for producing identical structures in a periodic fashion, however the focus of this chapter will be on the possibilities presented when machined features by sequential laser pulses are neither necessarily identical nor periodic. An image projection-based approach, achieved through the shaping of a laser pulse via a mask, can enable an entire pattern to be ablated in a single, or few, laser pulses. By using a DMD as a 'dynamic' intensity mask, which can be updated potentially thousands of times per second [21], in conjunction with mechanical translation stages for the repositioning of a given sample over the cm scale and femtosecond laser pulses, features produced in each pulse can be truly unique, as well as being positioned in an aperiodic manner. Figure 3.1 shows a simplified form of the setup, omitting focusing optics, to explain the process. A hollow square intensity mask is illuminated and imaged at the sample, machining hollow square features in a sample surface in a single pulse. The sample is translated mechanically between exposures to build up arrays of machined features.
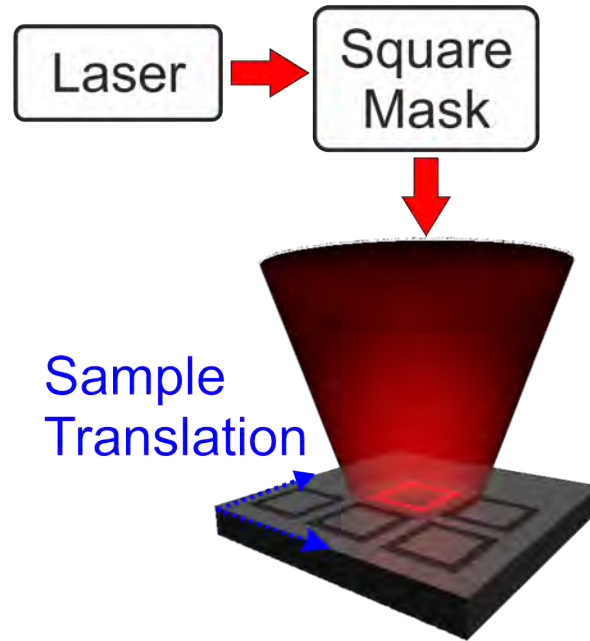
Figure 3.1: Simplified diagram of an array of identical hollow square features being built up with a combination of image projection-based machining and sample translation. Blue arrows highlight the two lateral directions the sample has been translated in between pulses. Homogenising and focusing optics have been omitted.

The first objective addressed in this chapter is to demonstrate and characterise subtractive patterning via DMD image projection-based laser machining in a range of materials. The ablation depths at particular fluences, required number of pulses for a given depth

and minimum lateral feature size were found by exposing arrays of regions of each material, which were translated between combinations of parameters to fresh regions of the samples. It was also informative for later experiments to observe the fidelity of image reproduction in the sample with increasingly complex masks displayed on the DMD (for instance, a wide range of feature sizes in a single mask). This consideration ultimately led to the adaptive optics approaches introduced in Chapter 6. The second objective was to demonstrate the machining of $\approx 1cm^2$ regions while maintaining the fidelity achieved in a single exposure, by stitching together many exposed regions of a sample which was translated between exposures; this would allow for macroscopic bespoke security markings, and the rapid prototyping of biomedical assays. Fluences stated in this chapter, and elsewhere in the thesis, were calculated by positioning a *Thorlabs* S120C photodiode power sensor beneath the objective, near the sample position, away from the focus such that the beam approximately filled the active area of the sensor. The DMD mask in question was displayed while the beam was switched to 1kHz mode, and highly attenuated via the continuous ND filter. The readings at low intensities on the photodiode were calibrated against the readings on the thermal power meter, and high intensity fluences were extrapolated linearly – high intensities could not be used directly for this measurement, as they would damage both the DMD and the photodiode. All intensity was assumed to be contained evenly within a perfectly minified image of the displayed DMD mask at the sample position, whose area was measured via SEM.

The image projection-based laser ablation of diamond has been demonstrated in section 3.1, with the published paper given in Appendix A. Minimum feature widths producible on the experimental setup in thin film materials has been tested in 3.2, in addition to the patterning of tens of square millimetres with features down to $\approx 1\mu$m achieved in section 3.3. Image projection-based subtractive patterning via DMD femtosecond pulse shaping is then used to produce stem cell growth assays in section 3.4.

3.1 Diamond ablation

The image-projection based ablation of polycrystalline diamond has contributed to published material [59], and this section will present results produced relevant to this work in the course of this PhD. Though diamond required significantly higher fluences to machine than other materials in this thesis, it was an existing objective within the group to machine the substance at the commencement of the PhD. Macroscopic area machining, reproducibility and minimum resolution size were not as of great a concern as simply demonstrating the feasibility of diamond machining via image-projection, and so it is shown as a promising first achievement in rapid laser micro-machining enabled by DMDs.

The high thermal conductivity, hardness and optical properties of diamond make it a widely used material across various industries [60]. Any process capable of high-resolution patterning of diamond, particularly at high speed, is then of interest. Laser

ablation via micro- and nanosecond pulses of diamond has been demonstrated previously, where the heat-affected zones associated with these longer pulse durations was noted [61] – using a 100μm spot, heat-affected zones of 350μm and 10μm extended diameter around the focused spot region were observed for micro- and nanosecond pulses respectively. Focused femtosecond pulses have been used to pattern diamond with a scanning point-wise approach, with minimum feature widths of 700nm achieved [62]. Micron-scale curved trenches and edges have been ablated in diamond using a phase-control SLM to produce accelerating femtosecond beams [63], while the combination of a deformable mirror and liquid crystal (LC) SLM has been used to correct for aberrations and allowed femtosecond machining inside bulk diamond [64]. At the time of publishing, no reports of image projection-based ablation in diamond were found.

Diamond is transparent across much of the visible spectrum, with an absorption edge at 225nm. For this reason, it is believed that on using an 800nm wavelength 150fs pulse, four photon absorption was responsible for most of the observed surface modifications. As m-photon absorption is proportional to the mth power of intensity, the ablation of diamond required the highest fluence at a sample position used in this thesis, $\approx 11.5 \text{J/cm}^2$. This fluence was used per pulse for each structure shown in the remainder of this section. Even so, modification was not clearly visible after a single pulse, and results in this section typically required ≥ 10 pulses to be observable under SEM. Interferometric profiling showed average depths of 69nm and 106nm after 10 and 50 pulses, respectively. Previous work on the femtosecond ablation of diamond [65] notes that initial pulses induce the graphitisation phenomenon, wherein at high temperatures a phase change occurs from diamond to graphite. As the thermal conductivity of diamond is high, a non-negligible amount of heating occurs over a thin layer even with femtosecond laser pulses, causing graphite to form, which is then more strongly absorbing during subsequent pulses.

Using the 100x microscope objective on the DLP3000 line to image DMD masks at the sample, which yielded a minification factor of $\approx 127\times$, the fluence used translated to $\approx 1.6 \text{mJ/cm}^2$ on the DMD itself. This was near to the damage threshold of the DMD, and was typically not possible to achieve on the DLP3000 line. In order to raise the incident fluence on the DMD, collimation lenses prior to the pi-shaper were repositioned such that the output of the pi-shaper was a near-homogenised circular intensity distribution of smaller diameter and higher peak intensity. Similar to the pi-shaper output seen in Figure 2.11, a smaller input beam diameter to the pi-shaper resulted in a 'ring' of high intensity around a near-homogeneous circular intensity distribution. While DMD masks were deliberately chosen such that they would be entirely exposed by the homogeneous region, the high number of pulses used in this experiment led to cumulative damage to DMD mirrors exposed to the high intensity ring, as shown in Figure 3.2.
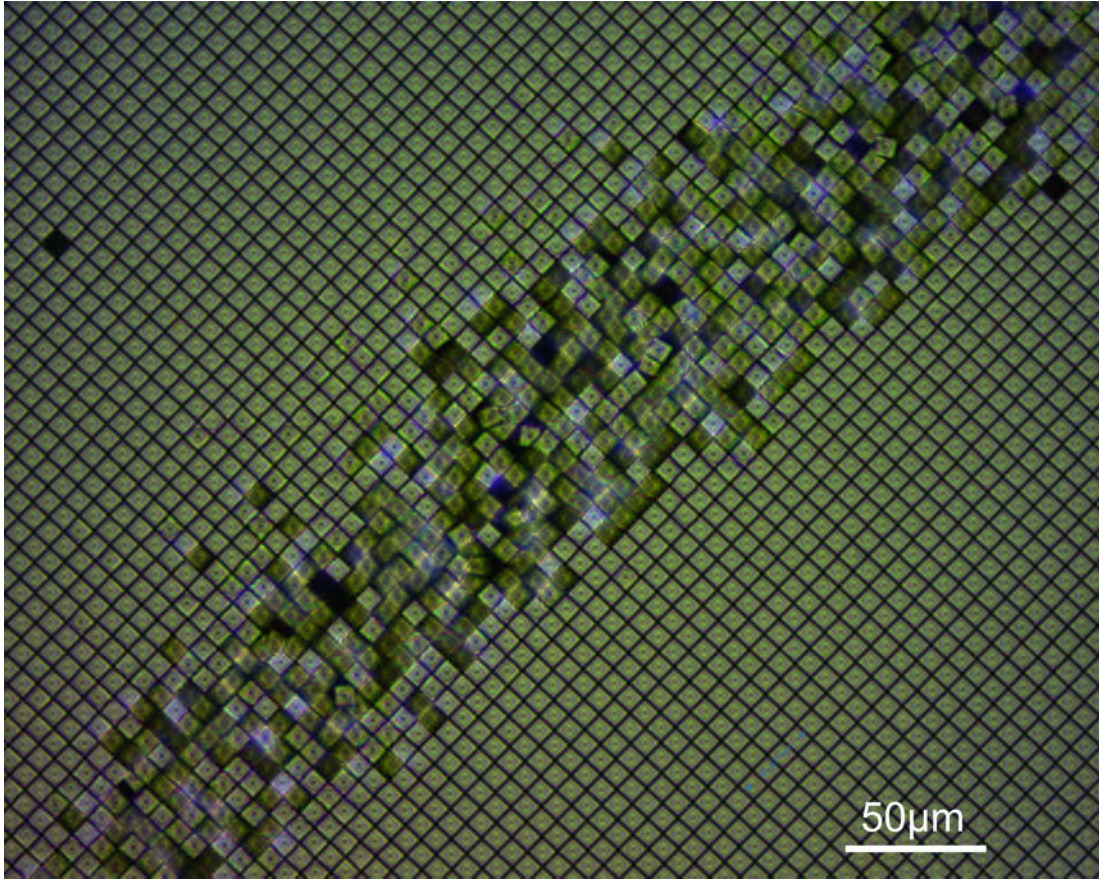
Figure 3.2: Optical microscope image of a damaged region of a DMD chip exposed to a high intensity 'ring'.

Alphanumeric characters were chosen as the shapes to display on the DMD as intensity masks during initial ablation tests on diamond. As large diamonds are a high-value item, the motivation for this was the possibility of rapidly ablating security codes onto diamonds' surfaces, for which alphanumeric characters are a natural choice. Additionally, alphanumerics provide a range of straight, curved and angled shapes, the machining of which helps to determine the fidelity of the technique.
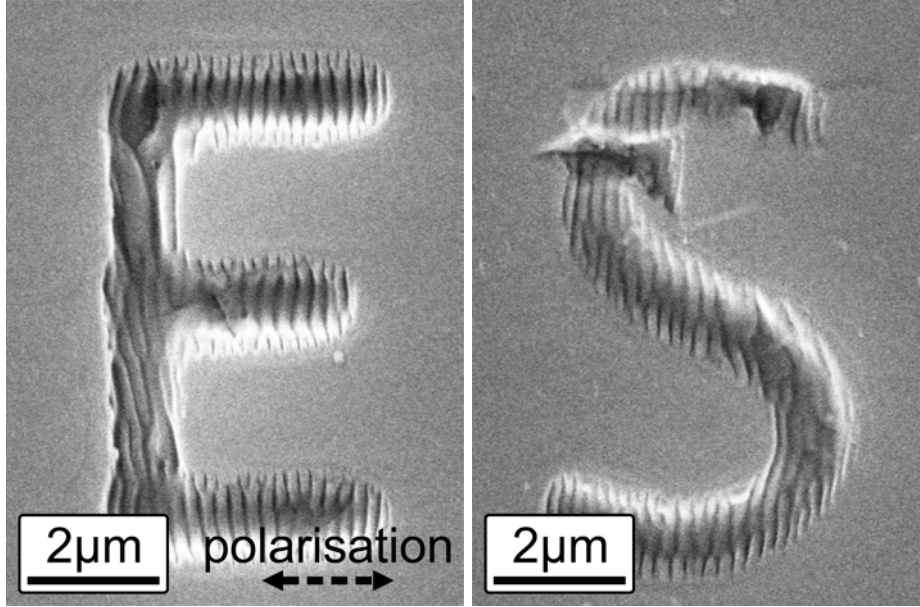
(a) The letter 'E' ablated in diamond in 10 pulses

(b) The letter 'S' ablated in diamond in 10 pulses
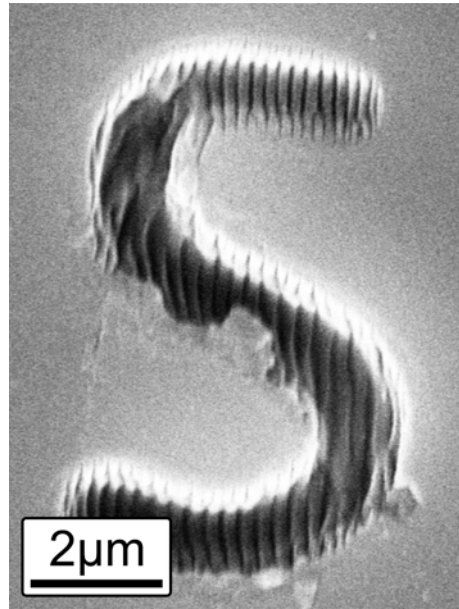
(c) The letter 'S' ablated in diamond in 50 pulses

Figure 3.3: SEM images of alphanumeric characters ablated into diamond in either 10 or 50 pulses at $\approx 11.5 \text{J/cm}^2$ per pulse.

Figure 3.3 shows the resulting features ablated in diamond after either 10 or 50 pulses. Figures 3.3(a) and 3.3(b) were machined using 10 pulses each, requiring 10ms total time to produce using a 1kHz repetition rate laser. Figure 3.3(c), produced in 50 pulses, accordingly required 50ms to machine. The average line width in each structure was measured to be ≈ 900nm. Visible in each of the three structures are ripple-like modulations, produced perpendicular to the direction of polarization of the incident pulses. These structures are typical of multiple femtosecond exposures at the same point on a

sample, and are known in the literature as Laser-Induced Periodic Surface Structuring (LIPSS); the effect can be reduced by using circularly polarized light [66].
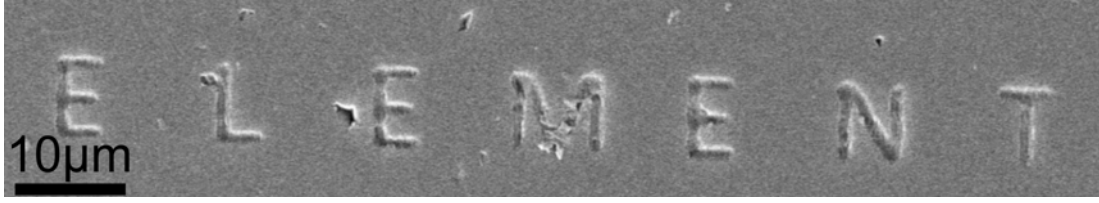
(a) The word 'ELEMENT' ablated in diamond in 10 pulses per letter
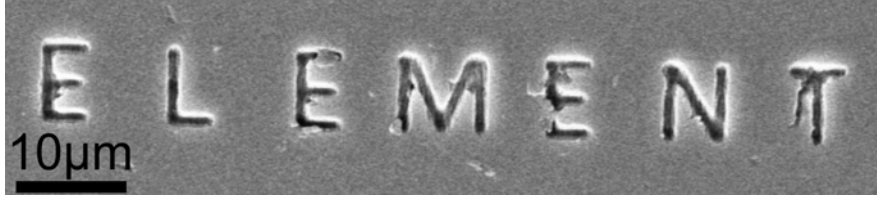
(b) The word 'ELEMENT' ablated in diamond in 50 pulses per letter

Figure 3.4: SEM images of the word 'ELEMENT' ablated into diamond using (a) 10 pulses per letter and (b) 50 pulses per letter. Individual letters were ablated in sequential pulses, and the sample translated to a new position between different letters.

Figure 3.4 shows the result of the technique when used to ablate features in close proximity in order to build up a final pattern. Each letter was machined in either 10 or 50 pulses, after which the sample was translated mechanically such that a nearby region would be exposed during subsequent pulses. The word 'ELEMENT' was machined in both cases, for a total of 70 pulses used to produce the structure seen in Figure 3.4(a) and 350 pulses to produce the structure in Figure 3.4(b). The technique clearly reproduced the letters displayed on the DMD in a recognisable form at the sample. To further test the technique, a 'bow-tie' pattern was displayed on the DMD – two opposite facing triangles with a gap between them. The result is shown in Figure 3.5.
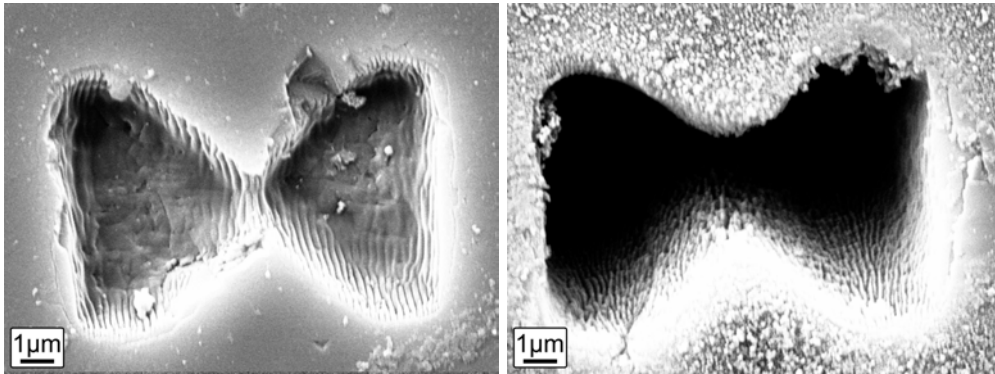
(a) A bow-tie shape ablated in diamond in 50 pulses

(b) A bow-tie shape ablated in diamond in 500 pulses

Figure 3.5: SEM images of a bow-tie shape ablated into diamond.

While the depth profile seen in Figure 3.5 is recognisably a bow-tie, the intended gap between the two triangles has not been produced. In Figure 3.5(a), produced in 50 pulses, the material in the region between the points of the two triangles has been removed, albeit at a shallower final depth achieved than in the majority of the exposed regions. After 500 pulses, the intended gap region has again experienced material removal, and the overall depth of the pattern is great enough that available spectroscopic and profilometer techniques could not discern the depth achieved. The material removal in the unintended region is a result of imperfect imaging of the DMD mask, an effect which will be present to some degree in the imaging of any spatial intensity distribution, to be considered in more detail in Chapters 5 and 6.

The line widths of the letters displayed on the DMD in order to produce the letters seen in Figures 3.3 and 3.4 were all approximately equal. However, when attempting to machine a complex pattern with multiple feature widths, the imperfect imaging problem which resulted in unintended material removal in Figure 3.5 may limit the range of line widths present in a DMD mask if an accurate reproduction at the sample is required. Figure 3.6 shows the result of the technique when attempting to ablate a complex pattern in 50 pulses. While the general form of the intended mask has been reproduced, clearly fine detail has been lost – particularly where fine line widths were intended, imperfect imaging has resulted in intensities too low to achieve ablation. An approach to address this problem is currently under development, and is discussed in section 6.4.
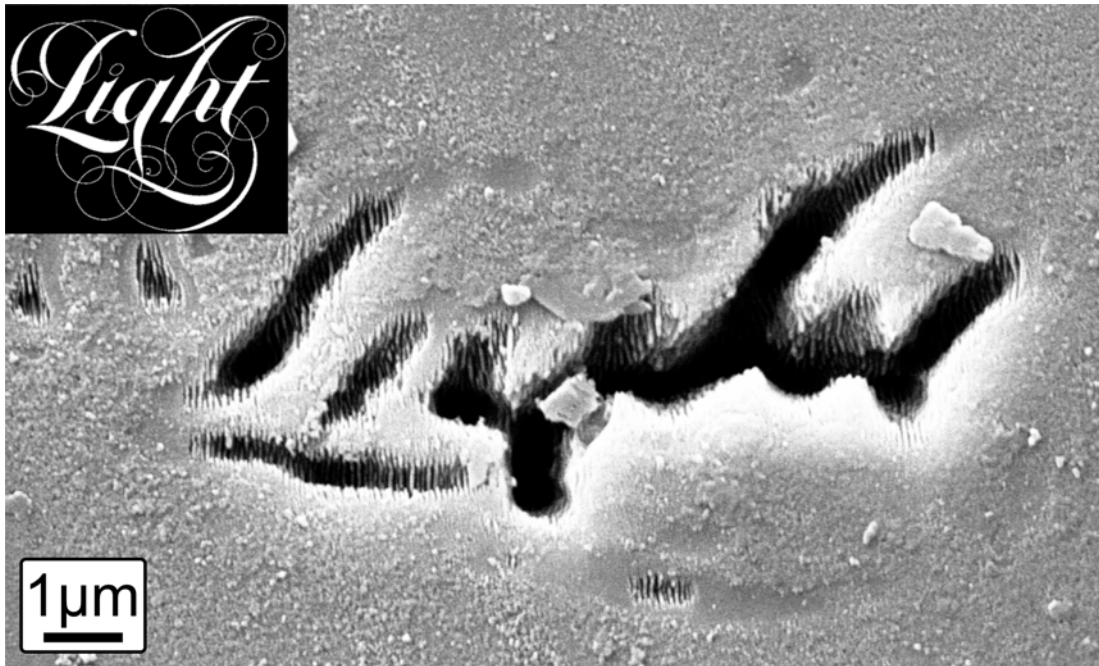
Figure 3.6: SEM image of the word 'Light', in complex script, ablated in diamond. The inset shows the mask as displayed on the DMD, while the SEM image shows poor reproduction in diamond.

In conclusion, image projection-based ablation has been used to pattern a typically difficult to machine material, namely diamond. In the published work, yttrium iron

garnet was also machined. Line widths of sub-micron sizes have been achieved, and the technique is adequate for the purpose of security marking high-value items with tags invisible to the naked eye. Future work would include characterising the optical properties of crystals machined with the technique, as the micron-scale feature sizes mean they would be suitable for some photonic applications.

3.2   Thin film ablation

In order to test the minimum separation attainable between subtractively patterned regions machined via the image projection of a single DMD mask, thin film materials (tens of nm) were chosen as samples. As ablation depths per pulse were typically on the order of tens of nm, ablation in undesired regions (as in Figure 3.5) after a single pulse in these thin films was expected to be visible with high contrast. Conductive materials (gold and carbon) were sputtered onto silica glass, so that both optical and SEM imaging could be used to readily observe the final result of the ablation. As the silica was transparent at 800nm and intensities were kept below levels where multi-photon absorption was likely to occur, this insulating substrate material was ideal for high contrast in both optical and SEM imaging. The threshold ablation fluence found for gold was 0.19J/cm^2; though the equivalent experimental conditions were not found in the literature, this agrees broadly with a threshold value of 0.25J/cm^2 using a 615nm 300fs source [67], and between 0.12–0.27J/cm^2 using a 400nm 150fs source. The threshold of 0.25J/cm^2 found in carbon agrees with behaviour observed by Lenner et al [68], where the ablation threshold when using a 100fs 800nm source was 0.13J/cm^2, but a sharp increase in ablated volume per pulse was observed above 0.2J/cm^2.

To investigate the minimum feature separation with the DLP3000 beam line using the 50x objective, a "split ring" pattern was chosen; a square with one side separated from the other three by a varying distance. Split ring resonators are a common structure in metamaterial design [69], where novel optical effects emerge when dimensions of the resonator are below the wavelength of incident light. While more commonly the final split ring will be comprised of conductive material, in this experiment a 'negative' of the split ring design will be produced in surrounding conductive material – a 'complementary split ring resonator' [70], which has been studied for applications in microwave device design.

(a) Rapid repeatability

(b) Low feature separation
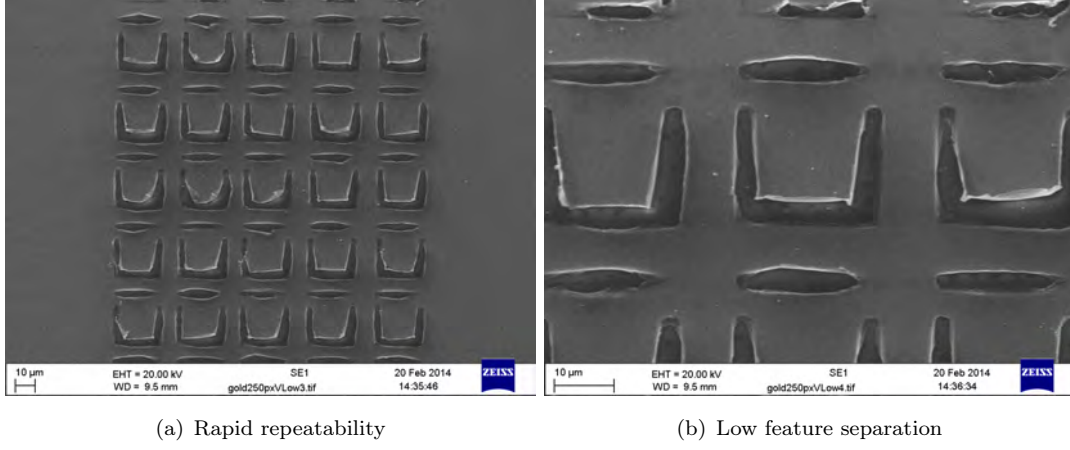
Figure 3.7: Split rings ablated in single pulses into a 30nm thick layer of gold coated on a glass slide using an energy density of 0.19J/cm^2. All four sides of each split ring were displayed on the DMD during each exposure.

Figure 3.7 shows the repeatability of the method, wherein arrays of dozens of split rings are produced sequentially using one pulse each. A range of split ring overall widths and line widths were displayed on the DMD during separate pulses. Feature separations of $\approx 2\mu m$ in a 30nm gold layer deposited on a silica glass slide were achieved, while line widths in the ablated regions making up the sides of the split rings are $\approx 4\mu m$. Though there is evidently some peeling of the gold layer from the underlying silica, in future a thin (≈ 5nm) layer of chromium could be deposited before the gold [71], or a post-deposition annealing step [72] could be performed, for better adhesion.

(a) Limit of separate features in gold

(b) Peeling problem in carbon
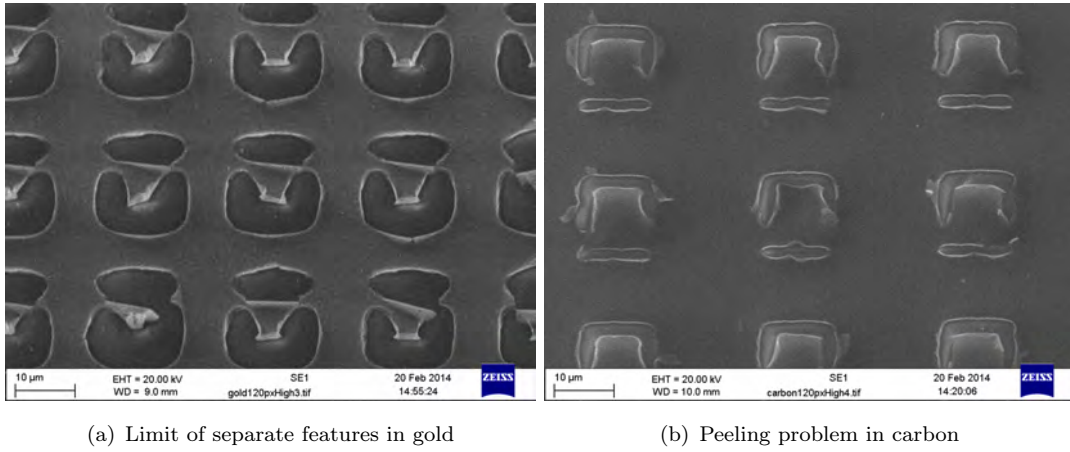
Figure 3.8: The limit of feature separation of a split ring displayed for (a) 30nm thick gold compared with the same image ablated in (b), a $\approx 50nm$ thick carbon layer. Both ablated with an energy density of 0.25J/cm^2. Carbon displays line widths as small as $\approx 2\mu m$, half the line width for the same projected image as gold.

Figure 3.8 shows a comparison of an image at the minimum recognisable ablated image size ablated in gold compared to that achieved in carbon. Total full feature widths

of $\approx 10\mu$m were achieved in both materials. The smaller line widths in Figure 3.8(b) than in Figure 3.8(a) ($\approx 2\mu$m in carbon vs $\approx 4\mu$m in gold) suggests that peeling is a material-dependent property which limits the technique in thin films. Diffractive effects, as discussed in Chapters 5 and 6, lead to the incidence of intensity at undesired regions around the edges of any projected intensity pattern, as in the previous section. In this case the undesired intensity appears to have been great enough to overcome the adhesive bond strength between gold (and to a lesser extent carbon) films and the underlying silica substrate, causing material removal via peeling outside of the intended area of intended removal via ablation.

While the split rings produced are clearly above the dimensions required for visible light metamaterial applications, their $\approx 10\mu$m scale may mean that they are viable for use in the terahertz – far infrared range. Future work would include a similar 'remaining feature' limit test when imaging the negative of the DMD masks used in this section, such that split ring resonators comprising conductive material remain on the silica substrate.

3.3   Rapid Patterning

A technique for the patterning of areas of tens of square millimetres with single micron accuracy is reported in the paper "Fabrication of variable period grating structures via laser ablation using a digital micromirror device", in Appendix A. This section will expand upon the content of this work.

Gratings are a common optical component, and the flexibility and rapidity of their manufacture is of interest to the optics community and industry. Femtosecond pulses have been used previously in the production of grating structures, commonly fibre Bragg gratings [73–75], using phase masks in combination with incident light to create a refractive index change in the target material; a more complete review of femtosecond fibre Bragg grating production can be found in [76]. Focused spot scanning of femtosecond pulses has also been used to write fibre Bragg gratings [77], as well as to ablate grating structures at a scale visible to the naked eye [78], while two-beam interference of femtosecond pulses has been shown to produce grating structures deep within materials [79] and with sub-wavelength periods [80].

In this section the versatility, rapidity and scale possible with DMD femtosecond laser machining is demonstrated. Many thousands of individual diffraction gratings are ablatively patterned in close proximity to one another, each of which may have a distinct period from its nearest neighbours. The final marked surface appears as a coloured image with a size of ≈ 1cm.

3.3.1 Method

The procedure involved in the fabrication of large-scale variable period grating arrays is shown via a simplified example in Figure 3.9, which shows the machining of individual letters into a surface. In all results shown, the target sample was a 750nm thick bismuth telluride (BiTe) film on a glass substrate. The ablation threshold of the BiTe film was found to be approximately 35mJ/cm^2. The energy density used to produce the sample in Figure 3.9 was $\approx$90mJ/cm^2 – this value, being over 2 times the ablation threshold, ensured ablation deep enough to be clearly visible under optical and scanning electron microscopes. Figure 3.9(a) shows an SEM image of a letter 'A', which was ablated using a single laser pulse, with the inset showing the pattern that was displayed on the DMD. Figure 3.9(b) shows an SEM image of six different letters, where each letter was also ablated using a single laser pulse, with DMD pattern updating and stage movement after each pulse. In this example however, the sample was actually moved continuously, and the timing of the updating process on the DMD was linked to the activation of the Pockels cells in the laser amplifier, which resulted in the generation of a laser pulse.

In the previous sections of this chapter, the sample was allowed to come to rest before ablation via image projection, which limited the processing speed. By continuously moving the sample during machining, it was possible to project multiple images per second at different regions of the sample; the repetition rate of the laser was 1kHz, and the DLP3000 capable of refreshing up to 4kHz, and so 1000 distinct subtractively patterned regions should be possible to machine per second. In order to maintain positional accuracy however, and due to the image upload method used (HDMI cable), results in this section were generated at a rate of 8 machined regions per second. The procedure could be repeated indefinitely to produce a desired final pattern by controlling the stage movement in 2D; a larger region is shown in Figure 3.9(c). Consecutive letters were machined in the vertical direction in Figure 3.9(c), the purpose of generating this structure was to ensure that little drift of the sample occurred between lines of letters, and that the DMD reliably updated at a particular frequency. Note that to the left of Figure 3.9(c) each letter is repeated 5 times before switching, while to the right a different letter is displayed during each pulse. The frequency of switching increases from left to right across the Figure; ten lines of letters were machined at each DMD mask switching frequency, all whilst moving at a speed of 0.25mm/s.

The automated process, which combined the laser pulse generation, stage movement and DMD update process, required an input *sample map*, which specified the structure that should be ablated at each position on the sample. In practice, the sample map was a 2D array of numbers, where each number corresponded to a particular DMD pattern. For the case in Figure 3.9(c), the sample map was a 2D array that consisted of the set of numbers [1 – 6] which corresponded to the projected letters [A – F].

To produce grating structures, the DMD patterns were specified as a set of parallel lines whose spacing and line width were both under computer control. Figure 3.10 shows the DMD patterns used together with corresponding SEM images of structures
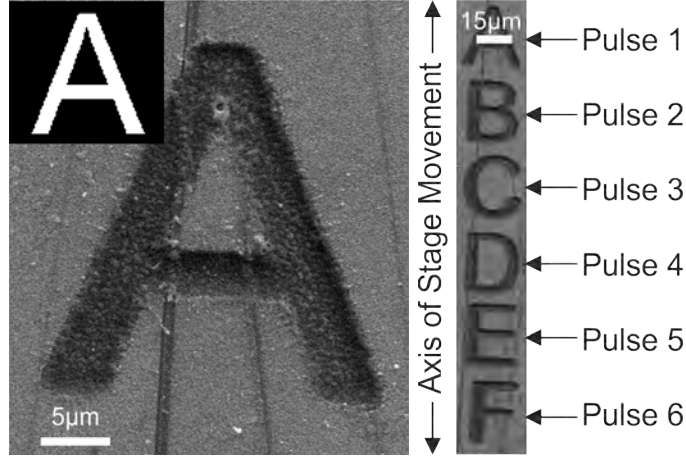
(a) Ablation of a single structure (with the DMD mask inset)

(b) Ablation of six distinct structures, machined using six sequential laser pulses
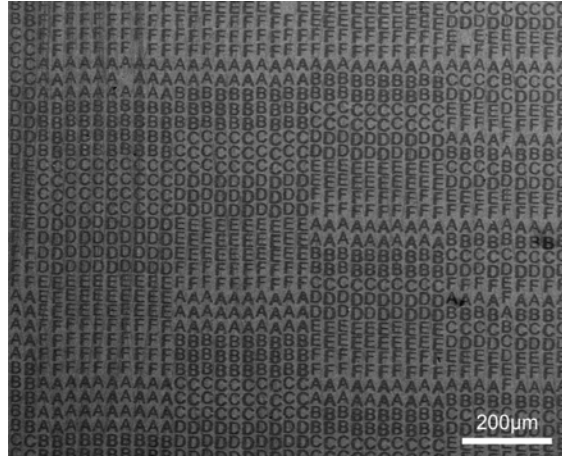
(c) 2D contiguous array of machined structures

Figure 3.9: Demonstration of the image projection machining technique in 750nm thick BiTe at a fluence of 90mJ/cm^2.

that were ablated in single pulses. Different grating periods corresponding to 2.0μm in Figure 3.10(a) and 2.5μm in Figure 3.10(b) are shown. Though the aspect ratios of the resultant ablated features matched the DMD patterns used to produce them, a slight rounding of the end of each line in the ablated grating patterns is evident. This effect, a result of the impossibility of collecting all spatial frequencies present in a mask for imaging, is discussed further in Chapter 6.

(a) Final period of 2.0μm

(b) Final period of 2.5μm
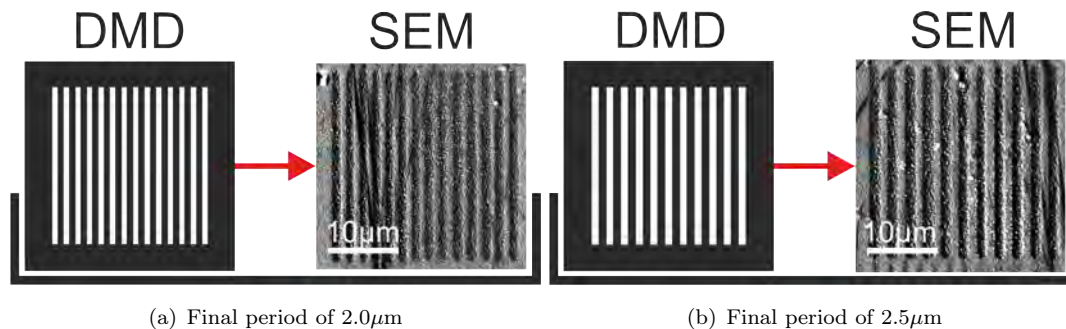
Figure 3.10: DMD grating images and associated SEM images of ablated structures in 750nm thick BiTe at a fluence of 90mJ/cm^2.

3.3.2 Large scale structures

The ablated gratings in Figure 3.10 produced from a single laser pulse were to produce observable diffraction under white light illumination, displaying a colour that was a function of grating period, illumination and viewing angle. Using the approach described in Figure 3.9, where a sample map was used to specify the structure that should be ablated at each position on a sample, it was possible to ablate an *array* of gratings that, when photographed, appeared as a 2D array of differently coloured squares. Figure 3.11 shows an example of this approach, where the sample map consisted of two different DMD patterns corresponding to two different grating periods, where the upper left pattern in Figure 3.11 was used to display colour corresponding to the letters 'DMD', and the lower pattern to generate the coloured background. Figure 3.11 shows a photograph of the final diffractive structure of size 9mm by 7mm, which contains 70200 separate gratings, written at a fluence 90mJ/cm^2 per pulse, with grating periods of 2.0μm and 2.5μm for the letters and background respectively. Due to the close proximity of the camera to the sample when taking the photograph, the viewing angle dependence translates into a variation in diffracted colour across the sample, and hence the three letters that formed the word 'DMD' display a colour gradient. At a longer distance, of 50cm, when viewed by eye all three letters displayed the same diffracted colour.
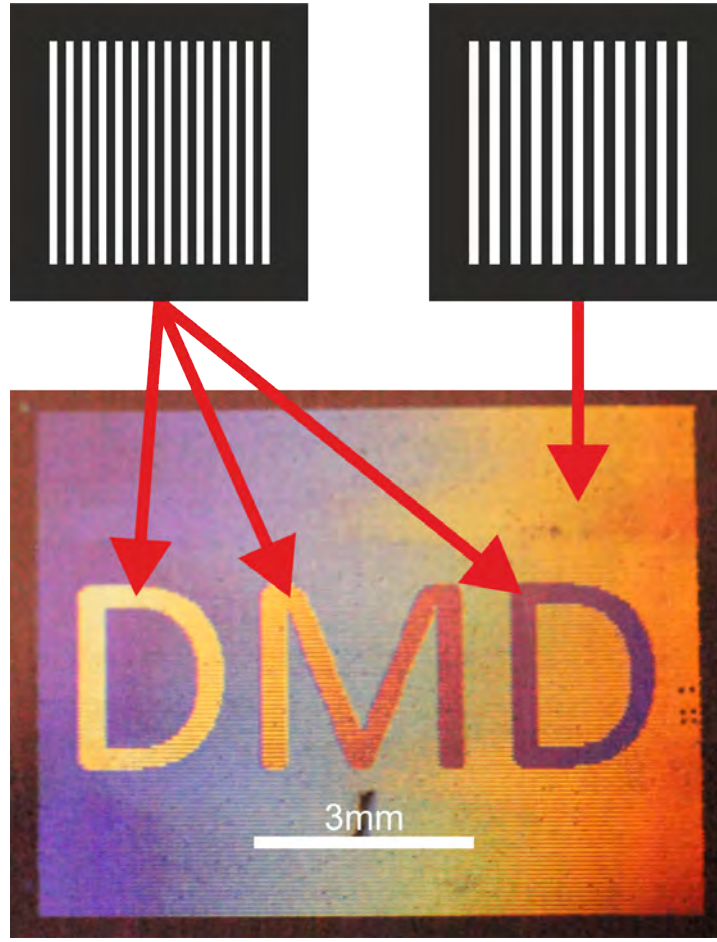
Figure 3.11: Schematic showing two different DMD masks which correspond to regions of a photograph of a 2D array of grating structures ablated in 750nm thick BiTe, with each structure ablated at a fluence of 90mJ/cm^2. The letters and background correspond to grating periods 2.0μm and 2.5μm respectively. The spacing between adjacent gratings was 30μm.

The method was extended to multiple grating periods, to fabricate a more complex sample. Figure 3.12 shows the effect of using 9 different DMD patterns, each with a different period, to form a sample of size 9mm by 7.5mm, comprising $\approx$43,000 gratings. Each grating was $\approx$30μm in lateral dimensions, and the gratings were also spaced by approximately this value. Noise in the velocity of the sample, likely introduced from the mechanism of the stepper motors on the translation stages, meant that there was an error in this spacing of $\approx \pm 2\mu$m. The sample map was defined to reproduce the appearance of the Morpho butterfly, whose wings display a striking blue colour due to their grating-like structures, typically of period $\approx$1μm [81].
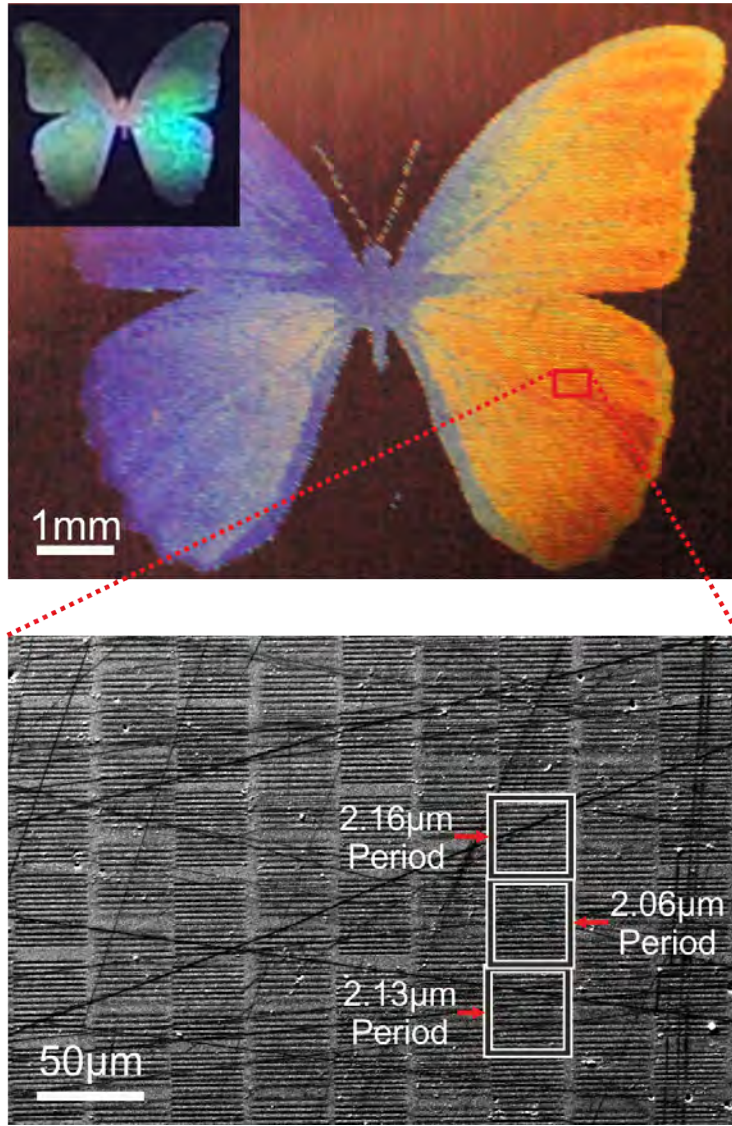
Figure 3.12: (Upper) Photograph of light diffracted from a 2D array of grating structures, with an inset showing a photograph of the structure from a greater distance which displays more symmetric colouration. (Lower) An SEM image of a section of the sample, showing a variety of different grating periods. The criss-crossed lines observable on the sample are pre-existing scratches on the sample. The sample substrate is 750nm thick BiTe, and each grating structure was produced at a fluence of 90mJ/cm^2.

While the colours produced in Figure 3.12 varied from blue to red in the horizontal direction due to the position of the camera and direction of incoming ambient light, when observed by eye at a larger distance, the reduced incidence and output angles correspondingly resulted in a reduced spectral range at the eye, i.e. gratings of identical period from different regions of the sample appeared as the same hue when viewed from a large distance, as in the inset of the photograph. The variation in colour at a large viewing distance was caused by variations in the period of the gratings that were ablated in the sample, where the position and periods of the ablated gratings were chosen in order to replicate the appearance of the vein-like detail present on butterfly wings. Whilst we have demonstrated here a butterfly profile, many other patterns, such as a logo or an identification code, could also be readily produced. The lower portion
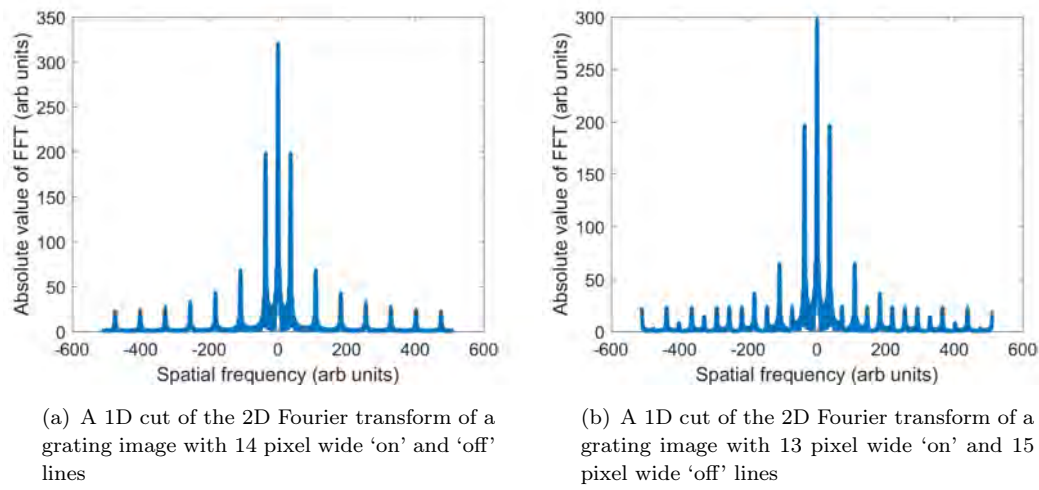
44

of Figure 3.12 shows an SEM image of a small section of the fabricated structure, and demonstrates the variation in the period of several adjacent gratings (2.16μm, 2.06μm and 2.13μm). The maximum resolution of the detail on the butterfly image corresponded to the size of the individual gratings, at 30μm. The region outside the butterfly profile was not ablated to increase the visibility of the fabricated sample, and demonstrates that arbitrary perimeter shaping is possible with the technique.

3.3.3 Discussion

In this section, patterns such as those shown in Figure 3.10 were ablated via single pulses into 750nm thick BiTe, which comprised 30μm$\times$30μm diffraction gratings, using the DLP3000 line. By covering macroscopic areas in these gratings, coloured images, which were visible to the naked eye, were formed. In order to diffract different colours at a given angle from different gratings, the periodicity of the gratings had to be varied. To obtain equal ablation depths of grating patterns, the intensity at each region in the imaged DMD surface should be equal. In a perfectly recreated image of the DMD surface, using a homogenised input pulse at the surface of the DMD, this would be trivial. However, a subtlety of the DLP3000 line had to be accounted for.

The collimating lens forms a diffraction pattern of the DMD image at the back of the 50x objective, before being imaged to a minified version at the sample. The opening at the back of the objective effectively creates a spatial filter, so that some proportion of high spatial frequencies are removed. The grating images can still be almost faithfully recreated using only lower spatial frequencies, but there is some power loss under some conditions. By taking the Fourier transform of various grating DMD images of various line separations, as one might expect, for smaller grating periods more intensity is lost in these high frequencies. As the pulses arrived at a rate of 8Hz, it was unfeasible to attenuate the input power differently for each pulse to account for this using a translating variable neutral density filter as was usually used.

This was then a limiting factor in the number of different grating separations that were possible to be recreated at a given input pulse intensity with the setup – for equal on/off line widths, large separations would ablate much more deeply than small separations, as a higher proportion of intensity entered the 50x objective in the central few maxima of the diffraction pattern of large period grating images. To compensate for this, the ratio of on/off line widths was varied – for instance, a total separation of 28 pixels was typically achieved with 'on' lines 13 pixels wide and 'off' lines 15 pixels wide. Considering the Fourier transforms, as shown in Figure 3.13, a greater proportion of total intensity is further from the central maximum for gratings of total period 28 composed of 13 pixel wide 'on' lines and 15 pixel wide 'off' lines than for 28 pixel period gratings of 14 'on' and 'off' lines. Thus, more power was lost for the 13 'on'/15 'off' gratings at the entrance to the 50x objective. By empirically testing different ratios of on/off line widths, appropriate values were determined to use in order to achieve similar ablation strengths for different total grating line separations.

45

(a) A 1D cut of the 2D Fourier transform of a grating image with 14 pixel wide 'on' and 'off' lines

(b) A 1D cut of the 2D Fourier transform of a grating image with 13 pixel wide 'on' and 15 pixel wide 'off' lines

Figure 3.13: A comparison of Fourier transforms for varying the ratio of on/off line widths.

Additionally, maintaining the imaging position (or 'focal position') with relation to the height of the sample was a difficulty. As described in section 2.4.2, prior to beginning a scan over a 2D region, the 3D positions of 3 'in focus' points at the corners of a square within which machining would occur would be manually found and provided to the software. Sample translation would then include repositioning parallel to the direction of the beam ('z direction'), to account for an initial 2D sample which was not ideally perpendicular to the beam line. This was sufficient to maintain focus to an acceptable degree during the production of results in this section, though backlash on the translation stages meant that, line-to-line, there was a slight change in z-position. Note in Figure 3.9(b) that sample translation occurs in both the positive and negative directions while trains of pulses are incident on the sample, i.e. for one line of machined patterns the sample would be translated upwards, while during the next line it would be translated downwards. The 3D interpolation of focal positions made no adjustments for the direction from which focal adjustments were being made, and so the assumed focal positions were off by as much as the backlash of the translation stages: a few microns. As the initial 3D points were set after a movement in one particular direction, this meant that focal position was maintained well while moving in one direction, while being maintained poorly in the opposite direction, as can be seen from Figure 3.14. The line widths of the letters 'A' and 'F' are clearly thinner in some vertical lines compared to adjacent lines – the result of diffraction of the optimally imaged DMD mask over the small backlash error distance. Though this error did not greatly impact the results of this section, when working with the 100x objective (which has a shorter working distance), or relying on multi-photon effects (which are more sensitive to small changes in intensity), it must be taken into consideration.

46
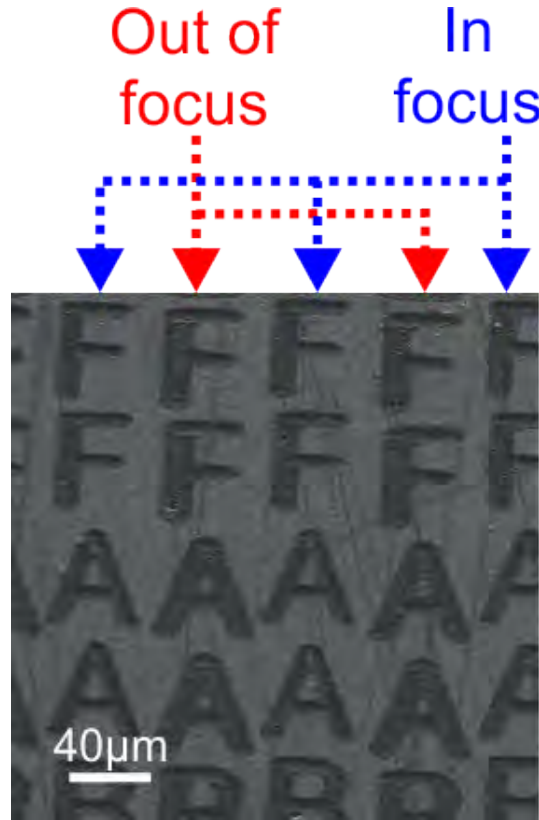
Figure 3.14: Image position is maintained while scanning vertical lines in one direction, but is a few microns off while scanning in the opposite direction. The diffraction of the optimum image over this small error distance amounts to wider line widths of ablated features.

Although the maximum repetition rate of the laser used was 1kHz, it was operated at 8Hz for these trials, limited by the positional accuracy and data upload method at our disposal; this should not be considered as an intrinsic manufacturing limitation. The sample shown in Figure 3.11, which contained 70200 gratings, took a total time of 150 minutes for fabrication. With faster stages, at the maximum repetition rate of the laser of 1kHz, the total fabrication time could be reduced to just over one minute. Although the work presented here used a 750nm thick BiTe compound semiconductor film on a glass substrate, other materials, including metals, ceramics, and polymers were also successfully laser-machined using this technique. Bismuth telluride's high absorption at 800nm wavelength [82], and hence efficient ablative machining with our laser source, led to its predominant use in this work. The smallest grating period achieved (2.06μm) was comparable to many results presented in [73–77], though larger than the smallest reported period of these of 1.07μm [77]. The interferometric gratings produced in [80] achieve yet smaller results of 400nm, though it should be noted that all of these results are produced by specialised grating-production methods, while DMD-based image projection laser-ablation is suitable for the writing of more diverse patterns. This shows that image projection laser-ablation using a DMD can yield comparable results in feature size to custom-built phase masks, while machining areas with non-identical patterns over an arbitrary area.

3.4 Stem cell scaffolds

Regenerative medicine is a branch of research dealing with the replacement, construction or regeneration of individual cells, tissues or whole organs. Stem cell research is then a subset of this field, dealing with 'pluripotent' cells which may develop into the various cell types in the body. There are several steps of development between 'embryonic' stem cells, which may follow a differentiation pathway to become *any* cell type found in the human body, and cells which have developed to a final state. Intermediate cell types are still referred to as stem cells, for instance Mesenchymal Stem Cells (MSCs), which may further develop into bone, cartilage, fat, tendon, muscle or marrow cells [83].

The work in this chapter relates to an ongoing collaboration with a group specialising in research into MSCs, led by Professor Richard Oreffo. Mounting evidence has been found by the group that surface topography of cell culture growth assays influences cell adhesion and differentiation [84–87]. Typical surface modulations thus far have been circular holes with depths of tens of nanometres, and centre-to-centre separations of a few hundred nanometres; a great deal of investigation into the parameter space of topographical modification remains to be made. A 'final product' for the team may take the form of an implant or prosthetic, made from a bio-friendly material, whose surface is micro- or nano-machined to promote cell adhesion and multiplication while controlling differentiation.

Image projection-based subtractive patterning with femtosecond laser pulses then presents a rapid method to trial a wide variety of materials and topographies. The motivation for particular topographies generated in this section will be given briefly where possible, but is largely up to cellular signalling pathways better understood by Oreffo's team. Thus far, feature sizes on the order of $\approx 10 \mu$m lateral dimensions of height/depth 10–100 nm, separated by $\approx 30 \mu$m have been the aim, roughly on the size scales of living cells.

3.4.1 Directly machined assays

One of the most important criteria for any final growth assay was that it be large enough for a statistically significant number of cells to be grown, as well as to be manipulated by hand – on the order of a few square millimetres to 1cm^2. In order to study whether cells would preferentially multiply, differentiate or even migrate between different topographies, a growth assay similar to that in Figure 3.15 was desired.
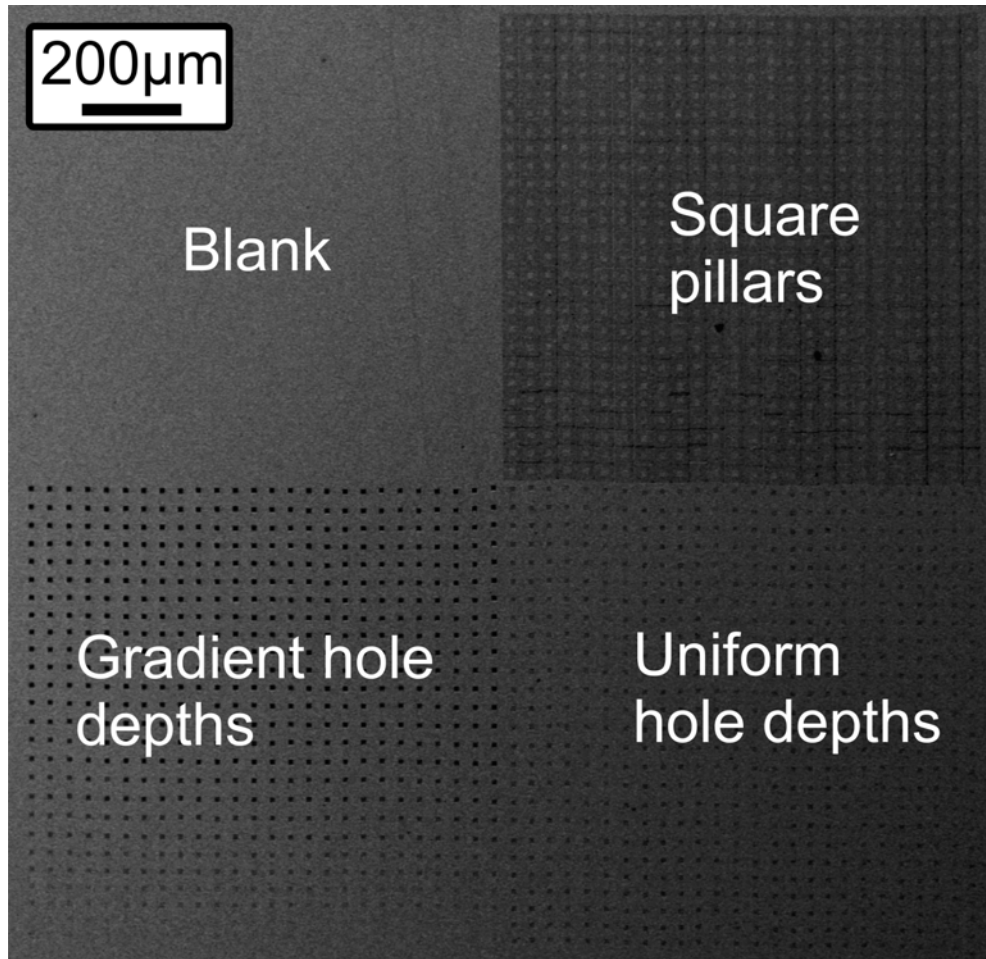
(a) SEM image of 4 adjacent quadrants
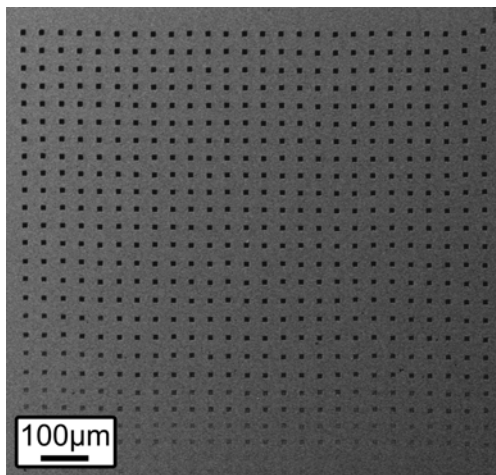
(b) SEM image of the 'gradient depth' holes quadrant
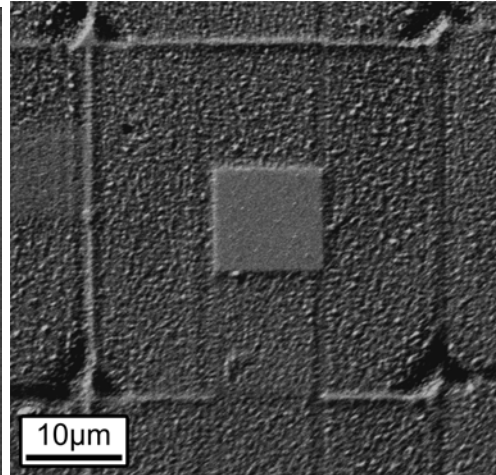
(c) SEM image of a single 'pillar' produced by the ablation of surrounding material

Figure 3.15: A 200nm thick BiTe substrate patterned with different DMD masks and numbers of pulses in 4 adjacent quadrants. All four quadrants are shown in (a), the four regions are (upper left) blank, (upper right) pillars, (bottom left) gradient depth, (bottom right) single depth. (b) shows a higher magnification image of the gradient depth holes, and (c) shows a yet higher magnification of a square 'pillar'. Each pulse used was at a fluence of 140mJ/cm^2 – a fluence well above threshold, to ensure high ablation depth per pulse.

49

While the blank quadrant required no modification, and the uniform depth quadrant in the bottom-right quadrant of Figure 3.15(a) required simple translation between pulses, the 'gradient depth' and 'pillar' quadrants in Figures 3.15(b) and 3.15(c), whose specifications are given below, required new methodology.

The square holes in the gradient depth quadrant were intended to be of uniform depth for one line of identical squares, separated by uniform distance, and of gradually decreasing depth for subsequent lines (reducing depth vertically in the figure). While this could have been achieved via intensity modulation, repeated exposures at the same locations on the sample were used for an increased range of depth modification – at the maximum available intensity tens of nanometres were ablated per pulse, while using up to 13 pulses as for Figure 3.15(b) it appeared possible to machine through the entire 200nm depth of BiTe. With a reduced energy per pulse, more pulses per exposed feature were required to produce a given depth modulation in the uniform square hole and pillar regions; 3 pulses per exposed feature were used for these.

The 'pillar' quadrant, i.e. square regions of material standing above the local average surface of the substrate, were generated by stitching together regions machined via the exposure to a hollow square-shaped intensity profile. In fact, earlier tests wherein entire hollow square patterns were exposed at once resulted in rounded corners of the remaining square pillar, likely due to the imperfect imaging seen in earlier sections of this chapter, and so each hollow square was ablated by exposing one 'side' of each square at a time. This meant that each pillar, as seen in Figure 3.15(c), required 12 pulses to be generated (3 pulses per side of each square). While square pillars were produced, it is clear that the 'stitching' of regions of removed material was sub-optimal – thin bridges of under-ablated material remain prominently on the upper and left sides of the square pillar shown in Figure 3.15(c), while too great a depth has been machined at the corners of the hollow square-exposed regions.

Although improved image-stitching may allow higher fidelity pillars to be produced in this way, ultimately the approach has had little further development due to fabrication time. Exposing the same region to multiple pulses requires acceleration of the sample between each machining point – a slow process compared to that shown in Section 3.3. The assay in Figure 3.15 was generated in ≈2 hours, and was ≈1mm on each side. This translates to an unfeasible ≈200 hours per assay of the desired size; this issue is compounded by ≈10 copies of each assay being required for cell behaviour to be demonstrably repeated. Rather than continuing to improve machining accuracy for a point-by-point ablation method, the continuous sample translation in Section 3.3 was paired with a moulding technique to more rapidly produce assays.

3.4.2 Moulded assays

The image projection-based subtractive manufacture of individual cell growth assays is a time-intensive procedure requiring specialised equipment. For the production of

unique structures it is an attractive tool for the reasons outlined earlier, however the requirement in this case of ≈10 copies of each assay meant that a moulding process could greatly reduce the cost of production.

Poly(dimethysiloxane) (PDMS *Dow Corning* SylGard 184 silicone elastomer kit) was used to drop-cast 'master' assays machined in other materials; curing on a hot-plate at 120°C for 1 hour, with or without a silica glass backing layer, meant that near-identical copies of a laser-machined master could be produced with little labour and inexpensive equipment. A release layer of 10% soap in ethanol by weight was applied and allowed to dry on masters before drop-casting. The assay in a cast would be the 'inverse' of the master, i.e. holes in the master would produce pillars in the cast. PDMS has a variety of properties beneficial to this study [88]. Flexibility and ease of bonding to other surfaces would mean a 2D assay could be bound to a curved surface, such as on an implant. Impermeability to water, permeability to gases and nontoxicity to cells are particularly important for biological studies. Being transparent down to 230nm, optical transmission microscopy can be readily used to observe cell growth in situ – a difficulty when working with other popular growth assay materials, such as titanium. Additionally, casts of the master assay could be used as 'secondary masters' as shown in Figure 3.16, typically reapplying the release layer and 'soft-baking' the second cast (≈90°C for 1 hour). Given a laser-machined master where the active region of the assay is patterned with holes, the first cast would then contain pillars, and the secondary cast would contain holes.
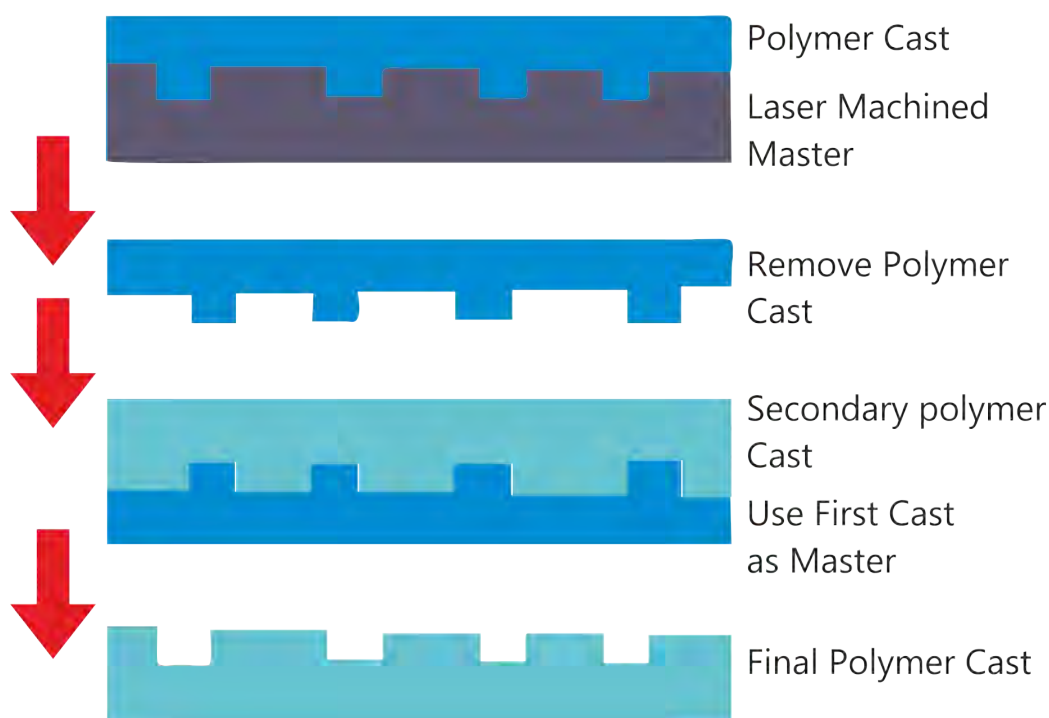
Figure 3.16: Polymer drop-casting is used to increase production speed of identical assays. Casts with inverse features to the master can be used to produce secondary casts with features identical to the master.

As well as allowing for the production of biologically-friendly assays with both holes or pillars, multiple primary casts could be used to produce many secondary casts in parallel, if the desire for more copies of a single assay arises. Though the secondary cast process has been used successfully with laser-machined masters in this section, an investigation into the fidelity of feature reproduction for successive generations of 'master' remains to be made.

Initially a 500nm layer of bismuth antimony telluride (BiSbTe) on silica was used as a master assay material. A similar 4-quadrant structure to that in Section 3.4.1 was produced using the continuous stage translation technique, albeit with trains of pulses incident on the DMD only during stage translation in a single direction, to avoid the backlash problem encountered in that section. Each feature was machined in a single pulse then, at a maximum fluence of $760 \mathrm{mJ/cm}^2$; variation below this fluence was achieved with the greyscale DMD mask display technique described in section 6.3, and was used intended to produce linear attenuation of intensity at the sample by a factor of 0–0.5 over the 'gradient hole' region. The pillars were achieved via attempted stitching of hollow-square features exposed in single pulses during sample translation, rather than ablating each side around the square pillar consecutively. The rounding of the corners on the square pillars was slightly greater than in Figure 3.15(c), as seen in the SEM image in Figure 3.17, and the stitching considerably poorer.
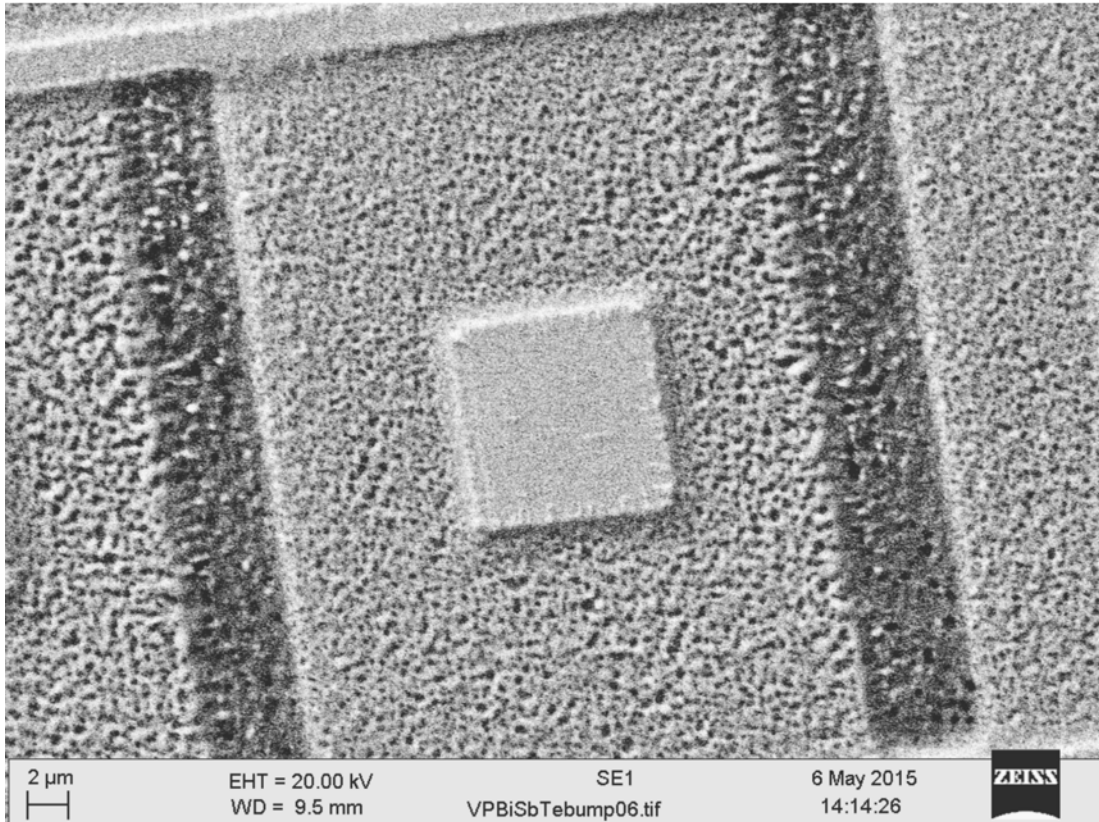
Figure 3.17: A pillar machined in BiSbTe via continuous sample translation and stitching of regions exposed to hollow square-shaped intensity distributions.

As the moulding process ultimately allowed the production of both pillar and hole-patterned assays, attempts to produce pillars directly via laser-machining were halted after this test. This will temporarily impede the study of migration of cells between regions patterned with holes and regions patterned with pillars, but the rapid production of assays with varying feature dimensions, even if the assay comprises only holes or only pillars, was deemed a priority. Incorporating image recognition techniques described in section 6.2 may allow the 4-quadrant design to be reliably produced in future.

A further complication associated with PDMS casting is highlighted in an extreme case by the optical microscope images in Figure 3.18. Contamination of the PDMS cast by master material, and damage to the master by the peeling of the PDMS cast, was a particular difficulty when using thin film materials as masters.


(a) Optical microscope image of pillar region of master post-casting

(b) Optical microscope image of pillar region of cast
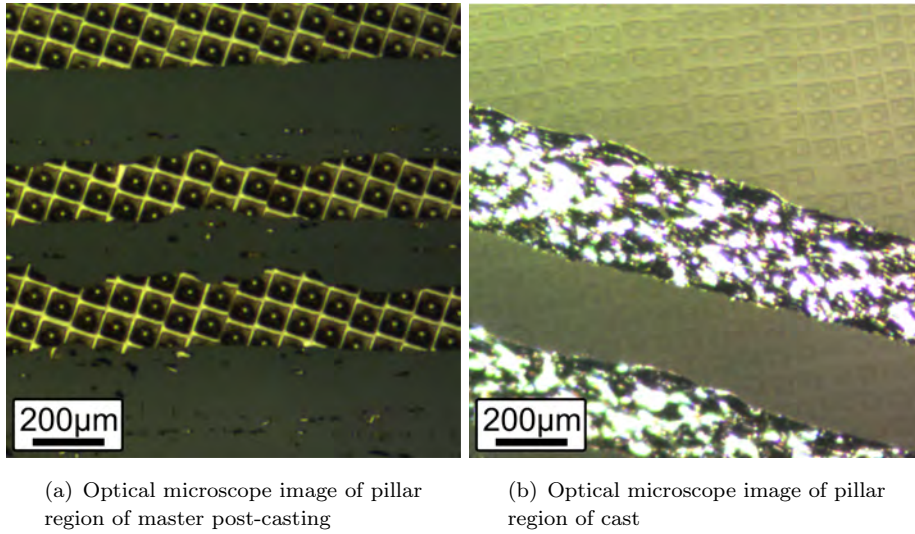
Figure 3.18: A 500nm thick BiSbTe master is torn after as a PDMS cast is peeled away.

Large strips of the thin-film master have been peeled off with the removal of the PDMS cast in Figure 3.18, ruining both master and cast. The damage in this example is extensive, though even a small level of contamination by toxic material would be detrimental to the final assay. One considered solution to this was the use of water-soluble (and hence easily removed), biologically-friendly thin film materials as masters. The original master would be treated as a sacrificial structure; regions of the thin film may adhere to the PDMS cast as before, destroying the master, but could be easily dissolved to leave a near-pristine cast. This cast could then be used for secondary castings – with a PDMS casting from PDMS, no toxic component is necessary. Both glucose and gelatin dissolved in water were spin-coated onto silica glass slides and allowed to dry/set. As both are transparent materials, it was expected that multi-photon effects would be necessary for ablation, and so the 100x objective on the DLP3000 line was used. Regions of square holes were ablated into each; the results in glucose are shown in the SEM images in Figure 3.19.
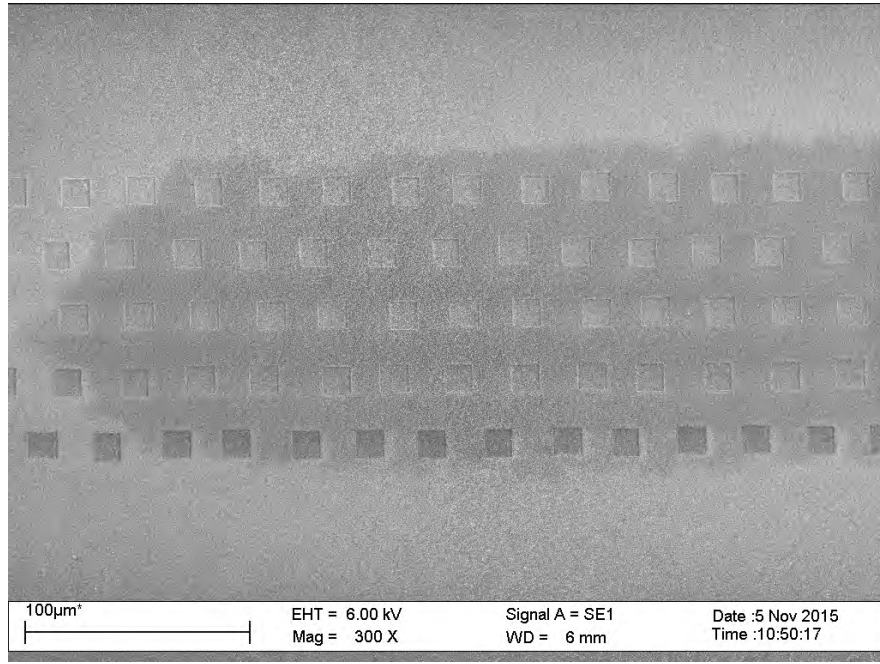
(a) SEM image of 5 lines of square holes ablated in glucose
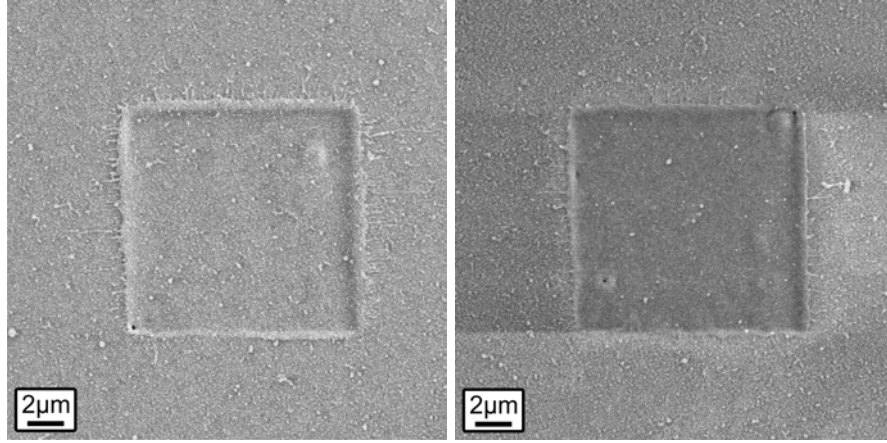
(b) SEM image of a square from the first machined line

(c) SEM image of a square from the last machined line

Figure 3.19: SEM images of the square hole ablation quality in glucose, each produced with a single pulse at 7.2J/cm^2.

The top line of squares in Figure 3.19(a) was the first line machined, and the bottom line the last. The bottom line of squares appears darker than the top in the SEM image, and higher magnification SEM images in Figure 3.19(b) and 3.19(c) show that this is due to a build up of debris, which may have been nanofoam, a substance associated with femtosecond machining [89]. Ablated material redeposits on surrounding areas in the form of foam, and hence features machined early in the process will experience more redepositions from adjacent machined areas than features machined later. While gas removal techniques could be used to reduce this concern (vacuum pump, nitrogen blower), the preparation of glucose films was found to be less repeatable than gelatin – possibly due to low control over ambient humidity in the laboratory. The fluence of 7.2J/cm^2 was known to be correspond to a fluence at the DMD surface below the

54

DMD's damage threshold, while being high enough to observe multi-photon effects in glass, and hence was chosen as the first trialled fluence for the ablation of glucose. The value corresponded to a reading of 600mW on the thermal power meter, which was typically used to define incident intensities on the DLP3000 line.
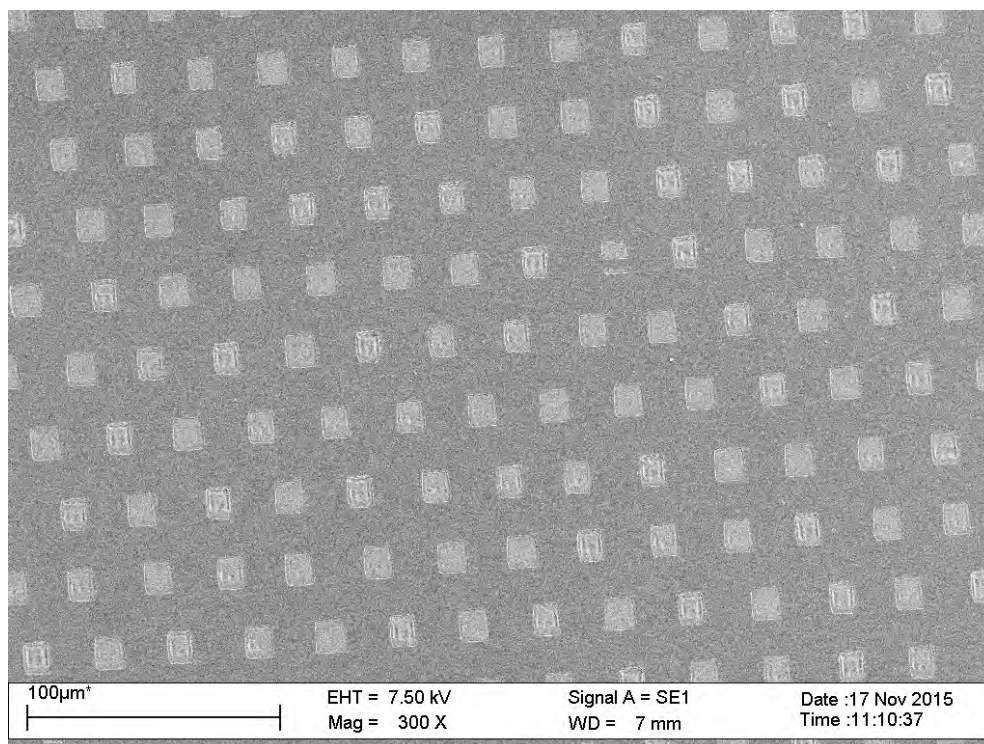
(a) SEM image of square holes ablated in gelatin
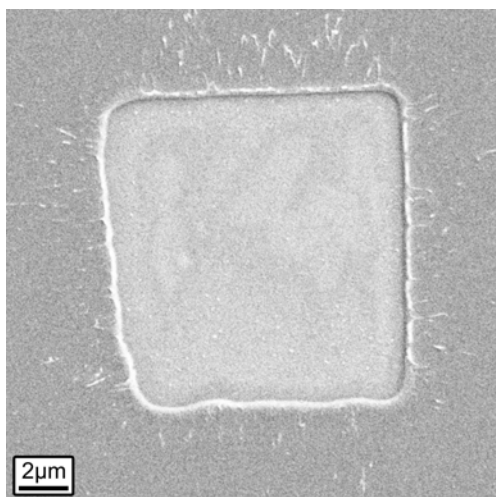
(b) SEM image of a square machined with projected intensity in focus
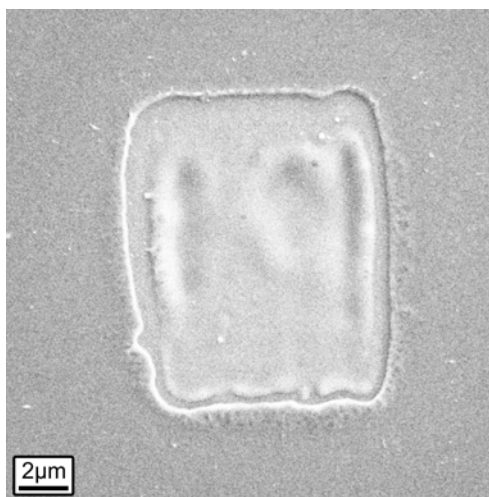
(c) SEM image of a square machined with projected intensity out of focus by $\approx 2\mu$m

Figure 3.20: SEM images of the square hole ablation quality in gelatin, each produced with a single pulse at $6.6\text{J}/\text{cm}^2$.

Material redeposition appears low in Figure 3.20, and structures were stable after several days at ambient conditions in the laboratory. The projected image-reproduction

quality was highly sensitive to focal position; squares which appear to have been ablated by projected intensity away from the imaging plane as in Figure 3.20(c) appear in close proximity to those ablated at the image plane in Figure 3.20(b). This effect was likely seen as a result of a large disparity in the z-direction between points used for the interpolation of focal positions described in Section 3.3; though the experiment should be repeated while ensuring that the entire sample plane is close to perpendicular to the beam line to verify this. Even in Figure 3.20(b), the bottom left corner of the square is not precisely a 90° angle; this is likely a result of a slight inhomogeneity at the DMD surface at the pi-shaper output. Figure 3.21 compares interferometrically measured (Zescope optical profiling system) depth profiles of the gelatin master and PDMS cast.

The flatness of the depth profiles of squares ablated in gelatin in Figure 3.21(a), as well as the lack of debris in Figure 3.20(b), suggests that ablation occurred through the entire depth of an 80nm thick gelatin film, exposing the silica beneath, which was not damaged at the used fluence. The 80nm high pillars in Figure 3.21(b) show that features in the cast have faithfully reproduced those of the master, and in fact no damage to the gelatin master was observed post-casting. A major disadvantage of using gelatin as a master material was its thermal stability – gelatin melts above 35°C, and so the PDMS cast was left to cure at room temperature for two days on the master. Using agar gel, a common substitute for gelatin, which is thermally stable up to 80°C, may allow for faster curing in future.

Though no damage was observed in the gelatin master after a single cast, it could not be expected to remain stable during long-term storage, and the time requirement for curing was excessive. Electroless nickel and silica glass were then tested as master materials. A depth profile for PDMS cast from a square hole-patterned region of electroless nickel is shown in Figure 3.22, while the depth profiles in both glass and PDMS cast from glass are shown in Figure 3.23.

The pillar heights achieved by casting electroless nickel are ≈40nm, corresponding well to typical depths expected per pulse in metals. Greater depth was achieved in glass, at ≈200nm, and was reproduced in the PDMS cast, however the depth profile was not uniform across each square region. This is likely a consequence of the multiphoton effects necessary to machine glass with 800nm femtosecond pulses; any small inhomogeneity in the spatial beam profile will have a larger effect on final machining uniformity than in materials which ablate under single-photon absorption.

The inhomogeneity in the depth profiles seen in Figure 3.23 may be reduced by simple beam realignment in future experiments – however advice from Oreffo's group was that some surface roughness may be *beneficial* to cell adhesion. Provided the same depth profile can be reliably reproduced, a 'flat top' is then not a priority, and was further reason not to investigate gelatin masters (which had achieved the most uniform depth profiles) in greater depth.
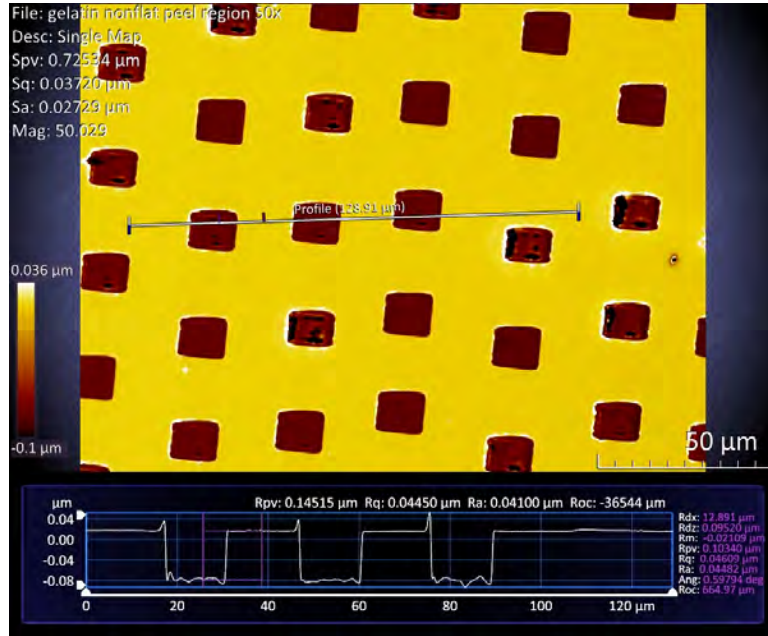
(a) Depth profile of gelatin master
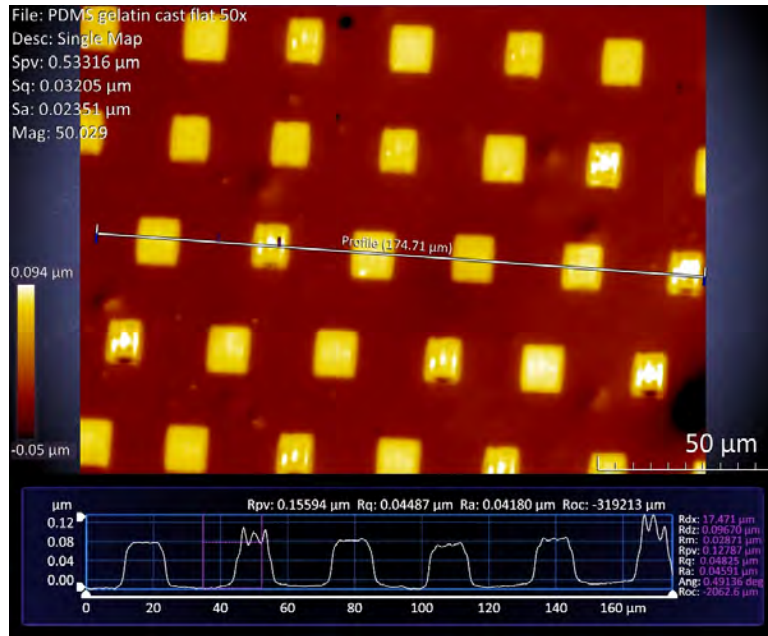
(b) Depth profile of PDMS cast

Figure 3.21: Interferometrically measured depth profiles of gelatin master and PDMS cast.

After repeated castings, a build up of PDMS debris was evident on both the electroless nickel and silica masters. Ultrasonic baths in acetone and isopropanol (standard cleaning procedures used for substrates throughout this thesis) appeared to have little effect in the removal of this debris. A suitable removal method must be found for the continued re-use of masters; the swelling, dissolution and debonding from glass of PDMS by various solvents has been investigated by others [90]. Any chosen solvent must be either nontoxic or itself reliably removed via cleaning procedures.
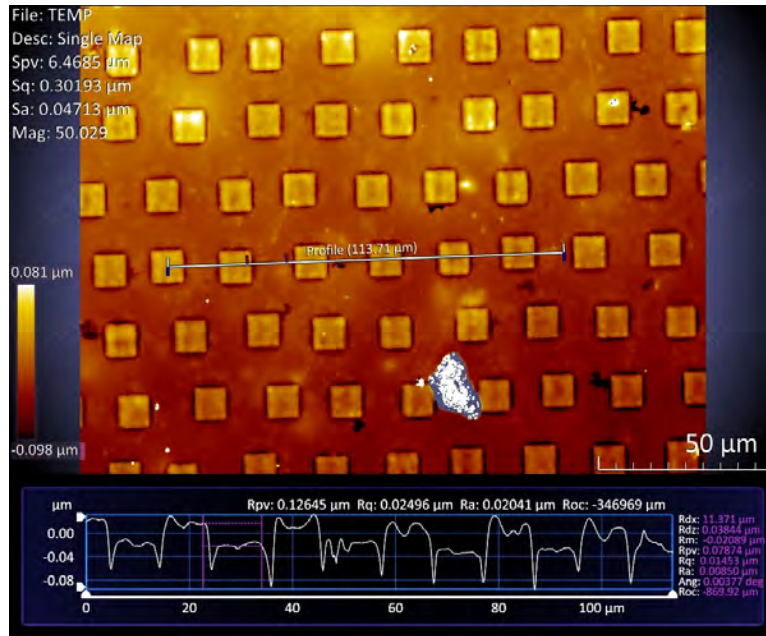
Figure 3.22: Interferometrically measured depth profile of a PDMS cast taken from a square hole-patterned region of electroless nickel

Cell growth viability has been tested on unpatterned PDMS, and compared to growth on tricalcium phosphate enriched polymer (a standard growth assay material). Optical microscope images of fluorescent-dyed cells are shown in Figure 3.24.

Though cell density is lower on the PDMS substrate in Figure 3.24 (Vitali Goriainov, who performed the cell cultures, asserts this, though numerical values were not provided), it is clearly still a viable growth medium. Work will soon begin on trialling cell growth on patterned PDMS assays, before moving onto systematic variation of the structures to characterise cell behaviours in response to different topographies.

DMD image projection-based rapid manufacturing is capable of producing square-centimetre scale samples in a matter of hours (or minutes, at full hardware specifications), with surface modifications of custom patterns at few micron resolutions. This makes it a promising technology to explore the parameter space required to fully understand surface-topography controlled stem cell differentiation, and would even feasibly be used for industrial scale patterning of clinical implants in future.

3.5 Discussion

Image projection-based subtractive patterning has been used to machine features with dimensions as small as $\approx 1\mu$m, over areas on the 1cm^2 scale. The use of a DMD as a dynamic intensity mask in conjunction with sample translation has allowed for distinct, and potentially unique features to be ablated in close proximity, to build up complex
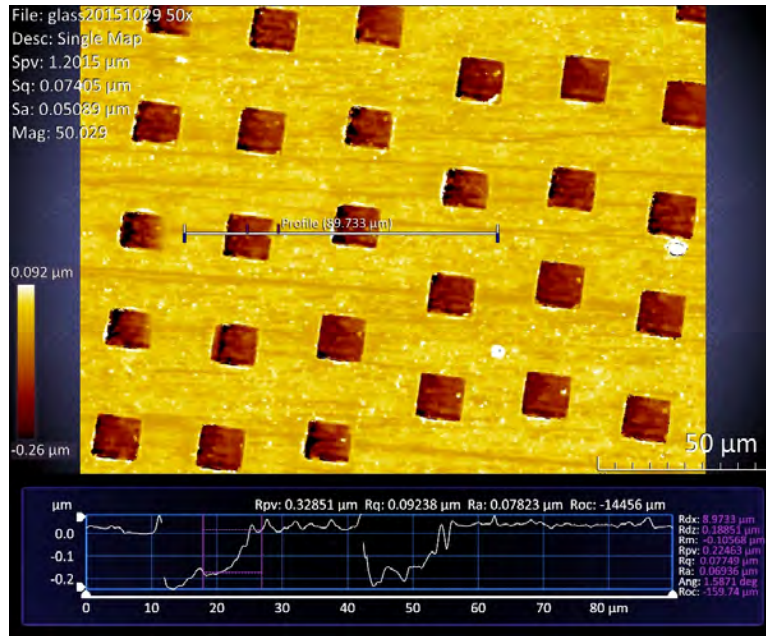
(a) Depth profile of silica glass master
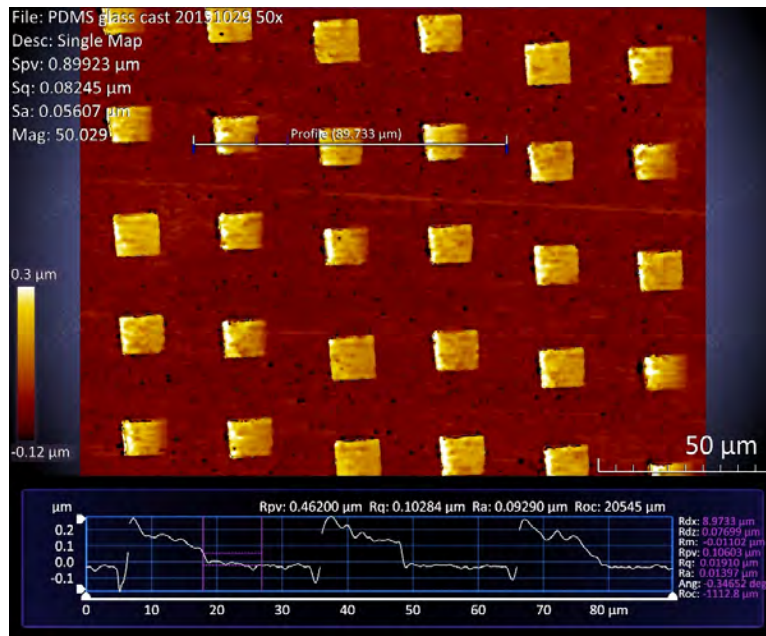
(b) Depth profile of PDMS cast

Figure 3.23: Interferometrically measured depth profiles of silica glass master and PDMS cast.

final structures. The high intensities available with femtosecond pulses have allowed materials typically difficult to machine (e.g. diamond), or those ordinarily transparent at the used wavelength (glass, gelatin) to be patterned.

The method has allowed for diffractive structures visible to the naked eye to be generated, and is being used for the rapid production of custom-designed cell growth assays. Patterning fidelity has been limited not only by diffraction, but by sample position
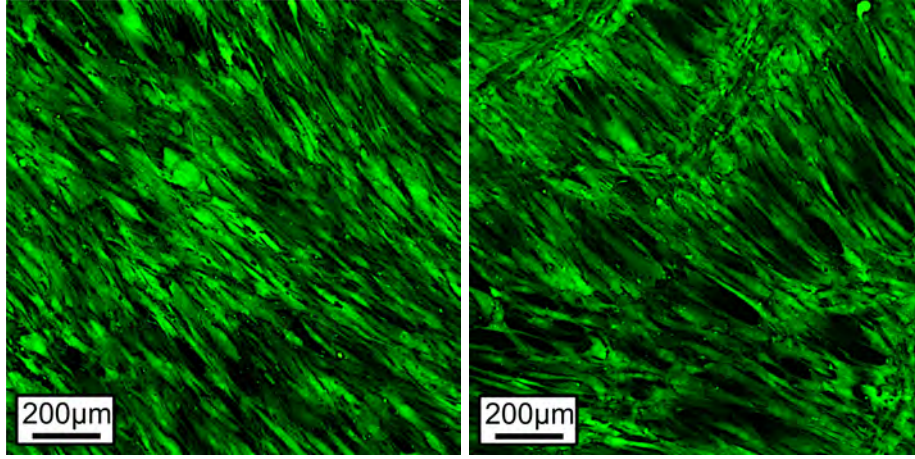
(a) Cell culture on tricalcium phosphate enriched polymer after 21 days' growth

(b) Cell culture on blank PDMS cast from silica glass after 21 days' growth

Figure 3.24: A comparison of cell growth after 21 days observed via green fluorescence of cells under an optical microscope on different growth media. Cell culture performed and imaged by Vitali Goriainov, of Professor Oreffo's group. While tricalcium phosphate enriched polymer is a standard cell growth substrate, this demonstrates that ordinary PDMS is also viable.

relative to the imaging position during translation. Future work will focus on accounting for expected diffractive aberrations through an adaptive optics approach, and on image-recognition techniques to better maintain focus at intended regions of the sample.

While the structures shown in this chapter have comprised tens of thousands of individually patterned features, precise stitching of these features has remained elusive. Even in a point-by-point approach, where translation of the sample was halted at the point of exposure to a pulse, it was not possible to align the edges of patterned features satisfactorily. Image recognition and an adaptive optics approach will be shown in Chapter 6 which may allow for the production of contiguous structures produced in many pulses.

Chapter 4

Additive Patterning

4.1 Introduction

In contrast to subtractive patterning, where targeted material *removal* results in a desired final structure, 'additive patterning' is the targeted *deposition* of material onto a supporting substrate. The field encompasses a wide range of techniques, including those associated with well-publicized '3D printers' such as filament extrusion, laser sintering, and layer-by-layer photo-curing [91], as well as those still largely confined to research, such as ion beam deposition [92]. The increase of diversity of micron-scale electronic, photonic and microfluidic devices has pushed the development of laser-assisted direct-write additive patterning technologies [93, 94]. Laser-induced forward transfer (LIFT) and laser-induced backward transfer (LIBT) are two closely related additive patterning techniques which were studied in this work.

In this chapter, LIFT and LIBT of complex shapes in the solid phase are demonstrated for the first time. The transferred material is either PMMA, in this case of LIFT, or SU-8 in the case of LIBT. In both cases, deposit thicknesses are on the order of 1μm, total lateral deposit dimensions are between 10—100μm, with individual sizes on the order of 10μm. The dynamics of the LIBT transfer process have also been characterised, and a nano-imprinting technique has yielded lateral features on deposits as small as 140nm wide. These results demonstrate an improved versatility in the LIFT and LIBT techniques as a result of this PhD.

4.1.1 LIFT

LIFT was first demonstrated by Levene et al. in 1970 as a laser-based printing process to transfer black ink from a Mylar substrate [95]. The technique went largely undeveloped until rediscovery by Bohandy et al. in 1986 [96] as a direct-write method of additive manufacturing of metal features. A pulsed laser is used to transfer solid or liquid (or intermediate materials, such as pastes) *donor* materials from a *carrier* substrate to a *receiver* substrate, as in Figure 4.1. The group has previously investigated the LIFT of metals where the donor material undergoes a melt-phase during transfer [97], however

all laser-induced transfer (LIT) methods shown in this thesis aimed to retain the phase of the donor material throughout transfer.

(a) Pulse absorbed by DRL or a thin layer of donor material

(b) Flyer is deposited on receiver
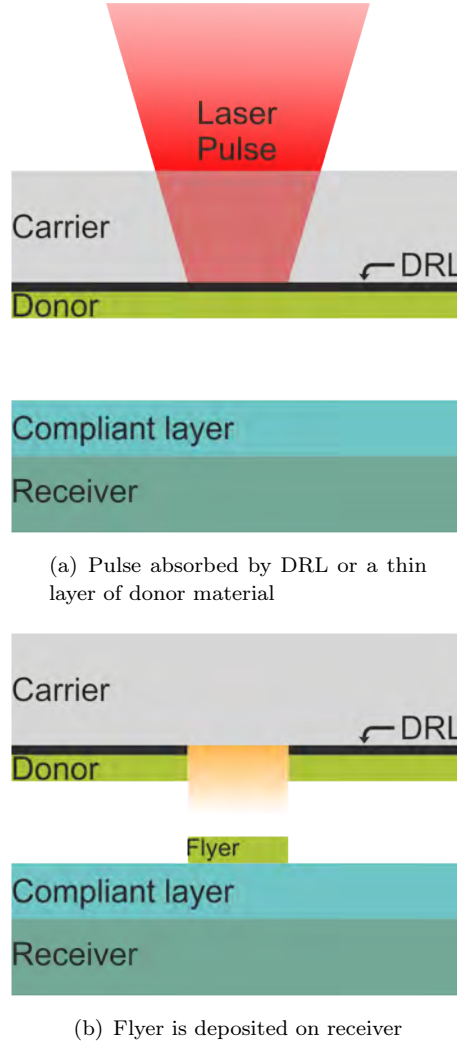
Figure 4.1: The LIFT process. The DRL and compliant layer are optional additions, depending on process requirements.

The laser pulse is focused (or imaged) at the interface between donor and carrier, such that a small volume of the donor at the interface absorbs a high proportion of the pulse energy and undergoes an explosive phase transformation, propelling the remaining donor material towards the receiver substrate. The LIFT process can be aided by the use of a dynamic release layer (DRL) [98] – a sacrificial substrate between carrier and donor which more readily absorbs the wavelength of choice; this leads to a more confined absorption of pulse energy and hence a lower fluence required for the explosive phase change for flyer propulsion, as well as less structural damage to the donor itself – making it possible to transfer transparent materials, or even living cells [99, 100].

A common choice for DRLs within the group are metals with shallow skin depths at the chosen wavelength (e.g. $\approx$15nm for gold at 800nm), or sputtered amorphous carbon

layers of $\approx$50nm – though there have been improved results using specialised polymer DRLs [101, 102]. LIFT can be performed with a few micron gap between donor and receiver, such that the propelled donor material is transported ballistically as a *flyer* [103] before impacting and adhering to the receiver, or with the donor placed with minimal separation from the receiver, for contact-LIFT. Due to the high speed of the flyer (shadowgraph measurements have shown speeds varying from 34ms^{-1} [103] to $\approx$2kms^{-1} [104], where flyer velocities with and without DRLs have been recorded at similar values [105]) and subsequent rapid deceleration when it collides with the receiver substrate, the flyer can experience significant forces that can result in damage. A compliant layer may also be present on the receiver – an extra layer of some soft material, such as polydimethylsiloxane (PDMS), of a few micron thickness; this reduces deceleration forces and hence reduces damage risk to the flyer.

LIFT is advantageous for manufacturing as the preparation conditions for donor and receiver are independent – by preserving the phase of the donor, it allows for the addition of structures on substrates which would be difficult with other techniques due to lattice mismatch [106], deposition temperatures or chemical interaction during growth etc. Multilayer donor materials have allowed the production of complex structures via LIFT, including metamaterials [107, 108] and light-emitting diodes [109, 110].

Most frequently, donor thicknesses of a few hundred nm to a few μm are used, though this depends on material properties of the chosen donor. Lateral dimensions of the flyer range from tens of nm [111] to a few mm [112]. Pulsed lasers, usually ranging from nanosecond to femtosecond pulse lengths, can be used for LIFT, with typical energy densities of a few tens of mJ to > 1J/cm^2.

Until recently, the majority of LIFT research has used focused or imaged laser pulses that had a Gaussian or 'top-hat' spatial intensity profile, with circular or rectangular beam-shaping (with extension to 'smart beam shaping' [113], or the use of custom masks [110]). Whilst individual deposits can be overlapped [97], this approach cannot be easily extended to produce less simple 2D structures. In order to build up more complex structures, the use of a variable illumination mask (or spatial light modulator, such as a DMD), has been explored by others for the shaped transfer of metallic inks [29, 114], though these inks require post-processing to solidify the final deposit. In this chapter, the first known instance of shaped transfer of solid polymeric material using a DMD is shown, which requires no post-transfer processing.

4.1.2   LIBT

LIBT follows a similar experimental procedure to LIFT in order to transfer material from a carrier to a receiver substrate, albeit with the flyer propagation direction being opposite to that of the incident laser pulse (i.e. 'backward'), as in Figure 4.2. The altered geometry leads to a combination of advantages and disadvantages as compared to LIFT. While LIBT and LIFT were reported simultaneously [95], research has largely

focused on LIFT since. LIBT has been used for the transfer of metal nanodroplets on the ≈500nm scale [115], oxides [116], and liquids [117], among other materials, and is closely related to a host of processes aimed at removal of a surface layer from a substrate, such as laser scribing, laser cleaning, or laser lift-off [118].

(a) Pulse absorbed by a thin layer of pre-structured carrier material

(b) Structured flyer is deposited on receiver
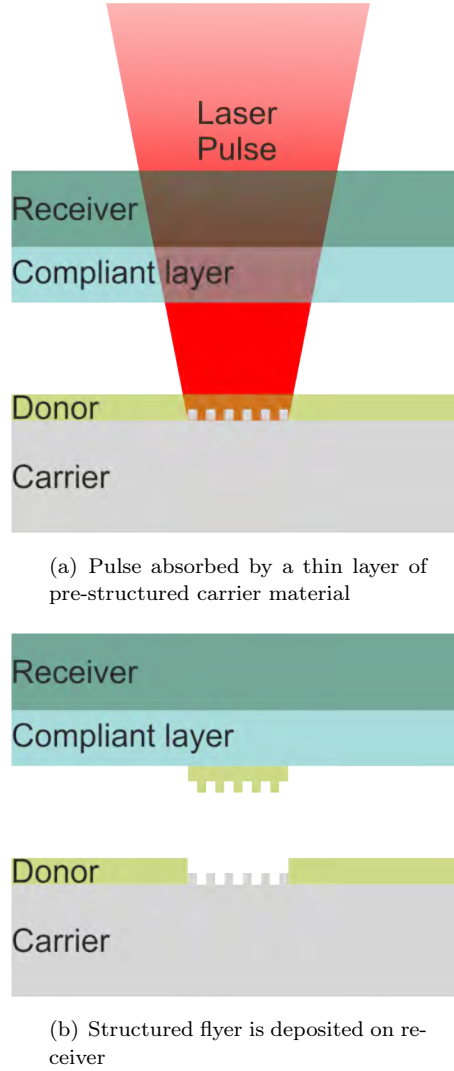
Figure 4.2: The LIBT process, with a pre-structured carrier.

As can be seen from Figure 4.2(a), for successful LIBT the absorption in the carrier (or at a DRL at the interface between carrier and donor, omitted in the figure) must be high compared to that in both the receiver and donor. While the carrier material is not usually of consequence to a final LIT-produced device, this transparency requirement of the receiver in LIBT is a limiting disadvantage. The difference between LIFT and LIBT is not only in the choice of materials and the direction of transfer, but in the form of absorbing material and its configuration with respect to the donor. Consider the 'pre-machined' features of the carrier in Figure 4.2; a final deposit's top surface can be patterned as a result of patterning of the carrier. In order to use such a patterned carrier for LIFT (with material vaporisation as the propelling mechanism [119]), either the back surface of the donor (top surface of the deposit) would necessarily be damaged

to propel a flyer, or a DRL layer would have to be applied to the carrier, which would require careful deposition in order to avoid 'filling in' the pre-machined features. An absorbing carrier and transparent donor combination however, as required in LIBT and impossible in LIFT, allows for straightforward faithful imprinting of the deposit. Vaporisation (or rapid thermal expansion) of the carrier acting as a propellant for the flyer leaves imprinted features on the deposit largely intact. This chapter will present deposits obtained with LIBT which are laterally shaped via DMD-shaped incident pulses, or whose surfaces and imprinted with nanoscale features using pre-machined carriers.

Studies have shown that thermal expansion might be a leading mechanism when using ultrashort laser pulses at fluences too low to achieve vaporisation [120–122] for LIFT, and it is expected that shocks from thermal stress will play a role in the release of flyers during LIBT also. If the thermally induced stress shocks are great enough to release and propel a flyer, while not damaging the carrier substrate, it may be possible to reuse pre-machined carrier substrates – FIB machined, high resolution carriers could be used to produce nano-imprinted deposits many times, greatly reducing the production time of deposits with nanoscale features. Such thermal-expansion driven transfer may be possible with an absorbing donor in LIFT, a current focus of ongoing research is the modelling of this mode of transfer in LIBT. Though incomplete, simulations suggest that thermal-expansion driven LIBT should be possible without damage to the carrier, though results are too premature for publication at this stage.

4.2 Experimental results

DMD image projection-based laser manufacturing has been used for the targeted deposition of material via the LIFT and LIBT methods, with the lateral shape of deposits defined primarily by the displayed mask on the DMD during pulse exposure. Additionally, pre-shaped carrier surfaces have been used for the nano-imprinting of flyer surfaces in the LIBT configuration, and the dynamics of flyer velocity have been studied via shadowgraphy.

4.2.1 LIFT

In this section the application of DMDs to LIFT is shown. The submitted paper in Appendix A, "Dynamic spatial pulse shaping via a digital micromirror device for patterned laser-induced forward transfer of solid polymer films", details much of the work undertaken. While beam-shaping has been used previously for LIFT [112, 113], and DMDs have been used for the shaped LIFT of pastes [29], this is the first demonstration to our knowledge of the LIFT of solid material with varying-complexity shapes. Additional details to those submitted for publishing in the experimental procedure follow below.

Crystalline materials were trialled for shaped LIFT before the poly(methyl methacrylate) (PMMA) used in the paper. Initially, Bi_2Te_3 was chosen as the donor material due

to the LIFTing of a 'C' shape in [123], an achievement made before the commencement of the work in this thesis by another member of the group, despite imperfect mapping from the intended image to final deposit and little repeatability. Ordinary silica microscope slides were used as both carrier and receiver. No DRL nor compliant receiver layer were used, resulting in only highly fractured material being deposited both in the contact LIFT regime or with a $3\mu m$ mylar spacer. The material was observed to remain more confined in contact-LIFT, in addition to previous work showing unpredictable rotations during transfer even for rotationally symmetric flyers [103], leading to future experiments always being performed via contact-LIFT. 700nm thick multicrystalline silicon with a $\approx$50nm carbon DRL and $10\mu m$ PDMS compliant receiver yielded the deposits shown in the optical microscope images shown in Figure 4.3. The intended shapes for this subset of results were the letters W—Y (with the whole alphabet being tested with similar results). While the deposited letters are recognisable, they were shattered, a problem which is as yet unsolved for shaped LIFT of crystalline donors – as only a small volume of a LIFTed flyer is vaporised, and the remaining volume does not undergo a phase transition, LIFT would appear to be capable of producing crystalline deposits. However, the stresses involved in release and im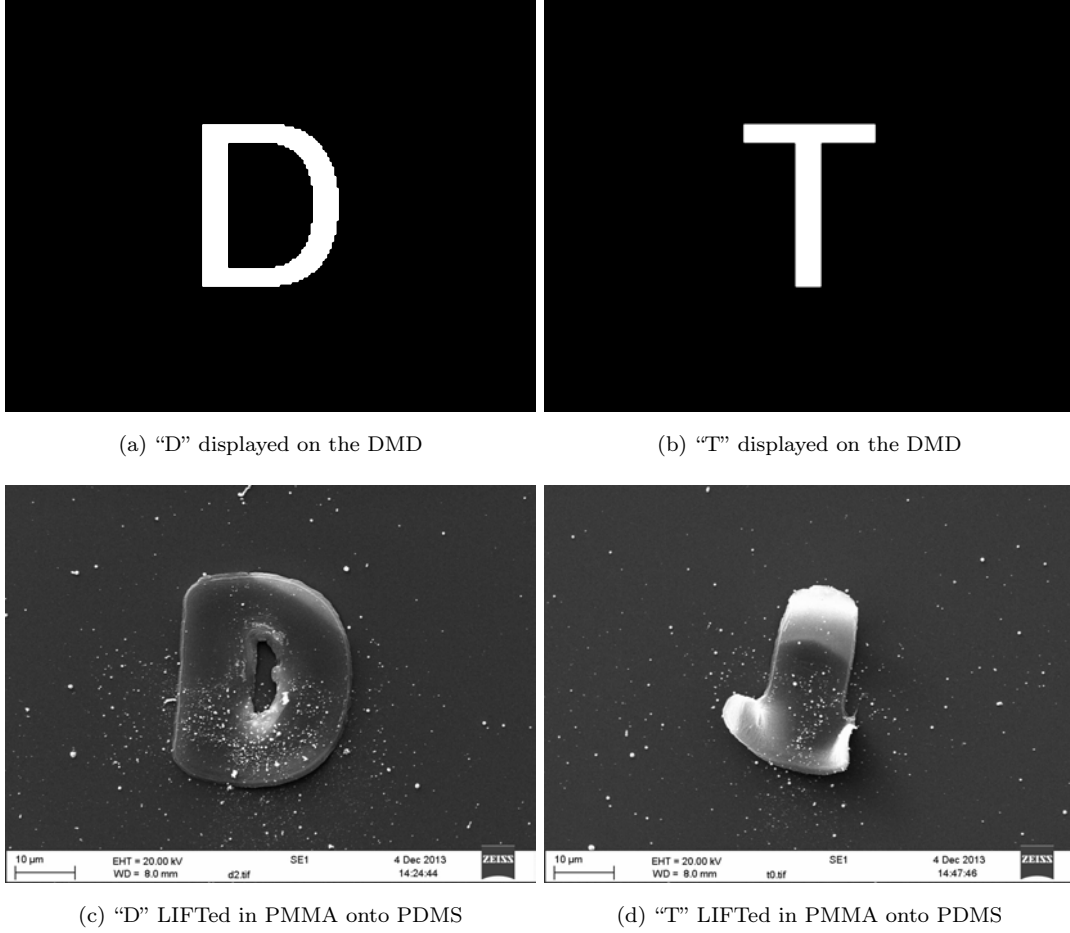pact appear to be too great for silicon deposits to remain in a single piece. Similarly shattered deposits were obtained when testing 500nm and 150nm thick donor layers of Bi_2Te_3, as well as 150nm thick GeSbTe.
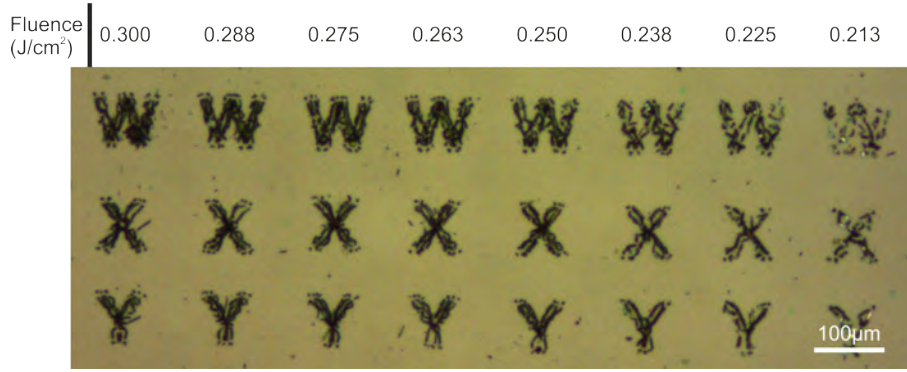
Figure 4.3: Shaped Si deposits LIFTed in single pulses at a fluence of $0.3J/cm^2$ in the left-most column and decreasing in steps of $12.5mJ/cm^2$ to the right.

Following the work of [98] and [113], the donor material was switched to one which could withstand some deformation, as well as adding a compliant receiver layer to reduce forces during deceleration. Poly(methyl methacrylate) (PMMA) was chosen as the donor, and PDMS as the compliant receiver. The PDMS was spin-coated at 5000rpm for 1 minute, yielding a final thickness of $\approx 10\mu m$, while the PMMA was similarly spin coated on silica glass for a $\approx 1.3\mu m$ thick donor layer. While the compliant receiver here was used primarily to preserve the integrity of the flyer, PDMS-coated substrates are widely used in microfluidics, contact-lithography and MEMS devices [124–128], and polymer-coated receivers have been used in the manufacture of electronic devices [109]. As PMMA is transparent at 800nm, a DRL was required. 80nm Al and 30nm Au DRLs were tested, before being supplanted by a 50nm carbon layer. Figure 4.4 shows results when using a gold DRL on the DLP3000 line with a 50x objective. While 4.4(c) shows that rounded shapes, such as the letter 'D', undergo a recognisable mapping from the

displayed DMD mask to final deposit shape, 4.4(d) shows that more indented shapes, such as 'T', suffer from curling and/or tearing as they leave the donor and travel to the receiver. Nanodroplets of DRL are also evident across the LIFTed samples.

(a) "D" displayed on the DMD

(b) "T" displayed on the DMD

(c) "D" LIFTed in PMMA onto PDMS

(d) "T" LIFTed in PMMA onto PDMS

Figure 4.4: A comparison of shapes displayed on the DMD and those LIFTed intact to the receiver using a 30nm Au DRL and 50× objective. (c) and (d) show transferred gold droplets spattered across the sample. These results for this preparation of samples was typical for energy densities between 0.2 and $0.3 J/cm^2$.

Similar results to those achieved in Figure 4.4 were found using the 50× objective and a 50nm carbon DRL, with the added advantage of no obvious deposition of DRL material. However, fine detail in the LIFTed shapes was still a problem; a combination of optical filtering and material response meant that the final deposits were not an exact mapping of the displayed DMD mask, similarly to the generation of features described in section 5.1, in this case line widths in the final deposits being broader than a perfectly minified mapping of the DMD mask. A 20× objective was used in the hope of achieving a more accurate mapping of intended images at the cost of minimum feature size. This procedure was successful in producing highly repeatable, complex solid LIFTed structures with no obvious transfer of carbon DRL, which was presumably vaporised and proceeded to dissipate in gaseous species or was deposited too finely for the SEM to reveal. SEM images of individual deposited structures are shown in Figure 4.5, with insets displaying the DMD patterns as loaded (and hence the intended spatial

intensity profile) when the laser pulse was incident on the DMD surface. Figure 4.5 shows a comparison of the deposited structures using (a–d) a 50× objective and fluence of 300mJ/cm^2, and (e–h) a 20× objective and fluence of 270mJ/cm^2.
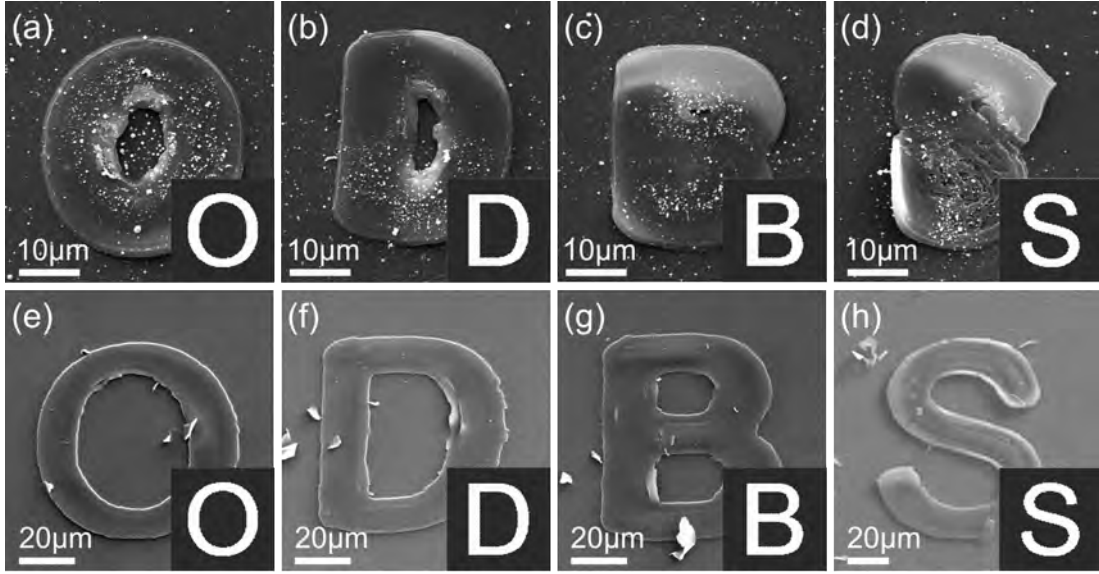
Figure 4.5: SEM images of 1.3μm thick polymer structures deposited via LIFT onto PDMS-coated glass slides, with the inset images showing the bitmap displayed on the DMD during exposure, for (a–d) a fluence of 300mJ/cm^2 using a 50× objective and a 30nm Au DRL and (e–h) a fluence of 270mJ/cm^2 and a 20× objective with a 50nm carbon DRL. Note the different scale bars on the figures. As will be seen in Figure 4.6, a wide range of fluences lead to successful LIFT transfer for this material, with little observable difference in deposit shape.

For the 50× objective, the size scales in the letter 'B' and 'S' appear to be at the limit of recognisable mapping from the displayed DMD mask to the deposit, which is LIFTed 1.3μm thick PMMA. For the 20× objective, the size scales were larger and both the letter 'B' and 'S' were reproduced accurately. While many letters were reproduced successfully using the 20× objective, with maximum lateral dimensions of ≈70μm, the quality of some, such as 'S', remained low until they were produced at lateral dimensions of ≈100μm (note the smaller scale bar in Figure 4.5 (h)). At this size, the entire alphabet was deposited accurately. In general, for successful LIFT, the region on the donor that is illuminated by the laser pulse must break free from the surrounding donor material, via the explosive phase transformation caused by absorption of the incident laser pulse. There is therefore a limit to the minimum width of a feature that can be successfully removed from the donor via the LIFT process, and is a value determined predominantly by the material properties and dimensions of the donor, and the presence of a DRL. This was an evident concern in the LIFT of solid donor material when compared to the LIFT of pastes by Piqué et al. [29], which could much more easily break free from the surrounding donor material. This limit is observed in Figure 4.5, where the features in (a–d) are too small to be removed in the same shape as the projected intensity pattern, whilst the features in (e–h) are almost perfectly replicated. Evidently in (a–d), the deposits' minimum feature sizes are larger than they would have been, had the deposit been a perfectly minified version of the projected intensity patterns (also shown as the insets). In order to test the adhesion

of the deposits to the carrier, a sample was left in a sonication bath filled with distilled water for 30 minutes (a common adhesion test in the literature for LIFT [129]), and out of a total of approximately 300 deposits, all of the structures remained in place.

Figure 4.6 demonstrates the effect of a variation in pulse energy on the deposited polymer structures, over a 25% range in laser fluences, with values reducing from 300mJ/cm^2 (left) to 235mJ/cm^2 (right) in steps of 17mJ/cm^2, for a series of letters. The shapes appear to be deposited similarly across this range. Successful deposition of shaped polymer structures was also achieved outside this range. In general, fluences from 200mJ/cm^2 to 380mJ/cm^2 were found to yield high-fidelity deposits for all letters (and arrays of squares, as in Figure 4.7), hence demonstrating robustness to energy fluctuations and reproducibility across an extremely wide variability of shapes. As each deposit only requires a single laser pulse, large areas of sample coverage can be achieved via rapidly LIFT-printing multiple deposits by taking advantage of the high refresh rate of the DMD (hence allowing each laser pulse to be used to deposit a different shape) when using a high-repetition rate laser.
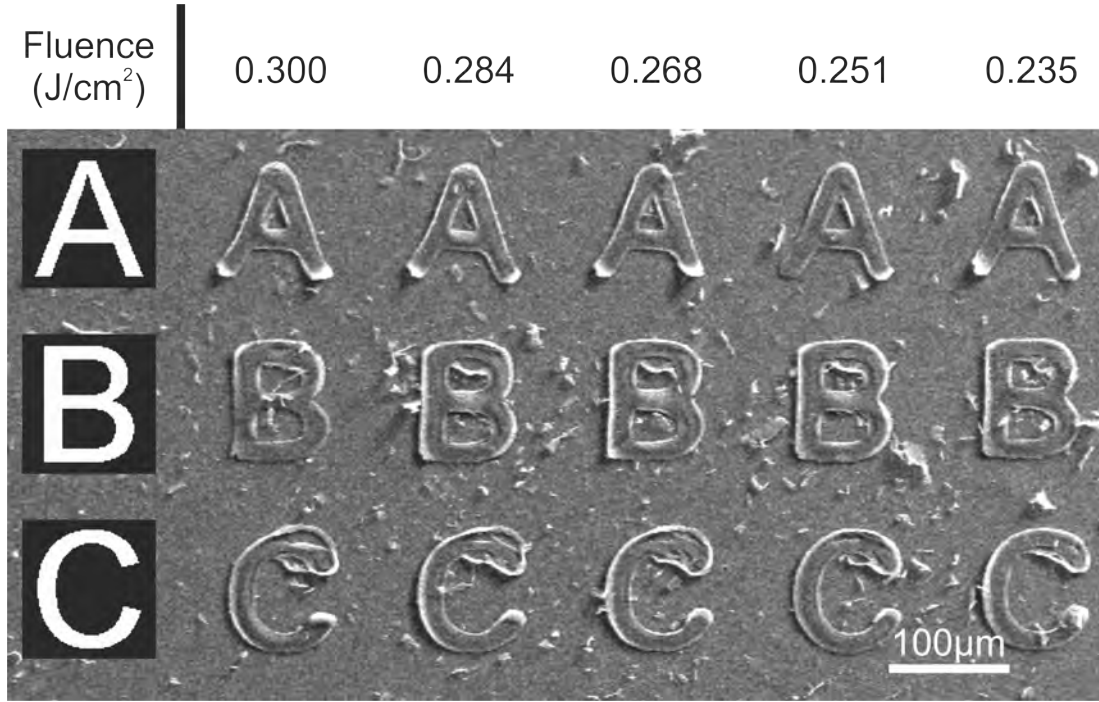
Figure 4.6: SEM image of an array of different shaped polymer deposits using a 50 nm thick carbon DRL and 20x objective, for a range of laser fluences reducing from 300mJ/cm^2 to 235mJ/cm^2. The insets show the projected intensity profiles.

In order to show another facet of the applicability of a DMD as a variable illumination mask for LIFT, multiple unconnected structures were deposited simultaneously using a single pulse. This approach is demonstrated in Figure 4.7, where SEM images show a two by two array of square deposits, for two different projected intensity patterns, namely (a) confined and (b) sparse, for the same conditions as in Figure 4.6, save for the use of different fluences. In solid-phase LIFT of PMMA, additional donor material

around the edge of the intended flyer can be ejected as the flyer shears free from the donor. In Figure 4.7 (a), the minimal separation between squares is reflected in the lower quality of the deposited structure, where additional and unintended donor material was ejected from the donor, resulting in the square deposits being larger than the corresponding intensity profile on the donor, which is shown in Figure 4.7 as dashed yellow lines.
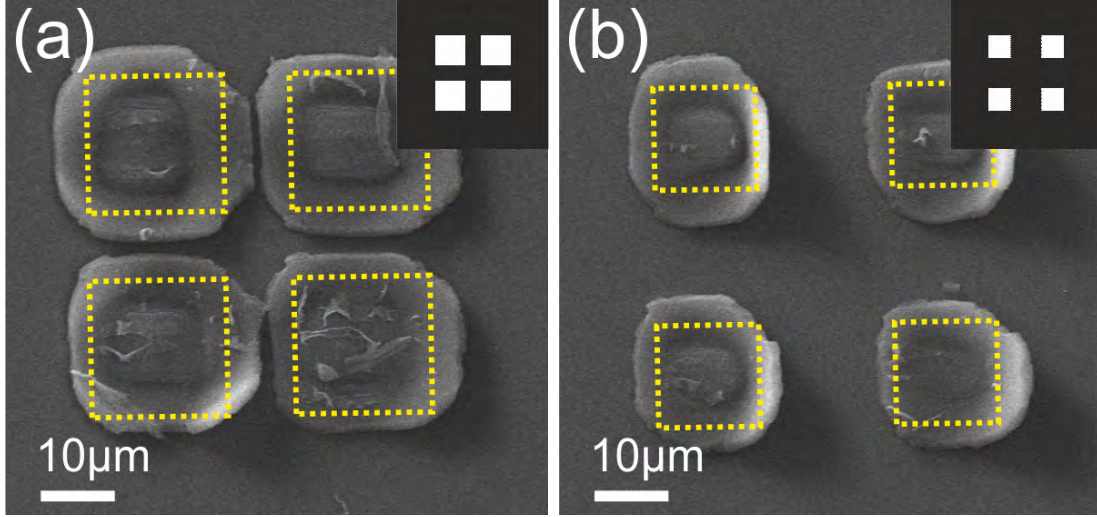
Figure 4.7: SEM images of arrays of two by two squares that were deposited simultaneously via the LIFT technique, with squares of different sizes and separations displayed on the DMD. Donor, receiver, objective and DRL are as in Figure 4.6. Produced at fluences (a) 250mJ/cm^2 and (b) 270mJ/cm^2. The inset shows the projected intensity pattern, where the correctly scaled outside edges of the pattern are also displayed as yellow dashed lines.

In agreement with results found in [130, 131], the smaller squares in Figure 4.7 (b) required a higher fluence than those in (a), to achieve transfer. An intended intensity pattern with finer features will usually contain a higher proportion of high spatial frequencies, some of which may be above the diffraction limit of a system, or be more prone to loss at any point of aperturing, for example the entrance to the microscope objective lens. This would have led to a greater 'blurring' of intensity at the edges of the squares in Figure 4.7(b), and potentially altered the LIBT threshold. However, the interfaces at which release occurs will also affect the transfer mechanism. For any LIFT transfer, energy will be required to shear the perimeter of the flyer, to release at the interface between carrier and donor, and to propel the flyer forward. Of these energy costs, it is important to compare that of shearing at the perimeter to releasing at the interface. As the region of contact at the interface is exactly the single-side surface area of the flyer itself, one would expect this release energy to scale linearly with area, and so would have no effect on the required fluence (energy per unit area). The energy required to shear at the perimeter will increase linearly with perimeter length, which will depend on the particular geometry of the flyer, but typically will increase with flyer area. However, the ratio of perimeter length to area increases as flyer area decreases, meaning that for smaller flyers a greater proportion of incident energy is required to shear at the perimeter. In order to account for the constant fluence needed to release at

the interface, and an increased share of total incident energy to shear at the perimeter, smaller flyers require higher fluences to transfer.

4.2.2 LIBT

During an experiment which aimed to characterise the limits of ablation of silicon on existing silicon waveguides, deposits such as those shown in Figure 4.8 were observed on the sample. Rather than being vaporised in the ablation process, well-defined shapes corresponding to the displayed DMD intensity masks appeared to 'peel away' from the silicon substrate. Contrary to the ordinary LIFT mechanism, which must occur in a single pulse for an explosive phase change of DRL/donor material at the donor/carrier interface, multiple shots were required to cause this effect. The letter "Y" in Figure 4.8 was achieved in ten shots at a fluence of $0.32J/cm^2$.
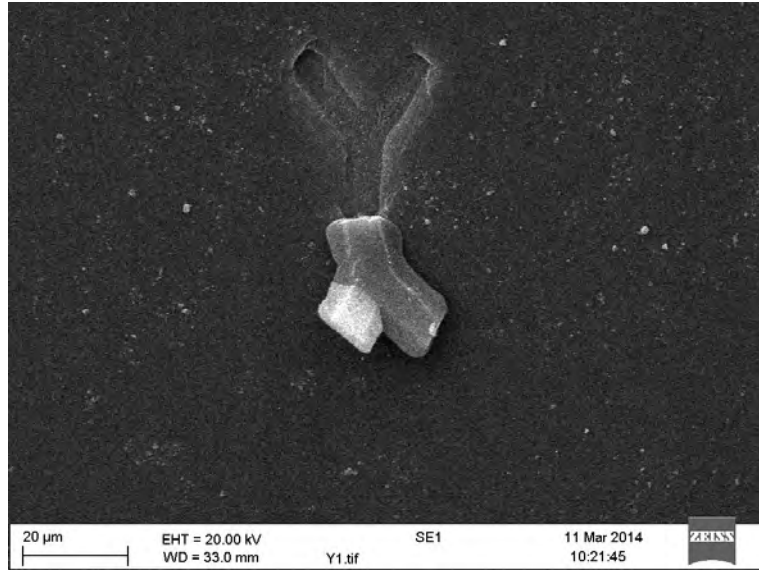
Figure 4.8: A 'LIBTed' letter 'Y' peeling away from the silicon substrate.

It was later determined that the waveguides, which were not prepared by members of the group, had likely been coated in PMMA. The deposits were not visible after an acetone wash, which would not have removed the deposits if they had been either silica or silicon, the expected constituent materials of the waveguides. As the absorption depth of silicon is known from the literature to be between 5–10μm at 800nm, it had not previously been considered probable as a candidate for the required pulse-absorption in LIT, either as DRL in LIFT or in this case absorbing as a carrier. Though two-photon absorption may have allowed silicon LIFT without a DRL, typically we focused on shallow skin-depth materials for absorption to maximise energy confinement in the sacrificial layer of either flyer or DRL.

71

The results in the remainder of this section were produced primarily by another member of the group, Matthias Feinauegle, and has contributed to a published work [132]. A few additional results to those given in the paper will also be shown.

S1813 and SU-8 photoresists were chosen as donor material, spin coated on carrier substrates and cured on a hotplate at 110°C for 5 minutes. Both of these resists are commonly used in lithography, and as solid polymers displayed similar material properties to PMMA which were necessary for successful LIFT in section 4.2.1. The carriers were either polished monocrystalline silicon wafers or silicon-on-insulator chips, the latter being patterned with grating structures and slot/rib waveguides and layer thicknesses from top to bottom of $\approx$400nm silicon, $\approx$2μm silicon dioxide and $\approx$600μm silicon. Fabrication of structures on the silicon-on-insulator chips was performed outside of the group via e-beam lithography and inductively coupled plasma etching. Donor thicknesses ranged between 1.4–2.25μm, and flyers were typically 20–50μm in lateral dimensions. Donor and receiver were in contact during transfer, and the receiver was either glass, $\approx$10μm thick PDMS on glass, or a free-standing PDMS layer obtained by peeling the PDMS layer post-curing from a glass substrate. Only simple shapes, such as squares and circles, were found to transfer successfully onto a glass receiver – more complex patterns shattering even at threshold fluence. Figure 4.9 shows a range of successfully transferred shaped S1813 photoresist deposits onto a PDMS-coated glass receiver at $\approx$500mJ/cm^2 from a silicon wafer carrier which had no pre-machined structures, i.e. there was no imprinting of the deposit by the carrier surface. Similar deposits to those shown in Figure 4.9 were obtained with 1.5μm thick SU-8 at a transfer threshold of $\approx$370mJ/cm^2
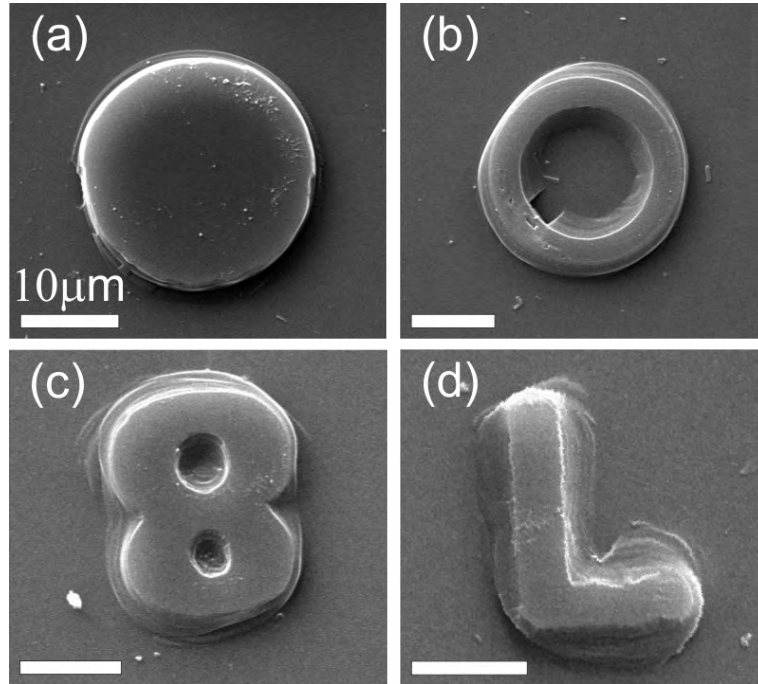
Figure 4.9: SEM images of $\approx$1.4μm thick S1813 shaped LIBT deposits on PDMS-coated glass at fluences of (a) $\approx$475mJ/cm^2 and (b–d) $\approx$510mJ/cm^2. Note the scale bar in each case is 10μm.

Figure 4.10 shows the results of the imprinting technique described in Figure 4.2. Donor material conformed to surface structures in a silicon-on-insulator waveguide during spin-coating, and retained these features after LIBT.
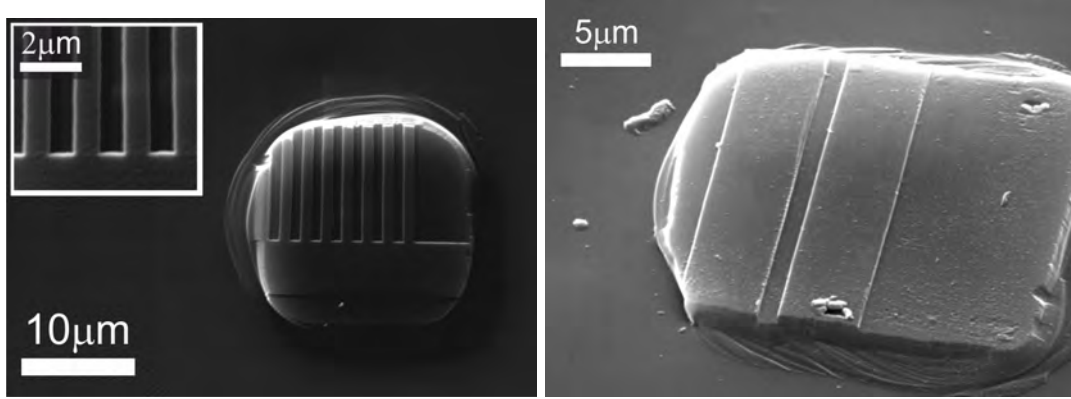
(a) SEM image of an SU-8 deposit imprinted with a grating structure, inset showing a higher magnification. The grating period was ≈900nm, with ≈200nm depth.

(b) SEM image taken at 45° tilt of a rib waveguide imprinted into an S1813 deposit

Figure 4.10: Imprinted LIBT deposits from a silicon-on-insulator waveguide. Both (a) and (b) transferred at ≈475mJ/cm^2 onto PDMS-coated glass receivers.

Figure 4.11 shows the limit of structured carrier imprinting achieved with the technique. A slot waveguide structure (two raised regions around a central trench) translated into an imprint of a rib (two sunken regions around a central raised line) on an S1813 LIBT deposit.
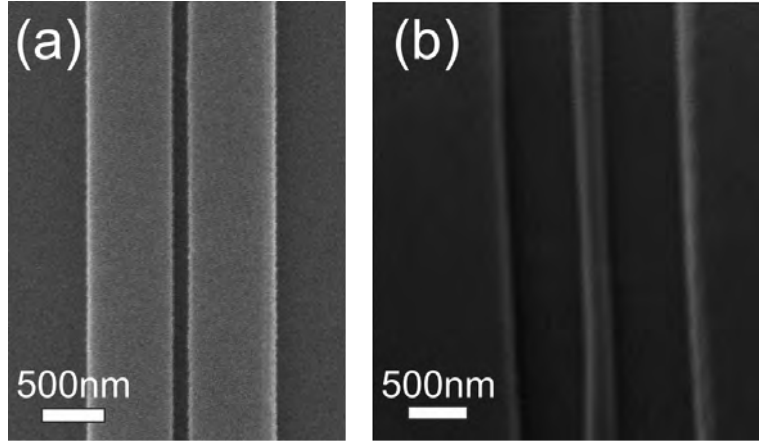
Figure 4.11: SEM images of (a) a slot waveguide used for as a pre-patterned carrier and (b) an S1813 LIBT deposited at a fluence of ≈475mJ/cm^2. The central vertical rib in (a) was ≈140nm wide and ≈220nm high.

As a first test of determining the release mechanism at the threshold of LIBT, the donor/carrier substrate was also examined under SEM at regions where donor material

had been released. Figure 4.12 displays one such region, where a central circle of donor material has been removed, revealing the underlying carrier substrate. An arrow indicates the path scanned by a stylus profilometer. While the SEM image in Figure 4.12(a) appears to show an undamaged carrier region exposed, the profilometer shows that there are surface corrugations on the order of a few nm towards the centre of the circle, and greater modulations on the order of 20nm depth towards the edge of the exposed region.

(a) SEM image of the donor/carrier substrate where a circular flyer has been released

(b) Stylus profilometer depth measurements across the radius of the circle
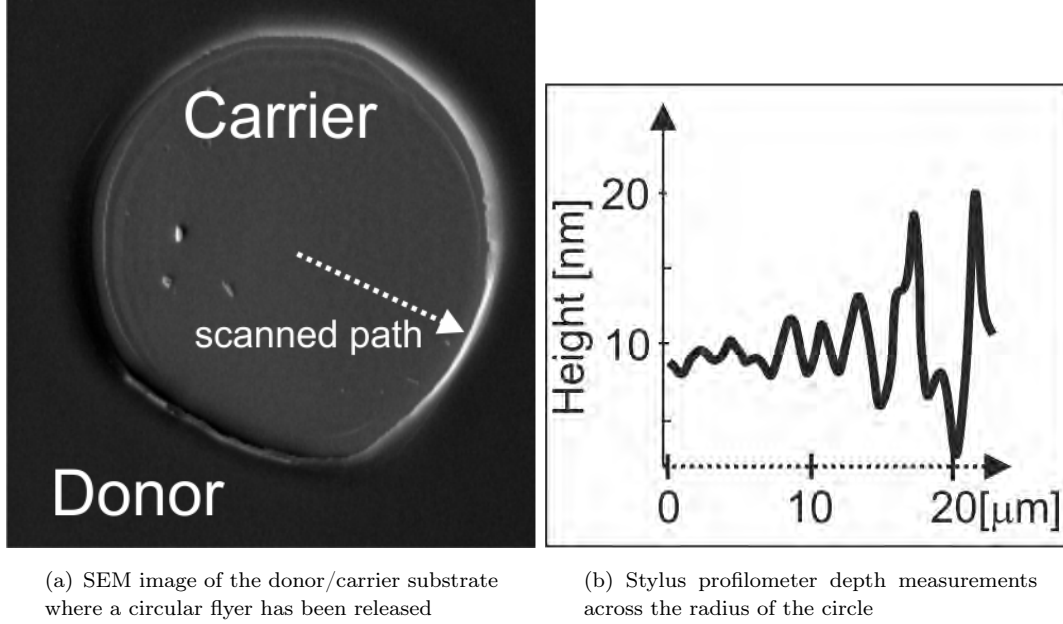
Figure 4.12: The donor/carrier substrate after flyer release.

The nanoscale depth modulations apparent on the carrier may in fact be residual donor material not released with the bulk of the flyer, though this seems unlikely given the fidelity of the imprints shown in Figures 4.10 and 4.11. Silicon has been found to ablate under 800nm $\approx$100fs irradiation at $\approx$300mJ/cm^2 with a single shot [133], while multi-pulse ablation has been found to occur at fluences as low as $\approx$200mJ/cm^2 (which may explain the ten-pulse requirement to release material in Figure 4.8. However, the low damage seen in Figure 4.12(a) merits further investigation into the degree of surface modification of the carrier by LIBT. If fine structures were found to be intact after a washing process, fresh donor material could be applied and a single carrier with highly complex patterning could be used to rapidly produce deposits with nanoscale features. Future work will focus on determining the mechanism of LIBT at threshold and the re-usability of carriers.

4.2.3   Shadowgraphy of LIBT

The LIBT deposits seen in section 4.2.2 appeared to suffer from less distortion and debris than the LIFT deposits in section 4.2.1. Reduced flyer velocity and hence shock generation have previously been shown to improve the success rate of intact deposits

74

via LIFT [134], and so a corresponding study to determine the dynamics of LIBT is also of interest.

The results in this section have featured in work to be published in *Applied Surface Science*, 'Time-resolved imaging of flyer dynamics for femtosecond laser-induced backward transfer of solid polymer thin films' [135], and were generated mainly by the lead author of the paper; contributions from the author of this thesis were in the form of assistance with data analysis and sample design.

A time-resolved shadowgraphy setup was used to image the surface of SU-8 donor layers of either 3.8μm or 6.4μm thickness (referred to as 'thin' or 'thick' respectively) during LIBT from either silicon or germanium carriers, with a variation in this thickness within $\pm$100nm, measured by stylus profiler. The silicon carriers were between 300–600μm thick, while the germanium carriers consisted of a 3μm layer grown on one of the 300–600μm thick Si substrates. The experimental setup used was similar to the DLP3000 line, with additional elements enabling shadowgraphy being a signal generator, white light spark discharge flash lamp (Nanolite KL-K, HSPS), a pair of objectives L1 and L2 to focus the flash lamp output at the donor target position, and a CCD camera with either a 100x or 20x objective lens positioned to record the images (or shadowgraphs) of the LIBT flyers. The setup is shown in Figure 4.13.
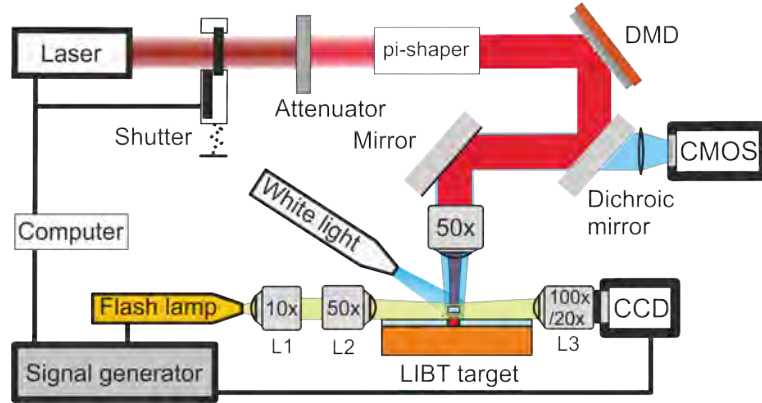
Figure 4.13: Shadowgraphy experimental setup. Laser pulses are homogenised via a pi-shaper and shaped into a circular lateral intensity distribution via DMD, then imaged at a LIBT donor. A computer triggers the laser pulses as well as a flash lamp and CCD to take 8ns snapshots of the process.

The flash lamp discharge was of duration 8ns, and corresponded to the exposure time of the shadowgraph recorded on the CCD camera (scA1400–17 fm, 1.4 Mpx, Basler AG), which was active for 20ms. Both flash lamp and CCD were activated by a signal generator, which was triggered via computer at the same time as a laser pulse. The minimum delay between triggering the signal generator and actuation of the flash lamp was 1.4μs. A continuous white light source was used for real-time viewing of the sample on the CMOS camera for positioning before shadowgraphs were recorded. The 20x and 100x objectives were used when either a larger field of view, or higher resolution

were desired, respectively. These objectives paired with the CCD camera provided either 420nm/pixel resolution with 400μm field of view in the direction of the flyer, or 90nm/pixel resolution and 120μm field of view images (though of course diffraction would limit the resolution of images incident on the CCD to 1μm with the 20x and 727nm with the 100x, as in Chapter 5). Figure 4.14 shows a more detailed schematic of the setup around a sample at the time of imaging in (a), while (b) shows a shadowgraph of a flyer taken, detailing the different parts of the sample visible.
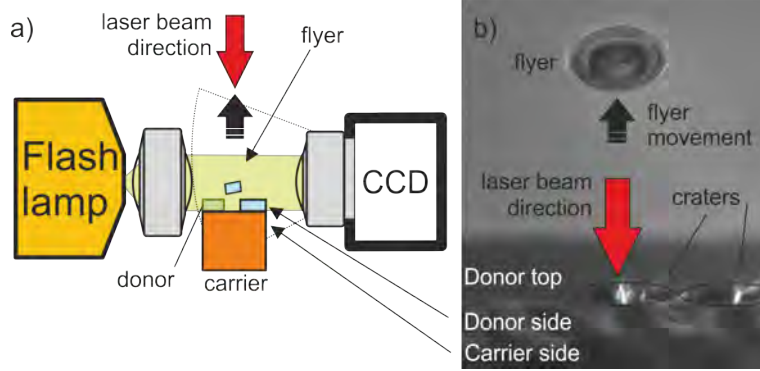
Figure 4.14: The setup during LIBT. (a) Schematic of a LIBT event being imaged via shadowgraphy and (b) a shadowgraphy image recorded on the CCD, a flyer is captured after ejection from the donor, craters where flyers have been removed are visible.

In order to capture near-side-on views of the LIBT process, it was optimal to target donor positions near the edges of samples. As spin-coating, which was used to produce the SU-8 donor layers, can produce a thick 'bead' of material at the perimeter of an underlying substrate, samples were cleaved in the centre so that regions of the intended, near-uniform thicknesses of donor could be positioned near to the objective-CCD imaging plane. Figure 4.15 shows a sequence of shadowgraphs taken of different flyers from the same 6.4μm SU-8 on silicon sample at different time delays. All flyers were produced in this example with a fluence of 1.39J/cm^2.
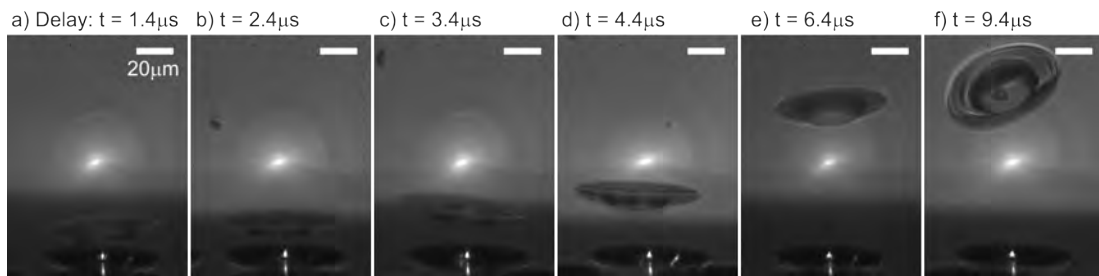
Figure 4.15: A sequence of different flyers taken at time delays between t=1.4μs and 9.4μs after femtosecond pulse exposure. The sample was 6.4μm SU-8 on silicon, and the 100x objective was used with the CCD. The scale bar was determined via the placement of a grating structure of known period at the image plane.

The bright spot seen in Figure 4.15 (a–f) is an image of the spark-gap illumination from the flash lamp, and a reflection of this can be seen in the side-wall of the craters at the

bottom of each image. Despite a near-top hat circular intensity profile being used to produce LIBT, the flyers emerge with a 'saucer' shape – a widening taper towards the top-side of the flyer from a smaller circular base. The base width corresponds to the $\approx 20\mu m$ wide circular imaged intensity pattern. While a slight widening taper can be seen in previous LIBT and LIFT deposits, it has not been clear whether this taper was a result of the impact of flyer on receiver, or produced during release from the donor as demonstrated here. The breadth of the tapered rim is on the order of 1/2 the width of the intended flyer width, which is large compared to previous results. This may be a result of the material, size, shape or propulsion mechanism of LIBT (a slower release would allow for shear-shock waves to travel laterally further during release, leading to a broader rim for example), but has not been studied further here.

The threshold fluences for silicon were 0.80J/cm^2 and 1.35J/cm^2 for thin and thick donors respectively, while for thin and thick germanium carriers yielded threshold fluences of 0.55J/cm^2 and 0.60J/cm^2 respectively. The difference in threshold fluences between thin and thick donor layers is much greater for silicon than germanium, which may be the result of a number of factors. Adhesion of SU-8 to the carrier material, carrier thermal expansion, carrier ablation threshold and carrier absorption depth are all likely factors to be considered in future study. The propulsion mechanism itself may be different between the two carriers; with a shorter absorption depth for germanium than silicon at 800nm, it is possible that energy is deposited over a greater depth in silicon which leads to thermal expansion being the dominant mechanism for LIBT, while a shorter energy deposition distance in germanium may lead to vaporisation being the dominant mechanism. Thermal expansion would increase approximately linearly with fluence, leading to a large fluence increase requirement for a thicker donor layer. At vaporisation threshold fluence, the phase change of the carrier leads to a near-step change in confined pressure, which may be sufficient to eject a range of donor thicknesses; only a small increase in fluence may then be required to eject the thick donor as compared to thin donor layer. However, this remains conjecture to form the basis of future study.

Figure 4.16 shows the distance travelled by flyers from various carrier/thickness combinations at different fluence as a function of imaging delay time. Though LIBT was performed in air, the distributions appear linear, in agreement with previous results which found no major influence of surrounding atmosphere on propagation velocity [104].

While most experiments were carried out at fluences just above threshold, an additional set of results for the thin donor from a silicon carrier were taken at a fluence 20% above threshold in order to test for an influence of fluence on velocity. Table 4.1 shows the average velocities of flyers from the different combinations. Velocity data was extracted by comparing the position of flyers at each time delay with the minimum delay position, and dividing by the relative time differences.

Velocity averages in the range 9m/s to 20m/s were observed, with thicker donor material yielding lower velocity flyers. While a 20% increase in fluence appeared to lead to
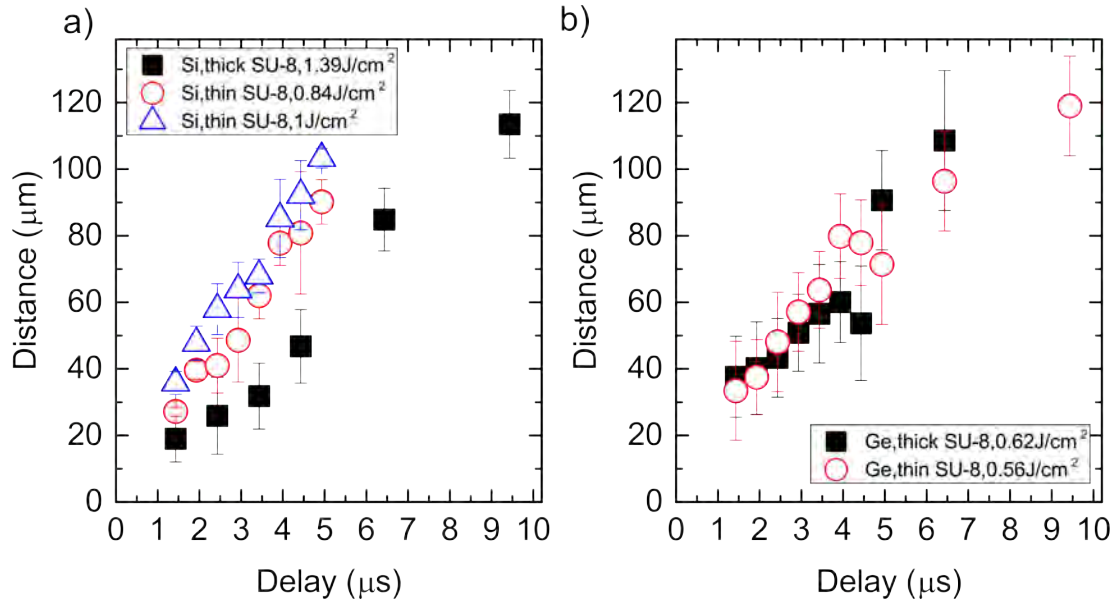
Figure 4.16: Distances travelled by flyers at different delay times for (a) silicon and (b) germanium carriers. Each delay/fluence/thickness combination was repeated multiple times, and the error bars represent the standard deviations in values recorded.

Table 4.1: Velocities of intact flyers from different donor thickness/carrier/fluence combinations

Carrier/Donor,(Fluence)	Mean,velocity (m/s)
Si/Thin,SU-8 (0.84 J/cm^2)	18.1±2.1
Si/Thin,SU-8 (1 J/cm^2)	19.8±2.3
Si/Thick,SU-8	9.3±2.8
Ge/Thin,SU-8	13.5±1.5
Ge/Thick,SU-8	9.1±5.4

an increased velocity of the thin SU-8 on silicon flyer, the values were within one standard deviation of each other. It is of note, however, that the distances travelled at set delay times of flyers of thin SU-8 from silicon were consistently higher when the higher fluence was used, suggesting that the time between pulse exposure and flyer release may decrease with increasing fluence.

In order to further investigate the influence of fluence on flyer velocity, flyer distances at two set time delays from thick donors on both silicon and germanium were recorded as a function of fluence. The results are shown in Figure 4.17.
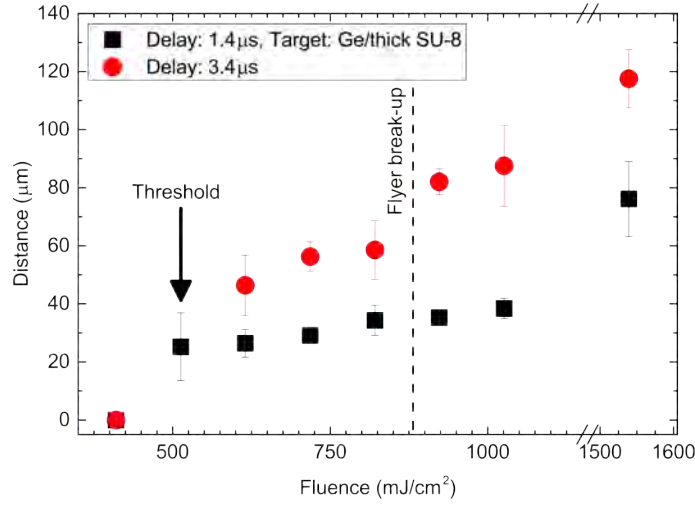
(a) Germanium
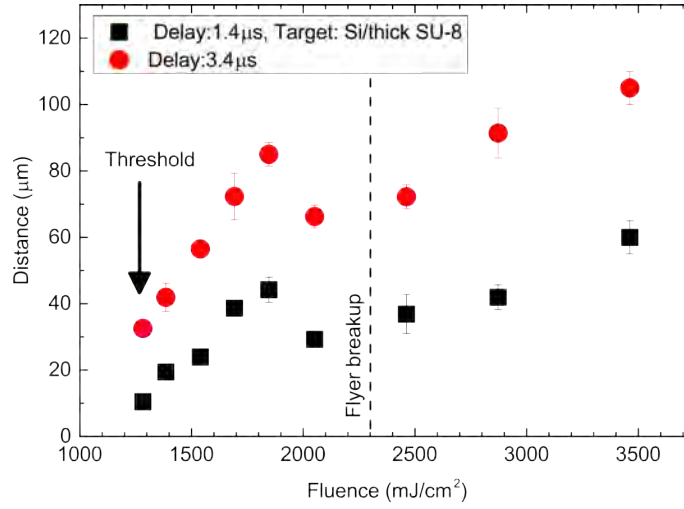
(b) Silicon

Figure 4.17: Distance travelled by the flyer after set times from the two carrier substrates.

From a germanium carrier, only flyers produced at fluences up to 0.9J/cm^2 remained in an intact state, while flyers remained intact when using fluences up to 2.3J/cm^2 from silicon. More than 90% of flyers were observed to be fragmented when using fluences above these values, and the additional data points plotted in Figure 4.17 beyond these fluences are a result of measuring the position of the largest fragment visible in the shadowgraphs taken. Figure 4.17(a) shows that distance travelled increases monotonically in a near-linear fashion for flyers from a germanium carrier, and the calculated increase in velocity with respect to fluence was $23\pm10\text{ms}^{-1}/(\text{Jcm}^{-2})$. The behaviour for flyers released from a silicon carrier is more complex, as seen in Figure 4.17(b). An initial linear region corresponds to a rate of change of velocity with respect to fluence of $14\pm10\text{ms}^{-1}/(\text{Jcm}^{-2})$, followed by a decrease in distance travelled before the flyer breakup threshold. Distance travelled, as well as velocity, begin increasing once more above this threshold. The reason for the dip may be unrelated to fragmentation, as a decrease in distance travelled has occurred at the data points immediately prior to the

threshold, and no such dip was observed from a germanium carrier. Instead, the dip may be indicative in a change of the dominant mechanism for flyer propulsion; perhaps from solid carrier thermal expansion to vaporisation. Analysis of the craters left in the donor layer after transfer lend more information; the diameter of craters as a function of fluence in thick SU-8 for both Si and Ge are shown in Figure 4.18.
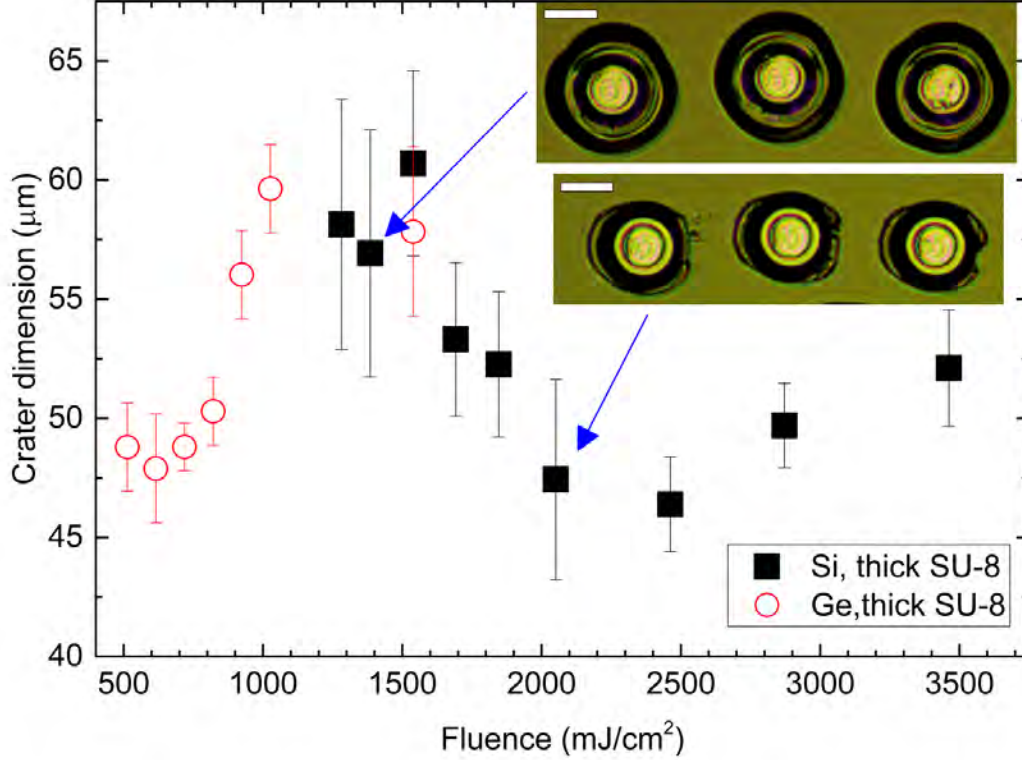
Figure 4.18: Crater diameter for varying fluence from SU-8 on Si and Ge carriers. Optical microscope images of SU-8 on silicon after LIBT are shown in the inset, where the scale bar is 25μm, and are arrowed to the corresponding fluences at which visible craters were produced.

A minimum of crater size in SU-8 on silicon for the intensity mask used was found at near 2.5J/cm^2, while no such minimum was found for germanium. Crater size was expected to remain constant or increase only slightly with increasing fluence when using an exposure mask. A slight increase may be explained by imperfect imaging at the edges of exposed regions; as there will be some finite decay distance of intensity at this boundary, it is only natural to assume that a higher intensity would yield a larger area over which the transfer threshold is exceeded. However, this would not explain the local minimum observed. The beam diameter was $\approx 20\mu$m, as measured from optical microscope images of the donor at regions where low fluences were used. The flyer diameter observed is much greater than this, at $> 40\mu$ in Figure 4.15. During flyer release, then, additional donor material, attached to the region immediately above the exposed area, must also shear free. The local minimum may represent a region where the volume immediately above the exposed region is propelled with too much force for the surrounding material to react; the velocity of shear waves in the donor material may

be too slow for surrounding material to be dragged upwards, instead the material limit being reached rapidly at the perimeter of the exposed region. This may explain the dip behaviour seen for silicon carriers in Figure 4.17(b); in the first region of the curve fluence is increasing and crater diameter is decreasing. A decreasing diameter implies a lower volume, and hence mass, of SU-8 is being released; a smaller mass undergoing the same propelling force over the same distance will reach a higher velocity. The propelling force, whether via thermal expansion or vaporisation, will increase with increasing fluence. This leads to the initial increase in velocity with fluence. As the crater diameter begins to expand past 2.5J/cm^2, however, the increasing mass may offset the increasing propelling force such that lower final velocities are reached. This is in absence of other possible effects, such as the switch between thermal expansion and vaporisation.

Different failure modes have been observed in polymers as a function of impact velocity [136], and may provide an explanation for the observed variation in crater diameter. Slow loading leads to tensile failure (brittle fracture), while fast loading leads to the dominance of a ductile failure regime in which shear crack growth is more likely. Hence, at higher fluences the flyer is more likely to shear vertically at the side-walls than taper outwards. For yet higher fluences, where crater diameter begins to expand, it may be that shearing is still the dominant mechanism, but enough kinetic energy is provided to unintended donor material during the shear that an additional 'rim' of donor is also removed; recalling that almost all flyers produced above 2.5J/cm^2, where the craters expanded, were fragmented. Figure 4.19 shows the changing profile of the taper for three fluences between threshold and near to the crater-minima, demonstrating the effect.
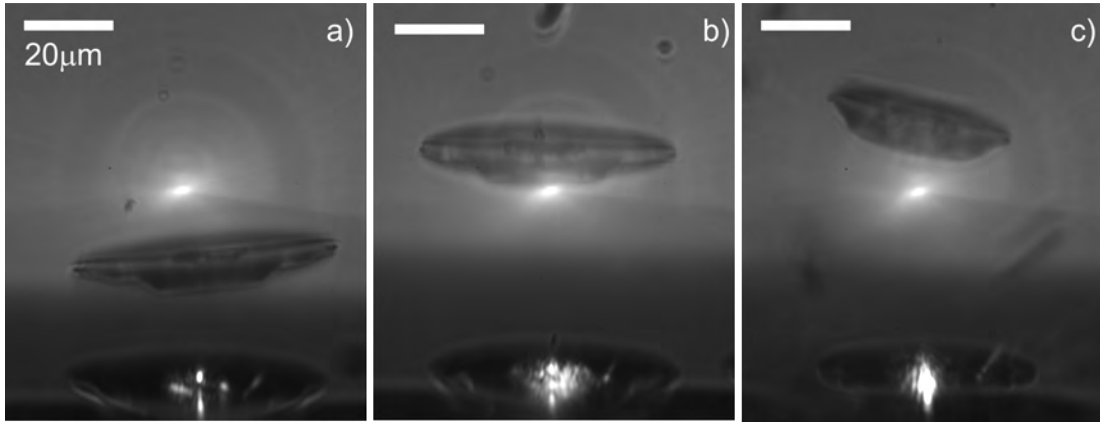
Figure 4.19: Shadowgraph images of flyers from a thick SU-8 layer on silicon produced at fluences of (a) 1.39J/cm^2, (b) 1.69J/cm^2 and (c) 2.05J/cm^2. The delay time was $3.4\mu\text{s}$.

While the exact transfer mechanism of LIBT is not determined from the results in this section, they provide valuable information salient to the optimisation of the process. An unexpected change in transfer regime has been discovered to occur, and must be accounted for in LIBT manufacturing. Transfer velocities have been found to be an order of magnitude lower than common values for LIFT, and may provide a method for intact transfer of more delicate structures.

4.3 Modelling of LIBT

The low damage to the carrier surface shown at the end of section 4.2.2, paired with the low transfer velocities of flyers released via LIBT, prompted the consideration of alternative flyer propulsion mechanisms in LIBT rather than the vaporisation often observed by the group when performing LIFT. Others have shown that thermal expansion may be a mechanism of flyer propulsion for LIFT [120] via numerical simulation, while the confinement of solids during exposure to high energy laser pulses (such as the carrier confined underneath a donor in LIBT) can prevent explosive decomposition and alter phase change behaviour [137].

In this section, highly preliminary results from a 3D thermal expansion model are shown and compared to the flyer behaviour seen in section 4.2.3. Several of the model's aspects must be expanded to account for higher-order effects, such as non-linear absorption and stress-strain relations, thermally-dependent material properties, and a study of the model's output dependency on the resolution and number of grid points used. The MATLAB code used to define the differential equation describing the carrier/donor behaviour is given in Appendix B, with a brief description given below. Material properties of silicon and SU-8 photoresist were used throughout, specified in Appendix B, with a donor thickness of 3.8 or 6.4μm, to reflect experimental results in section 4.2.2. Though the model was applied briefly to study the LIBT mechanism from a germanium carrier, germanium's stronger absorption at 800nm led to far higher initial temperatures in smaller volumes of the carrier, and ultimately required impractical levels of computer memory and processing time for the adaptive time-step algorithm used to converge to a solution. This stronger absorption, paired with no evidence of low carrier surface damage as for silicon, meant that germanium carriers were not the focus of this modelling effort.

Point masses representing either carrier or donor material are arranged in a cubic lattice, each point connected to the nearest surrounding six points. A single connection between two point masses is considered as a pair of 'springs', capable of transmitting extensive, compressive and cantilever forces. A volume element containing a point mass is then defined by the six springs associated with that point mass.

A uniform, square lateral spatial intensity laser pulse undergoes Fresnel reflections at air/donor and donor/carrier interfaces, then deposits energy throughout the carrier depth according to the Lambert-Beer law and heats a laterally central region of the carrier lattice. The temperature change associated with this energy transfer is assumed instantaneous, and a starting condition of the simulation.

Volume elements in equilibrium which have been heated would naturally undergo thermal expansion; fully thermally expanded lengths for each of the six springs associated with each point mass are set as 'rest lengths', and spring constants are defined from these using the Young's moduli of the materials. Tensions across a spring pair between

point masses are assumed uniform, as any change in force over a finite distance acting on zero mass would be non-physical – this means that each volume element must have some instantaneous extension in each direction to equal the tension acting in adjacent elements. This allows for the calculation of the instantaneous dimensions of each volume element.

From these dimensions, compressions are calculated, and Poisson compression (the tendency of an object, when compressed in one axis, to expand in the orthogonal axes) is applied to update the 'rest length' in each direction of each volume element. Rest lengths are updated once more via the same assumptions of uniform tension and subsequent instantaneous compressions to give a second-order approximation of instantaneous dimensions of each volume element.

Tensile and cantilever forces are then calculated from standard formulae. Stresses are calculated between each volume element. Vertical accelerations were observed to oscillate with a period of the round-trip time of a pressure wave across the thickness of the donor – in order to account for unequal lateral and vertical grain sizes in the mesh, a weighting factor was applied to cantilever stresses depending on adjacent velocities, with a maximal increase which would effectively reduce the cantilever length down to the donor thickness – the maximum distance information of a shear wave could travel before acceleration reversed.

A simplified von Mises yield criterion is calculated between each volume element, and any springs with stress exceeding the material yield stress is considered 'snapped' for future time points. In the special case of the interface between donor and carrier, this yield stress is set as an adhesion strength from the literature [138]. Any snapped springs no longer transmit cantilever or tensile forces, or heat flow, though compressive forces may still exist.

The numerical ordinary differential equation solver used was based on the Dormand-Prince method, with an adaptive time step. The required time step then varied depending upon number of elements, fluence and material constants, but was typically not below 10^{-14}s. Simulations designed to determine fluence-velocity curves of the flyer used a total of 1215 volume elements, comprising 10 layers of 9x9 lateral elements to simulate the carrier, and 5 layers of 9x9 lateral elements to simulate the donor. Though this is a somewhat coarse granularity for a finite-element model, extending beyond these values was not practical given the memory requirements of the solution. The range of the time solution was varied by carrier/donor combination, as flyers were found to release more rapidly in some cases, however typically flyer release would occur on the tens of ns timescale; each simulation was set to solve until 500ns to ensure adequate time for flyer release to occur. Fluences tested were matched to those used experimentally, and ranged between 0.01 to 3.11J/cm^2. The total depth of the carrier layer was defined to be 5 times the absorption depth of silicon at a wavelength of 800nm.

Though the experimental results in section 4.2.2 showed fliers with a circular intensity profile, the feasible grid size of 9x9 lateral elements to be used in the majority of simulations meant that a square intensity profile of 3x3 central elements of similar lateral dimensions would be used. At the end of a 500ns solution, the final arrangement of point mass velocities and broken springs would be known. A flyer, flyer fragments, and their velocities were detected by searching for contiguous chunks of points of donor material originally near to the central donor region, disconnected from the underlying carrier point masses. The flyer velocity was taken as the average of the point masses within the largest contiguous disconnected region of donor point masses. The resulting fluence-velocity curves for the two tested thicknesses of donor material are shown in Figure 4.20 as solid lines, as well as experimental data points provided after further data analysis of shadowgraphy results provided by Matthias Feinauegle.
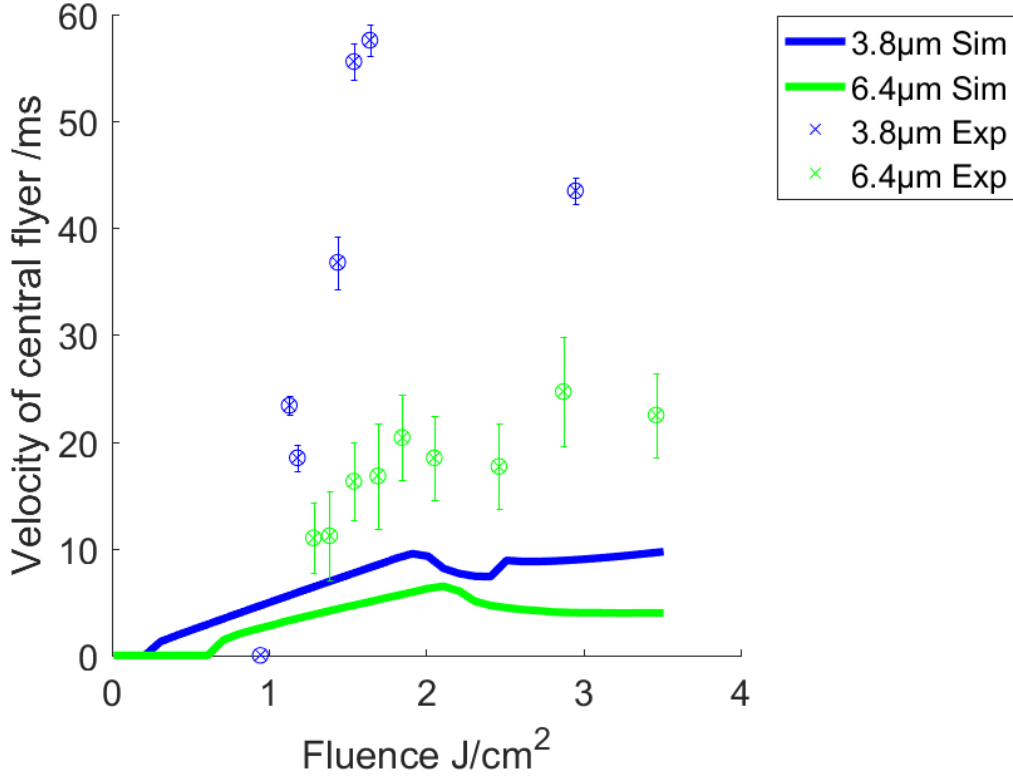
Figure 4.20: Simulated fluence-velocity curves for 3.8 and 6.4μm thick SU-8 donor flyers ejected from a silicon carrier, as well as experimental data points. Error bars are the standard deviation of velocities at the given fluences.

Though the magnitude of the resulting simulated curves is approximately a factor of $\approx$5 lower than experimental values, some key features of the experimental distributions are recreated. Following the trend of experimental points back to their intersection of the fluence axis, the simulation would appear to provide thresholds for the LIBT at the correct order of magnitude, between 100mJ/cm^2 and 1J/cm^2. The simulation correctly predicts a lower velocity across all fluences for the thicker donor layer, an approximately linear increase in velocity with intensity up until a 'dip' at $\approx$2J/cm^2, and in the case of the 6.4μm thick donor, a levelling out of points beyond this dip. In the case of the

3.8μm thick donor, few experimental points at fluences beyond this dip were available, as flyers became highly fragmented. Analysis of the 3D array data at the end of each simulation provided a clue as to the mechanism of the dips in the curves; it was at a fluence of $\approx$2J/cm^2 that flyer fragmentation began, with small chunks of flyer breaking off at high velocity. If the average velocity of all point masses no longer connected to the underlying carrier is taken, the linear trend continues for the full extent of velocities tested; i.e. the total momentum of released mass increases linearly, but small fragments breaking off of the central flyer with high velocity lead to a reduction of the central flyer velocity at the onset of fragmentation.

While the model shows some agreement with experimentally recorded data, the number of assumptions and simplifications made make it unsuitable for publication in its current state. Methods exploiting the radial symmetry of the circular flyers produced experimentally could reduce memory requirements, for a finger grid resolution, and non-linear material behaviours must be accounted for. The essential feature of the model – snapping of interconnections between point masses – is far beyond the linear approximation of stress/strain relations used, and is considered the key element of the method to be updated in future.

4.4 Conclusion

Laser-induced transfer has been shown to produce solid polymeric deposits on the microscale in both forward and backward regimes. The phase of the donor material was preserved throughout transfer, and the first demonstration of the DMD-enabled shaping of these deposits was made.

It has been shown that donor material may be imprinted with nanoscale features via a pre-patterned carrier, and that these features are well reproduced in final deposits. Lateral features as small as 140nm were produced with this method up to a depth of 220nm. LIBT has been observed to occur from regions of carrier substrate which show little damage; if the carriers prove to be reusable, this may allow for the rapid reproduction of nanoscale patterning on LIBT deposits. The applications for the deposition of microfluidic devices or polymer waveguides on substrates which preclude the use of other additive manufacturing methods are readily apparent.

The dynamics of LIBT have been studied via shadowgraphy, and show a 'slow' propagation speed for flyers compared to previous studied of LIFT (tens of m/s compared to hundreds or even above 1000m/s). The underlying mechanism of propulsion for LIBT in this case is yet to be determined; though preliminary modelling work has shown that thermal expansion may be capable of providing the driving force on the flyer. Stresses observed during simulation at the perimeter of donor volumes immediately above exposed areas exceeded the ultimate tensile limits of SU-8, in addition to the stresses at the interface of the carrier and donor exceeding ultimate limits of adhesion strength between the two materials known from the literature, while thermal expansion in the

solid phase was the only driving mechanism.

Laser induced transfer has been a developing technique in research for several decades. The level of deposit shaping fidelity shown in this work may aid the translation of the technique into the production of more functional, commercial devices, as well as opening up avenues for further research.

Chapter 5

Multiple Exposures

An ongoing goal in optics is the reduction of individual feature size, and hence improvement of overall patterned resolution, producible via laser machining. The finest resolution, R, feasible in a single optical projection is given by the well-known Abbé diffraction limit, $R = \lambda/(2\text{NA})$, where λ is the wavelength used and NA is the numerical aperture of the imaging system.

Much progress has been achieved by pursuing the use of shorter wavelengths, with 13.5 nm wavelength EUV technologies poised to produce features on the $\approx$10nm scale [139]. Such technologies have necessitated the invention of short wavelength lenses, or even all-reflective optical systems for EUV lithography, while various image-formation techniques and material improvements have also contributed to the achievement of ever-finer resolution by optical techniques [140]. EUV lithography is a masking process which employs a laser-produced plasma (typically tin [141]) to generate the 13.5nm wavelength light. As all known solids have poor reflectivity at this wavelength, multi-layer mirrors enabling Bragg reflection are required – 7nm thick Mo/Si bilayers for instance. The first collector optic (either lens or mirror) is exposed to the tin plasma, and hence steps must be taken to mitigate tin deposition on the collector; magnetic deflection of ions, buffer gases and in situ tin etching via hydrogen radicals are all potential methods to solve this concern. Clearly, the level of complexity involved in imaging with shorter wavelengths increases dramatically, even for such elementary components of a beam line as mirrors.

Other approaches to increase final feature density do not focus on the factors of the Abbé diffraction limit. One such class of techniques is double patterning [142–144], also often referred to as multiple patterning or, as will be used here, pitch-splitting multiple exposures (PSME) [144, 145].

While the feature sizes were limited with thin films due to peeling in section 3.2, and resolution by the diffraction limit in section 3.3, PSME allows for the modification of material in regions separated by less than the diffraction limit. Figure 5.1 shows the premise of the technique. In one shot, many points on a sample can be simultaneously exposed, provided no features within the image have a separation below the diffraction

limit. A second pulse then exposes features (which may be the same as the first shot, as in Figure 5.1, or different) at a different position on the sample. All features produced in this second shot must be separated by at least the diffraction limit, however this is not a constraint on their separation from *previous* exposed patterns. The same is true of producing yet more features with subsequent pulses. As the Abbé diffraction limit places a limit on the *separation* between features, but not on the size of the features themselves, this means that PSME can be used to build up a final structure with periodicity below the diffraction limit.
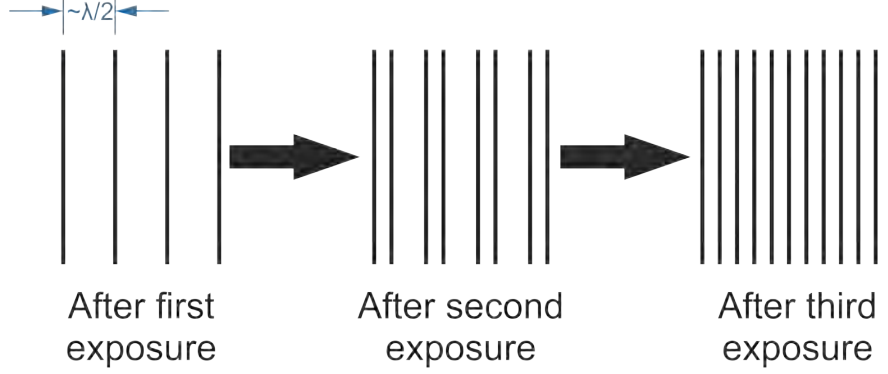
Figure 5.1: Multiple exposures used to produce sub-diffraction limit spacing between features, where $R \approx \lambda/2$.

As PSME requires multiple intensity masks, there is a requirement for accurate positioning of a mask image at the sample compared to the positions of previous images of masks. This concern in PSME, referred to as critical dimension (CD) uniformity is discussed in depth by Hazelton et al. [143].

A solution to the above case of CD uniformity control is to use a spatial light modulator, such as a DMD, as a dynamic intensity mask. The DMD requires no repositioning, as masks are updatable digitally on a millisecond timescale [21]. This method is hence inherently orders of magnitude faster than mechanically replacing intensity masks, and suffers no risk of sample drift with respect to projected intensity position. This section describes results from the use of a DMD acting as a dynamic intensity mask for PSME femtosecond ablation and multi-photon polymerisation. DMD-enabled ablation and multi-photon polymerisation has been demonstrated previously [27, 146, 147], and the method described here is expected to enhance achievable resolution for these techniques.

Individual feature widths as small as 250nm are produced in BiSbTe via ablation. Reductions of resolution from the limits of 1μm and 727nm, using two different microscope objectives, to 370nm and 270nm respectively are shown via ablation in nickel. The reduction factor of $\approx 2.7\times$ is greater than the factor of $2\times$ shown in a two-photon resist, and hence represents an exciting new mechanism to exploit via PSME.

5.1 Thin bridge production

Any material property modification due to exposure to a spatial intensity pattern is a result of the material response to said intensity. This concept may seem obvious, but the nature of the material response linked to a particular property modification will be shown to allow for novel machining techniques involving PSME for the remainder of this chapter. While the results produced in this section do not reduce final resolution of a machined pattern, and hence are not strictly PSME, they show a reduction in the achievable feature sizes in multiple exposures as compared to single exposures, and are illustrative of the concepts used in later sections of this chapter.

5.1.1 Non-overlapping exposures

Consider the depth profile of a sample in a one-dimensional model after i successive ablations, $D_{ai}(x)$. The change in depth, $\Delta D_{ai}(x)$ due to the ith incident intensity distribution $I_i(x)$ will, of course, depend on $I_i(x)$. As is clear from previous chapters, ablation will not generally occur in a material until some 'threshold' intensity, I_{th} is reached. Above this threshold, increased intensity will generally lead to increased ablation depth, and so the first-order dependence on intensity of $D_{ai}(x)$ is given in Equation 5.2. Gamaly et al. explore analytical solutions for the estimation of ablation thresholds for various pulse lengths and materials [4]. In brief, they argue that the minimum energy density to achieve ablation must translate to the energy required to remove an individual atom. In metals, for femtosecond pulses, the threshold fluence is proportional to the wavelength, density of conductive electrons, and the sum of the atoms' binding energy and the work function of the metal in question. In dielectrics a similar expression is deduced, where the threshold fluence is proportional to the skin depth, the number density of atoms, and the sum of the atoms' binding energy and ionisation potential.

$$D_{ai}(x) = D_{a(i-1)}(x) + \Delta D_{ai}(x) \tag{5.1}$$

$$\Delta D_{ai}(x) \propto \begin{cases} (I_i(x) - I_{th}) & \text{Where } I_i(x) > I_{th} \\ 0 & \text{Otherwise} \end{cases} \tag{5.2}$$

Figure 5.2 shows the resulting depth profile, intensity and threshold in arbitrary units after 2 successive exposures to Gaussian intensity profiles of the form in Equation 5.3.

$$I_i(x) = \exp(-2(x - x_i)^2/(\omega_s^2)) \tag{5.3}$$

Where x_i is the peak intensity location and ω_s the spot size. In the following example, arbitrary units (au) are used throughout, with the results shown in Figure 5.2 being generated with $x_2 = x_1 + 18$ and $\omega_s = 3\sqrt{(2)}$, while the threshold was set at $I_{th} = 0.9$.

Figure 5.2(a) shows the threshold intensity, I_{th}, the current Gaussian exposure intensity distrubution, I, the depth profile before exposure D_{a0} and after the first exposure D_{a1}. Figure 5.2(b) shows the intensity profile shifted by 18au to the right, with depth profiles D_{a1} and D_{a2} after the first and second exposures respectively. A 'bridge' of unaffected material of width 3 is visible in Figure 5.2(b). In this first-order approximation, in fact, the width of this unaffected bridge could be made *arbitrarily* narrow, and the peak intensity reduced to an arbitrarily small amount above threshold, such that a depth modulation of *any* period could be generated (albeit with a vanishingly small amplitude as the peak intensity is reduced towards threshold).
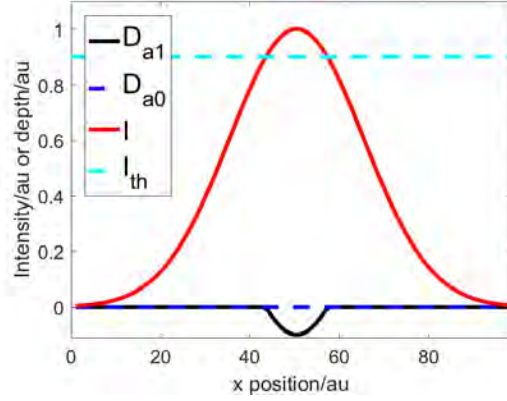
(a) First intensity profile, and depth and before and after 1 exposure
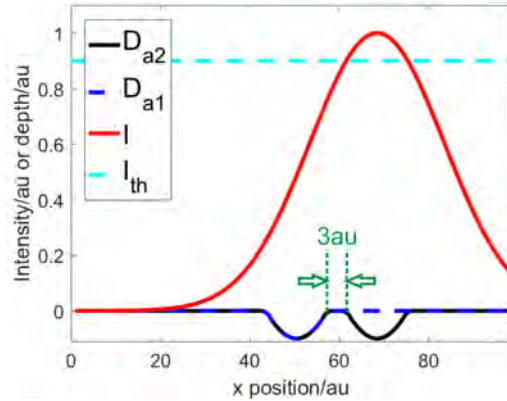
(b) Second intensity profile, and depth before and after 2 exposures

Figure 5.2: The depth profile of a material before and after 2 exposures of laterally shifted Gaussian intensity profiles.

There are, of course, more complex effects to take into account which would likely limit the process. Some degree of heating, and hence melting, will occur in a material around an ablated volume, even when femtosecond machining is employed (which reduces such untargeted heating, as described in section 2.2.2). This melting would tend to damage surrounding fine structures, and effectively 'flatten out' depth modulation. Any existing translational asymmetry in the substrate material (grain structure, for instance [148]), could affect the uniformity of ablation pulse-to-pulse. Such asymmetries would

undoubtedly be created by previous pulses at small enough separations – melting and resolidifying, or pressure shock waves around an ablation site could alter material properties in the immediate vicinity. Additionally, any power instability in the laser source would represent an increasingly large fraction of the 'above threshold' intensity; supposing peak intensity were set at $1.01\times$ the threshold in order to ablate very narrow regions, a 1% instability in the laser intensity would mean that ablation would often occur over a much larger region than intended, or not at all; a similar argument could be made for the stability of the beam shape. Finally, at an atomic level, it is incorrect to describe *thresholds* for material removal; rather, at a given intensity, there would be a *probability* of removal – one that sharply increases from near-zero to near-unity around I_{th}. On the nanometre scale, this probabilistic removal may affect results, and as ablation depths at the used fluences during the following experiments were typically on the tens of nanometres scale, it may have some impact.

A single minified DLP7000 13.6μm pixel using a 50x objective corresponds geometrically to ~90nm (measured from the SEM images of ablated patterns and compared to the loaded binary images on the DMD) at the sample. To reach the minimum possible separation between ablated features, single-pixel control of the DMD was desired. Hence, the DLP7000 line was preferred for this experiment, as the DLP3000 suffers from the dithering problem shown in Figure 2.9. For the initial tests, a 200nm thick bismuth antimony telluride (BiSbTe) sample was used, which was thick compared to a single-shot ablation depth and hence was expected to avoid the peeling problems seen in section 3.2.

(a) First image displayed on DMD

(b) Second image displayed on DMD

(c) Third image displayed on DMD

(d) Fourth image displayed on DMD

(e) Ablated pattern in bismuth antimony selenside

(f) Sub-wavelength feature remains after two lines ablated in bismuth antimony selenside - top right corner of 5.3(f)
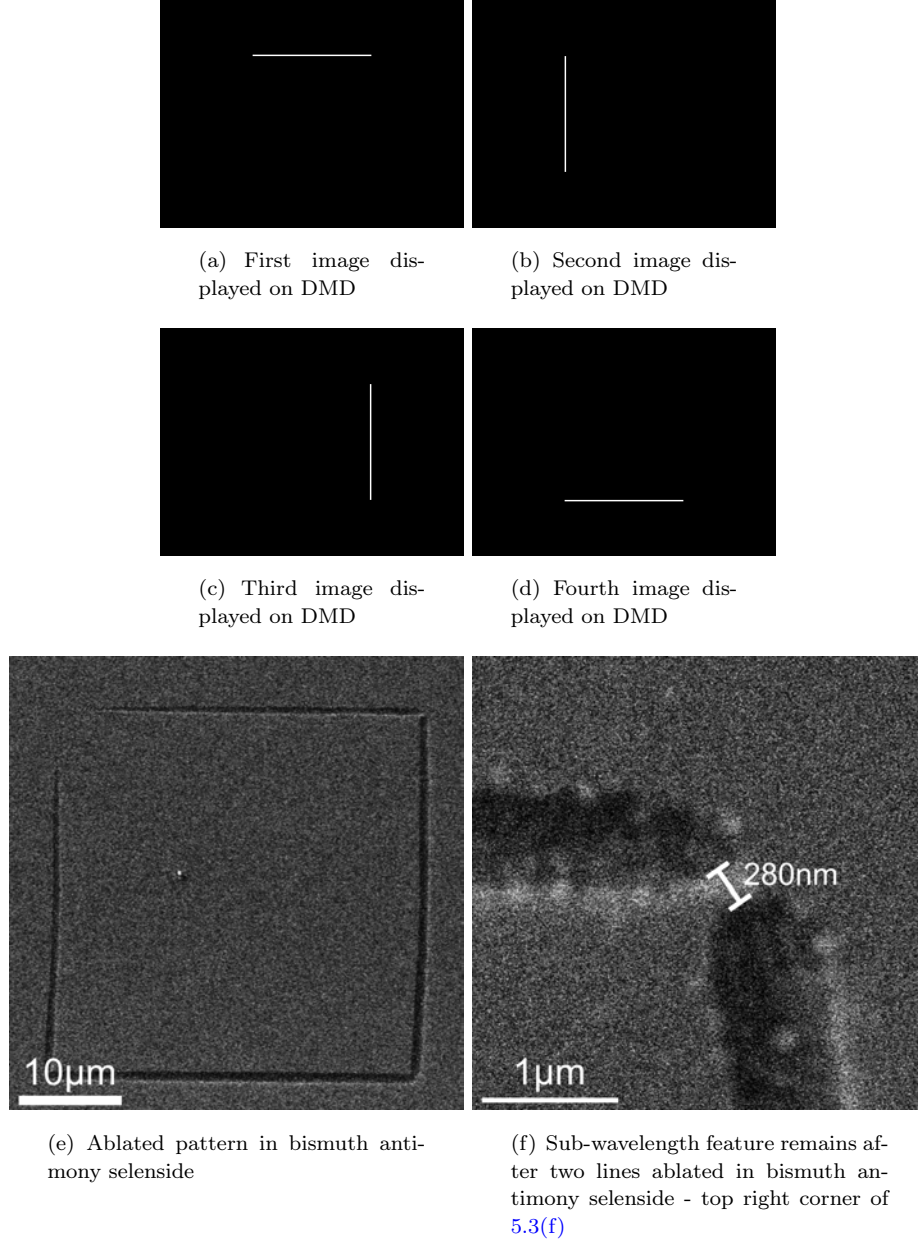
Figure 5.3: A split ring pattern ablated into 200nm thick BiSbTe in four shots, each at $0.125J/cm^2$.

Figure 5.3 shows the result of the technique for creating a split ring pattern. Four sequential shots are used to ablate the four sides. The whole ring was also displayed and ablated in a single shot, i.e. all images in Figure 5.3(a)—5.3(d) were displayed during a pulse simultaneously, forming a complete square on the DMD. This resulted in an ablated square shape with no gaps left between the ends of each side, except for the gap due to low ablation depth in the top left corner, similar to Figure 5.3(e). The unequal ablation depth in Figure 5.3(e) is suspected to be a result of the inhomogeneous beam intensity on the DLP7000 line. In this particular example, the 'split' side of the ring is in fact not separated by any pixels on the DMD from the other three – although separations of greater than 0 pixels on the DMD were tested, 0 separation yielded the

smallest feature sizes. In a perfectly minified intensity pattern, there would be no gap in Figure 5.3(f); it is suspected that optical filtering (loss of some, typically high, spatial frequencies as a result of limited NA optics and passing through apertures) led to the intensities at the end of each side of the square being lower than the ablation threshold of the sample at the corner in Figure 5.3(f), as described in Figure 5.4.

(a) Wide aperture   (b) 100 pixel radius aperture

(c) 50 pixel radius aperture   (d) 30 pixel radius aperture
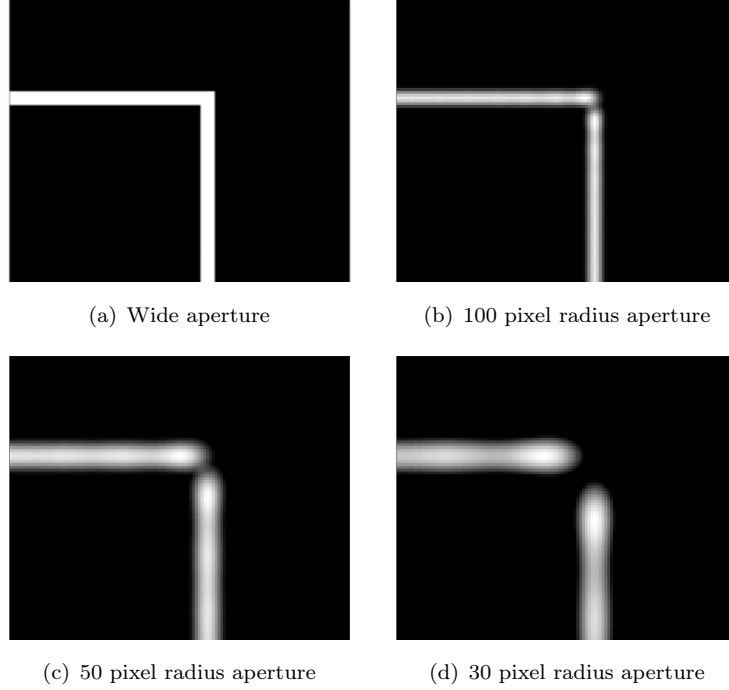
Figure 5.4: A close up of the the simulated combined intensity above threshold, after optical filtering through different radii of aperture, of two sides of the split ring.

While the theory described thus far has used Gaussian intensity distributions as examples, some extra consideration must be given to the effect as it applies to image-projection. In any imaging system, some spatial frequencies will be lost (typically higher spatial frequencies, due to finite lens diameters or apertures for example). A simple simulation of this effect is shown in Figure 5.4, in which the binary images in Figures 5.3(a) and 5.3(c) are Fourier transformed (to give the electric field at the focus), field components below a certain radius of pixels at the centre of the transform are retained (simulating aperturing), the inverse Fourier transform is taken, with its absolute square value giving the final intensity distribution. With no truncation in spatial frequencies, as in Figure 5.4(a), no gap is produced, and the linewidth corresponds exactly to that in the masks in Figure 5.3. With a decreasing aperture radius, which in practice could correspond to the finite aperture at the entrance to a microscope objective or other clipping along the beam line, the linewidth widens, and a thin bridge of unaffected material is predicted between the end-points of the projected intensity patterns. The uploaded DMD masks in Figure 5.3 had linewidths of 5 pixels, which would scale geometrically to ~500nm for this setup at the sample. Clearly from Figure 5.3(e) the final linewidth is close to 1μm – both the broader linewidth and remaining thin bridge

are predicted by optical filtering effects.

5.1.2 Overlapping exposures

Thin bridges of unaffected material have been demonstrated, however multiple exposures can be used to generate fine features even when affected regions overlap. The case for ablation is shown in Figure 5.5.

(a) Depth profile before and after 1 exposure   (b) Depth profile before and after 2 exposures
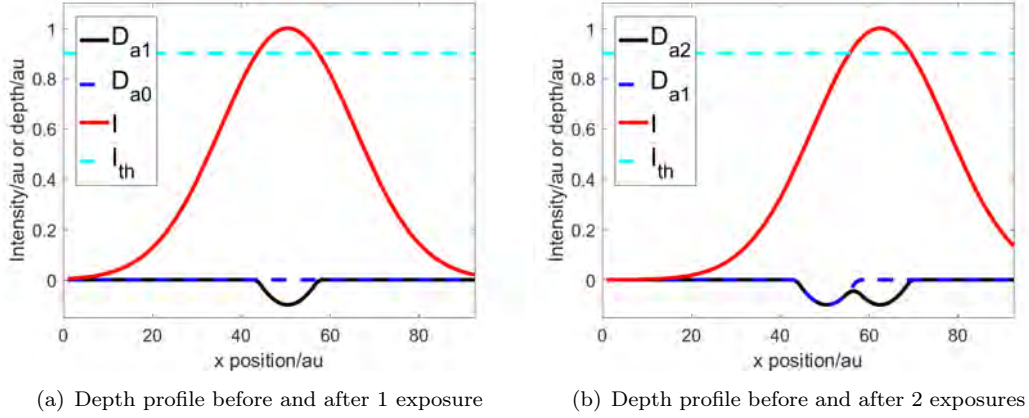
Figure 5.5: The depth profile of a material before and after 2 exposures of laterally shifted Gaussian intensity profiles, with affected regions overlapping.

Figure 5.5 has been produced using the same assumptions and values as Figure 5.2, with the only difference being that the lateral translation between pulses has been reduced to 12au from 18au. A central region which has experienced less material removal than adjacent troughs is evident – the 'contrast', i.e. the ratio of the central peak height above the adjacent troughs to trough depth, depends on the threshold intensity, beam shape and lateral translation, and has not been investigated extensively. However, as is clear for Gaussian exposures, the contrast is expected to generally decrease with decreasing translation between exposures. Figure 5.6 was produced via the exposure of 3 successive lines at $240mJ/cm^2$ in BiSbTe using a 20x objective, where each line in the DMD mask was 7 pixels wide and was translated downwards by 7 pixels between each exposure. Though the profile of the remaining bridge lacks an accurate mathematical description to properly define width, it appears to be on the order of 250nm.

5.1.3 Overlapping exposures on thin film

As can be seen from the shaping of the end regions, the overlap of affected regions in Figure 5.5 was quite low – at even 1 pixel lower translation between exposures, contrast rapidly diminished. In order to enhance contrast while testing the limit of the technique, a thin film (50nm) of germanium-antimony-tellurium (GST) on silica was used
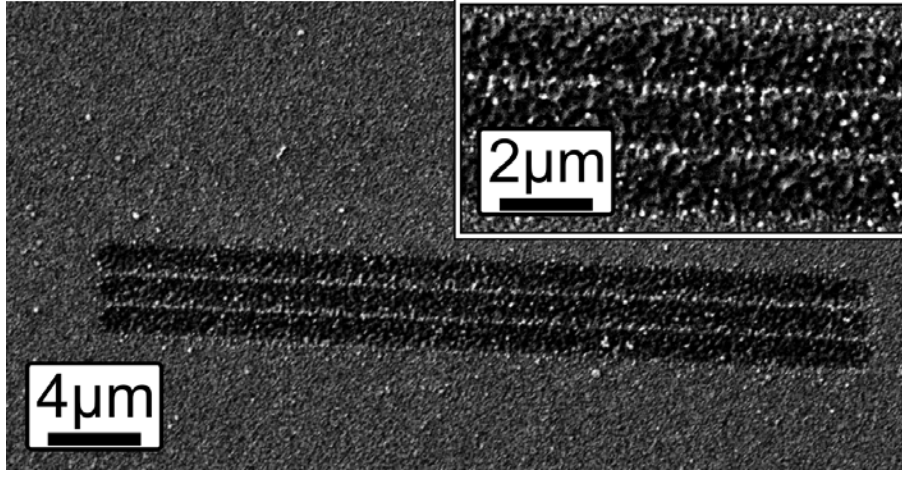
Figure 5.6: SEM image of thin bridges produced in BiSbTe via three exposures of a single line, translated between exposures. Here, the minimum feature size is ≈250nm, while the resolution remains close to what was seen in Chapter 3, at ≈2μm.

for the final tests. Figure 5.7 shows how this sample improves contrast; ablation may only occur to a maximum depth (-0.05au in the Figure), beyond which the transparent silica does not ablate at the used fluence. A central bridge of non-transparent GST then shows clearly atop a near-flat, transparent silica background. The flatness of the silica improves visibility under SEM, while the transparency enhances contrast under optical microscopy.
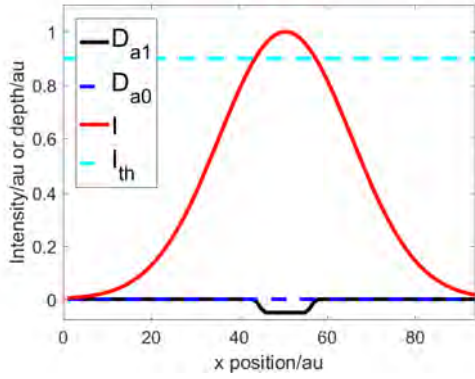
(a) Depth profile before and after 1 exposure
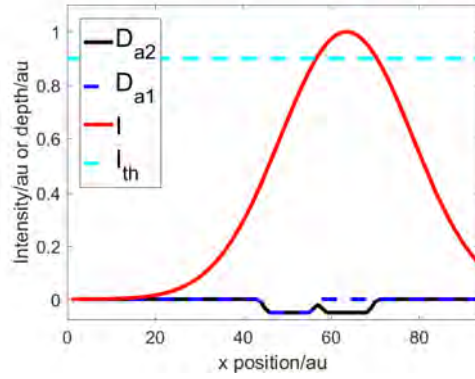
(b) Depth profile before and after 2 exposures

Figure 5.7: The depth profile of a material before and after 2 exposures of laterally shifted Gaussian intensity profiles, with affected regions overlapping on a thin film material.

Sequentially rotated Archimedean spirals were chosen as the DMD masks (the choice of which is expanded upon below). Described by $r_{arch} = a_{arch}\theta^{R_{arch}}$ where r_{arch} is the radius, θ the angle in polar coordinates, a_{arch} and R_{arch} are constants ($R_{arch} = 2$ in this case, and $a_{arch} = 0.39$), the spacing between adjacent lines in the spirals decreases towards the centre (when $R_{arch} > 1$, as in this case; for $R_{arch} < 1$, the spacing increases

towards the centre). Making the replacement $\theta \to \theta + \phi$ 'rotates' the spiral clockwise by ϕ. Remaining bridges of width $\approx$160nm were produced at a fluence of $0.125J/cm^2$ per exposure, as shown in Figure 5.8.
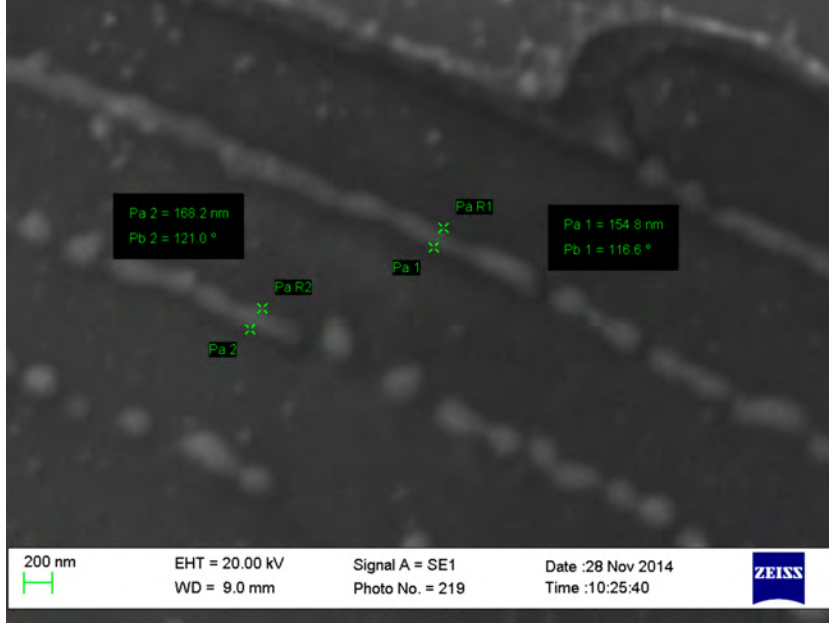
Figure 5.8: Archimedean spirals ablated into 50nm thick GST at a fluence of $0.125J/cm^2$ per shot resulting in $\approx$160nm unablated regions.

5.2 PSME for improved resolution

While sub-wavelength features have been demonstrated with multiple exposures, periodicities below the resolution limits of the optical systems used have not yet been produced (which were 1μm, 952nm and 727nm when using the 20x, 50x and 100x objectives respectively). Initially, it was expected that the method of reducing peak intensity towards threshold and leaving unaffected regions between sequential patterns (as in Figure 5.2) could produce sub-diffraction limit resolutions. In order to efficiently test the technique, sequentially rotated archimedean spirals were displayed on the DMD and ablated in 200nm BiSbTe. This procedure was designed to test that large, more complex shapes could be placed in sub-wavelength proximity, as well as testing a near-continuous range of exposure-to-exposure feature separations (enabled by the decreasing spacing between 'turns' of the spirals towards the centres, and mutual rotations between successive spiral exposures, as in the previous section). In this section, PSME is explored via both ablation and multi-photon polymerisation patterning of materials.

5.2.1 PSME using ablation

Initially, ablation was chosen as the patterning mechanism to explore the PSME technique. Figure 5.9 shows an example spiral as displayed on the DMD, a diagram of

sequential rotations of the same image, and SEM images of the resulting structure ablated into BiSbTe after eight exposures.

(a) A single archimedean spiral as displayed on the DMD

(b) An example set of four archimedean spirals sequentially rotated, each being displayed on the DMD during a single shot – different colours in the image for different shots

(c) Ablated pattern after 8 spirals have been displayed on the DMD and ablated on the sample. Each spiral displayed on the DMD is rotated further with respect to previous spirals, each produced with a fluence of $0.125J/cm^2$.

(d) Close up of small features in part (c)

Figure 5.9: Archimedean spirals ablated into 200nm thick BiSbTe in eight exposures.

Features as small as $\approx$400nm are evident in Figure 5.9(d), with spacing between adjacent bridges of material as low as $\approx$600nm, below the diffraction limit of 952nm when using the 50x objective for this experiment. Towards the centre of the spirals, where separations between lines were smaller, a 'bridge' of unablated material between ablated lines was not routinely obtained (as can be seen at the centre of Figure 5.9(c)). It can also be seen from Figure 5.9(c) that ablation depth is not equal across the whole pattern, which was due to a lack of homogeneity in the incoming intensity distribution

at the DMD in the DLP7000 setup; a beam realignment was made to ameliorate this during later tests.

Though features with spacings below the diffraction limit were produced (600nm spacing when the limit of the 50x objective was 952nm), the depth profile in Figure 5.9 was not of the expected form. Instability in the beam intensity and shape pulse-to-pulse meant that when the peak power was reduced to near threshold ($\approx 0.125 J/cm^2$), large regions of the projected intensity pattern would fluctuate below threshold, or further above threshold than intended, causing poor reproduction of the desired pattern. Single-exposure feature widths in Figure 5.9 remain on the order of 1μm, and yet 600nm feature separations have been achieved. The mechanism for the production of this resolution is similar to the 'low material removal' method described in Figure 5.5, and is shown in Figure 5.10.
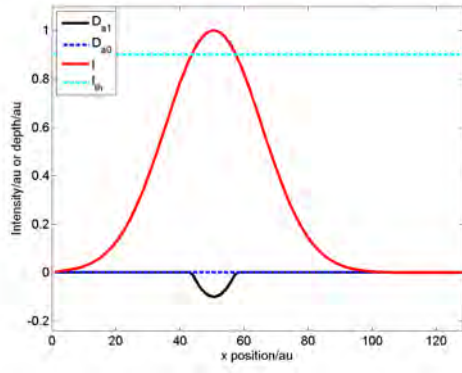
(a) Depth profile before and after 1 exposure
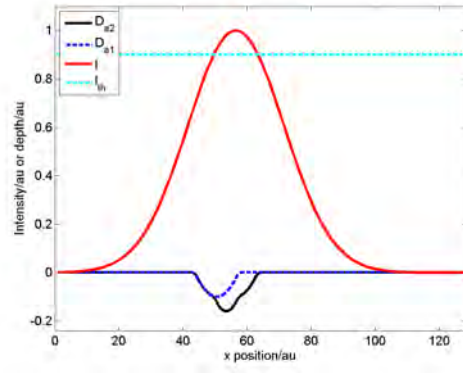
(b) Depth profile before and after 2 exposures
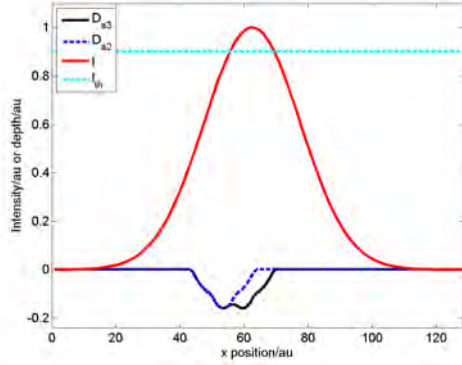
(c) Depth profile before and after 3 exposures
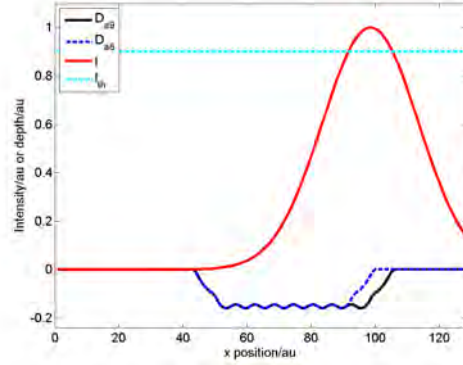
(d) Depth profile before and after 9 exposures

Figure 5.10: The depth profile of a material before and after 9 exposures of laterally shifted Gaussian intensity profiles. The emergence of corrugations, which has not occurred after 2 exposures in (b) but has after 3 exposures in (c) depends on the relative translation between pulses, and the shape of the intensity profile. Were the intensity profile to have been shifted by a greater value after the first exposure, corrugations would occur after only 2 exposures. The period of the corrugations, when they emerge, is equal to the relative translation between intensity profiles.

Figure 5.10 shows the expected depth profile for a Gaussian intensity with similar parameters to that used in the previous section, whose centre is shifted by 6au between each exposure. Note that after 2 exposures there is no 'less affected bridge', or corrugation, as was found for greater exposure-to-exposure shifts as in Figure 5.5 – the peaks of the Gaussians are too close for this to occur. However, after 3 exposures, and later after 9 exposures as in Figures 5.10(c) and 5.10(d), corrugations at the bottom of the ablated region have been produced. Note also that relatively broad slopes occur either side of the peridodic region of depth modulation; these correspond to the broad non-periodic regions which can be seen at the edges of the final machined pattern in Figure 5.9(c). In simulation, the width of this non-periodic border region is typically wider when the shift between exposures is small compared to the width of the above-threshold regions of the intensity distribution. A mathematical description of this border region has not yet been attempted, though it appears that periodic modulations occur after sufficient shifted exposures for *any* shift size, albeit with reducing contrast for smaller shifts as in the previous section. Of course, other effects would limit the technique beyond some level of pitch-splitting, as described in section 5.1.
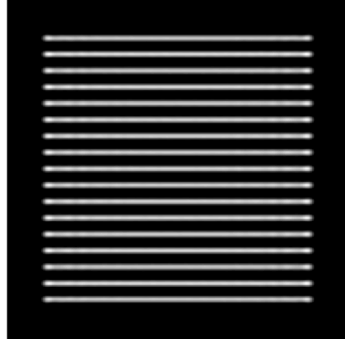
(a) Theoretical depth profile after 1 exposure
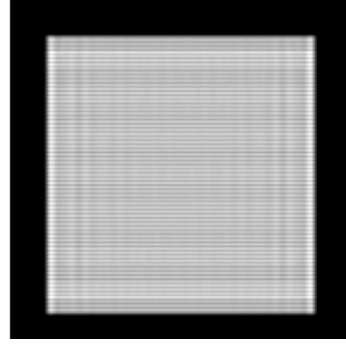
(b) Theoretical depth profile after 4 exposures
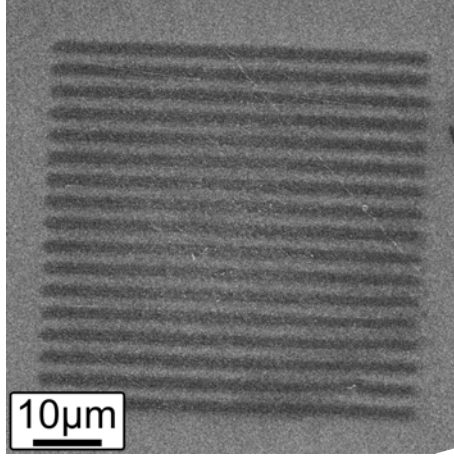
(c) SEM image of structure after 1 exposure

(d) SEM image of structure after 4 exposures
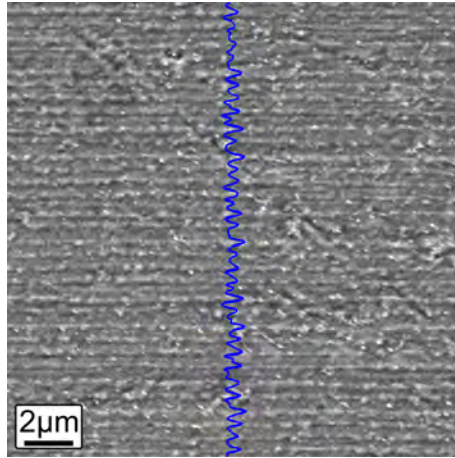
(e) SEM image of structure after 6 exposures

Figure 5.11: Theoretical and SEM images of depth profiles in electroless nickel using the 20x objective. $38mJ/cm^2$ was the fluence used for each pulse.

Figure 5.11 compares theoretical to experimental results in electroless nickel when applying PSME with a grating pattern. The result of a single exposure can be seen in Figure 5.11(c), and an aperture radius and threshold were chosen to approximate this

in the theoretical profile in Figure 5.11(a), which was generated similarly to Figure 5.4. The period of the grating was 24 pixels on the DMD mask, Figure 5.11(d) shows the result of 4 exposures, shifting the mask downwards by 6 pixels between exposures, while Figure 5.11(e) resulted from 6 exposures, shifting the mask by 4 pixels between exposures, both at $38mJ/cm^2$, close to the ablation threshold of the material [149]. Blue line profiles represent a horizontal averaging of the greyscale image values in order to highlight the periodicities. The period in the single exposure case was $\approx 3\mu$m, while periods of 750nm and 500nm were achieved with 4 and 6 exposures respectively – 'splitting' the single exposure pitch by 4 and 6, as expected. Beyond 6 evenly spaced exposures with the 20x objective for this grating pattern any periodic structuring of the expected form could not be resolved under SEM. This was, however, only the limit for this particular intensity mask, and finer resolutions may be achievable with alternative masks. The theoretical profile in Figure 5.11(b) shows a qualitative resemblance to the experimental result, as in the previous section.

Figure 5.12 shows the result of the same grating pattern exposed 8 times, shifted 3 pixels between exposures. Laser-induced periodic surface structuring (LIPSS) [150] has occurred – a known phenomenon with repeated exposures to femtosecond pulses – and has dominated the patterning process. The LIPSS are not of further interest here, other than to show a limit of the technique.
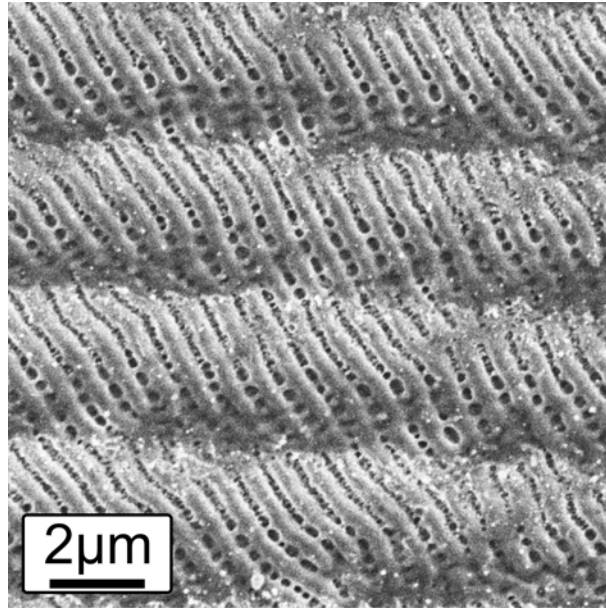
Figure 5.12: Laser-induced periodic surface structuring dominates the patterning process at 8 exposures with features in close proximity. The grating pattern translated between exposures on the DMD was comprised of horizontal lines w.r.t. the orientation of the figure.

Multiple exposures of a similar grating pattern on the DLP3000 line with a 100x objective were also tested, despite the potential dithering problem of DMD mirrors for fine features on this setup. At the time of the experiment, the beam width at the objective

entrance position on the setup for the DLP7000 line was too broad for the aperture of the 100x objective, and it was for this reason the DLP3000 line was used for experiments involving the 100x objective.

The grating pattern was not well-reproduced in a single exposure, as seen in Figure 5.13(c). The loss of spatial frequencies high enough to faithfully recreate a grating pattern may have been a result of the smaller aperture at the entrance to the 100x objective than the 20x, such that the spatial frequencies required were not captured – in either case, the depth profile is approximated once more by a computational aperturing of the Fourier transform in Figure 5.13(a). Each exposure used a fluence of $5.25J/cm^2$ (though this value assumed the projected intensity pattern perfectly recreated the DMD mask; hence the true value would be lower), and after 3 exposures produced the structure in Figure 5.13(d).

Though the intended overall structure was not produced, these results are included to compare the predicted depth profile with the experimental result when a high proportion of high spatial frequencies are lost. A small region at the top of the SEM image is arrowed, showing a region with a period of ≈350nm, however elsewhere no reduced period is observable compared to the single exposure case in Figure 5.13(c). Following the same procedure as before to produce a theoretical depth profile in Figure 5.13(b), a similar lack of fine structuring is apparent over most of the predicted profile. The fine structure region is also visible (albeit faintly), however theoretically it is predicted at both top and bottom of the final structure. As the projected intensity pattern was translated downwards between pulses, and the structure experimentally remains at the top, it is suspected that the expected fine structure was melted across the above-threshold region during each exposure, which consequently removed any fine structure produced at the bottom of the pattern.
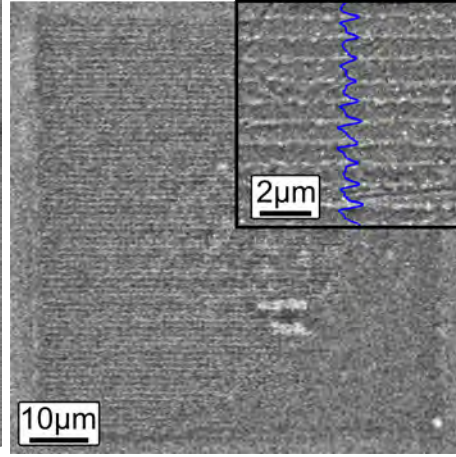
(a) Theoretical depth profile after 1 exposure

(b) Theoretical depth profile after 3 exposures

(c) Depth profile before and after 1 exposure

(d) Depth profile before and after 3 exposures
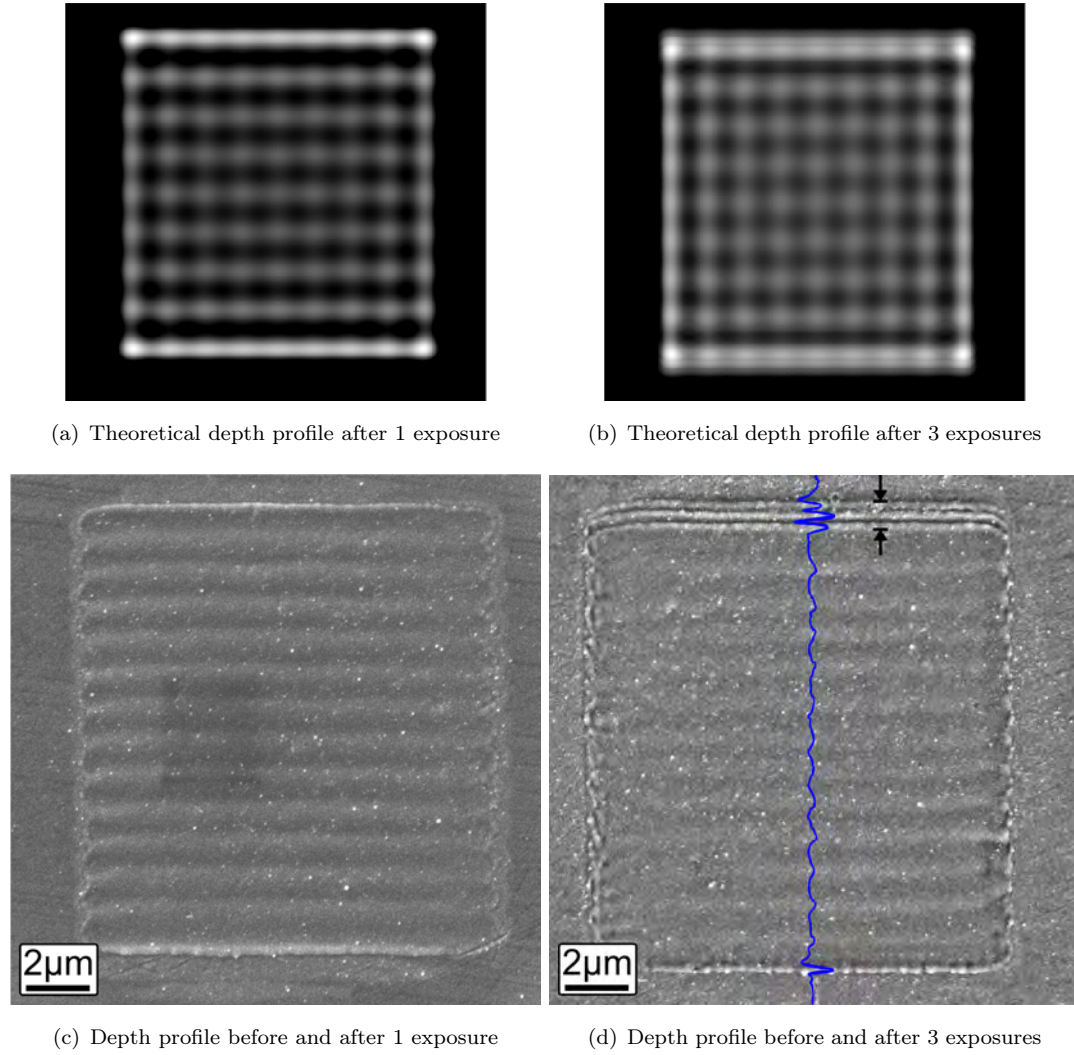
Figure 5.13: Theoretical and SEM images of depth profiles in electroless nickel using the 100x objective. $5.25 J/cm^2$ was the fluence used for each pulse.

Periodic structuring can be seen in the single-exposure case in Figure 5.13(c), however diffractive effects ultimately produced enough intensity in intended 'off' regions of the projected intensity pattern that the ablation threshold was exceeded across the whole structure, and limited the technique. The method may be implemented on the 100x objective, however, provided features within the single-exposure mask have a great enough separation that threshold is only exceeded in localised areas around the intended high intensity regions. Pairing this with effects explained in Figure 5.10, wherein periodic structures emerge for a particular spacing of sequential exposures only after an unknown number of exposures, with unknown contrast and unknown 'border region' width, Archimedean spirals again become an attractive option for rapid experimental testing of the technique. The space between 'coils' of the spiral in a single mask varies, and rotating the entire spiral through some angle between exposures will mean a greater separation between exposed features at the centre than the outer edge. This allows for the simultaneous variation of many of the key variables in this technique. While the range of angles the spirals were rotated through in Figure 5.9 was small, once the impact

103

of feature separation between exposures was better understood, sequential spirals were evenly rotated between 0° and 360°, for varying total numbers of rotated exposures. Figure 5.14 shows SEM images of results in electroless nickel from both the 100x and 20x objectives.

(a) An example eight sequentially rotated Archimedean spirals, with the inset showing the DMD mask used

(b) The resulting structure after 13 pulses at $4.70 J/cm^2$ with the 100x objective

(c) The structure after 25 pulses at $38 mJ/cm^2$ with the 20x objective, the inset shows a higher magnification

(d) The structure after 10 pulses at $38 mJ/cm^2$ with the 20x objective
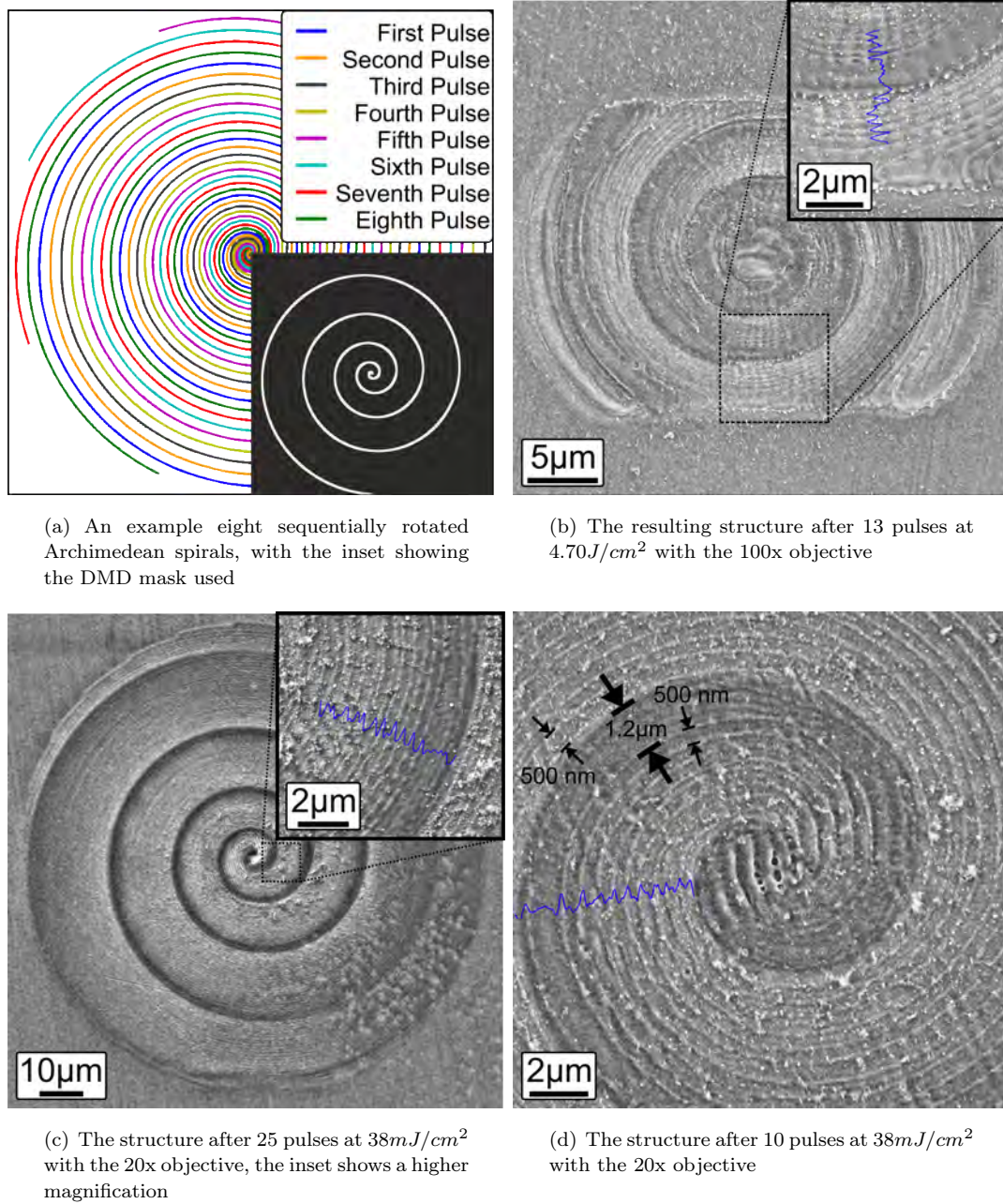
Figure 5.14: SEM images of structures produced in electroless nickel after repeated exposures to Archimedean spiral intensity patterns.

The results in Figure 5.14 are fundamentally similar to those in Figure 5.9; the major difference is the angular spacing between sequential rotated spirals. The realisation that fine resolution may emerge only after some number of pulses, and that the size of shift between exposures may affect this number, as explained in Figure 5.10, led to

this change of approach; the wider spacing allowed for a more efficient search of the parameter space. Figure 5.14(b) shows a resulting final structure machined using the 100x objective, with the inset displaying a higher SEM magnification image, produced in 13 pulses at $4.70J/cm^2$. The pattern appears cropped in the vertical, as the DLP3000 chip has an 854:480 aspect ratio display, and was not able to display the entire spiral as in the Figure 5.14(a) inset. The finest period of 270nm was achieved near the centre of the structure, with a period of 350nm seen nearer to the edge, both visible near the top and bottom of the inset of Figure 5.14(b), respectively.

Figure 5.14(c) shows a similar structure machined with the 20x objective, which was produced in 25 pulses at $38mJ/cm^2$. The finest resolution of ridges in the structure was 370nm, shown at the centre of the inset. Figure 5.14(d) shows the central region of a spiral produced with 10 pulses at $38mJ/cm^2$ with the 20x objective, demonstrating 500nm spacing of features almost to the very centre of the structure. Visible in Figures 5.14(b), 5.14(c) and highlighted with black arrows in 5.14(d) are broad spirals, surrounded by regions which appear to have large periodicity – e.g. a 1.2μm linewidth spiral of little depth modulation with 500nm linewidth spiral features to either side, as indicated in Figure 5.14(d). These broad curves correspond to the 'border region' associated with the technique; the broad slopes of depth modulation either side of the periodic region predicted in Figure 5.10. Also apparent is a build-up of debris, which may be prevented via nitrogen gas assist for debris removal at the time of machining, or removed post-process via standard wet chemical cleaning procedures. At the centre of the spiral, visible in Figure 5.14(d), LIPSS occurred as a result of the rotating pattern in the central region being exposed to all pulses.

In conclusion, a diffraction limit of 727nm and final feature resolution of 270nm with the 100x objective, and a limit of 1μm and final feature resolution of 370nm with the 20x objective, resolutions approximately 3 times smaller than the diffraction limit were produced by DMD multiple exposures in both cases.

5.2.2 PSME of photoresist

In order to demonstrate DMD image translation for the purpose of PSME where minimum feature sizes produced in a single pulse are below the diffraction limit (recalling that only minimum periodicity is limited, not minimum feature size), a resist optimised for two-photon polymerisation at 780nm wavelength (Nanoscribe IP-G 780) [151] was used. The probability of two-photon absorption is proportional to the square of the incident intensity; considering an incident Gaussian intensity distribution, the FWHM of two-photon absorption is $1/\sqrt{2}$ that of single-photon absorption. Provided single-photon absorption is suppressed, such that material response depends predominantly on two-photon absorption, the material response will correspondingly behave as a single-photon absorbing material would to a Gaussian of $1/\sqrt{2}$ the incident width. This 'sharper' material response means that finer features are more reliably reproduced; in the previous sections it was shown that intensity would have to be maintained close to threshold to achieve finer features, while two-photon absorption naturally produces a reduction factor of $1/\sqrt{2}$ without this concern.

Only the 50x and 100x objectives on the DLP3000 line were capable of producing the high intensities needed for two-photon polymerisation. The results in Figure 5.15 show a ≈10μm thick structure produced in 13 exposures of sequentially rotated Archimedean spirals at $3.0J/cm^2$ per pulse using the 50x objective, with a final lateral features at a minimum period of ≈500nm, which was equal to the width of single lines produced during each pulse. The high number of exposures at the central region resulted in damage to the structure; just outside the damaged region, polymerised regions appear to have overlapped to the point that periodic structuring is not evident. Incomplete polymerisation was observed at $2.4J/cm^2$, with polymerisation fluences in this range being typical for similar experimental conditions [152].
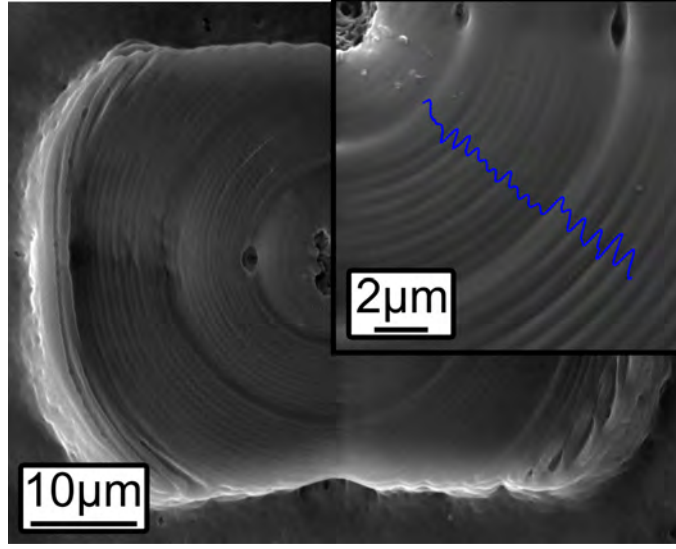
Figure 5.15: Structure produced via two-photon polymerisation in 13 exposures at $3.0J/cm^2$ per exposure. The finest spacing between adjacent turns of the spirals is ≈500nm.

The minimum period observed in Figure 5.15 was approximately a factor of 2 below the limit achievable in a single exposure. It is interesting to consider why this reduction factor was smaller than that achieved via ablation, and the proposed mechanism, explored in the discussion section below, comes down to the different material response to incident illumination.

5.3 Discussion and Future Work

PSME via DMD image projection has been shown to beat the diffraction limit with two-photon polymerisation by a factor of almost 2 (500nm period on a setup diffraction limited to 952nm), and with ablation by a factor of almost 3 (370nm on a setup limited to 1μm, and 270nm when limited to 727nm). Ooki et al. [144] argue that a sinusoidal intensity pattern shifted by a half-period in a two-photon resist will at most result in a halving of the period of the final material response. Their argument can be extended to explain why PSME via photopolymerisation was limited to a resolution reduction

factor of 2, and via ablation to a greater value, as follows.

A two-photon resist contains a photo-initiator chemical at initial density J_0, whose rate of decrease with respect to time is proportional to the square of the incident intensity, such that after 1 exposure at intensity I_1 the initiator density J_1 is given by Equation 5.4.

$$J_1(t) = J_0 \exp(-c_{2P} I_1^2 t) \tag{5.4}$$

c_{2P} is a constant of integration, and t is time. To ease notation, explicit dependence on spatial dimensions has been omitted, and the intensity distribution is assumed to have a constant profile in time, though the current argument trivially extends to arbitrary intensity time profiles, provided the spatial profile does not change during each exposure. If the total exposure time for exposure N is T_N, then the initiator density after N exposures will be of the form in Equation 5.5.

$$J_N(T_N) = J_{N-1} \exp(-c_{2P} I_N^2 T_N) = J_0 \exp(-c_{2P} \sum_{n=1}^{N} I_n^2 T_n) \tag{5.5}$$

The final photo-initiator density will then be in response to an *effective* squared intensity-time product given by the summation in Equation 5.5. By considering the Fourier transform of this effective squared intensity-time product, we can infer the upper limit to the spatial frequencies present in the final material response. A given intensity distribution will have a maximum spatial frequency k_{max} as a result of the diffraction limit, the square of this intensity may then contain a maximum spatial intensity of twice this limit, $2k_{max}$. The time component in the product has no spatial dependence, and hence will not affect the spatial frequency limit in any squared intensity-time product. The maximum frequency present in the Fourier transform of the sum of two functions may not be greater than the maximum frequency present in the Fourier transform of either function, hence regardless of the value of N in Equation 5.5, the maximum spatial frequency limit remains $2k_{max}$.

The doubling of the spatial frequency limit in the above argument is deduced from properties of the Fourier transform of a function f, $\mathcal{F}(f)$, and of the convolution of two functions f and g, $(f * g)$. The Fourier transform of any real function (such as intensity) will be even, and the diffraction limit imposes that the the bounds of the transform of intensity will be at some $\pm k_{max}$. Convolution theorem then states that the Fourier transform of a product of two functions (such as intensity multiplied by itself) will be equal to the convolution of the Fourier transforms of the two functions $\mathcal{F}(f \cdot g) = \mathcal{F}(f) * \mathcal{F}(g)$. The maximum non-zero frequency at which the convolution of band-limited Fourier transforms occurs is then clearly the sum of the maximum frequencies present in each transform (or double the maximum, for the convolution of identical transforms). The invariance of the maximum frequency from additional terms in the effective squared intensity-time product is a consequence of the distributive property of the Fourier transform, $\mathcal{F}(f + g) = \mathcal{F}(f) + \mathcal{F}(g)$.

This argument corresponds with the experimental result seen in Section 5.2.2, where the minimum period observed was half that allowed by the single-exposure diffraction limit. The argument should extend such that for an m-photon resist, a factor of m reduction in final period compared to the single-exposure limit is possible.

Now consider the form of the material response for ablative PSME as proposed in Equation 5.2. The material response, the ablation depth, is in response to a sum of *thresholded* intensity distributions. This thresholding, to first order, is a discontinuous function switching between 0 to 1 wherever incident intensity during a given exposure exceeds threshold. The frequencies present in the material response after a single exposure can be calculated from the Fourier transform of the product of the incident intensity and the threshold function. Similarly to the above argument, this means that the maximum possible spatial frequency will be equal to the sum of the maximum spatial frequency in the intensity distribution, and the maximum spatial frequency in the threshold function. However, a discontinous function such as this will require infinitely high spatial frequencies, such that there is no physical limit to first order for the final spatial frequencies present in the material response. Of course, other effects described in this chapter will ultimately mean that the thresholding function is not truly discontinuous, and hence that a finite frequency limit will exist.

A Fourier transform-based approach to the limits of material responses then explains why a resolution reduction factor of 2 was the limit with two-photon polymerisation techniques, while a higher limit was found via ablation. The model fails to provide any predictive calculation for the limit of PSME resolution via ablation, which will rely on the thresholding inherent to the technique. Determination of the dependencies of the thresholding function would be critical to extending the technique – for example, thermal conductance and melting temperature would likely effect the gradient of the depth profile at a boundary between a region exposed to intensity above threshold, and one exposed to intensity below threshold, where in the first order model the gradient would be assumed infinite.

An adaptive optics approach using the DMD could allow any inhomogeneities in the beam before shaping to be corrected for, hence allowing complex patterns with peak intensity closer to threshold to be reliably projected. This would allow consistent thin film production, as well as higher contrast in the PSME via ablation.

It may be possible to improve the resolution found in two-photon polymerisation PSME. The theory presented assumes photo-initiator density only undergoes change during exposures, however this may not be true. As the multi-photon resist is in a liquid state before exposure, diffusion will take place. Instantaneously after a femtosecond pulse, initiator density may have reduced in some region as expected. If the intensity in some region is not sufficient to fully cure the resist however, the partially cured region can be thought of as a suspension of solid particles in liquid – diffusion between these regions and unexposed regions will, over time, return the initiator density to near the initial

value. This might be represented mathematically as a thresholding function, where curing is complete enough above some intensity such that diffusion is negligible, and lead to a further reduction in final resolution.

Only two forms of material response have been studied in this chapter, ablation and two-photon polymerisation. It would be of interest to determine the limits of PSME in more diverse laser-matter interactions; the periodicity of any material response to a single exposure will be bound by the Abbé diffraction limit, however the exact nature of a material's response to an intensity pattern may radically change the limit after multiple exposures. Work presented in Chapter 6 enables a greater degree of control over the spatial intensity distribution, as well as relative shifts between intensity profiles. Theoretical work on the generation of binary holograms, which require adaptation for ultrashort pulses, will even allow for translations of intensity profiles below a single pixel width on the DMD. An exploration of PSME via other material interactions will be returned to once these enhanced capabilities have been developed, as they will clearly be of great benefit to the technique.

Chapter 6

Mask correction

6.1 Introduction

Thus far DMDs have been used as a low-cost, rapid method to produce bespoke intensity masks. The pattern displayed on the DMD is imaged at target positions on a sample, with any aberrations associated with the experimental setup or physical limits being accepted. While the dynamic nature of the DMD surface allows for a great deal of variation in the imaged pattern, in principle it is little different than imaging static intensity masks, with binary intensity values and no phase control.

This chapter will introduce the possibility of 'mask correction' using a DMD. Image-recognition will be shown to allow for enhanced positional accuracy of exposure positions at samples, reduced to the live camera resolution of 1.04μm when machining is performed with the 20x objective. Simulated beam propagation techniques will be shown to predict diffractive behaviour from a DMD mask. The point-spread function (PSF) of a single pixel will be exploited for continuous intensity control and correction for diffractive loss of image reproduction fidelity. This correction of diffractive losses is demonstrated for a complex image mask, featuring a range of line widths, on the DLP3000 diagnostic line. Continuous intensity control has been used to ablate a variety of multi-level structures into nickel, with resolutions approaching the 2μm accuracy seen for single exposures in Chapter 3. Two methods for the iterative generation of 'binary holograms' with multiple useful features will also be presented, including multiple image planes during a single exposure, continuous intensity control, phase control and sub-pixel image translation.

6.1.1 Optical proximity correction

As was seen in chapters 3 and 5, differences between an intended pattern and that produced in a sample may occur as a result of diffractive losses and material response. These errors may be reduced by using shorter wavelengths, or systems with higher NAs, but an alternative approach is to compensate for the expected errors by modifying the mask

itself, via a broad range of techniques known as optical proximity correction (OPC).

OPC often amounts to small modifications in the perimeter of any contiguous shape in an exposure mask, to correct for defects such as 'rounded corners' or differing intensities due to different linewidths. An example is shown in Figure 6.1; the corners of a square are rounded in the final structure if ordinary imaging is used, while the structure can more closely conform to a square shape if additional regions at the corners in the mask are exposed.

(a) Original mask and final structure

(b) Corrected mask and final structure
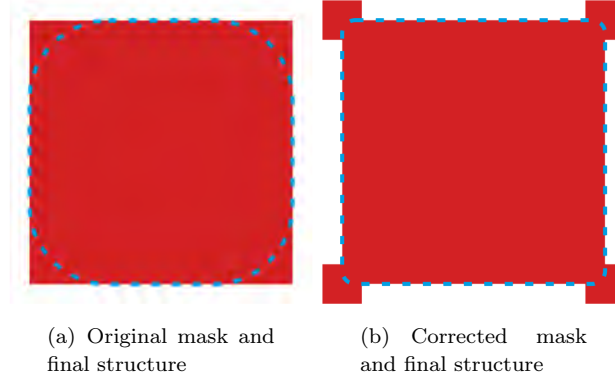
Figure 6.1: A comparison of (a) original and (b) OPC masks used to produce a square structure. The masks are in red, while the dashed green outline shows the perimeter of the final structures produced.

The methods for determining how to modify a mask to best produce a final structure vary, with analytic approaches [153] and rules-based look-up tables [154] both being used, depending on the process, material, laser system and desired mask shapes being used. While look-up tables work well for simple designs, such as rectangles or regular polygons, they quickly become untenable as more arbitrary, complex designs are required. A simple, iterative method for OPC mask generation accounting for the effects of optical filtering when focusing an intensity distribution through an aperture will be described in this chapter, and the results as viewed on the DLP3000 line diagnostic camera will be shown.

6.1.2   Angular Spectrum Method

The Angular Spectrum Method (ASM) is a rapid Fast Fourier Transform (FFT)-based technique for simulating the propagation of light fields between two parallel planes; derivations are common in the literature, e.g. [155, 156]. Briefly, if one considers a field propagating in the z direction with some distribution in the orthogonal x and y directions, then the field at some $z \neq 0$ can be calculated from the $z = 0$ plane by transforming from spatial (x, y) space to frequency space (ξ, η), multiplying by a propagator for each of the real frequencies present, and transforming back to real space, as in equation 6.1.

111

$$E(x, y, z) = \int \int \tilde{E}(\xi, \eta; 0) \exp\left[i2\pi(wz + \xi x + \eta y)\right] d\xi d\eta \qquad (6.1)$$

Where $w(\xi, \eta)$ is the Fourier frequency in the z direction, given by equation 6.2.

$$w(\xi, \eta) = \begin{cases} \left(\lambda^{-2} - \xi^2 - \eta^2\right)^{1/2} & \text{Where } \xi^2 + \eta^2 \leq \lambda^{-2} \\ 0 & \text{Otherwise} \end{cases} \qquad (6.2)$$

This provides fast, accurate solutions for beam propagation simulation, provided aliasing issues with the FFT are avoided (frequencies at the $z \neq 0$ plane should be below half the Nyquist frequency to avoid 'folding' of the simulated field at the edges of a given sampling window) and evanescent field effects are negligible at the propagation distance. Evanescent decay distances are on the order of the wavelength of light used; in this work the propagation distance was always large compared to this. To reduce aliasing concerns, the method of Matsushima and Shimobaba was employed [155] – in short, the bandwidth of frequencies ξ and η is limited in accordance with consideration of the Nyquist sampling theorem.

6.1.3 Gerchberg-Saxton algorithm

Often, when imaging an object in an optical system, diffracted light from the object is collected by a lens and imaged onto a detector. However, there are circumstances in which this is not practical. When imaging with wavelengths for which it is difficult to produce lenses, such as XUV radiation, or when aberrations caused by a lens are undesirable, all-optical imaging systems may not suffice. An alternative method is to use phase retrieval algorithms [157–159].

Rather than imaging an object onto a detector using a lens, the (usually far-field) intensity diffraction pattern from the object is recorded directly on the detector at the 'image plane'. The task of 'focusing' this diffraction pattern with a lens is then transferred to an algorithm, which numerically searches for an object at the 'object plane' that would produce such a diffraction pattern. Given both electric field strength and phase of the diffraction pattern, this would of course then be trivial – if the diffraction pattern was recorded in the far-field, a simple FFT would lead immediately to the solution, or if recorded in the near-field a propagation algorithm, such as the ASM, could be used. All phase information is lost, however, when recording the intensity of the diffraction pattern on the detector. It is the task of the phase retrieval algorithm then to find an object with appropriate intensity and phase which produces the recorded image intensity distribution. The method of choice in this work is the Gerchberg-Saxton algorithm [160].

The iterative steps of the Gerchberg-Saxton algorithm [160] are shown in Figure 6.2. Of the various extensions to the algorithm, the Hybrid Input-Output (HIO) and shrinkwrap steps were considered in this work, and are also shown in Figure 6.2. The mathematical

arguments for the improved efficacy of these extensions is beyond the scope of this thesis, however summaries can be found in [158].
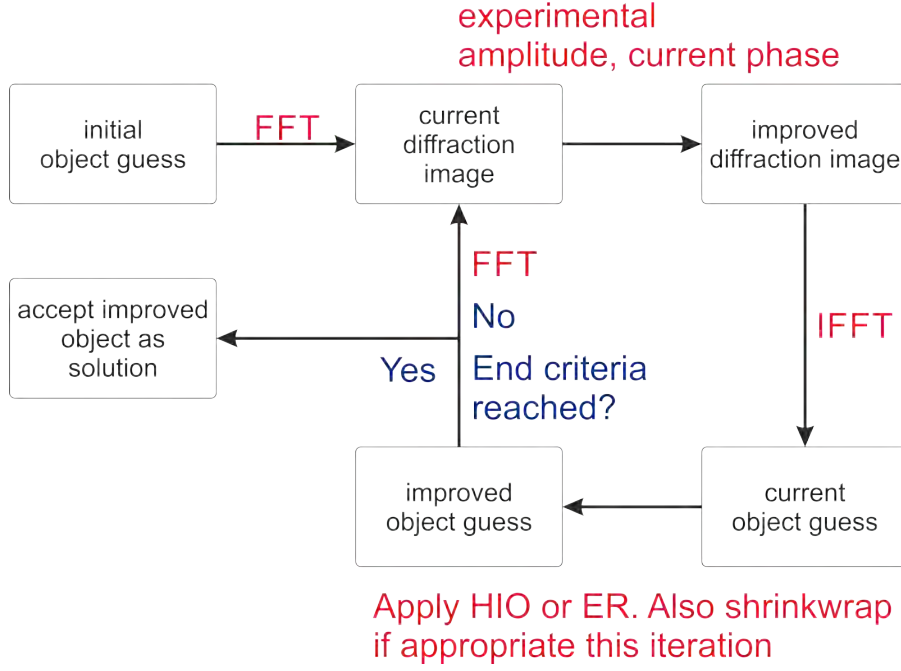
Figure 6.2: The steps of the Gerchberg-Saxton algorithm, with HIO and shrinkwrap.

The algorithm begins by making a guess of the 2D electric field at the plane of the object, the 'object guess', which is orthogonal to the direction of propagation of light, defined on a grid of $m \times n$ points, which may comprise randomly chosen amplitude and phase, or have a more specific first guess – for instance the inverse Fast Fourier Transform (IFFT) of the intensity at the image plane. The true diffraction pattern is also recorded on an $m \times n$ grid of points. A mask is also chosen, which describes which points within the $m \times n$ grid must contain the entire object. The ratio of the $m \times n$ points in the object guess to the number of points in the mask must exceed 2 for a solution to be found [161].

The object guess is then propagated to the image plane, which contains the recorded intensity pattern, to get a 'diffraction image' of $m \times n$ points; this is typically performed via an FFT, though one may use other propagation algorithms as mentioned previously. On this first iteration of the algorithm, the amplitude and phase distribution will likely bear little resemblance to the recorded intensity pattern. Each point in the recorded pattern's amplitude (square root of recorded intensity) is then multiplied by the phase of the corresponding point in the diffraction image, and propagated back to object space (via IFFT) to give a 'current object guess' for this iteration. Typically, there will be non-zero elements in the $m \times n$ grid of the current object guess outside those defined by the mask to give an 'improved object guess'. In the ER method, these points are simply set to zero, while in the HIO method these points are defined by equation 6.3.

$$\rho'_j = \rho'_{j-1} - \beta \rho_j \qquad (6.3)$$

Where ρ'_j is the improved object guess of this iteration, ρ'_{j-1} the improved object guess of last iteration, ρ_j the current object guess of this iteration, and $0 < \beta < 1$. In this work, it was found that using the HIO for every iteration until a stable solution was found, then using the ER method once before returning to the HIO method improved solutions.

Every set number of iterations, the available region for a solution to exist within the mask is then reduced, retaining those corresponding to points in the improved object guess that are above a threshold intensity; known as 'shrink-wrapping'. This step increases the speed at which the solution converges, by restricting the solution to regions more likely to contain the object. These extensions to the Gerchberg-Saxton algorithm were not found to be beneficial to binary hologram generation as described in section 6.5, however, which was the predominant use of the algorithm in this work.

Finally, end criteria of the algorithm are applied. These criteria are typically either a set number of iterations being completed, or the propagated field of the improved object guess being below some threshold difference from the recorded diffraction pattern. If the end criteria are satisfied, the improved object guess is accepted as a solution, otherwise a new iteration begins, taking the improved object guess as the starting object guess.

6.2 Mask shifting

The flat-top intensity incident on the DMD surfaces in both experimental lines imparts translational symmetry to any displayed mask within the homogenised intensity region; relative intensities within the overall output shaped beam will be the same, but the position will have shifted laterally in the (x,y) plane. Figure 6.3 shows the idea when the displayed DMD mask is a small square, with circular top-hat intensity illumination. Relative to a 'central' position in Figure 6.3(a), shifting the square image on the DMD up and to the right results in a corresponding shift of the output, while the relative intensity distributions within each square are the same.

(a) Centrally displayed square   (b) Square displayed with shift
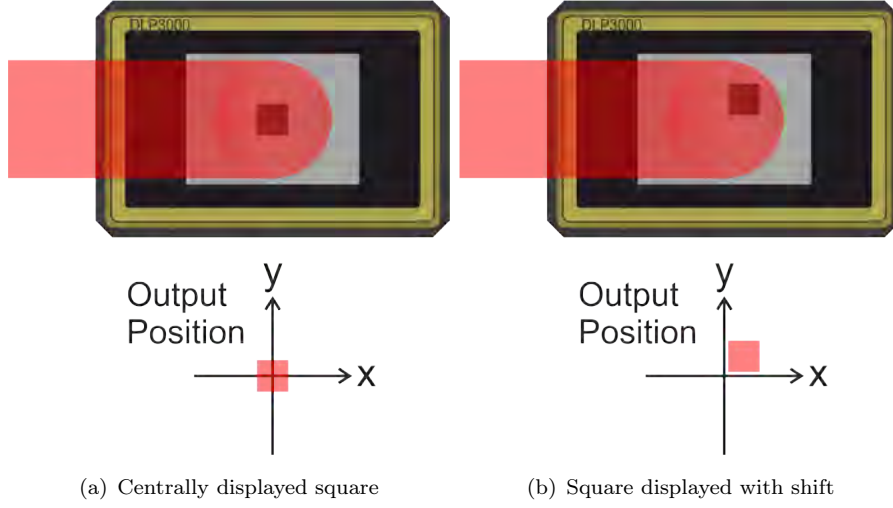
Figure 6.3: A circular top-hat intensity incident on the DMD surface allows for repositioning of a mask on the DMD such that the only difference in outputs is a lateral shift.

The idea is identical to that used in Chapter 5, in that the same intensity distribution can be shifted or rotated on the sample purely through updating of the DMD mask, but the scale of the shifts used here will allow for new functionality. While shifts of a few pixels were used to overlay grating images previously, here shifts of up to a few hundred pixels will be used to correct for translation stage positional errors.

The CMOS cameras in both experimental lines had a field of view of several hundred microns, while typical separations between adjacent target positions on samples was rarely $>100\mu$m. During experiments where sample translation was paused during exposures there was then the potential to record an image of the sample prior to each exposure, and use image-recognition techniques to detect whether the expected stage translation had occurred.

Phase correlation is an FFT-based method of rapidly extracting the relative shift between an image and a translated copy of the image. The Fourier shift theorem states that multiplying a vector of N values, x_n where $1 \leq n \leq N$, by a linear phase $\exp((2\pi inm)/N)$ where m is an integer value, results in a circular shift of the output frequency components X_k. The kth value in the frequency vector is replaced by the $(\mathrm{mod}(k\text{-}m,N))$th value, i.e. $X_k \rightarrow X_{k-m}$, where here the *modulo N* has been omitted for brevity. Multiplying the vector of frequency components by a similar phase term results in a shift of the x_n components; the results are summarised in equations 6.4, 6.5 and 6.6.

$$\mathcal{F}(x_n)_k = X_k \tag{6.4}$$

$$\mathcal{F}(x_n \cdot e^{\frac{2\pi i}{N}nm})_k = X_{k-m} \tag{6.5}$$

$$\mathcal{F}(x_{n-m})_k = X_k \cdot e^{-\frac{2\pi i}{N}km} \tag{6.6}$$

These results can be understood via convolution theorem. The Fourier transform of a product of two vectors is equal to the convolution of the two vectors' transforms; the linear phase factors in equations 6.5 and 6.6 are then dirac delta functions after transformation, which have the effect of shifting any vector with which they are convoluted.

Now consider two discrete images defined on $M \times N$ grids in (x, y) space, g_a and g_b, where g_a has been circularly shifted by $(\Delta x, \Delta y)$ to give g_b. The corresponding Fourier transforms in (u, v) space are then defined by equation 6.7.

$$G_b(u, v) = G_a(u, v)e^{-2\pi i(\frac{u\Delta x}{M} + \frac{v\Delta y}{N})} \tag{6.7}$$

The phase difference can be extracted simply by equation 6.8. The left hand side can be rapidly calculated from FFTs of the original images, and then inverse transformed to give a dirac delta function positioned in (x, y) space corresponding to the relative image shift.

$$\frac{G_a G_b^*}{|G_a G_b^*|} = e^{2\pi i(\frac{u\Delta x}{M} + \frac{v\Delta y}{N})} \tag{6.8}$$

While this result is exact for circularly shifted images, in practice the edges of each image after a sample translation will be extraneous data, rather than 'cycled' pixels from the edges of the previous image. Additionally, noise in the camera signal and a static illumination source will mean that any regions of the sample visible in both camera images will not necessarily yield identical readings at their two separate positions. Further, there is no guarantee that a translation of the sample will lead to an integer number of pixels shifted on the camera. These factors were expected to act as perturbations, such that the inverse transform of the left hand side of equation 6.8 would yield a sharp, yet non-zero width, peak. The position of the maximum value of this peak would then correspond to the integer-rounded number of camera pixels in x- and y-directions shifted between images. The robustness of the method to size of shift, as well as other factors, has not yet been tested, though the camera field of view was large compared to the viable intensity distribution shifting with the DMD, and so the method has been accepted as satisfactory thus far without further error detection.

Figure 6.4 shows a comparison of the technique for the same intended distribution of ablated features in BiTe. The final pattern consisted of an array of 'X' shapes, in a 5x5 grid, such that the end points of each 'X' should touch the ends of adjacent 'X' features. The centre-to-centre separation of each 'X' was intended to be 30μm. Figure 6.4(a) shows the resulting structure with no image shifting on the DMD, when the stage simply translates linearly along each row of features, incrementing by 30μm between exposures. In this case, it is clear that the largest point of error is at the start of each row, when the stages have had to return to the initial x-position, and suffered from backlash error. The majority of remaining 'X' shapes in this case align as expected quite

well. In general, when laser machining, one cannot rely on translation stages translating repeatedly in the same direction for the majority of a process; a spiral, or sinusoidal positioning of features, for example, would require many reversals of direction. Figure 6.4(b) was then generated by approaching each position in the array from a position randomly offset by a small amount in the (x,y)-plane, i.e. after each exposure the translation stages would move to a random nearby point, and then to the intended next exposure location. Clearly, the positional accuracy is much poorer across all machined points in this case. Figure 6.4(c) then employed the same translation stage path as that used in 6.4(b), but with mask shifting enabled. Images were recorded at each position, and used to generate DMD masks with the same 'X' shape shifted by an appropriate number of pixels in (x,y) directions to ensure that each exposure ablated material in the intended region. Note that while the features appear more deeply ablated in Figure 6.4(a), and indeed were produced at a higher fluence, the relative intensities used here are irrelevant provided feature placement can be observed.
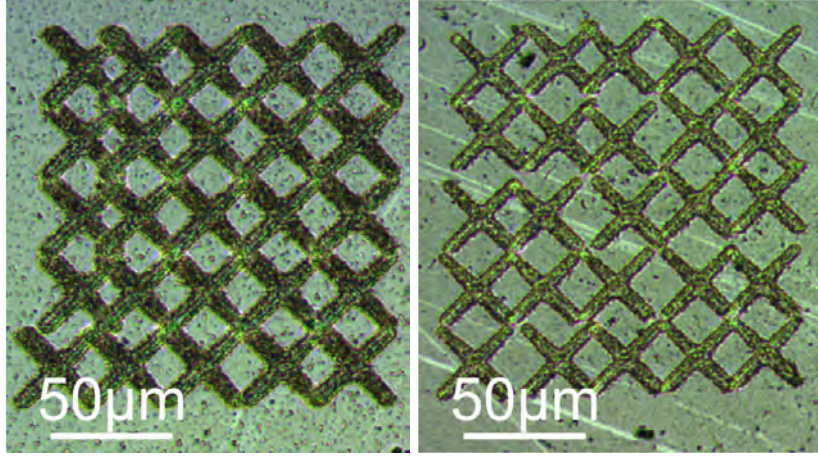
(a) Array of 5x5 'X' shapes ablated in BiTe with a simple translation path used.

(b) Array of 5x5 'X' shapes ablated in BiTe with each point approached from a random direction
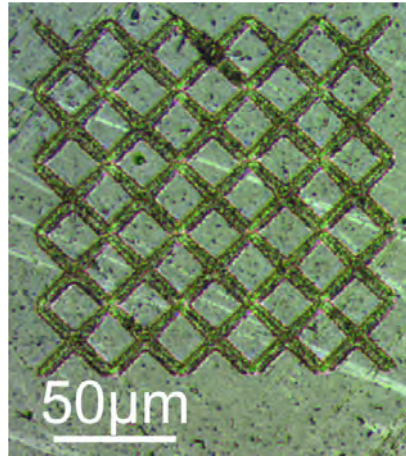
(c) Array of 5x5 'X' shapes ablated in BiTe with each point approached from a random direction and image shifting enabled

Figure 6.4: A comparison of positional accuracy achieved with and without DMD image shifting. These features were made using the 20x objective; on the live camera view of the sample a resolution of 1.04μm was available, and represents the limit of repositional accuracy with this objective.

DMD image shifting was able to correct for the $\approx$10μm backlash error of the translation stages, in addition to other, smaller positional accuracy errors inherent to the stages. The final accuracy was then limited by the resolution of the camera used to view the experiment, rather than the stages used. In this case, the 50x objective was used on the DLP3000 line, where a single DMD pixel corresponded geometrically to $\approx$100nm. The pi-shaper output on the DMD illuminated a circle of approximately diameter 500 pixels, while the 'X' pattern was $\approx$300 pixels wide and tall. This meant that the DMD image shifting solution was capable of correcting for positional errors up to $\approx$10μm from the ideal point of each feature. The calculation and new image-creation steps took around 1 second prior to each exposure; with no image-shifting, moving between points and pausing to send a pulse also took $\approx$1s. The time taken to complete the array was then

effectively doubled, though this was with non-optimised code, and is expected to be reduced in future versions.

Extensions to the phase correlation technique already exist to detect sub-pixel shifts between images, as well as rotations and changes of size. Future work will focus on implementing these extended features to DMD enabled image-shifting, as well as quantifying and correcting for errors introduced by the perturbations mentioned previously. DMD mask shifting allows improved accuracy when using low-cost translation stages, and faster realignment than mechanical translation of a sample.

6.3   Continuous intensity control

As a result of the binary nature of DMD pixels, image projection-based machining involving DMDs dynamic intensity masks thus far has aimed to project intensity patterns of either a single intensity value, uniform across all 'on' pixels in the mask, or zero intensity at regions corresponding to 'off' pixels. In commercial projectors, DMDs overcome this issue by rapidly switching between on and off states, to produce an averaged greyscale value over a time period which is short compared to minimum timescales perceived by the human eye. With a mirror cross-over time (time taken to switch between 'on' and 'off' states) in the microsecond range, this approach is of course not appropriate for greyscale, or 'continuous', intensity control when illuminating a DMD with femtosecond pulses.

The diffractive and optical filtering effects seen in Chapters 3 and 5, sources of unwanted image degradation previously, have in this section been exploited to achieve a close approximation to continuous intensity control. The method relies on the point-spread function (PSF) of a single DMD pixel in an intensity pattern at the sample position being large compared to the geometrically scaled down size of a single pixel, and is similar to work by others Auyeung et al. [131].

In the previous work by Auyeung et al., DMD pixels were alternately switched on or off in a checkerboard pattern of squares gradually reducing in size, such as that shown in Figure 6.5(a). The researchers found that their material response became uniform across the exposed region at some point between squares whose width was between 10 and 2 pixels, though these values would depend on the specifics of their setup. In the current method, a greyscale field pattern of $N \times M$ points with values ranging between 0 and 1 was compared with a random matrix of values uniformly distributed between 0 and 1 of the same size. Any point where the greyscale pattern was greater than or equal to the corresponding point in the random matrix was set to on in the DMD mask, while any point lower than that in the random matrix was set to off. The result of a 5×5 checkerboard of value 1 and value 0.5 squares, each square being 56 pixels across, is shown in Figure 6.5(b).
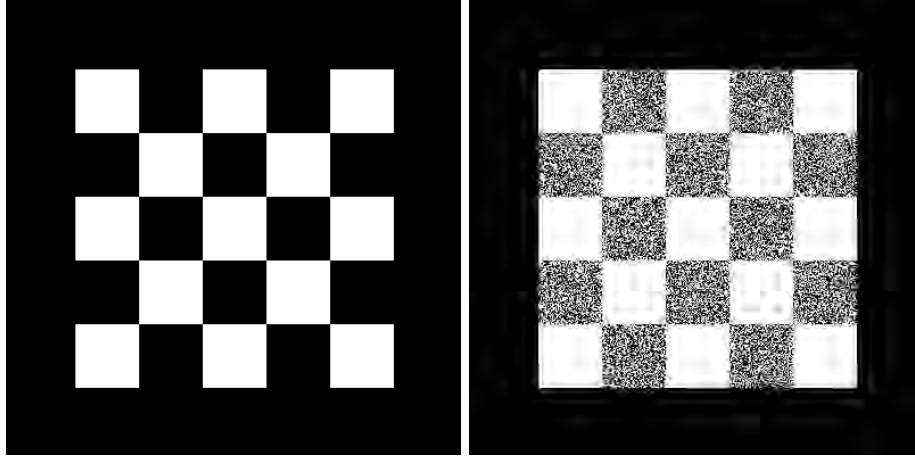
(a) Array of 5x5 squares of alternating intensity 1 and 0.

(b) Array of 5x5 squares of alternating intensity 1 and 0.5.

Figure 6.5: Checkerboard patterns of on/off pixels as displayed on the DMD. (a) shows the pattern used for binary intensity, while (b) shows that used for a three-level (0, 0.5 and 1) intensity pattern.

A simple approximation to the loss of higher spatial frequencies incurred in the setup can be made by applying a low-pass filter on the 2D Fourier transform of the DMD image, and taking the inverse transform. This was achieved by multiplying an $N \times N$ (where the image will be cropped to $N \times M$ post-filtering) Fourier transform by an aperture function element-wise; the aperture function was effectively an array of $N \times N$ points where those within a set radius number of pixels of the centre were set to 1, and those outside the radius set to 0. Results of low-pass filtering for the binary mask in Figure 6.5(a) and generated continuous mask in Figure 6.5(b) for apertures of radii 100, 60 and 20 pixels are shown in Figure 6.6, where the absolute value of the final image in the (x,y) plane orthogonal to the beam direction has been taken.

(a) Binary image, aperture radius 100 pixels.

(b) Three-level intensity image, aperture radius 100 pixels.

(c) Binary image, aperture radius 60 pixels.

(d) Three-level intensity image, aperture radius 60 pixels.

(e) Binary image, aperture radius 20 pixels.

(f) Three-level intensity image, aperture radius 20 pixels.
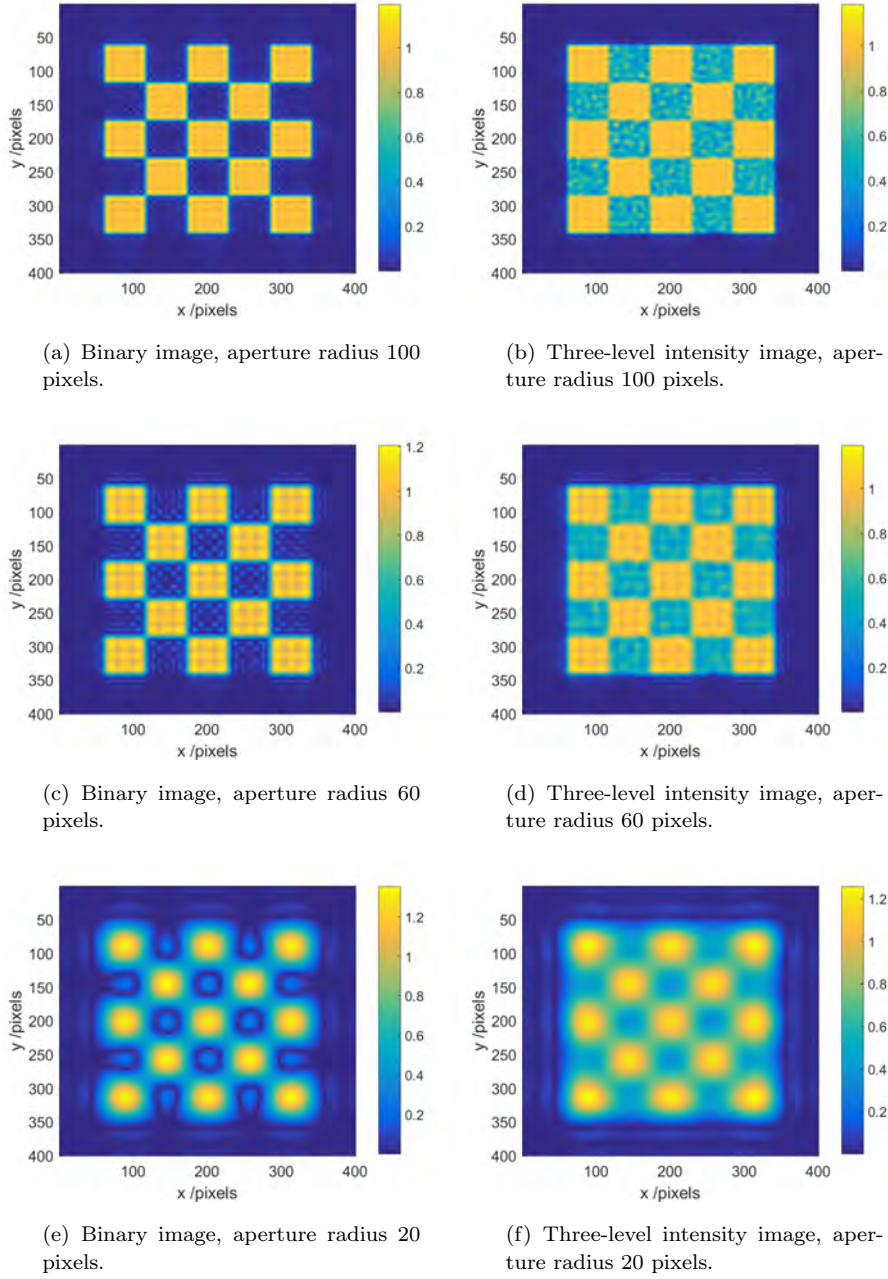
Figure 6.6: A comparison of the DMD masks in Figure 6.5 after optical filtering through apertures of varying pixel diameters.

After filtering through the 100-pixel aperture, the image of the binary mask in Figure 6.6(a) shows little intensity outside of the intended 'on' regions. The 100-pixel filtered grayscale image in Figure 6.6(b) shows approximately the 3 intended levels of field (0, 0.5 and 1) at the correct positions, though with some noise. This level of noise in the grayscale images reduces as the aperture radius is decreased in Figure 6.6(d) and 6.6(f), however the field distribution becomes less step-like, with more gradual transitions between levels of intensity. For the binary images, reduced aperture sizes in Figures 6.6(c) and 6.6(e) lead to similar effects, with higher field amplitudes in the intended 'off' regions. Figure 6.7 shows a 1D plot of the absolute value of the field at each radius

aperture for both binary and greyscale DMD masks, taken from the central row of each each 2D pattern in Figure 6.6, to more accurately show the final amplitudes of the fields in each case and highlight the trade-off between noise and accuracy of intended field recreation when changing the aperture size.
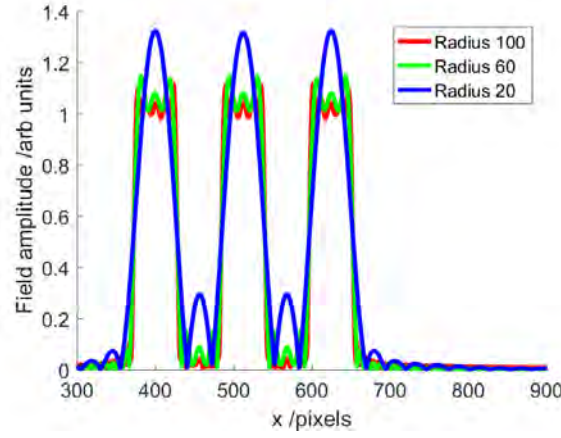
(a) Field amplitudes for filtered binary mask.
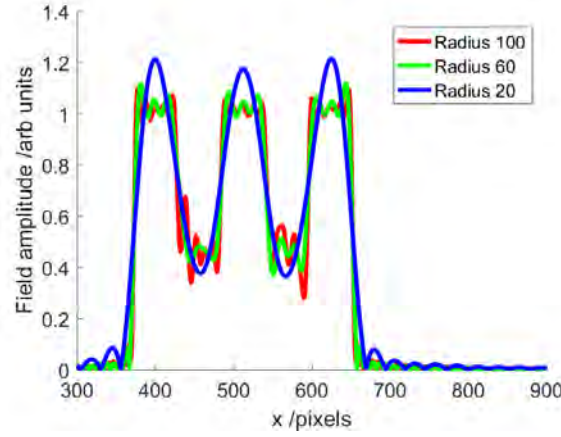
(b) Field amplitudes for filtered greyscale mask.

Figure 6.7: 1D cut of the field amplitudes for the filtered DMD masks in Figure 6.5.

While the method has not reproduced the exact greyscale values desired, and variation in the greyscale regions occurs in each test, the mean value in each case appears approximately correct. An in-depth analysis of the dependence of this variation on a given pattern and aperture has not been performed, however an iterative correction technique as used in the next section may aid the greyscale pattern design. Ablation in electroless nickel at varying input intensities, greyscale levels and periodicity of repeating squares in the checkerboard pattern were tested. Additional distributions were tested, including concentric squares of alternating greyscale values, and continuous distributions. Figure 6.8(a) shows an array of 3 by 3 checkerboard patterns, where the maximum intensity (assuming perfect imaging) would be 3.05J/cm^2 on the bottom row, reducing to 2.92J/cm^2 on the middle row and 2.80J/cm^2 on the top row, and the greyscale regions were set at a value of (from left to right) 0.25, 0.5 and 0.75. Figure 6.8(b) shows a

similar array for concentric squares, where each square layer on the DMD was 16 pixels wide. The 50x objective and DLP3000 line were used for these experiments.
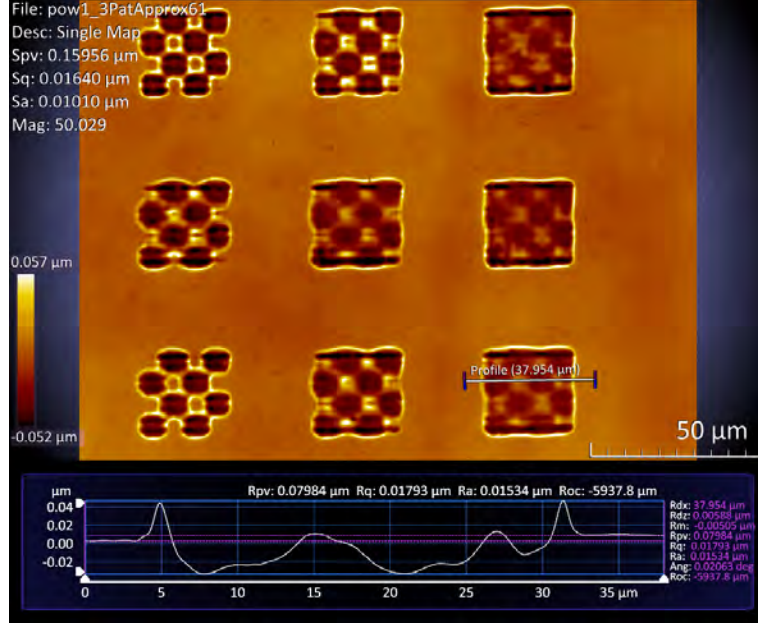
(a) Checkerboard greyscale patterns.
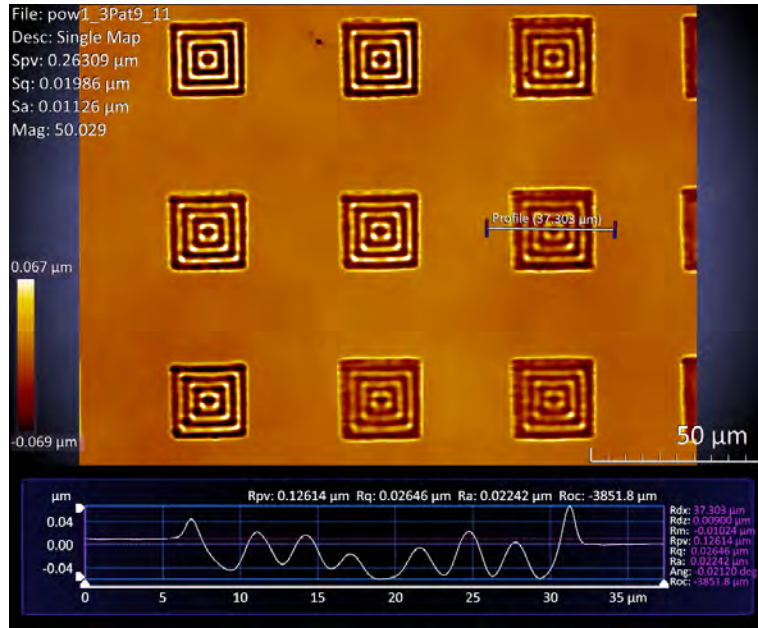
(b) Concentric squares greyscale patterns.

Figure 6.8: Greyscale patterns ablated into electroless nickel.

Modulations on the order of ≈ 50nm have been generated, while the patterns on the right of each array in Figure 6.8 show a smaller difference between maximum and minimum ablation depth, as would be expected for patterns produced via the smallest range of greyscale values. It is important to recall that it is the *material response* to intensity that determines the final ablation depth, rather than simply incident intensity, as in Chapter 5; as can be seen on the left of Figure 6.8(a), imaged regions of the DMD checkerboard mask where pixels were 'on' with probability 0.25 appear to have resulted

in little or no ablation – the imaged intensity at these points may have been below the ablation threshold. Figure 6.9(a) shows the minimum periodicity checkerboard pattern achieved in electroless nickel, for similar intensities and greyscale values as before, while Figure 6.9(b) shows the minimum achieved with concentric squares. The original data associated with the interferometric images presented in Figures 6.9 through 6.3 is no longer available, and the image files created at the time of measurement are shown. In each case, a 2D depth profile is shown, with a 1D plot of the depth profile across a single feature (highlighted by a gray bar in the 2D plot) shown beneath.

(a) Checkerboard greyscale patterns.

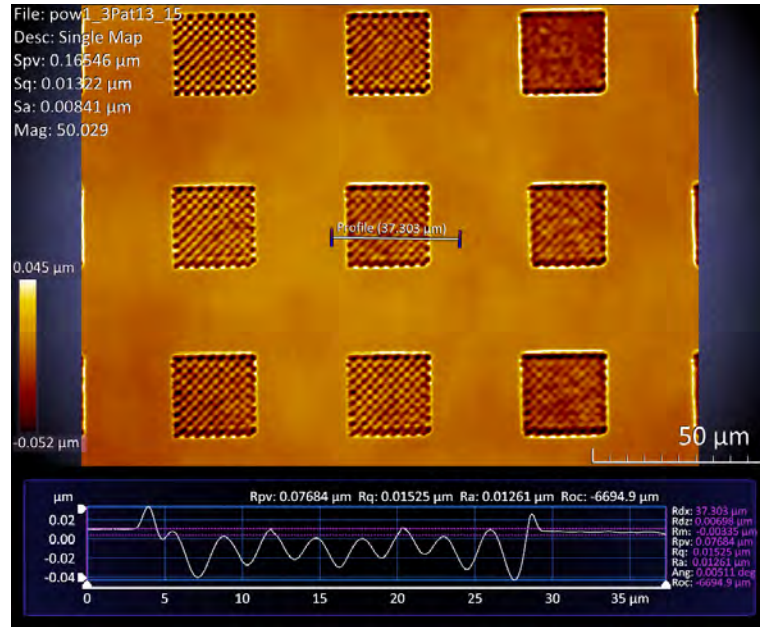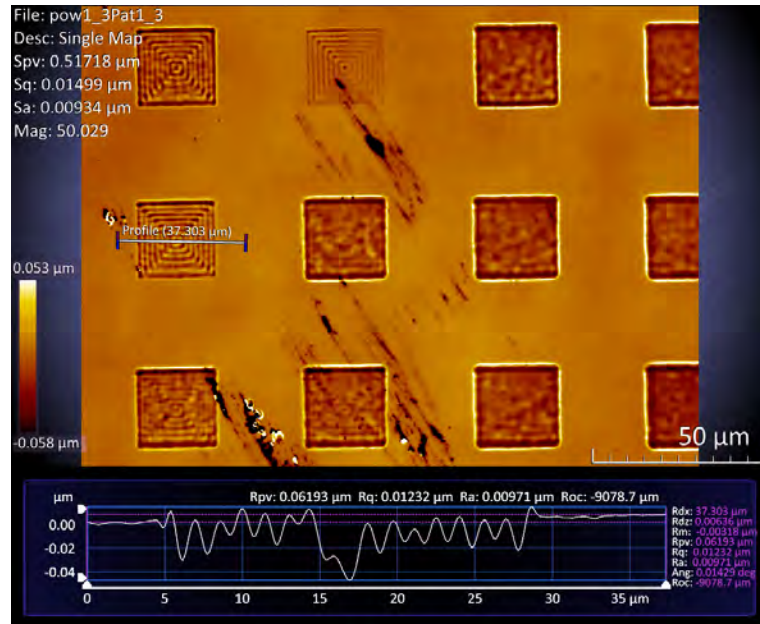
(b) Concentric squares greyscale patterns.

Figure 6.9: Greyscale patterns ablated into electroless nickel. The finest resolution of modulations achieved for checkerboard and concentric square patterns are shown.

It is of note that in many cases in Figures 6.8 and 6.9 the modulations reach an amplitude greater than the surface of the surrounding material, i.e. raised 'lips' of material at the border of exposed regions. This may be an artefact of the interferometric depth measurement, or a result of the material undergoing a melt phase and resolidifying in this structure.

Figure 6.10 shows three patterns with continuous, rather than step, changes in intensity. The masks are shown in Figures 6.10(a) to 6.10(c). The ablated patterns from each of these, respectively, with similar intensity input values to the previous figures, are shown in Figure 6.10(d).

(a) Continuous greyscale mask used for first column of features in (a).

(b) Continuous greyscale mask used for second column of features in (b).

(c) Continuous greyscale mask used for third column of features in (c).
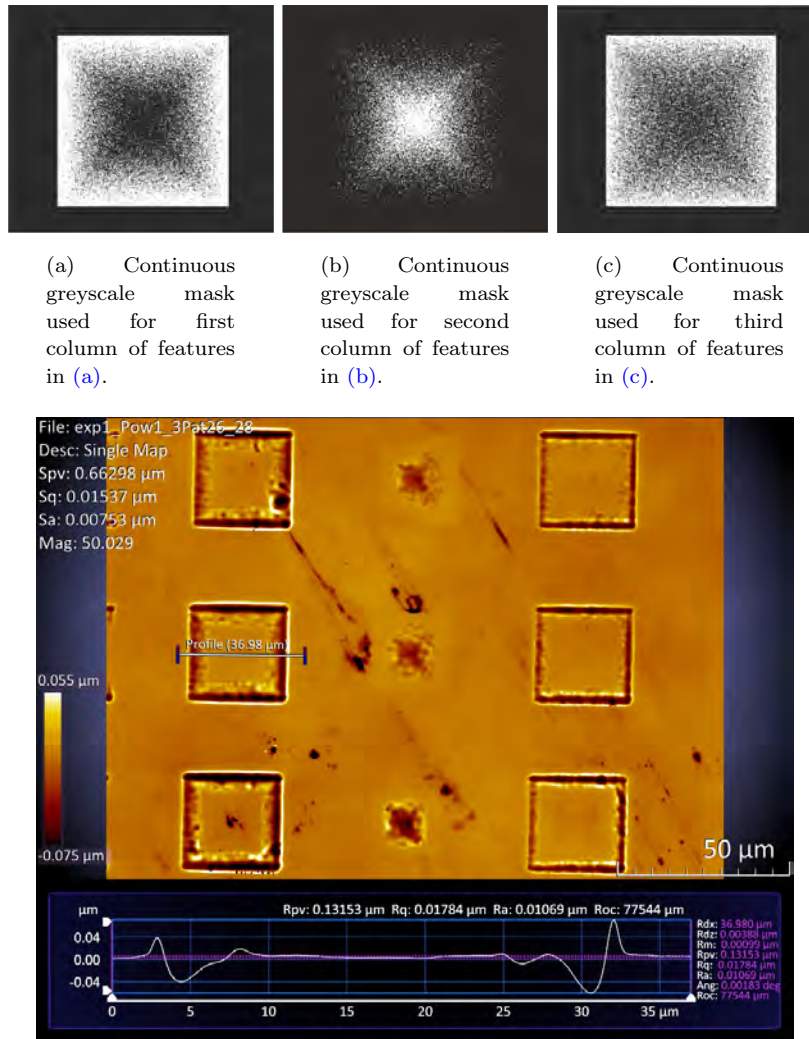
(d) Interferometric depth measurement of the features generated using greyscale DMD intensity masks.

Figure 6.10: Greyscale patterns ablated into electroless nickel. While fidelity achieved does not perfectly recreate the greyscale patterns used, a gradient of depth in the sample is generated.

Clearly, at low level intensity regions ablation has not occurred. The masks in this case were always varied between 0 and 1; in order to improve the technique, a threshold

greyscale value at a given intensity for ablation must be determined, and allowed for during mask generation. Nevertheless, a degree of depth gradient has been generated, following the form of the greyscale gradient used during mask production.

In conclusion, the limited bandwidth of a system has been shown to allow greyscale intensity mask projection using DMDs and ultrashort laser pulses. These masks have been used for multi-level ablation depths in single exposures, with lateral resolutions of $\approx 2\mu$m, close to those observed when projecting simple binary masks in Chapter 3. In future, the ablation threshold of any material to be exposed with the technique must be determined, and incorporated into mask generation; there is little benefit in a mask where regions of pixels will be 'on' with probability 0.1, if the ablation threshold with the exposure intensity to be used is not reached until pixels are 'on' with probabilty 0.5, for example. Additionally, an enhanced model for predicting the loss of particular spatial frequencies would improve the technique – currently the aperture is assumed to be at exactly the Fourier plane (as intended), and exactly centred on the beam line, which may not be correct. Though a simple FFT-based method has led to the results in this section, a simulated propagation befitting the actual experimental setup would be more accurate.

6.4   OPC automation

OPC methods aim to alter an intensity mask such that subsequent to a beam's propagation through a system, alterations to the beam profile as a result of said propagation return an intended image. The determination of *how* to generate an OPC mask such that the resultant profile is as intended is then of great interest. The FFT-based, low-pass filter approach in the previous section provides a rapid method for testing OPC masks, for propagation through a lens and aperture to an image plane, giving complex field information about the resultant beam profile.

By comparing the resultant field to the 'ideal' field, regions requiring correction can be identified. Consider the case in Figure 6.11 – a highly stylised 'Test' image on a 1024 by 1024 pixel bitmap is used as the input image, as in Figure 6.11(a), and after passing through an aperture of radius 50 pixels the absolute value of the resultant image field is as shown in Figure 6.11(b). The difference between this and the ideal field is shown in Figure 6.11(c). The ideal field here has been normalised to the mean absolute value of the intended 'on' points in the resultant field, and multiplied by the corresponding complex phase factor in the resultant field before subtraction. The purpose of this phase factor is to ensure iterative corrections made to the mask interfere contructively. In this section, only the final intensity is of interest, and so the phase profile across the final image is free to vary.
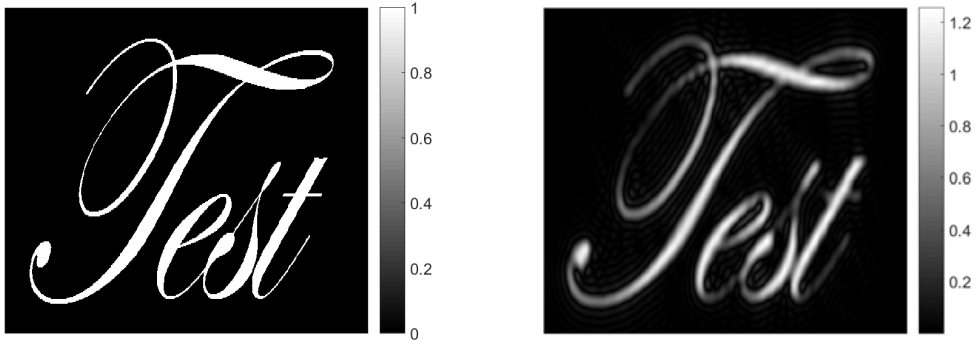
(a) Binary-valued bitmap of stylised word 'test'

(b) Absolute field after the mask in (a) is imaged through a 50 pixel radius aperture
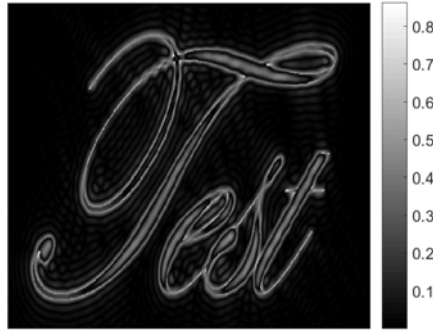
(c) Absolute difference between imaged field and ideal field

Figure 6.11: A simulated binary intensity mask of 1024 by 1024 pixels is imaged through a circular aperture of radius 50 pixels: the resultant image is a poor recreation of the mask. The images have been cropped to a region of 640 by 340 pixels for the figure. Field values are in arbitrary units.

At this point, the difference between the resultant field and the ideal field is known, and some method of updating the image mask to correct for this difference is needed. Following the example of the Gerchberg-Saxton algorithm, it is then tempting to back-propagate this new field information to the mask position as the next step. However, as a result of the reciprocity of optical systems, any useful information extracted from the resultant field must be contained in frequencies below the band-limit imposed by the aperture. As the resultant field in Figure 6.11(b) is comprised entirely of frequencies below the band-limit, and the difference field in Figure 6.11(c) is simply a linear combination of the resultant field and the original mask (save for a phase factor), a simple back-propagation of either at this point will yield no useful input for mask modification.

In order to predict the effect this aperturing has on the final laser machining fidelity, additional considerations must be made. By considering the *material response*, as in Chapter 5, useful information can be extracted from the resultant field. A detailed description of the algorithm is given in Appendix C, and relies on allowing the field

to vary within thresholded values which are different for regions with intended 'on' intensity and 'off' intensity. The Random Complex Summation (RCS) method of representing a complex field on a binary intensity mask is also explained in Appendix C, a technique developed over the course of this PhD; as well as binary-rounding, a binary hologram generation method used by others [162].

As an experimental test of the technique, an aperture was placed at the focus on the DLP3000 line before the diagnostic camera, and closed to ≈0.5mm diameter. As the actual scale of the diffraction pattern produced with the imaging lens was unknown a priori, the technique was used to prepare corrected masks for a range of simulated aperture diameters. Figure 6.12 shows the results, for the four combinations of an uncorrected/corrected mask, and open/closed aperture. More complex optical elements, such as an objective lens, are expected to require more advanced beam propagation techniques to provide accurate correction.

(a) Uncorrected mask, open aperture

(b) Uncorrected mask, closed aperture

(c) Corrected mask, open aperture

(d) Corrected mask, closed aperture
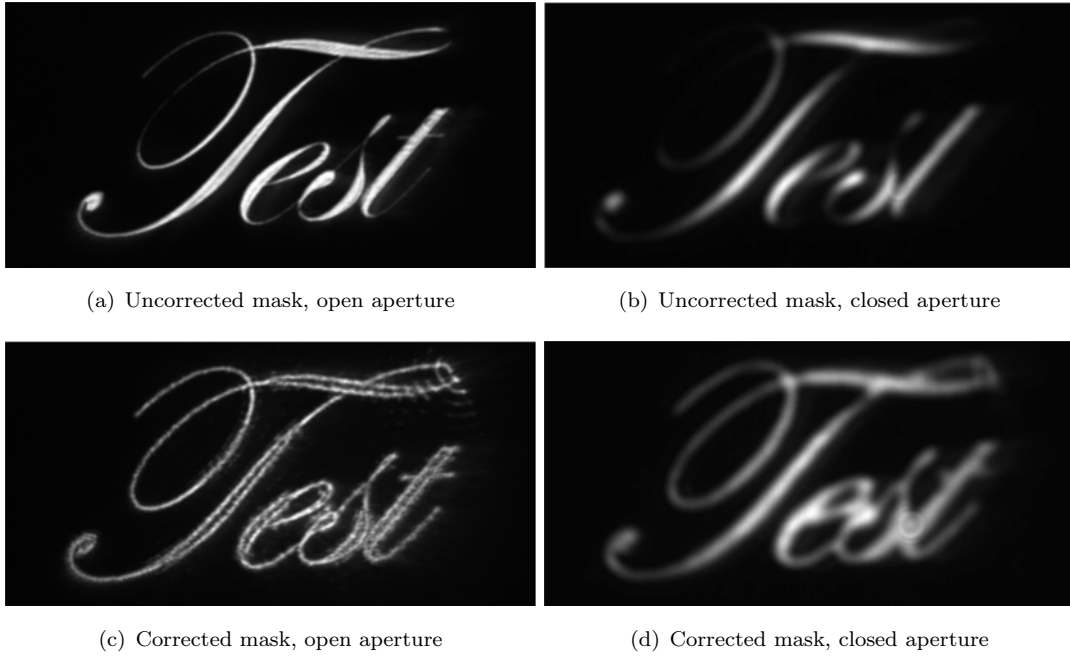
Figure 6.12: Images taken on the DLP3000 via diagnostic camera under illumination by a continuous train of 800nm ultrashort pulses. Note the fine line regions that are recovered in (d) compared to (b); loops on the first 'T', the connecting line between 'e' and 's', crossbar on the final 't', etc.
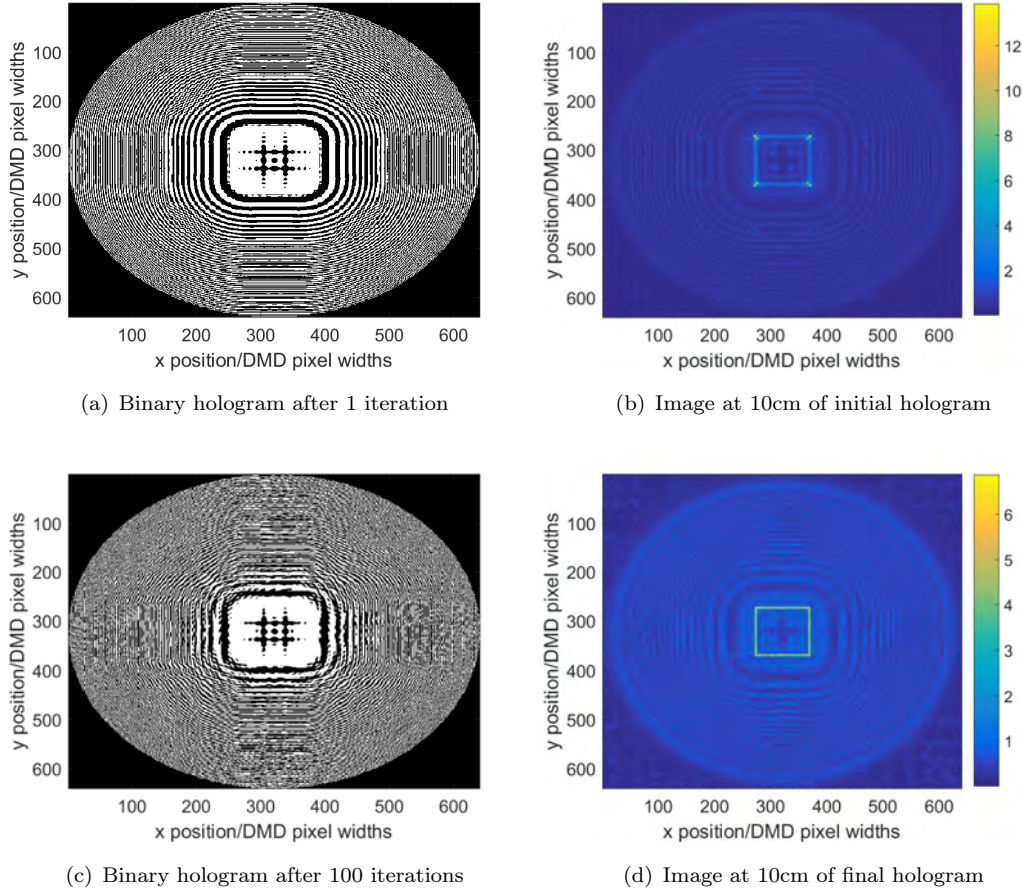
6.5 Binary holograms

The feasibility of representing a complex field on a binary intensity mask, along with arbitrary distance field propagation simulation, allows for the possibility of generating *binary holograms*; masks comprised purely of on/off pixels at a set (or unadjustable) phase, which will diffract into a desired intensity pattern at designated distances from

the mask surface. Both an RCS-based hologram (RCSH) generation method and binary-rounding paired with an adapted version of the Gerchberg-Saxton algorithm, referred to as Gerchberg-Saxton Binary Rounding (GSBR) here, have been developed for this purpose, and will be compared in this section. The steps of RCS and binary-rounding to represent a complex field on a binary intensity mask are described in Appendix C. Here, 'image plane' will refer to the position an intended field pattern is formed, while 'object plane' will refer to the position where the intensity mask, or DMD, is positioned. All quantities stated are given in arbitrary units, unless stated otherwise. An in-depth discussion comparing the GSBR and RCSH algorithms is given in Appendix D, including peak intensity control, greyscale control, 3D field control, phase control, and sub-pixel image shifting.

For the remainder of this section, results will be generated using physical values approximately appropriate for the experimental setup. Masks will be generated on a 1024×1024 array, with each pixel representing a 10μm wide DMD pixel, with a 320 pixel radius section of the mask illuminated by a flat-top, in-phase field distribution unless stated otherwise. For ease of relating to the scale of the DMD surface, axes and image dimensions will be labeled in units of DMD pixel widths. The wavelength used for calculation is 800nm, while the propagation distances are on the order of 10cm. The anti-aliasing bandwidth-limiting method of [155] is used for ASM beam propagation, and each result unless stated otherwise was generated in 100 iterations of the respective algorithm. The majority of results are purely from simulation, and further complications remaining to be solved for the use of binary holograms with the current experimental setup will be discussed; however, an image resulting from a simple binary hologram under femtosecond illumination taken on the DLP3000 line diagnostic camera will be shown at the end of the section. The techniques presented in this chapter and Appendix D have formed the basis for a successful Doctoral Prize Award application, which will provide 1 year of funding to develop the underlying algorithms for use with ultrashort laser pulses and apply them to laser machining, specifically for the production of three lines of medical devices.

6.5.1 Single intensity, single image plane

As a first test of binary hologram production via both GSBR and RCSH, a hollow square shape with linewidth of 5 pixels, and of width 100 pixels, with amplitude 1au (arbitrary units) was intended to be recreated at 10cm from the DMD surface. Figure 6.13 shows the results after 1 iteration and 100 iterations of GSBR for the binary hologram to be displayed on the DMD, and the simulated result after 10cm of propagation. Figure 6.14 shows similar results for RCSH.

(a) Binary hologram after 1 iteration

(b) Image at 10cm of initial hologram

(c) Binary hologram after 100 iterations

(d) Image at 10cm of final hologram

Figure 6.13: Binary holograms and resulting images of a hollow square as simulated with the GSBR algorithm. A very faint square image is visible after a single iteration in (a); after 100 iterations the square image is clearer in (d), but a background of unintended intensity still diminishes its contrast.

The hologram produced after a single iteration via RCSH in Figure 6.14(b) clearly reproduces the hollow square more accurately than the GSBR hologram's first iteration in Figure 6.13(b), however both methods recreate the desired image at the final iteration. Upon inspection, it seems that the RCSH may produce a more uniform intensity distribution within the desired region, at the cost of a higher relative background intensity. In order to measure this uniformity, as well as time taken to reach a near-optimal solution achievable with either method, the standard deviations of the absolute field values within the hollow square shape was recorded at each iteration, with results shown in Figure 6.15.

The results show that both methods reach a near-stable level of standard deviation by iteration 20; the reason for a slight increase after iteration 20 for the GSBR method in Figure 6.15(a) is not yet determined. While not definitive for all possible patterns and depth projections, 100 iterations is taken to be sufficient to reach stable solutions for the remainder of this chapter. The GSBR method reaches a stable deviation of around 0.6, while RCSH reaches approximately 0.02. Note that the peak intensity in each case is different in Figures 6.13(d) and 6.14(d); the GSBR method peaks at around 6, while

(a) Binary hologram after 1 iteration

(b) Image at 10cm of initial hologram

(c) Binary hologram after 100 iterations

(d) Image at 10cm of final hologram
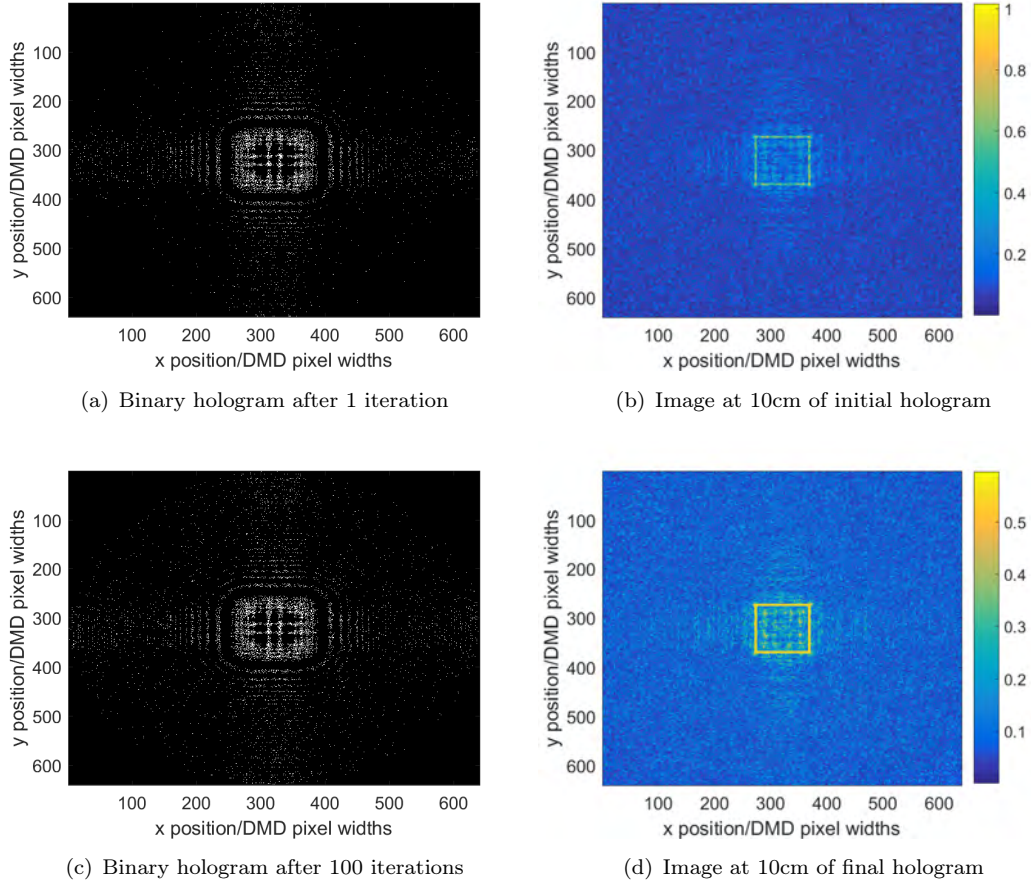
Figure 6.14: Binary holograms and resulting images of a hollow square as simulated with the RCSH algorithm. The final square image in (d) is of much higher contrast than that produced by GSBR in Figure 6.13(d).

the RCSH peaks at around 0.6. This is a consequence of the RCSH method relying on amplitude as well as phase, while the GSBR method uses only phase – a higher uniform amplitude square, when propagated back to the object plane, will result in the same shaped distribution with proportionately higher amplitude. When compared to the random matrix of complex values in the RCSH method then, this will 'turn on' more pixels, while it will have no effect on the on/off distribution generated in GSBR. After normalising by the peak value, RCSH then has a standard deviation of $0.02/0.6 = 0.033$, and GSBR of $0.6/6 = 0.1$, demonstrating that the RCSH method does indeed produce a more uniform distribution.

6.5.2 Under femtosecond illumination

While the algorithms are not yet expected to be suitable for the production of holograms under ultrashort pulse illumination, holograms intended to reproduce the stylised 'Test' image used in section 6.4 have been produced with both algorithms and the resultant

(a) Standard deviation for GSBR method   (b) Standard deviation for RCSH method
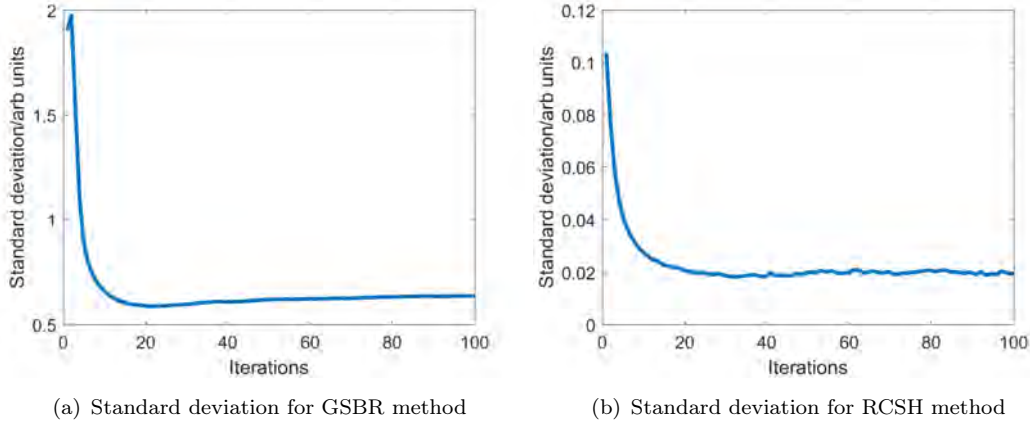
Figure 6.15: The standard deviation of absolute field value within the hollow square regions at the image plane as a function of iteration number for the GSBR and RCSH algorithms. Note the different y axes scales; the RCSH method in (b) displays a standard deviation more than 10× below that of the GSBR method in (a) throughout.

image captured via the diagnostic camera on the DLP3000 line. The results are shown in Figure 6.16.

Though the camera images recognisably produce the word 'Test', there is a great deal of distortion compared to what one might expect from simulated results, on indeed, from simply displaying an ordinary intensity mask and imaging at the regular imaging plane, as in Figure 6.12(a). In particular, vertical lines are blurred strongly in the camera images, and this is likely due to the high b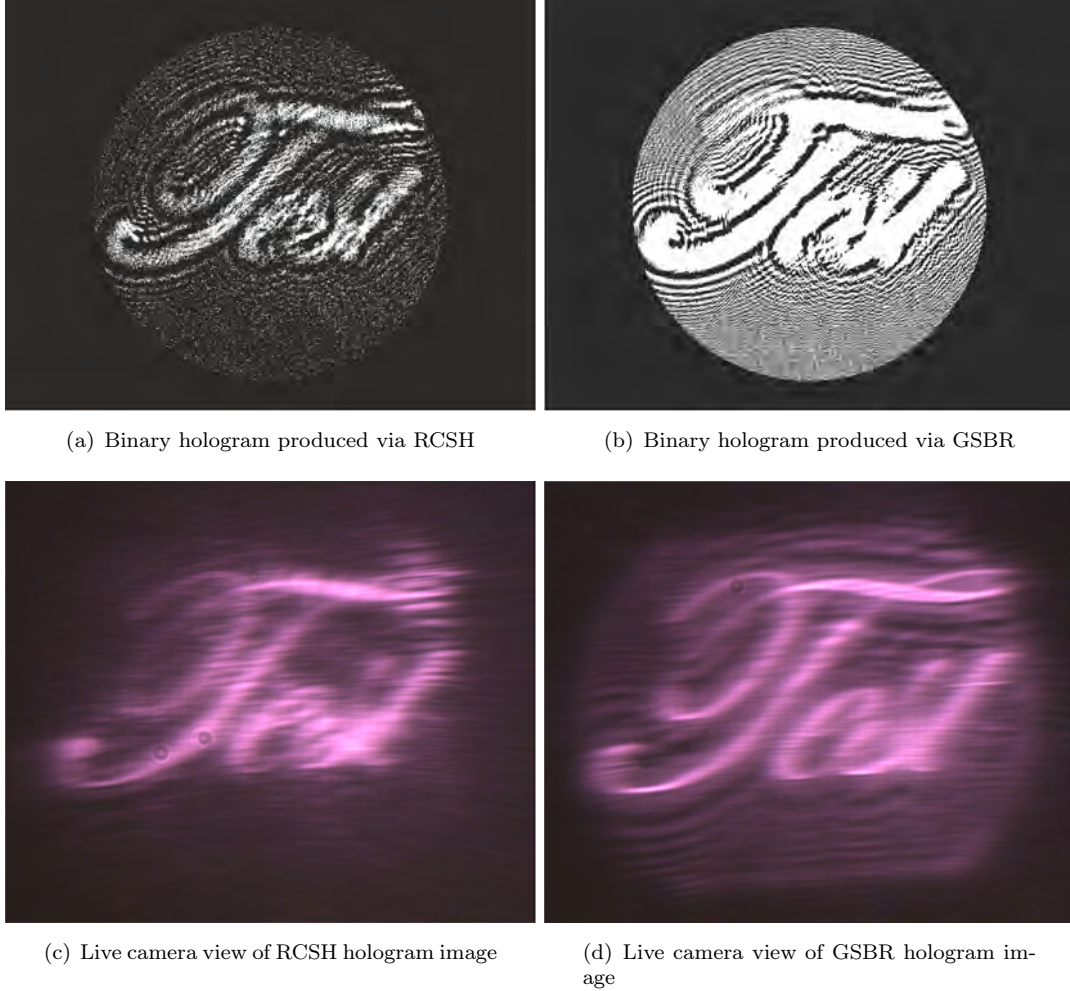andwidth in femtosecond pulses. The problem is illustrated in Figure 6.17, where the grating structure of the DMD causes dispersion at different wavelengths.

In both cases in Figure 6.17, there is a dependence on the wavelength of light for the direction diffraction orders form from the DMD surface. These slight angular differences cause a negligible problem in (a), where the variation is analogous to a slight misalignment of multiple beams of different wavelengths, sharing a common position and distribution at the object plane. Beyond the lens, the multiple beam paths overlap once more and form a crisp image. The effect is more problematic in Figure 6.17(b). The BH produces the desired field distribution at some distance from the DMD surface, with a continuum of laterally shifted copies resulting from different wavelengths (there will be further distortion at any wavelength not equal to the exact one at which the BH was generated for). When attempting to image the hologram plane, then, this is analogous to multiple beams of different wavelengths, with the same distribution but *not* a common position, and so the result is the image of a continuum of shifted images, imperfectly overlapping.

This dispersion could be accounted for by the addition of a grating of opposite and equal dispersion before the DMD, or perhaps by accounting for the continuum of wavelengths *in silico*. The technique as it exists currently could prove useful for various work

(a) Binary hologram produced via RCSH

(b) Binary hologram produced via GSBR

(c) Live camera view of RCSH hologram image

(d) Live camera view of GSBR hologram image

Figure 6.16: Binary holograms produced via the two methods to image the word 'Test' 10cm from the DMD surface. The live camera images shown were taken after imaging the plane 10cm from the DMD through a lens on the DLP3000 diagnostic line.

involving narrower bandwidth illumination, however this was not the focus of this thesis and would have required restructuring of the beamlines during the course of other work. Nonetheless, it is a promising avenue of development for DMD-enabled laser micromachining.

6.6 Discussion and future work

Mask correction techniques have been applied to allow for a host of new functionality when using DMDs as dynamic intensity masks. Beam propagation simulation methods have allowed the generation, and experimental demonstration, of greyscale intensity control, positional error correction, and rapid optical proximity corrections.

Surface depth modulations on the order of 10nm were shown resulting from greyscale mask exposures of nickel samples, with the lateral resolution of these modulations being

| (a) Imaging of the DMD surface, simple mask displayed on DMD | (b) Imaging of a hologram plane some distance from the DMD, binary hologram displayed on DMD |
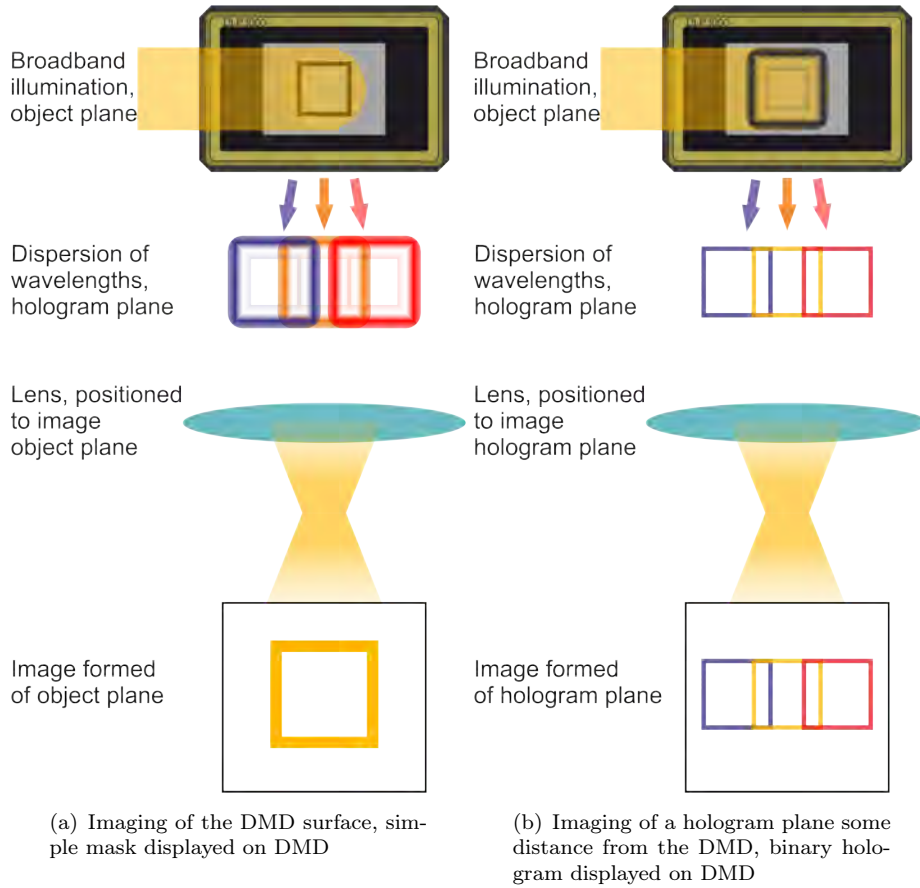
Figure 6.17: The effect of dispersion on broadband illumination of DMD masks for imaging.

on the few micron scale. The lateral resolution limit for step changes between greyscale values will depend on other optical elements in a given experimental setup, and factoring these into the mask design process more explicitly would enhance the method's value. Currently, the greyscale mask generation depends on a single comparison of a multi-valued 2D array to a random matrix. For small regions, this could clearly result in a large error in the final projected intensity. With knowledge of the PSF of a system, the minimum region on the DMD within which pixel contributions at the image will greatly interact could be defined, and then an annealing-type process could be used to ensure that the correct proportion of mirrors are 'on' and 'off' within the desired areas of the masks.

The positional error resulting from translation stages has been ameliorated, with the optical resolution of the camera in an experimental setup becoming the limiting factor. The bottleneck for this corrective step currently is the communication between LabVIEW, the hardware-control software, and MATLAB, which handles the FFT calculations. More streamlined software could allow this step to be applied with lower impact on production time in future experiments. There is no detection of whether the sample has stabilised position, instead an arbitrary wait time is set before taking each image for calculation – some stabilisation detection would likely reduce this time cost.

Additionally, the entire camera image of the sample position is used for the pixel-shift calculation, while a small fraction of the image, at minimum containing a view of some fraction of the previous sample position, would likely be adequate; the impact of reducing this image size of repositioning accuracy could be determined. The current camera resolution is $\approx$ 500nm, while the DLP3000 DMD imaged through the 100x objective is capable of $\approx$ 100nm shifts – detecting for sub-pixel shifts in the camera view would allow for even more accurate corrections to be applied via mask shifting on the DMD.

Lost fine features in a beam line where high spatial frequency components were removed via aperturing have been partially recovered with simple FFT-based beam simulations and a novel method of representing a complex field on a binary mask. In order to demonstrate the relevance to micro-machining, more complex optical elements, such as collimating lenses and objective lenses, must be incorporated into the simulation of iterative beam propagation.

A pair of binary hologram generation methods have been tested in simulation for monochromatic illumination, showing multiple functionalities. 3D image control, continuous intensity control, phase control and sub-pixel repositioning all appear successfully demonstrated. The GSBR method followed the example of binary hologram examples in the literature, while the RCSH technique is a novel scheme which allows for the phase control shown here. Despite the success in simulation of the method, it has not shown high fidelity under femtosecond pulse illumination, as seen in Figure 6.16, with the target field being the highly stylised word 'Test' used in section 6.4. DMD-enabled binary holograms under femtosecond illumination have been shown, in 2016, to greatly improve the fidelity of 2D laser micro-machining [163]; however using binary holograms on the microscale for full 3D field control, greyscale intensity control and sub-pixel shifting capability appears not to have yet been demonstrated in the literature. The enhanced binary hologram control described in this chapter and Appendix D have formed the cornerstone for a year of future research, whose funding has been awarded under the Doctoral Prize program, and will go on to be used for the rapid laser micro-machining of 3D medical devices.

Chapter 7

Conclusions and future work

Results produced over the course of this PhD will be summarised in this chapter. A description of future work to be undertaken in each case will also be described.

7.1 Image projection-based subtractive patterning

Regions with lateral dimensions of $\approx 30\mu$m and resolutions as low as $\approx 2\mu$m were patterned in various materials, including metals, polymers, glass and crystalline substrates. The use of a DMD as a dynamic intensity mask in conjunction with sample translation has allowed for distinct, and potentially unique features to be ablated in close proximity, to build up complex structures with overall sizes of ≈ 1cm.

Structures with diffractive properties visible to the naked eye have been produced, and a reverse-moulding technique has allowed the rapid prototyping of custom cell growth assays for regenerative medicine. The precise stitching of regions patterned in separate pulses after sample translation has remained a problem for the production of samples where $< 10\mu$m accuracy in point-to-point positioning is desirable. The image-shifting technique presented in section 6.2 could be applied in future to address this, though in its current state this approach is only suitable to correct for positional errors when the translation stages pause at the point of each exposure. A camera with a fast shutter-speed may be sufficient to apply the technique while the sample remains in motion during exposures.

The greyscale intensity control demonstrated in section 6.3, while requiring some calibration depending upon choice of materials such that relative ablation depths are predictable, is ready to be applied generally in DMD dynamic intensity mask use with pulsed laser sources. The immediate area where this control will find use is in the generation of more complex cell growth assays, and will be developed during upcoming work packages to be undertaken by the group. Additionally, correcting for aberrations

due to loss of high spatial frequencies, as in section 6.4, will be implemented as a standard step in the generation of DMD intensity masks, for higher fidelity laser machining.

7.2   Laser-induced transfer

The first demonstration of shaped, solid phase material LIFT was made via the use of DMD mask exposure was seen in Chapter 4. The deposits replicated alphabetical letter shapes, and varied in overall size between 30–100μm, with line widths between 10–20μm.

LIBT of similar quality deposits was performed by another member of the group, who also demonstrated nano-imprinted patterns on the LIBT deposits via the use of a pre-machined carrier substrate. Shadowgraphy revealed the flyer dynamics in the LIBT process, and the LIBT flyer release process was modelled based on a thermal expansion model, with a similar distribution of laser fluence to flyer velocity being produced by shadowgraphy and simulation.

LIT allows for the targeted deposition of donor material on substrates which would usually make for difficult combinations (i.e. metal on polymer, for example). The extension of LIT to complex shapes of deposits enhances the technique for more general use. Of particular interest for future work are the nano-imprinted structures demonstrated via LIBT; micro-scale waveguides, or microfluidic chips could be deposited in single exposures from a carrier onto surfaces of interest, without requiring the targeted surface to undergo the usual development steps for producing such structures. If, as appeared to be the case in section 4.2.2, the carrier suffers minimal damage during LIBT, pre-machined carrier substrates with nano-scale features could be re-used, leading to a rapid method of nano-scale feature production.

7.3   Multiple exposures

It was shown in Chapter 5 that features spaced by periods below the limit imposed by diffraction achievable in a single exposure can be patterned with the use of multiple exposures. The technique was demonstrated in nickel, BiSbTe and a multiphoton resist. A reduction of resolution of 2$\times$ was found for the two-photon resist, which agreed with the limit predicted from the literature. A reduction from 1μm to 370nm was observed when using the 20$\times$ objective, and from 727nm to 270nm when using the 100$\times$ objective, representing a greater improvement than was possible via a two-photon resist, and the first such demonstration of the technique via ablation.

The structuring achieved via ablation with multiple exposures merits further exploration; a proposed first order model recreates the observed structure, but this work was

performed with identical intensity masks either translated or rotated. Using a DMD to produce a final structure via the exposure of many distinct masks at the same location would be a natural extension of the method. The technique should, in theory, apply to any laser source, and such a general method for a simple reduction in feature resolution is of course of interest to the laser machining community.

7.4   Binary holograms

Though little has been demonstrated experimentally, the potential for laser micro-machining presented in section 6.5 is substantial. With the new functionalities of 3D field control, greyscale control, phase control and sub-pixel shifting of images, binary holograms offer the next revolutionary step in DMD image projection-based laser micro-machining. This potential has been recognised with funding from EPSRC under the Doctoral Prize Award scheme. Developing the hologram generation algorithms for implementation with femtosecond laser pulses, as well as applying them for the rapid prototyping of medical devices with collaborators from the field of health science, will be the focus of research for the year subsequent to the submission of this thesis.

Appendix A

Published Work

In this section, published papers relating to works described in this thesis are shown, and a list of published works and presentations are given. The paper "Dynamic spatial pulse shaping via a digital micromirror device for patterned laser-induced forward transfer of solid polymer films" has been published in *Optical Materials Express*, the paper "Fabrication of variable period grating structures via laser ablation using a digital micromirror device" has been published in *Applied Optics*, and the paper "Laser ablation via programmable image projection for submicron dimension machining in diamond" has been published in the *Journal of Laser Applications*. "Laser-induced backward transfer of nanoimprinted polymer elements" was published in *Applied Physics A*, and "Time-resolved imaging of flyer dynamics for femtosecond laser-induced backward transfer of solid polymer thin films" was published in *Applied Surface Science*.

D. J. Heath, M. Feinäugle, J. Grant-Jacob, B. Mills, R. W. Eason, *Dynamic spatial pulse shaping via a digital micromirror device for patterned laser-induced forward transfer of solid polymer films*
Optical Materials Express 2015 Vol.5(5) pp.1129-1136

D. J. Heath, B. Mills, M. Feinäugle, R. W. Eason, *Rapid bespoke laser ablation of variable period grating structures using a digital micromirror device for multi-colored surface images*
Applied Optics 2015 Vol.54(16) 4984-4988

D. J. Heath, B. Mills, M. Feinäugle, J. A. Grant-Jacob, R. W. Eason, *Laser Induced Forward Transfer of shaped solid polymer donors using a beam spatially modulated via a Digital Multimirror Device*
E-MRS '14 Materials Research Society Spring Meeting Lille 26-30 May 2014

D. J. Heath, B. Mills, J. Grant-Jacob, M. Feinäugle, R. W. Eason, *Multi-shot laser ablation and digital micromirror device mask translation for sub-diffraction-limit machining resolution*

European Conference on Lasers and Electro-Optics and the European Quantum Electronics Conference Munich 21-25 Jun 2015

D. J. Heath, B. Mills, J. Grant-Jacob, M. Feinaeugle, V. Goriainov, R. Oreffo, R.W. Eason, *Digital micromirror device based adaptive optics approach for enhanced micromachining fidelity*
SPIE Photonics West San Francisco 28 Jan- 2 Feb 2017

B. Mills, D.Heath, M. Feinäugle, R. W. Eason, *Using a digital micromirror device for high-precision laser-based manufacturing on the microscale*
11th International Symposium on Emerging and Industrial Texas Instruments DLP Technology Applications Dresden 6 Oct 2016 (Invited)

M. Feinäugle, P.Gregorčič, D.Heath, B. Mills, R. W. Eason, *Time-resolved imaging of flyer dynamics for femtosecond laser-induced backward transfer of solid polymer thin films*
Applied Surface Science 2016 pp.1-16

M. Feinäugle, D.Heath, B. Mills, R. W. Eason, *Shaped deposition via laser-induced backward transfer from a nano-structured carrier using a digital micromirror device*
E-MRS Spring Meeting (European Materials Research Society) Lille 2-6 May 2016

M. Feinäugle, D. J. Heath, B. Mills, J. A. Grant-Jacob, G.Z.Mashanovich, R. W. Eason, *Laser-induced backward transfer of nanoimprinted polymer elements*
Applied Physics A Materials Science and Processing 2016 Vol.122(4) pp.1-5

R. W. Eason, B. Mills, M. Feinäugle, D. J. Heath, J. Grant-Jacob, *Laser-induced backward transfer of intact nano-structured polymer deposits*
International High Power Laser Ablation and Directed Energy Santa Fe, New Mexico 4-7 Apr 2016

M. Feinäugle, D. J. Heath, B. Mills, J. A. Grant-Jacob, G.Z.Mashanovich, R. W. Eason, *Femtosecond laser-induced patterned transfer of intact semiconductor and polymer thin films via a digital micromirror device*
16th International Symposium on Laser Precision Microfabrication (part of LAMP2015) Kitakyushu, Fukuoka, Japan 26-29 May 2015

M. Feinäugle, D. J. Heath, B. Mills, J. A. Grant-Jacob, G.Z.Mashanovich, R. W. Eason, *Simultaneous patterning and deposition of thin films via femtosecond laser-induced transfer using a digital micromirror device for spatial pulse shaping*

European Conference on Lasers and Electro-Optics and the European Quantum Electronics Conference Munich 21-25 Jun 2015

R. W. Eason, M. Feinäugle, D. J. Heath, J. A. Grant-Jacob, B. Mills, *Deposition of thin films via forward and backward femtosecond laser-induced transfer using spatial beam shaping via a digital micromirror device*
E-MRS Spring Meeting Lille 11-15 May 2015

B. Mills, D. J. Heath, M. Feinäugle, R. W. Eason, *Digital micromirror devices for laser-based manufacturing on the micro-scale*
SPIE Photonics West San Francisco 7-12 Feb 2015

B. Mills, D. J. Heath, M. Feinäugle, J. A. Grant-Jacob, R. W. Eason, *Laser ablation via programmable image projection for submicron dimension machining in diamond*
Journal of Laser Applications 2014 Vol.26(4) pp.41501

R. W. Eason, B. Mills, M. Feinäugle, J. A. Grant-Jacob, D. J. Heath, *Digital micromirror devices for laser-based manufacturing*
EPSRC: Manufacturing the Future Strathclyde University, Glasgow 23-24 Sep 2014

M. Feinäugle, B. Mills, D. J. Heath, C.L.Sones, R. W. Eason, *Laser-assisted transfer for rapid additive micro-fabrication of electronic devices*
EPSRC: Manufacturing the Future Strathclyde University, Glasgow 23-24 Sep 2014

M. Feinäugle, R. W. Eason, C.L.Sones, B. Mills, J. A. Grant-Jacob, I.N.Katis, D. J. Heath, *Making additive manufacturing functional - The laser-assisted fabrication of electronic and photonic devices*
The Institution of Engineering and Technology (IET) Reading 22 May 2014 (Invited)

R. W. Eason, B. Mills, M. Feinäugle, D. J. Heath, J. A. Grant-Jacob, I.N.Katis, C.L.Sones, *Digital multimirror devices for precision laser micromachining*
ORC Industry Day University of Southampton 2 Apr 2014

R. W. Eason, B. Mills, M. Feinäugle, D. J. Heath, D.Banks, C.L.Sones, J. Grant-Jacob, I.N.Katis, *Nanofabrication technologies: high-throughput for tomorrow's metadevices*
Metamaterials retreat Chamonix, France 17-21 Mar 2014

B. Mills, D. J. Heath, M. Feinäugle, R. W. Eason, *Digital Micromirror Devices for rapid fabrication of large-area laser-ablated multicolour-grating patterns*
Photon 14 Imperial College, London 1-4 Sep 2014

141

R. W. Eason, D.Banks, K.S.Kaur, C.L.Sones, M. Feinäugle, J. Grant-Jacob, B. Mills, I.N.Katis, D. J. Heath, *LIFT: Laser-induced forward transfer printing of solid-phase materials for photonic and electronic applications*
Invited seminar University of Nottingham 22 Jan 2014 (Invited)

B. Mills, D. J. Heath, J. A. Grant-Jacob, M. Feinäugle, R. W. Eason, *Femtosecond ablation using an intensity spatial light modulator: What is the minimum machinable feature size?*
E-MRS '14 Materials Research Society Spring Meeting Lille 26-30 May 2014

Dynamic spatial pulse shaping via a digital micromirror device for patterned laser-induced forward transfer of solid polymer films

Daniel J Heath*, Matthias Feinaeugle, James A Grant-Jacob, Ben Mills, and Robert W Eason

Optoelectronics Research Centre, University of Southampton, Southampton, SO17 1BJ, UK
*djh2v07@soton.ac.uk

Abstract: We present laser-induced forward transfer of solid-phase polymer films, shaped using a Digital Micromirror Device (DMD) as a variable illumination mask. Femtosecond laser pulses with a fluence of 200-380 mJ/cm^2 at a wavelength of 800 nm from a Ti:sapphire amplifier were used to reproducibly transfer thin films of poly(methyl methacrylate) as small as ~30 µm by ~30 µm with thickness ~1.3 µm. This first demonstration of DMD-based solid-phase LIFT shows minimum feature sizes of ~10µm.

OCIS codes: (140.3390) Laser materials processing; (240.0310) Thin films; (140.7090) Ultrafast lasers; (220.4000) Microstructure fabrication; (070.6120) Spatial light modulators.

References and links

1. J. Bohandy, B. F. Kim, and F. J. Adrian, "Metal deposition from a supported metal film using an excimer laser," J. Appl. Phys. **60**, 1538–1539 (1986).
2. W. A. Tolbert, I.-Y. Sandy Lee, M. M. Doxtader, E. W. Ellis, and D. D. Dlott, "High-speed color imaging by laser ablation transfer with a dynamic release layer: fundamental mechanisms," J. Imaging Sci. Technol. **37**, 411–421 (1993).
3. B. Hopp, T. Smausz, Z. Antal, N. Kresz, Z. Bor, and D. Chrisey, "Absorbing film assisted laser induced forward transfer of fungi (Trichoderma conidia)," J. Appl. Phys. **96**, 3478–3481 (2004).
4. M. Nagel, R. Hany, T. Lippert, M. Molberg, F. A. Nüesch, and D. Rentsch, "Aryltriazene Photopolymers for UV-Laser Applications: Improved Synthesis and Photodecomposition Study," Macromol. Chem. Phys. **208**, 277–286 (2007).
5. D. P. Banks, K. Kaur, R. Gazia, R. Fardel, M. Nagel, T. Lippert, and R. W. Eason, "Triazene photopolymer dynamic release layer-assisted femtosecond laser-induced forward transfer with an active carrier substrate," EPL (Europhysics Lett.) **83**, 38003 (2008).
6. M. Feinaeugle, A. P. Alloncle, P. Delaporte, C. L. Sones, and R. W. Eason, "Time-resolved shadowgraph imaging of femtosecond laser-induced forward transfer of solid materials," Appl. Surf. Sci. **258**, 8475–8483 (2012).
7. R. Fardel, M. Nagel, F. Nüesch, T. Lippert, and A. Wokaun, "Laser-induced forward transfer of organic LED building blocks studied by time-resolved shadowgraphy," J. Phys. Chem. C **114**, 5617–5636 (2010).
8. M. Feinaeugle, P. Horak, C. L. Sones, T. Lippert, and R. W. Eason, "Polymer-coated compliant receivers for intact laser-induced forward transfer of thin films: experimental results and modelling," Appl. Phys. A **116**, 1939–1950 (2014).
9. A. I. Kuznetsov, A. B. Evlyukhin, M. R. Goṇalves, C. Reinhardt, A. Koroleva, M. L. Arnedillo, R. Kiyan, O. Marti, and B. N. Chichkov, "Laser fabrication of large-scale nanoparticle arrays for sensing applications," ACS Nano **5**, 4843–4849 (2011).
10. M. Feinaeugle, C. L. Sones, E. Koukharenko, and R. W. Eason, "Fabrication of a thermoelectric generator on a polymer-coated substrate via laser-induced forward transfer of chalcogenide thin films," Smart Mater. Struct. **22**, 115023 (2013).
11. L. Rapp, C. Constantinescu, Y. Larmande, A. P. Alloncle, and P. Delaporte, "Smart beam shaping for the deposition of solid polymeric material by laser forward transfer," Appl. Phys. A **117**, 333-339 (2014).
12. J. A. Grant-Jacob, B. Mills, M. Feinaeugle, C. L. Sones, G. Oosterhuis, M. B. Hoppenbrouwers, and R. W. Eason, "Micron-scale copper wires printed using femtosecond laser-induced forward transfer with automated donor replenishment," Opt. Mater. Express **3**, 747–754 (2013).

13.   R. C. Y. Auyeung, H. Kim, N. A. Charipar, A. J. Birnbaum, S. A. Mathews, and A. Piqué, "Laser forward transfer based on a spatial light modulator," Appl. Phys. A **102**, 21–26 (2010).
14.   Texas Instruments, "DLP & MEMS," http://www.ti.com/lsds/ti/analog/dlp/overview.page, accessed 14th Nov 2014.
15.   A. Piqué, H. Kim, R. C. Y. Auyeung, and A. T. Smith, "Laser Forward Transfer of Functional Materials for Digital Fabrication of Microelectronics," J. Imaging Sci. Technol. **57**, 40401–40404 (2013).
16.   Texas Instruments, "DLP 0.3 WVGA Series 220 DMD," http://www.ti.com/lit/ds/symlink/dlp3000.pdf , accessed 14th Nov 2014.

1. Introduction

In recent years, there has been much commercial interest and technological advances in additive manufacturing, processes that enable the controlled addition of material onto a substrate. Whilst there are a wide range of deposition techniques, a subset of methods for micron to mm printed devices uses a focused laser beam to interact with a surface, causing a localised reaction that results in the addition of material.

In these methods, a user controls the position of a laser spot, enabling a great deal of flexibility with regards to the fabricated structure, as the path of the laser focus with respect to the surface of the sample can be programmed to produce almost any desired pattern. However, this processing method can be relatively slow due to the need to scan a single laser beam over a sample. An alternative method, the use of a fixed illumination mask, can be considerably faster as no laser-scanning may be required, and hence can be ideal for the manufacturing of a large number of identical devices. However, this approach can be a costly technique for rapid prototyping, where the printed device may need several design updates. The use of a *variable* illumination mask however retains the advantage of both approaches, namely the flexibility that allows rapid prototyping but also the speed advantage of using an illumination mask.

In this paper we demonstrate the use of a spatial light modulator, namely a Digital Micromirror Device (DMD), as a variable illumination mask for femtosecond laser pulses, for the shaped deposition of polymer films with features as small as 10 µm, via the technique of laser-induced forward transfer (LIFT).

2. Laser-induced forward transfer

LIFT is an additive laser direct-write technique [1] in which laser pulses are used to transfer solid, liquid or paste *donor* materials from a *carrier* substrate to a *receiver* substrate, as shown schematically in Fig. 1. A single laser pulse is focused or imaged at the interface between the donor and the carrier, such that a small volume of the donor, or an optional dynamic release layer (DRL) at this interface, absorbs a large fraction of the laser pulse energy and undergoes an explosive phase transformation, propelling the remaining donor material, referred to as the *flyer*, towards the receiver substrate.

In general, the use of a DRL [2], acting as a sacrificial thin film, leads to a more confined absorption of the incident pulse energy and hence can result in a lower fluence required for flyer propulsion, as well as less structural or functional damage to the donor and resultant flyer. DRLs of metals [2,3] and polymers [4,5] have been successfully demonstrated. Due to the high speed of the flyer (shadowgraph measurements have shown speeds varying from 34 ms^{-1} [6] to ~2 kms^{-1} [7]) and subsequent rapid deceleration when it collides with the receiver substrate, the flyer can experience significant forces that can result in cracking or more substantial damage. However, it has been shown [8] that use of an additional 'soft' compliant receiver (such as polydimethylsiloxane (PDMS), deposited onto the receiver) can dampen the forces sufficiently and thereby dramatically improve the integrity of the deposited flyer.
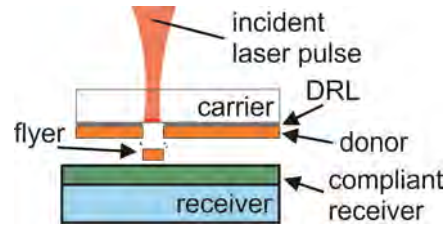
Fig. 1. Schematic of the LIFT technique, showing the use of a
laser pulse to deposit donor material onto a receiver substrate.

Most frequently, donor thicknesses of a few hundred nm to a few µm are used, though in general the usable thickness of donor and final quality of the deposited flyer depend on material properties of the chosen donor. Lateral dimensions of the flyer range from tens of nm [9] to a few mm [10]. Pulsed lasers, usually ranging from nanosecond to femtosecond pulse lengths, can be used for LIFT, with typical energy densities of a few tens to hundreds of mJ/cm^2.

Until recently, the majority of LIFT research has used focused or imaged laser pulses that had a Gaussian or 'top-hat' spatial intensity profile, with circular or rectangular beam-shaping (with extension to "smart beam shaping" in the work of Rapp et al. [11]), and hence, in these cases, the shape of the deposited material followed these profiles. Whilst individual circular deposits can be overlapped, for example for the fabrication of millimetre-length conductive copper wires [12] via a donor-replenishment tool, this approach cannot be easily extended to produce less simple 2D structures. In order to build up more complex structures, an alternative approach, namely the use of a variable illumination mask (or spatial light modulator, such as a DMD), has recently been explored [13].

DMDs can offer a significant speed advantage (30 kHz repetition rate devices are currently possible [14]) over liquid-crystal spatial light modulators, and hence can enable dramatically faster additive manufacturing, when used with an appropriately high repetition rate laser. This paper describes results from use of a DMD, acting as an intensity spatial light modulator, for the shaped LIFT of polymer films with minimum lateral dimensions ~30 µm, and builds upon recent results by Piqué et al. [13,15], which show DMD-assisted LIFT (referred to as Laser Decal Transfer in their work) of a paste-like donor material that produces solid structures after post-processing. In our work, we demonstrate for the first time, the use of a variable illumination mask for the LIFT of intact solid phase materials, which do not require any post-processing step.

3. The digital micromirror device

The DMD used in this work was a Texas Instruments DLP3000 [16], which consisted of an array of 608 by 684 individually controllable, ~7.6 µm wide mirrors, arranged in a diagonal-square lattice. The centre-to-centre distance between adjacent mirrors in the horizontal and vertical planes was 10.8 µm. Here, the mirrors are described as being either 'on' or 'off', which refers to their angular orientation of either +12° or -12° respectively, relative to the plane of the DMD surface.

Due to the periodic structure of the DMD, when working with a spatially coherent light source, as was done in this work, multiple diffraction peaks were produced, where the output angles of these peaks can be determined from the grating equation for non-normal incidence, $\sin(\theta_i) - \sin(\theta_m) = m\lambda/d$, where θ_i and θ_m are the incident and diffracted angles, d is the mirror spacing, λ is the laser wavelength and m is the order of diffraction. In this case, the angular orientation of the mirrors resulted in the mirror array acting as a blazed grating, which was taken advantage of in this work in order to increase the percentage of diffracted light present in a single diffraction order.

4. Experimental setup

A Ti:sapphire amplifier was used to produce ultrashort (150 fs, 800 nm wavelength) laser pulses with a maximum energy of 1 mJ at a 1 kHz repetition rate. The pulses were spatially homogenized (using an AdlOptica 'π-shaper' model 6_6) to produce a 'top-hat' spatial intensity distribution. The homogenized pulses were incident onto the DMD, where they underwent diffraction into multiple orders. By choosing an incident angle of ~24° (taking advantage of the blaze angle), the m=5 diffraction order (at an optimal output angle of 0°) contained ~30% of the incident pulse energy. A collimating lens captured the chosen order, which was then imaged using a 50x or 20x infinity-corrected objective onto the DRL, as shown in Fig. 2, to replicate the binary pattern loaded on the DMD as a spatial intensity profile at the DRL. A diagnostic beam line, consisting of a flip mirror (FM), lens (L1) and a CMOS camera, enabled the surface of the DMD to be imaged for alignment purposes. The beam path used for LIFT consisted of two mirrors (M2 and M3), a collimation lens (L2), a dichroic mirror (D) and the imaging objective (50x or 20x). A white light source (WL) allowed viewing of the sample in real-time as it was imaged back through the objective and dichroic onto a second CMOS camera. The sample was loaded on a 3-axis stage, which had a positional accuracy of ~1 µm and 50 mm total travel in each direction. By sending monochrome bitmap images via computer to the DMD, all mirrors were switched to their intended on/off positions.
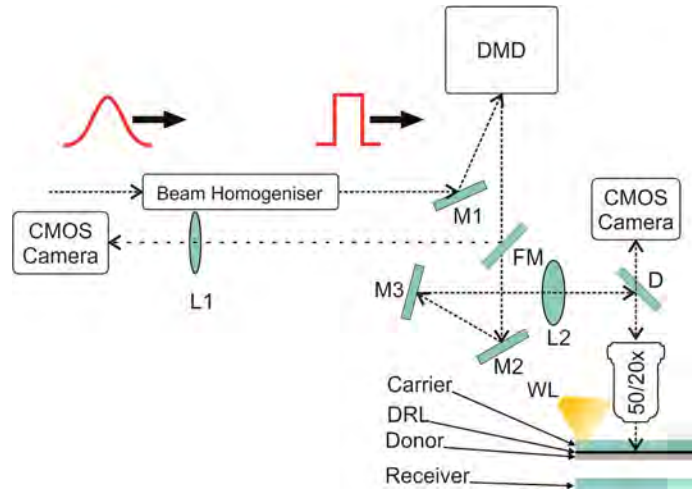

Fig. 2. Schematic of the experimental setup.

The carrier substrate (a glass slide, Electroverre extra-white) was coated with either a 30 nm gold or 50 nm thick carbon film via sputtering or evaporation respectively, both acting as a DRL. The donor used throughout the experiments was poly(methyl methacrylate) (PMMA, a common material in micro-optical-electro-mechanical system production, purchased from MicroChem), prepared on the receiver substrate via spin coating, resulting in a 1.3 µm thick layer. The receiver had a ~10 µm thick spin-coated PDMS layer, acting as a compliant receiver. The donor and compliant receiver were placed in contact during the LIFT process in order to reduce the possible rotation of the flyer during transfer. Previous work [6] has shown instability even in approximately rotationally symmetric flyers – the highly asymmetric shaped flyers demonstrated here would likely be released in a non-uniform fashion, leading to an increased chance of damage.

5. Experimental results

Projected spatial intensity patterns (a selection of alphabetic letters) ranging in complexity and size were trialled for a range of laser fluences, in order to determine the optimal conditions for the LIFT of the chosen samples. Scanning electron microscope (SEM) images of individual deposited structures are shown in Fig. 3, with insets displaying the DMD patterns as loaded (and hence the projected spatial intensity profile) when the laser pulse was incident on the DMD surface. Fig. 3 shows a comparison of the deposited structures using (a-d) a 50x objective and fluence of 300 mJ/cm^2, and (e-h) a 20x objective and fluence of 270 mJ/cm^2. For the 50x objective, the size scales in the letter 'B' and 'S' appear to be at the limit of what is possible for this particular material, as the features were not reproduced correctly. For the 20x objective, the size scales were larger and both the letter 'B' and 'S' were reproduced accurately. While many letters were reproduced successfully using the 20x objective, with maximum lateral dimensions of ~70 µm, the quality of some, such as 'S', remained low until they were produced at lateral dimensions of ~100 µm (note the smaller scale bar in Fig. 3 (h)). At this size, the entire alphabet was deposited accurately. In general, for successful LIFT, the region on the donor that is illuminated by the laser pulse must break free from the surrounding donor material, via the explosive phase transformation caused by absorption of the incident laser pulse. There is therefore a limit to the minimum width of a feature that can be successfully removed from the donor via the LIFT process, and is a value determined predominantly by the material properties and dimensions of the donor, and the presence of a DRL – an evident concern in the LIFT of solid donor material when compared to the LIFT of pastes by Piqué et al. [15], which could much more easily break free of surrounding donor. This limit is observed in Fig. 3, where the features in (a-d) are too small to be removed in the same shape as the projected intensity pattern, whilst the features in (e-h) are almost perfectly replicated. Evidently in (a-d), the deposits' minimum feature sizes are larger than they would have been, had the deposit been a perfectly minified version of the projected intensity patterns (also shown as the insets).

Measurements showed that when using a 50x objective to produce deposits of size ~30 µm, although the overall size of ~30 µm corresponded to the minified image projected from the DMD, minimum feature widths in each deposit were ~10 µm, which were 3-3.5x as wide as in the imaged DMD masks. For the ~70 µm sized deposits in (e-g), minimum feature widths were ~15 µm and 1.5-1.7x those in the imaged intensity patterns. For the ~100 µm deposit in (h) and also in Fig. 4, minimum feature widths were ~20 µm and 1.3-1.5x wider than the intended minified features projected from the DMD. We attribute these discrepancies between the projected intensity pattern and the shape of the deposits in (e-h), in particular the fact that the deposits have curved (rather than square) corners in (b-d, f-h), to the difficulty in removing a section of the donor that had such sharp features, and hence the typically chamfered results on LIFTed deposits.

Although the results shown in Fig. 3 (a-d) corresponded to the use of a 30 nm gold DRL and (e-h) with a 50 nm carbon DRL, in general the particular characteristics of the DRL were not found to affect the quality of the deposit, but rather only the amount of fine debris present after the LIFT process, which generally resided on top of the deposit (visible in (a-d) but not in (e-h)). In order to test the adhesive qualities of the deposits and to demonstrate the applicability of this technique for additive manufacturing, the sample was left in a sonication bath filled with distilled water for 30 minutes, and out of a total of approximately 300 deposits, all of the deposited structures remained in place.
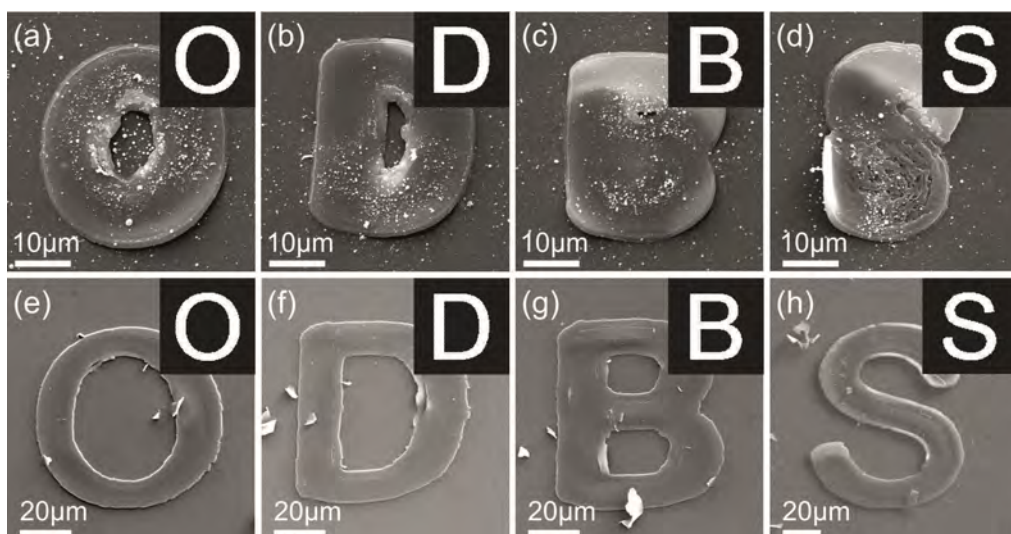
Fig. 3. SEM images of 1.3 µm thick polymer structures deposited via LIFT onto a PDMS-coated glass slide, with the inset images showing the projected spatial intensity patterns, for (a-d) a fluence of 300 mJ/cm2 using a 50x objective and a 30 nm Au DRL and (e-h) a fluence of 270 mJ/cm2 and a 20x objective with a 50 nm carbon DRL. Note the different scale bars on the figures.

Fig. 4 demonstrates the effect of a variation in pulse energy on the deposited polymer structures, over a 25% range in laser fluences, with values reducing from 300 mJ/cm^2 (left) to 235 mJ/cm^2 (right) in steps of ~17 mJ/cm^2, for a series of letters. The shapes appear to be deposited similarly across this range. Successful deposition of shaped polymer structures was also achieved outside this range. In general, fluences from 200 mJ/cm^2 to 380 mJ/cm^2 were found to yield high-fidelity deposits, for all letters, hence demonstrating robustness to energy fluctuations and reproducibility across an extremely wide variability of different shapes. As each deposit only requires a single laser pulse, large areas of sample coverage can be achieved by taking advantage of the high refresh rate of the DMD (hence allowing each laser pulse to be used to deposit a different shape) when using a high-repetition rate laser.
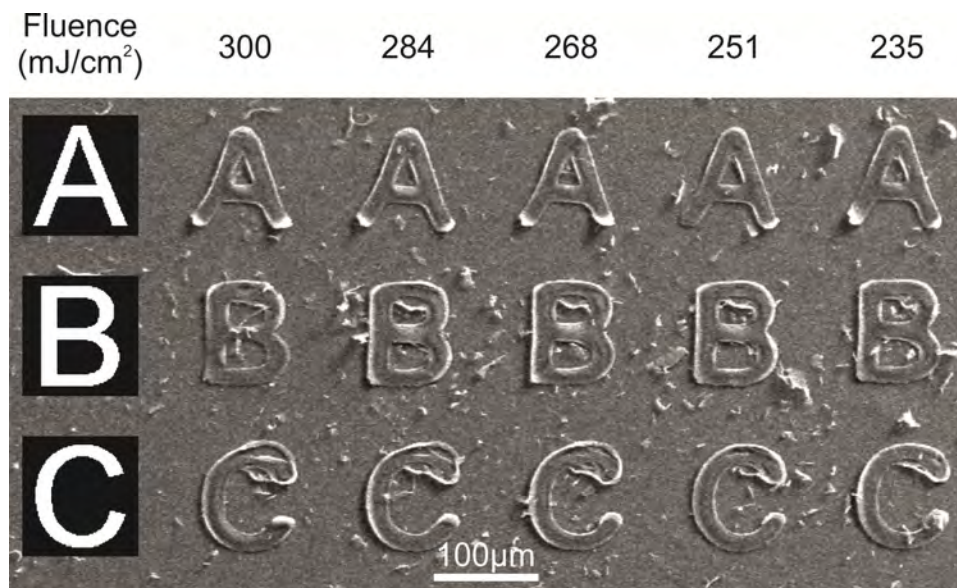
Fig. 4. SEM image of an array of different shaped polymer deposits using a 50 nm thick carbon DRL and 20x objective, for a range of laser fluences reducing from 300 mJ/cm^2 to 235 mJ/cm^2. The insets show the projected intensity profiles.

In order to show another facet of the applicability of a DMD as a variable illumination mask for LIFT, multiple unconnected structures were deposited simultaneously using a single pulse. This approach is demonstrated in Fig. 5, where SEM images show a two by two array of square deposits, for two different projected intensity patterns, namely (a) confined and (b) sparse, for the same conditions as in Fig. 4, save for the use of different fluences. In solid-phase LIFT of PMMA, additional donor material around the edge of the intended flyer can be ejected as the flyer shears free from the donor. In Fig. 5 (a), the minimal separation between squares is reflected in the lower quality of the deposited structure, where additional and unintended donor material was ejected from the donor, resulting in the square deposits being larger than the corresponding intensity profile on the donor.
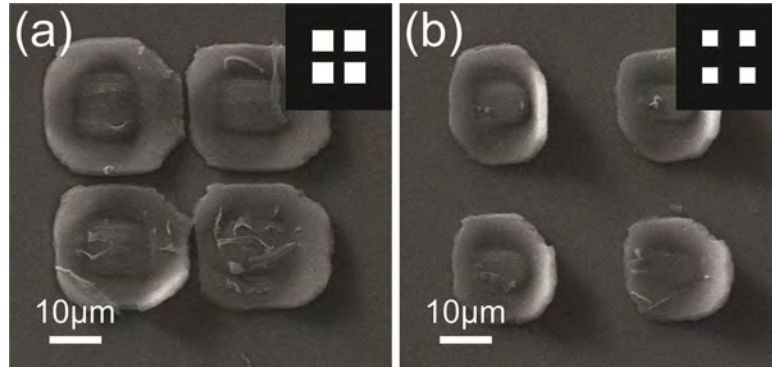

Fig. 5. SEM images of arrays of two by two squares that were deposited simultaneously via the LIFT technique, with squares of different sizes and separations displayed on the DMD. Donor, receiver, objective and DRL are as in Fig. 4. Produced at fluences (a) 250 mJ/cm^2 and (b) 270 mJ/cm^2. The inset shows the projected intensity pattern.

6. Conclusion

In conclusion, we have presented the use of a DMD, acting as a spatial light modulator, for laser-induced forward transfer of shaped 2D deposits from a solid thin polymer (PMMA) film, with lateral dimensions as small as ~30 µm by 30 µm, and minimum features of 10 µm. This first demonstration of DMD-assisted LIFT of solid, intact donors without the need for additional post-processing for the placement of structures with controllable shape and position with high repeatability and adhesion provides added versatility to the LIFT process.

Acknowledgements

applied optics

Rapid bespoke laser ablation of variable period grating structures using a digital micromirror device for multi-colored surface images

DANIEL J. HEATH,* BEN MILLS, MATTHIAS FEINAEUGLE, AND ROBERT W. EASON

Optoelectronics Research Centre, University of Southampton, Southampton, SO17 1BJ, UK
*Corresponding author: djh2v07@soton.ac.uk

A digital micromirror device has been used to project variable-period grating patterns at high values of demagnification for direct laser ablation on planar surfaces. Femtosecond laser pulses of ~1 mJ pulse energy at 800 nm wavelength from a Ti:sapphire laser were used to machine complex patterns with areas of up to ~1 cm^2 on thin films of bismuth telluride by dynamically modifying the grating period as the sample was translated beneath the imaged laser pulses. Individual ~30 by 30 μm gratings were stitched together to form contiguous structures, which had diffractive effects clearly visible to the naked eye. This technique may have applications in marking, coding, and security features. © 2015 Optical Society of America

1. INTRODUCTION

Laser-based manufacturing and direct laser-writing techniques offer unique benefits in terms of reduced fabrication and processing times when compared to techniques that require multiple steps such as photolithography or chemical etching. While mask-based processing is routinely used when identical and often intricate patterning is to be repeated many times, for example, in the semiconductor industry, if a variable or bespoke pattern is required on a shot-to-shot basis a different approach must be adopted. Serial processing using laser machining is a very straightforward method but does have some drawbacks in terms of the repetitive sample translation required, which must take account of absolute stage position, the time penalties associated with stage acceleration/deceleration, as well as mechanical problems such as backlash. Although optical rather than engineering solutions can be invoked to offset some of these constraints, such as the use of multiple foci [1] via the use of diffractive optical elements, the ability to process an entire image in a single laser pulse can achieve the best of both worlds. This way a given pattern can be produced at a predetermined position followed by sample translation before the next and different pattern is produced.

Femtosecond pulses have been used previously in the production of grating structures, commonly fiber Bragg gratings [2–4]. In these cases phase masks were used in combination with incident light to create a refractive index change in the target material. A more complete review of femtosecond-fiber

Bragg grating production can be found in [5]. Focused spot scanning of femtosecond pulses has also been used to write fiber Bragg gratings [6] as well as ablate grating structures at a scale visible to the naked eye [7]. Two-beam interference of femtosecond pulses has been shown to produce grating structures deep within materials [8] and with sub-wavelength periods [9]. In this paper we demonstrate the use of femtosecond laser machining using a digital micromirror device (DMD) that can display arbitrary binary patterns that are imprinted onto the incident laser pulse for machining of thin-film materials in a single laser pulse. We illustrate the versatility of this technique by machining multiple (many thousands) of individual diffraction gratings, each of which can have a unique period, for application in surface marking to produce a final colored image with a size of ~1 cm^2.

A. Image-Projection-Based Laser-Ablation

Image-projection-based machining, achieved through the shaping of a laser pulse via a spatial light modulator (SLM), can enable an entire pattern to be ablated in a single laser pulse rather than via the serial raster-scanning approach whereby a focused beam is moved along a predetermined path on the sample. SLMs, such as liquid crystal (LC) [10,11] or DMDs [12,13], allow modification of their transmission or reflective properties, and hence can enable the modification of the phase or intensity of a laser pulse. While LC SLMs can offer both intensity and phase control, DMDs typically only enable

control of the reflected intensity profile. However, DMDs can offer significantly higher switching speeds, where >30 kHz is available in some models compared to around 1 kHz for the fastest LC SLMs [12,14]. DMDs therefore have the potential to enable significantly faster machining if each laser pulse requires a different spatial profile. In this paper we show a significant improvement on previous work where the concept of high-resolution image-projection-based laser-machining via DMDs was initially demonstrated [15]. We offer a proof-of-principle approach for using a DMD for both rapid and precise machining of a planar surface.

2. EXPERIMENTAL SETUP

A 1 mJ, 150 fs pulse-duration, 1 kHz repetition-rate, 800 nm wavelength, Ti:sapphire amplifier was used (see Fig. 1 for details) in combination with a Texas Instruments DMD (DLP3000 [16]). The laser pulses were first spatially homogenized via a refractive beam homogenizer (π-shaper) in order to ensure that all mirrors on the DMD were illuminated with equal intensity. As discussed previously [15], the DMD used for this work consisted of 608 by 684, individually controllable, 7.6 μm width, aluminum mirrors. Each mirror could be independently positioned at an angle of either $+12°$ or $-12°$ relative to the DMD surface, and these specifications are given in Table 1. In this work we refer to these two angular positions as on or off, respectively. In our experimental setup, these two positions determined whether the specific mirror projected light toward the sample (on) or a beam dump (off). The laser-ablated pattern on the sample was therefore a demagnified version of the binary image displayed on the DMD.

In practice, a black/white image file, corresponding to the desired projected intensity profile, was sent via computer to the DMD, which reset all the DMD mirrors to their intended on/off positions. In all subsequent descriptions, for ease

Table 1.   DMD DLP3000 Specifications

Property	Specification
Micromirror array size	608×684
Micromirror dimensions	7.6 μm $\times$ 7.6 μm
Micromirror material	Aluminum
Micromirror tilt angle	$\pm12°$
Maximum refresh rate	4000 Hz
Micromirror crossover time	5 μs

of interpretation, white pixels on an image file correspond to mirrors in the on position while black pixels correspond to mirrors in the off position.

An important consequence of the periodicity of the DMD mirrors was that when using a spatially coherent incident beam, the DMD behaved as a two-dimensional (2D) grating and hence produced a 2D array of diffraction peaks. However, each diffraction order contained the spatial frequency information corresponding to the on/off state of all of the DMD mirrors, and hence only a single diffraction peak needed to be imaged on to the sample. The DMD mirror tilt of $\pm12°$ in the horizontal plane enabled its operation as a blazed grating. By choosing angles of incidence and reflection of $\sim24°$ and $\sim0°$, respectively, in the horizontal plane, diffraction into a single (the $m = 5$ horizontal, 0 vertical) order was maximized and contained >30% of the incident pulse energy.

The selected single diffraction order was imaged via a lens and a 50x objective onto the surface of the sample with a corresponding measured demagnification of 85 times. The sample was mounted on a three-axis translation stage (Thorlabs APT stepper motor) with each axis having a total travel of 50 mm.

3. EXPERIMENTAL RESULTS

We illustrate the procedure involved in the fabrication of variable period grating arrays via a simplified example in Fig. 2, which shows the machining of individual letters into a surface. In all results shown, the target sample was a 750 nm thick bismuth telluride film on a glass substrate. The energy density used to produce the sample in Fig. 2 was ~90 mJ/cm^2. The ablation threshold of the bismuth telluride film was found to be approximately 35 mJ/cm^2. Figure 2(a) shows a scanning electron microscope (SEM) image of a letter A, which was ablated using a single laser pulse. The inset shows the pattern that was present on the DMD. Figure 2(b) shows an SEM image of six different letters where each letter was also ablated using a single laser pulse with the DMD pattern updating and stage movement after each pulse. In this example however, the sample was actually moved continuously and the timing of the updating process on the DMD was linked to the activation of the Pockels cells in the laser amplifier, which resulted in the generation of a laser pulse. Although only six adjacent letters are shown in this case, this procedure can be repeated indefinitely to produce any desired final pattern by controlling the stage movement in 2D. See Fig. 2(c) for an example.

In this image the vertical direction corresponded to the axis undergoing continuous translation with the horizontal position being shifted by one step after each completed vertical line. As seen in Fig. 2(c) there are regions where the DMD pattern was
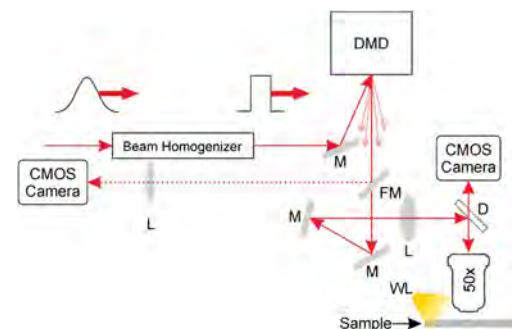
Fig. 1. Experimental schematic showing a 150 fs pulse homogenized to a top-hat spatial intensity, reflected from a mirror (M) onto the DMD. A single diffraction order (the $m = 5$ horizontal, 0 vertical) was reflected via two more mirrors and imaged via a lens (L) and a 50× objective onto the surface of the sample, via a dichroic mirror (D), which allowed real-time viewing of the sample via a CMOS camera under illumination by a white-light source (WL). Other diffraction orders from the DMD were not collected. A flip mirror (FM) was positioned after the DMD to reflect to a second CMOS camera to inspect the intensity profile.
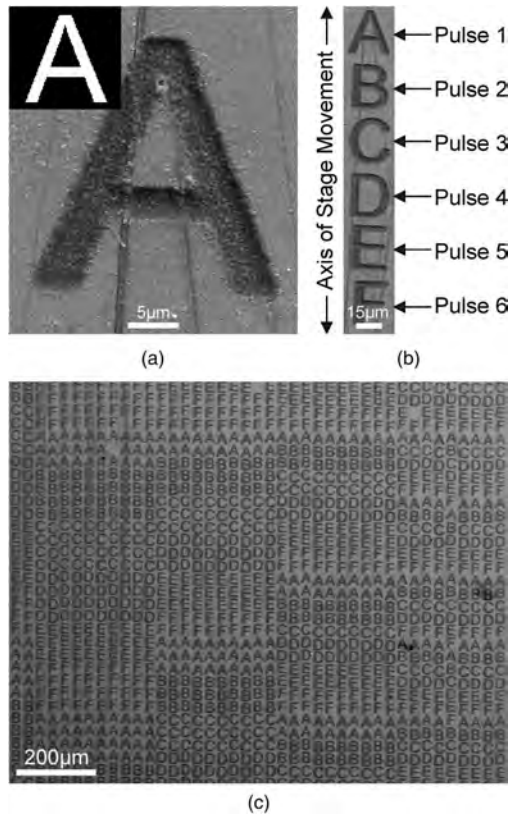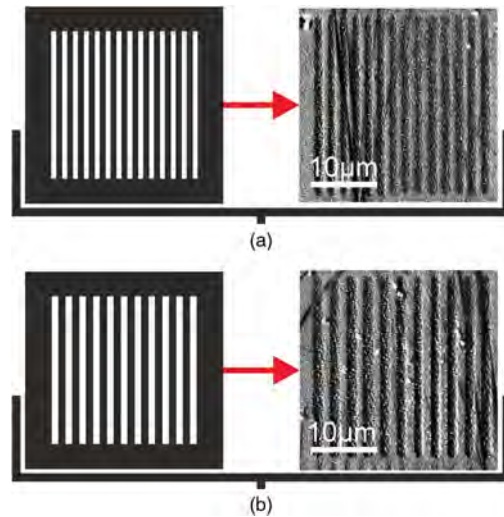
Fig. 2. Demonstration of the image-projection machining technique in 750 nm thick bismuth telluride at a fluence of 90 mJ/cm² showing (a) ablation of a single structure (with the DMD pattern inset). (b) Ablation of six distinct structures, machined using six sequential laser pulses and (c) 2D contiguous array of machined structures.


Fig. 3. Schematic showing the DMD pattern and an SEM image of the corresponding grating that was ablated in a single pulse in 750 nm thick bismuth telluride at a fluence of 90 mJ/cm² for grating periods of (a) 2.0 μm and (b) 2.5 μm.

not changed between pulses so that blocks of identical text could be machined at will within the 2D pattern. The automated process, which combined the laser pulse generation, stage movement, and DMD update process required an input *sample map*, which specified the structure that should be ablated at each position on the sample. In practice, the sample map was a 2D array of numbers where each number corresponded to a particular DMD pattern. For the case in Fig. 2(c), the sample map was a 2D array that consisted of the set of numbers (1–6), which corresponded to the projected patterns (A–F).

A. Fabrication of Grating Structures
To produce grating structures, the DMD patterns were specified as a set of parallel lines whose spacing and linewidth were both under computer control. Figure 3 shows the DMD patterns used together with corresponding SEM images of structures that were ablated in single pulses. Different grating periods corresponding to (a) 2.0 μm and (b) 2.5 μm are shown.

The ablated gratings in Fig. 3 produced from a single laser pulse were found to be of sufficient definition (spatial resolution and depth) to produce observable diffraction under white-light illumination, displaying a color that was a function of grating period, illumination, and viewing angle. Using the approach described in Fig. 2, where a sample map was used to specify the structure that should be ablated at each position on a sample, it was possible to ablate an array of gratings that when photographed, appeared as a 2D array of differently colored squares. Figure 4 shows an example of this approach where the sample map consisted of two different DMD patterns corresponding to two different grating periods. The upper pattern in Fig. 4(a) was used to display color corresponding to the letters DMD, and the lower pattern to generate the colored background. Figure 4(b) shows a photograph of the final diffractive structure of size 9 by 7 mm, which contains 70200 separate gratings written at a fluence 90 mJ/cm², with grating periods of 2.0 and 2.5 μm for the letters and background, respectively. Due to the close proximity of the camera to the sample when taking the photograph, the viewing angle dependence translates into a variation in diffracted color across the sample in the horizontal direction. Therefore, the three letters that formed the word DMD display a color gradient. At a longer distance of ∼50 cm, when viewed by eye, all three letters displayed the same diffracted color.
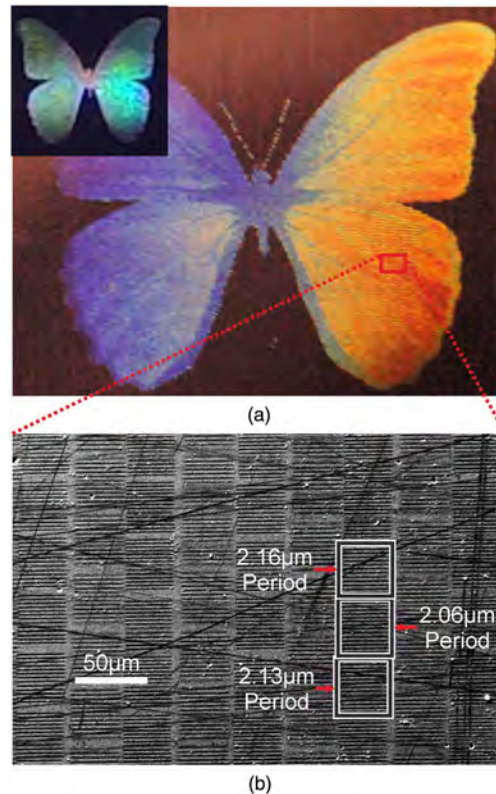
B. Fabrication of More Complex Grating Structures
The results in Section 3A showed the effect of using a sample map that contained just two grating periods. The next step was to extend this concept to multiple grating periods to fabricate a more complex sample. Figure 5 shows the effect of using 9 different DMD patterns, each with a different period, to form a
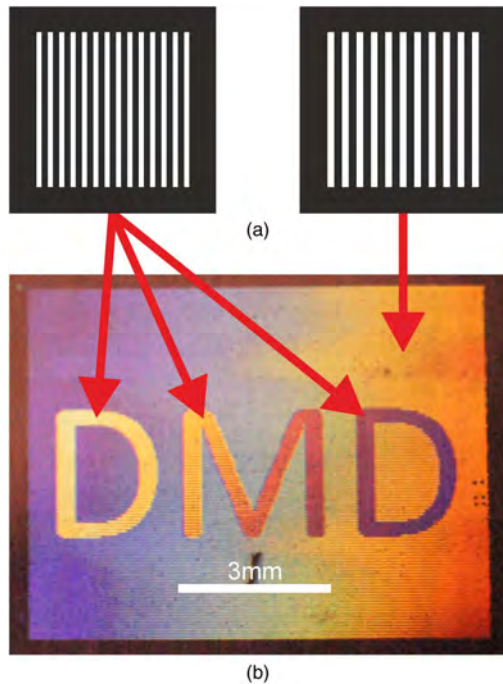
Fig. 4. Schematic showing (a) two different DMD patterns; (b) photograph of a 2D array of these structures ablated in 750 nm thick bismuth telluride with each structure ablated at a fluence of 90 mJ/cm^2. The letters and background correspond to grating periods 2.0 and 2.5 μm, respectively.

Fig. 5. (a) Photograph of light diffracted from a 2D array of grating structures with an inset showing a photograph of the structure from a greater distance, which displays more symmetric coloration. (b) SEM image of a section of the sample showing a variety of different grating periods. The sample substrate is 750 nm thick bismuth telluride, and each grating structure was produced at a fluence of 90 mJ/cm^2.

sample of size 9 by 7.5 mm [see Fig. 5(a)] comprising ~43,000 gratings. The sample map was defined to reproduce the appearance of the Morpho butterfly, whose wings display a striking blue color due to their grating-like structures, typically of period ~1 μm [17].

The colors produced in Fig. 5(a) varied from blue to red in the horizontal direction due to the position of the camera and direction of incoming ambient light. When observed by eye at a larger distance, the reduced incidence and output angles correspondingly resulted in a reduced spectral range at the eye, i.e., gratings of identical period from different regions of the sample appeared as the same hue when viewed from a large distance. This can be seen in the inset of Fig. 5(a). The variation in color along the vertical direction was caused by variations in the period of the gratings that were ablated in the sample, where the position and periods of the ablated gratings were chosen in order to replicate the appearance of the vein-like detail present on butterfly wings. While we have demonstrated here a butterfly profile, many other patterns such as a logo or an identification code could also be readily produced. Figure 5(b) shows an SEM image of a small section of the fabricated structure and demonstrates the variation in the period of several adjacent gratings (2.16, 2.06, and 2.13 μm). The maximum resolution of the detail on the butterfly wings corresponded

to the size of the individual gratings at ~30 μm. The region outside the butterfly profile was not ablated to increase the visibility of the fabricated sample.

4. DISCUSSION

Although the maximum repetition rate of the laser used was 1 kHz, it was operated at ~8 Hz for these trials, which were limited by the maximum stage speed and acceleration rate at our disposal. This should not be considered as an intrinsic manufacturing limitation. The sample shown in Fig. 4, which contained 70200 gratings, took a total time of 150 min for fabrication. With faster stages, at the maximum repetition rate of the laser of 1 kHz, the total fabrication time could be reduced to just over one minute. Although the work presented here used a 750 nm thick bismuth telluride-compound semiconductor film on a glass substrate, other materials, including metals, ceramics, and polymers, were also successfully laser-machined using this technique. Bismuth telluride's high

absorption at 800 nm wavelength [18], and hence efficient ablative machining with our laser source, led to its predominant use in this work.

The smallest grating period achieved (2.06 μm) was comparable to many results presented in [2–6], though larger than the smallest reported period of these of 1.07 μm [6]. The interferometric gratings produced in [9] achieve yet smaller results of 400 nm, though it should be noted that all of these results are produced by specialized grating-production methods. DMD image-projection-based laser-ablation, however, is suitable for the writing of more diverse patterns. This shows that image-projection laser-ablation using a DMD can yield results comparable in feature size to custom-built phase masks, while machining areas with non-identical patterns.

5. CONCLUSION

In conclusion, we have demonstrated an image-projection-based laser-machining technique for writing a large number of unique patterns into a range of materials using a DMD as an intensity spatial light modulator. Feature sizes on the order of 1 μm were produced and regions of tens of square millimeters were patterned with further dramatic improvements in speed possible with faster stage movements. We anticipate this flexible and versatile machining technique to find applications in a range of laser-based machining applications that could include bespoke or personalized security markings for high-value items.

REFERENCES

1. L. Kelemen, S. Valkai, and P. Ormos, "Parallel photopolymerisation with complex light patterns generated by diffractive optical elements," Opt. Express **15**, 14488–14497 (2007).
2. S. J. Mihailov, C. W. Smelser, P. Lu, R. B. Walker, D. Grobnic, H. Ding, G. Henderson, and J. Unruh, "Fiber Bragg gratings made with a phase mask and 800-nm femtosecond radiation," Opt. Lett. **28**, 995–997 (2003).
3. C. Smelser, S. Mihailov, and D. Grobnic, "Formation of type I-IR and type II-IR gratings with an ultrafast IR laser and a phase mask," Opt. Express **13**, 5377–5386 (2005).
4. J. Thomas, E. Wikszak, T. Clausnitzer, U. Fuchs, U. Zeitner, S. Nolte, and A. Tünnermann, "Inscription of fiber Bragg gratings with femtosecond pulses using a phase mask scanning technique," Appl. Phys. A **86**, 153–157 (2006).
5. G. Della Valle, R. Osellame, and P. Laporta, "Micromachining of photonic devices by femtosecond laser pulses," J. Opt. A **11**, 049801 (2009).
6. G. D. Marshall, M. Ams, and M. J. Withford, "Direct laser written waveguide-Bragg gratings in bulk fused silica," Opt. Lett. **31**, 2690–2692 (2006).
7. T.-L. Chang, S.-W. Luo, H.-P. Yang, and C.-H. Lee, "Fabrication of diffraction grating in polydimethylsiloxane using femtosecond-pulsed laser micromachining," Microelectron. Eng. **87**, 1344–1347 (2010).
8. Y. Li, W. Watanabe, K. Yamada, T. Shinagawa, K. Itoh, J. Nishii, and Y. Jiang, "Holographic fabrication of multiple layers of grating inside soda–lime glass with femtosecond laser pulses," Appl. Phys. Lett. **80**, 1508 (2002).
9. S. Sakabe, M. Hashida, S. Tokita, S. Namba, and K. Okamuro, "Mechanism for self-formation of periodic grating structures on a metal surface by a femtosecond laser pulse," Phys. Rev. B **79**, 033409 (2009).
10. Z. Kuang, D. Liu, W. Perrie, S. Edwardson, M. Sharp, E. Fearon, G. Dearden, and K. Watkins, "Fast parallel diffractive multi-beam femtosecond laser surface micro-structuring," Appl. Surf. Sci. **255**, 6582–6588 (2009).
11. R. J. Beck, J. P. Parry, W. N. MacPherson, A. Waddie, N. J. Weston, J. D. Shephard, and D. P. Hand, "Application of cooled spatial light modulator for high power nanosecond laser micromachining," Opt. Express **18**, 17059–17065 (2010).
12. Texas Instruments, "DLP & MEMS," http://www.ti.com/lsds/ti/analog/dlp/overview.page, accessed 1st May 2015.
13. C. Sun, N. Fang, D. M. Wu, and X. Zhang, "Projection microstereolithography using digital micro-mirror dynamic mask," Sens. Actuators A **121**, 113–120 (2005).
14. G. Thalhammer, R. W. Bowman, G. D. Love, M. J. Padgett, and M. Ritsch-Marte, "Speeding up liquid crystal SLMs using overdrive with phase change reduction," Opt. Express **21**, 1779–1797 (2013).
15. B. Mills, M. Feinaeugle, C. L. Sones, N. Rizvi, and R. W. Eason, "Sub-micron-scale femtosecond laser ablation using a digital micromirror device," J. Micromech. Microeng. **23**, 35005 (2013).
16. Texas Instruments, "DLP 3000," http://www.ti.com/product/dlp3000#parametrics, accessed 1st May 2015.
17. S. Kinoshita, S. Yoshioka, and K. Kawagoe, "Mechanisms of structural colour in the Morpho butterfly: cooperation of regularity and irregularity in an iridescent scale," Proc. Biol. Sci. **269**, 1417–1421 (2002).
18. M. Shaik and I. A. Motaleb, "Investigation of the optical properties of PLD-grown Bi_2Te_3 and Sb_2Te_3," in *Electro/Information Technology (EIT) Conference of IEEE*, Rapid City, South Dakota, 11 May 2013, pp. 1–6.

Laser ablation via programmable image projection for submicron dimension machining in diamond

B. Mills, D. J. Heath, M. Feinaeugle, J. A. Grant-Jacob, and R. W. Eason

---

Articles you may be interested in

Programmable fabrication of spatial structures in a gas jet by laser machining with a spatial light modulator
Phys. Plasmas **13**, 110701 (2006); 10.1063/1.2372795

Microstructuring using femtosecond pulsed laser ablation
J. Laser Appl. **18**, 227 (2006); 10.2351/1.2227020

Double-pulse machining as a technique for the enhancement of material removal rates in laser machining of metals
J. Appl. Phys. **98**, 033302 (2005); 10.1063/1.1996834

Photonic bandpass filter for 1550 nm fabricated by femtosecond direct laser ablation
Appl. Phys. Lett. **83**, 216 (2003); 10.1063/1.1592619

Microscopic mechanisms of ablation and micromachining of dielectrics by using femtosecond lasers
Appl. Phys. Lett. **82**, 4382 (2003); 10.1063/1.1583857

Laser ablation via programmable image projection for submicron dimension machining in diamond

B. Mills,[a] D. J. Heath, M. Feinaeugle, J. A. Grant-Jacob, and R. W. Eason
Optoelectronics Research Centre, University of Southampton, Southampton, SO17 1BJ, United Kingdom

A digital micromirror device is used as an intensity spatial light modulator, in conjunction with a femtosecond laser, for programmable image-projection-based laser ablation of polycrystalline diamond. Results show the machining of complex structures on the diamond surface, where individual structures have submicron features, covering a total area of 10×10 μm and fabricated using ten laser pulses. This dynamic image-based machining technique may offer speed advantages over serial-writing procedures, whilst still producing wavelength-scale feature sizes. © 2014 Laser Institute of America. [http://dx.doi.org/10.2351/1.4893749]

I. INTRODUCTION

The technological advances in the development of femtosecond lasers over the past few decades have established a wealth of applications in photonics, material science, and medicine. Of particular importance is the quality of ablation that can be produced when these ultrashort laser pulses are incident on a target material, as a very limited amount of damage will occur to regions adjacent to the irradiated area, as effects, such as shock waves and heat conduction, which are typically associated with nanosecond pulses, are no longer important, due to the shorter timescales involved.[1]

However, whilst femtosecond pulse machining can provide very high quality material-removal, typically machining is performed in a serial process, where a focussed laser spot is raster-scanned over the target material to produce the desired final structure. Understandably, therefore, there is a need to minimize the total machining time, while simultaneously maintaining the flexibility to machine patterns of arbitrary spatial extent. Several options are available, either through a greater degree of freedom via programmed movement of the beam or sample stage or by using an image-projection-based machining technique, where a complete pattern or image is machined via a single laser pulse, to achieve the desired structure. The difference between these two approaches can be envisaged by considering the process of machining a pattern, such as a capital letter E, by either sequentially ablating the horizontal and vertical lines that constitute the shape of the letter (serial or linear processing) or shaping the laser pulse spatially into a letter E, and performing the ablation via one single pulse (which we term image-projection-based ablation).

Galvanometer scanning,[2] in which the angular position of a small and light mirror is digitally controlled to reflect the laser focus to the desired point on the target, can often provide faster relative beam movement than can be achieved

by the equivalent, but much slower, translation of a more massive sample stage. However, the maximum area that can be machined with high precision may be relatively limited using galvanometer scanning, as the 2D surface, corresponding to the possible foci positions, is curved, and hence regions that lie far from the normal on-axis position on the sample will inevitably be out of focus, unless a spherically concave-shaped sample or additional focussing optics are used. Multiple foci,[3] such as those produced via propagation through a diffractive optical element, can be used to pattern multiple, but identical, regions simultaneously, and this technique can work well for a standard repetitive or periodic pattern. However, each machined structure will be identical, and hence this technique cannot be used for machining structures that either are aperiodic or are intended to be different for each of the multiple focussed spots. Other improvements on the direct write process include the projection of interference patterns on the surface and inside bulk samples for the fabrication of photonic crystal structures,[4] the use of multi-lens arrays for the ablation of periodic structures,[5] and the projection of intensity masks to aid the quality of the fabricated structures.[6] These serial processing approaches, whilst clearly being able to machine complex features when scanning the laser focus or sample stage, are generally considered to be slow compared to a parallel machining approach, where the entire complex pattern could be machined ideally in a single laser pulse without the need for any scanning or sample moving. For this reason, an alternative approach, namely, using a spatial light modulator (SLM), presents an excellent solution to the problem.

A. Spatial light modulator approach to ablation

SLM, which include liquid crystal[7] and digital micromirror devices (DMD),[8] enable image-projection-based machining, where, instead of performing laser machining using a single focussed spot, an entire pattern can be machined at once, hence offering the opportunity for dramatic

[a]Author to whom correspondence should be addressed; electronic mail: bm602@orc.soton.ac.uk. Telephone: (+44) 23 8059 6875

improvements in machining speed. In general, liquid crystal modulators can enable both intensity and phase control of the light, whilst DMD operation allows only a binary on/off intensity modulation. In this work, the DMD approach was chosen, as this offers several important advantages over the liquid-crystal approach, namely, a higher refresh rate (30 kHz is possible as of April 2014), lower cost (the basic DMD chip costs only a few hundred Dollars), and a relatively high damage threshold ($\sim$1 mJ/cm^2 being typical for fs pulse durations in our experience, for damage free operation at the 100 000 pulse level), and generally slightly higher than typical damage thresholds for liquid crystal SLMs of 100 μJ/cm^2 to 1 mJ/cm^2.[9] The ability of a liquid crystal SLM to control the phase of the beam[10] was not required in the work reported here, as the intensity pattern on the device was directly imaged onto the target sample, and therefore only intensity control was needed.

In the case of image-projection-based machining using a DMD, each square mirror, which is generally of size $\sim$10 $\times$ 10 μm, is either in the "on" or "off" position, corresponding to whether laser light will be imaged via reflection from that mirror onto the sample. Therefore, the DMD acts as a binary intensity SLM, rather than a "greyscale" intensity modulator, where each mirror therefore projects a square pattern of light towards a specific point on the sample (mirror in the "on" position) or to a beam dump (mirror in the "off" position).

Use of all the mirrors in a typical DMD device could therefore allow projection of an image that contains up to 1M individually addressable pixels; however, for our work, the magnification in the system meant that each mirror scaled geometrically to $\sim$60 nm, which was well below the diffraction limit (see Ref. 11 for a discussion on this topic), and so for this work, rather than using single lines of mirror in their "on" position, we used lines of greater than ten mirrors, corresponding to $\sim$600 nm on the target sample. The positional accuracy of each projected mirror on the sample was dependent on the fidelity of the scaled-down spacing of the mirrors on the DMD, rather than the accuracy of the stage movement, as would be the case for the serial-beam-writing process as described earlier.

Previously, we have applied this image-projection-based machining technique to the machining of highly absorbing, thin films.[11] We now present our results for machining of diamond, one of the most demanding materials for laser processing. In this work, the laser fluence on the DMD was approaching the damage threshold, and hence care must be exercised during ablation trials. The practice we adopted was to work just below the damage threshold for the DMD and to use multiple pulses (10 per image), to ensure good quality machined features as shown in Sec. III.

The underlying rationale for our diamond machining trials was threefold: first, diamonds represent perhaps the archetypal high-value item and are hence a prime candidate for security marking via a unique stamp or identification mark, on each and every diamond. Second, as diamond presents one of the greatest challenges in terms of the laser fluence required for marking, we would have confidence that many other materials of interest, such as alternative gemstones or

the ceramic casing of microprocessor chips, which would likely have lower ablation thresholds, would also be amenable to this processing technique. Finally, our intention was to mark the item with lettering that was as small as feasibly possible, to demonstrate that we could write security codes that were invisible to the naked eye and hence difficult to identify unless their position was known in advance.

B. Laser machining of diamond

Diamond plays a key technological role within many industries and across many applications, due to its high thermal conductivity and optical properties[12] and hence there is interest in high-throughput, high-resolution machining and marking techniques, of which laser-based machining is one of many approaches. Direct laser machining of diamond via laser ablation has been demonstrated before through using microsecond and nanosecond pulses, which highlighted the associated problems of the heat-affected zone,[13] and via femtosecond pulses, using a serial-scanning arrangement, which showed minimum line widths of 700 nm.[14] Femtosecond machining of micronsized structures with curved features and trenches has also been demonstrated through use of accelerating beams.[15]

Previous work has demonstrated the use of a liquid crystal SLM, for the reduction of focussing aberrations when machining inside bulk diamond, caused by the high refractive index mismatch at the interface of the bulk diamond and air,[16] while using a single focal spot, but the authors are not aware of any previous reports of image-projection-based laser-machining of diamond, where entire complex patterns are machined with no requirements for beam scanning or sample translation, other than to move to the next printed feature (for example, the next letter or number in the security code). Here, we show work using a DMD-based parallel laser machining approach to machine the surface of polycrystalline diamond samples, which required only ten pulses to see clearly noticeable features, with submicron sizes, corresponding to a total machining time of 10 ms per letter, as shown in Sec. III.

II. EXPERIMENT SETUP

In this work, a 1 mJ, 1 kHz repetition rate, 150 fs pulse, 800 nm wavelength ultrafast laser, was used, in conjunction with a DMD acting as an intensity spatial light modulator, for the machining of polycrystalline diamond. The DMD (Texas Instruments, DLP3000) consisted of an array of 608 $\times$ 684 square mirrors, each of dimension $\sim$7.6 μm and switchable via a computer interface, hence enabling a specific binary intensity pattern to be loaded onto the DMD on demand. A detailed discussion of this experimental setup has been described previously.[11] The input laser pulses were spatially homogenized, in order to illuminate the DMD with an acceptably flat intensity profile, and the schematic of the setup is shown in Fig. 1(a). The pulses were then collimated and demagnified onto the work-piece via a 100 $\times$ microscope objective. At the sample, the spatial laser intensity profile was therefore a scaled-down version of the intensity pattern on the DMD. The scaling factor of the DMD pattern to the
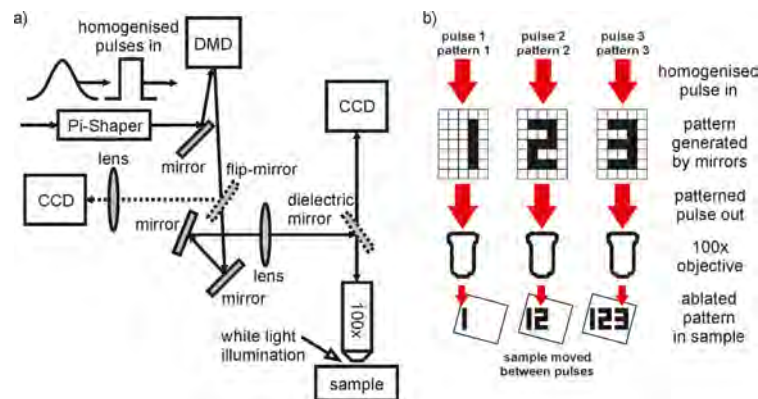
FIG. 1. Schematic of (a) experimental setup and (b) the ablation process, showing the step-and-repeat process used for ablating a longer structured pattern.

ablated pattern of the sample surface was measured to be ~127, corresponding to a combination of the 100× objective and a collecting lens positioned 5 cm before the objective. If the energy density on the sample was set above the damage threshold of the target material, a region on the sample identical to the shape of the DMD pattern was ablated. This approach has been used to machine individual letters, and other complex shapes, into the surface of the polycrystalline diamond. Figure 1(b) shows a schematic of the process required for machining a series of different patterns, in order to build up a contiguous structure. As the laser light illuminating the DMD was coherent, the array of mirrors on the DMD acted as a diffraction grating, causing multiple diffracted peaks to be produced in two orthogonal directions. For this work, only a single order was imaged, and hence the DMD was aligned to maximize the energy in a single chosen peak. This was achieved through taking advantage of the tilt angle of the mirrors ($\pm 12°$), in order to use the DMD as a blazed grating. For the 800 nm light used here, the combination of an incident angle of 57° and a diffracted angle of 33° (corresponding to the $m = +4$ order) gave 75% of the diffracted energy in this single peak and a total useable energy of 44% of the incident laser pulse. It is important to consider that the depth of field of the projected pattern (the distance until the projected pattern is out of the focus) may only be on the order of 10 μm. Therefore, whilst the surface of a material can be machined very accurately, this technique may not be appropriate for bulk machining. However, this disadvantage is countered by the ability to very rapidly pattern large areas on the surface of materials, with submicron resolution.
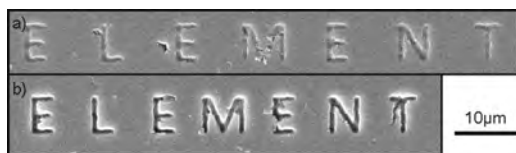

FIG. 2. SEM images of ablation in polycrystalline diamond, using (a) 10 pulses and (b) 50 pulses.

III. MACHINING RESULTS

Figure 2 shows scanning electron microscope (SEM) images of the polycrystalline diamond surface, where the word "ELEMENT" has been ablated, where each individual letter was fabricated via laser ablation in (a) 10 pulses and (b) 50 pulses, followed by a stage movement to the position of the subsequent letter. Therefore, the total number of pulses for the entire sample in (a) and (b) was 70 and 350, respectively. This word was chosen, due to its relatively long length and mixture of letters that have only square edges (later results in this manuscript show the effect of machining curved edges). Separate measurements, using an optical profilometer (Zescope), show an average depth of 69 nm and 106 nm for 10 and 50 pulses, respectively. The different letter separations (10 and 15 μm) are to highlight one aspect of the flexibility of the system, which allows images to be ablated with essentially any separation. For this work, an energy density of ~11.5 J/cm^2 was incident on the target sample, which corresponded to an energy density of ~1.6 mJ/cm^2 on the DMD surface. For each letter, a static image was displayed on the DMD for the duration of the multiple pulses. After each letter had been ablated, the sample stage was moved by the set amount, and the DMD image was changed to the next letter. The letters in Fig. 2(b) are darker in appearance, as more material was removed by the laser ablation process. In the case of diamond, which is transparent across much of the visible spectrum and has an absorption edge at 225 nm, damage via single photon absorption is not believed to have been the dominant process for material removal. Instead, we believe that multiphoton absorption, via either three photon (266 nm) or four photon (200 nm) absorption provided the means for ablation, which also explains the need for significantly higher laser fluence, as compared to most other materials. Using a 1 kHz repetition beam and automated sample movement stages to stitch individual ablated regions together, this laser machining approach could enable a laser-machined sample coverage of 1 × 1 mm in approximately 100 s.

Figure 3(a) shows a SEM image of the letter "E," ablated using ten pulses, corresponding to a total machining time of
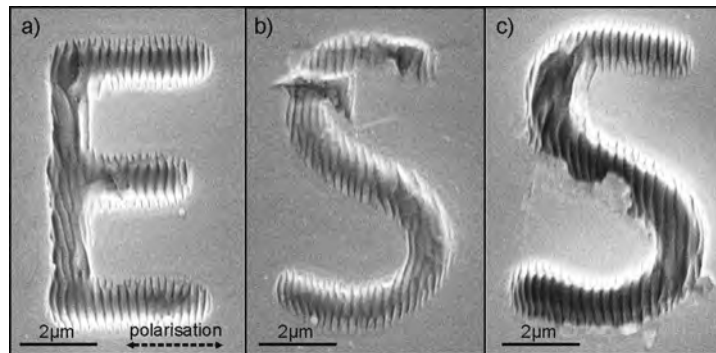
FIG. 3. SEM images of ablation in polycrystalline diamond, using (a) and (b) 10 pulses and (c) 50 pulses.

10 ms. Clearly observable are significant ripplelike structures on the surface, which were found to be perpendicular to the direction to the laser polarization. This effect is well known in the literature and is referred to as laser-induced periodic surface structures (LIPSS).[17] The average width of the letters, determined by measuring the distance across the structure at several positions, was found to be 900 nm. The ripple pattern itself can be made less prominent via use of circularly polarized light or avoided when single pulse ablation is used.[18] Figures 3(b) and 3(c) show ablation of the curved letter S, for both 10 and 50 pulses, showing that, whilst there is some degradation of edge-quality due to both LIPSS and imaging of a curved object from a rectangular array of pixels, overall the effect is not significant. The lack of "pixelation" in the projected patterns that make up the curved letters can be explained by taking into account first the fact that the projected features were always at least ten mirrors wide, and second, that the size of the projected light pattern from a single mirror was geometrically scaled to well below the diffraction limit and hence did not result in a square cross-sectional intensity profile on the target sample (as might be expected from projection from a single mirror) but rather a cross-sectional intensity profile resembling a Gaussian. The latter effect results in a similar outcome to rudimentary anti-aliasing effects used in 2D graphics, where a single pixel line that is required to be drawn at an angle is made smoother by introducing adjacent low intensity pixels. Figure 4 shows ablation of a bow-tie shape, for 50 and 500

pulses, highlighting that deeper trenches can be fabricated, when using higher number of pulses.

Although the results shown here correspond to a minimum of ten pulses, limited surface modification was observed when only a single pulse was incident onto the sample. This is consistent with the graphitization phenomenon,[19] whereby the first pulse incident onto the sample can cause a slight surface growth, produced by the phase change from diamond to graphite, and causes a damage accumulation mechanism where the ablation from subsequent pulses can be more significant. Here, we have operated above the damage threshold of diamond, described elsewhere to be in the range of 1.5–9.6 J/cm^2,[14,19,20] in order to increase the ablation removal rate.

A. Ablation in yttrium iron garnet (YIG)

In addition to image-projection-based laser ablation of diamond, we have explored the ablation properties of another crystal, also transparent at 800 nm, namely, a 500 nm thick YIG sample, grown via pulsed laser deposition, on an yttrium aluminum garnet (YAG) substrate.[21] Figure 5 shows SEM images of ablation of the YIG crystal, for (a) 1, (b) 10, and (c) 50 pulses, respectively, using a DMD pattern corresponding to an annular profile, with line-width of 700 nm and internal diameter of 5 μm, using an energy density on the sample of 3.1 J/cm^2. Results clearly show that even a single pulse ablation leads to noticeable material removal, and
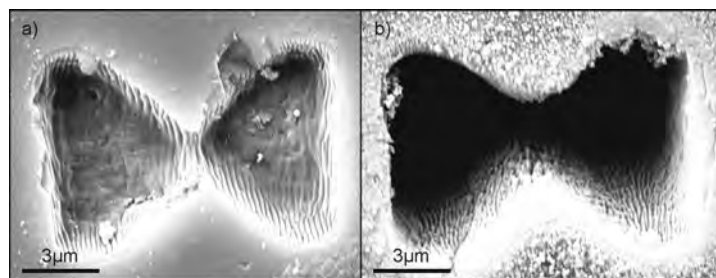

FIG. 4. SEM images of ablation in polycrystalline diamond, using (a) 50 pulses and (b) 500 pulses.
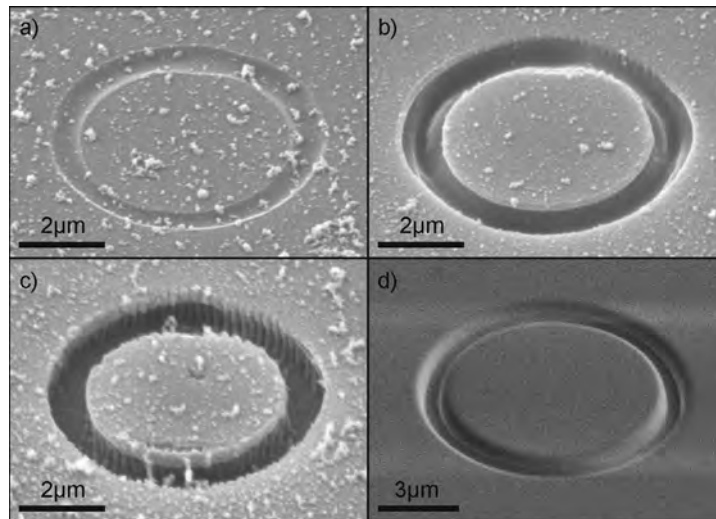
FIG. 5. SEM images of laser-ablation of YIG crystal on a YAG substrate, using (a) 1 pulse, (b) 10 pulses, (c) 50 pulses, and (d) machining of the same sample using focussed ion beam milling.

that the pattern is machined through the entire YIG film within ten pulses, implying a material removal rate of ~50 nm per pulse. As the YAG crystal had a higher damage threshold than the YIG crystal, subsequent pulses did not machine deeper into the sample, hence showing the strong contrast between the two layers in Fig. 5(c). For a comparison and shown in (d), this machining experiment was repeated using focussed ion beam (FEI Helios NanoLab DualBeam) and required 18 s for a comparable machining appearance, highlighting the many orders-of-magnitude time difference between these two machining approaches.

IV. CONCLUSIONS

In conclusion, we have demonstrated a rapid laser-based machining technique for writing patterns into transparent crystals, including polycrystalline diamond, via use of a digital micromirror device acting as an intensity spatial light modulator. Line widths of submicron size were observed. This technique may have applications in both direct machining of crystals or for the marking of identification tags onto diamond or gemstones such as emerald or ruby.

References

[1]E. G. Gamaly, A. V. Rode, B. Luther-Davies, and V. T. Tikhonchuk, "Ablation of solids by femtosecond lasers: Ablation mechanism and ablation thresholds for metals and dielectrics," Phys. Plasmas **9**, 949–957 (2002).

[2]H. Niino, Y. Kawaguchi, T. Sato, A. Narazaki, T. Gumpenberger, and R. Kurosaki, "Laser ablation of toluene liquid for surface micro-structuring of silica glass," Appl. Surf. Sci. **252**, 4387–4391 (2006).

[3]L. Kelemen, S. Valkai, and P. Ormos, "Parallel photopolymerisation with complex light patterns generated by diffractive optical elements," Opt. Express **15**, 14488–14497 (2007).

[4]S. Juodkazis, T. Kondo, H. Misawa, A. Rode, M. Samoc, and B. Luther-Davies, "Photo-structuring of As2S3 glass by femtosecond irradiation," Opt. Express **14**, 7751–7756 (2006).

[5]S. Matsuo, S. Juodkazis, and H. Misawa, "Femtosecond laser microfabrication of periodic structures using a microlens array," Appl. Phys. A **80**, 683–685 (2005).

[6]V. Mizeikisa, S. Juodkazis, J.-Y. Yeb, A. Rodea, S. Matsuob, and H. Misawab, "Silicon surface processing techniques for micro-systems fabrication," Thin Solid Films **438–439**, 445–451 (2003).

[7]Z. Kuang, D. Liu, W. Perrie, S. Edwardson, M. Sharp, E. Fearon, G. Dearden, and K. Watkins, "Fast parallel diffractive multi-beam femtosecond laser surface micro-structuring," Appl. Surf. Sci. **255**, 6582–6588 (2009).

[8]Texas Instruments, see http://www.ti.com/lsds/ti/analog/dlp/overview.page for Overview: DLP & MEMS.

[9]K. O'Keeffe, T. Robinson, and S. M. Hooker, "Generation and control of chirped, ultrafast pulse trains," IOP J. Opt. **12**, 015201 (2010).

[10]S. Hasegawa, Y. Hayasaki, and N. Nishida, "Holographic femtosecond laser processing with multiplexed phase Fresnel lenses," Opt. Lett. **31**, 1705–1707 (2006).

[11]B. Mills, M. Feinaeugle, N. Rizvi, and R. W. Eason, "Sub-micron-scale femtosecond laser ablation using a digital micromirror device," J. Micromech. Microeng. **23**, 035005 (2013).

[12]I. Aharonovich, A. D. Greentree, and S. Prawer, "Diamond photonics," Nat. Photonics **5**, 397–405 (2011).

[13]G. F. Zhang, B. Zhang, Z. H. Deng, and J. F. Chen, "An experimental study on laser cutting mechanisms of polycrystalline diamond compacts," CIRP Ann. **56**, 201–204 (2007).

[14]O. H. Y. Zalloum, M. Parrish, A. Terekhov, and W. Hofmeister, "On femtosecond micromachining of HPHT single-crystal diamond with direct laser writing using tight focusing," Opt. Express **18**, 13122–13135 (2010).

[15]A. Mathis, F. Courvoisier, L. Froehly, L. Furfaro, M. Jacquot, P. A. Lacourt, and J. M. Dudley, "Micromachining along a curve: Femtosecond laser micromachining of curved profiles in diamond and silicon using accelerating beams," Appl. Phys. Lett. **101**, 071110 (2012).

[16]R. D. Simmonds, P. S. Salter, A. Jesacher, and M. J. Booth, "Three dimensional laser microfabrication in diamond using a dual adaptive optics system," Opt. Express **19**, 24122–24128 (2011).

[17]Q. Wu, Y. Ma, R. Fang, Y. Liao, Q. Yu, X. Chen, and K. Wang, "Femtosecond laser-induced periodic surface structure on diamond film," Appl. Phys. Lett. **82**, 1703–1705 (2003).

[18]R. Buividasa, M. Mikutis, and S. Juodkazisa, "Surface and bulk structuring of materials by ripples with long and short laser pulses: Recent advances," Prog. Quantum Electron. **38**, 119–156 (2014).

[19]G. Dumitru, V. Romano, H. P. Weber, M. Sentis, and W. Marine, "Femtosecond ablation of ultrahard materials," Appl. Phys. A **74**, 729–739 (2002).

[20]D. Ramanathan and P. A. Molian, "Micro- and sub-micromachining of type IIa single crystal diamond using a Ti: Sapphire femtosecond laser," J. Manuf. Sci. Eng. **124**, 389–396 (2002).

[21]A. Sposito, S. A. Gregory, P. A. J. de Groot, and R. W. Eason, "Combinatorial pulsed laser deposition of doped YIG films on YAG," J. Appl. Phys. **115**, 053102 (2014).

Laser-induced backward transfer of nanoimprinted polymer elements

Matthias Feinaeugle[1] · Daniel J. Heath[1] · Benjamin Mills[1] · James A. Grant-Jacob[1] ·
Goran Z. Mashanovich[1] · Robert W. Eason[1]

Abstract Femtosecond laser-induced backward transfer of transparent photopolymers is demonstrated in the solid state, assisted by a digital micromirror spatial light modulator for producing shaped deposits. Through use of an absorbing silicon carrier substrate, we have been able to successfully transfer solid-phase material, with lateral dimensions as small as ~ 6 μm. In addition, a carrier of silicon incorporating a photonic waveguide relief structure enables the transfer of imprinted deposits that have been accomplished with surface features exactly complementing those present on the substrate, with an observed minimum feature size of 140 nm.

1 Introduction

Laser-induced transfer, which relies on the energy of an incident laser pulse to transfer a deposit (or variously termed *voxel*) of material (the *donor*) from a carrier substrate towards a receiver substrate, encompasses a range of techniques for rapid microfabrication of electronic, photonic and biomedical devices [1–5]. Recent results have shown the lateral shaping of deposits in a dynamic fashion for laser-induced forward transfer (LIFT), via the use of a digital micromirror device (DMD) acting as a spatial light modulator [6, 7], hence enabling the rapid prototyping of complex shapes with micron-scale fabrication resolution. This approach provides a more flexible alternative to

focussing or imaging of an aperture [8, 9] and complements alternative beam-shaping approaches previously used for LIFT, which assist in the pre-machining of the donor for transfer of structures with small dimensions [10], smooth side walls [11] or reduced amount of debris [12].

While the ability to shape the deposit in the lateral direction is undoubtedly useful, many applications in electronics and photonics can often require feature sizes down to the nanometre range, far below the optical diffraction limit, and hence cannot be directly achieved via beam shaping. Transfer of nanodroplets can be achieved with the donor in a molten or liquid state [13], although this limits one of the main benefits of laser-induced transfer, namely the possibility of maintaining a previously optimized phase and structure of a thin film.

In this work, we present the results from a different approach whereby the intact transfer of solid deposits has been achieved via laser-induced backward transfer (LIBT), where the deposits produced can have feature sizes well below the diffraction limit. This was achieved via use of a silicon carrier substrate that incorporated a prefabricated photonic waveguide relief structure, so that the donor material was imprinted with the complementary waveguide relief features before the LIBT process. This imprint transfer is a process allowing the fabrication of nanostructures which has not been demonstrated on such a small deposit scale with a direct-write laser technique [14], and such pre-structuring of a voxel prior to transfer could increase the complexity and hence functionality of the printed device. The transfer of solid-phase donors is integral to this technique, as transfer of donors via partial or complete melt or liquid phase does not allow the preservation of the intended surface structure.

In this study, the overall shape (but not the sub-diffraction-limited structures) of the deposited material was

✉ Matthias Feinaeugle
  Matthias.Feinaeugle@soton.ac.uk

1 Optoelectronics Research Centre, University of
   Southampton, Highfield Campus, Southampton SO17 1BJ,
   UK

controlled via DMD-based image projection. Conventional lithography or direct exposure of the photoresist on the receiver would not allow such partial structuring of a voxel surface and would not work with photoinsensitive polymer materials. Compared with laser photopolymerization direct-write techniques, the receiving substrate is not exposed to undeveloped liquid resist or chemicals required during development or washing steps. Also, a DMD allows the pixelated transfer of voxels in a single process step and combines other advantages of laser-induced transfer such as high speed, non-contact, the possibility to use non-planar receiver substrates and the lack of required post-processing steps. Using this combination of techniques, we have been able to obtain overall minimum lateral dimensions of a few microns and carrier-imprinted surface feature dimensions of ~ 140 nm. In this paper, we discuss LIBT in comparison with LIFT and present experimental results for LIBT using unstructured and structured carrier substrates.

2 Background

In the LIBT process, the propagation direction of the deposit is typically at an angle of 180° with respect to the direction of the incident laser pulse (hence the term 'backward'). As shown in Fig. 1a, a small volume from the donor is transferred to the receiving substrate, via absorption of a laser pulse that has been directed through the transparent receiver and donor before being absorbed at the interface of the donor and absorbing carrier. In the literature, LIBT has been used for the deposition of Bi_2O_3 [15], for fabricating diffractive structures [16], for plasmonic nanospheres [13] and for liquids aimed at biomedical applications [17], but has been less widely adopted so far than LIFT-based processes and mainly with the donor in a molten or liquid state.

While the release mechanism responsible for LIBT is not the main focus of this work, contributing processes are suspected to be either thermal [18], shock induced via spallation [19], through the vaporization of carrier or donor

volumes to enable a vapour-driven release of the deposit [20], or via ultrafast expansion if using femtosecond laser pulses [21]. Although we have not yet looked at LIBT with other laser sources (e.g. nanosecond pulse duration), we believe the localization of the laser-induced effects in both space and time that are caused by femtosecond pulse exposure plays an important role in the LIBT mechanism. However, of immediate interest is to briefly compare the two transfer techniques as there is likely an important difference in the absorption profile of the laser energy within the carrier (for LIBT) and at the carrier–donor interface (for LIFT).

In LIBT, reported here, the receiver and donor must be transparent to the incident laser light, which is absorbed in the interfacial volume of the carrier. This requirement would suggest that fabrication of, e.g., photonic or microfluidic devices would be an appropriate end goal for such LIBT-based transfer, due to the possibility to work with flexible and thin polymer donors and receivers. For LIFT of non-absorbing donors, required for a fair comparison of the two techniques, a dynamic release layer (DRL) which is sandwiched between the donor and the carrier needs to be present to absorb the incident laser pulse and initiate the transfer of the donor. In the case of solid-phase LIBT, the majority of the laser energy is absorbed in the first $\sim$ few 10 s of nm of the carrier and not within the non-absorbing donor. There is therefore a very strong thermal gradient originating at the carrier–donor interface, and this interfacial region of the carrier experiences the largest change in its physical properties which is likely responsible for the subsequent detachment and backward propagation of the donor deposit.

In the case of LIFT, the majority of the laser energy is absorbed within the skin depth of a DRL. In contrast to LIBT, therefore, in LIFT the region of maximum laser-induced change in physical properties occurs on the rear side of the DRL and not on the side facing the donor, and thus, release of the deposit is possibly governed by different physical mechanisms. There is also the additional contamination problem for forward transfer that some DRL material may remain on the released donor deposit or receiver after transfer as a thin film DRL is released or even dissociated easier from the carrier than during LIBT where a bulk carrier substrate is present. This important difference between LIBT and LIFT, we suggest, represents an important factor in the nature of the deposition process which could lead to higher-quality deposition when using LIBT.

In addition, as presented for the first time here, the LIBT technique enables imprinting of the donor via use of a pre-structured carrier substrate as shown in Fig. 1b. We do not believe, and to date have not seen within the literature, that this imprinting approach is as practical with LIFT, due to
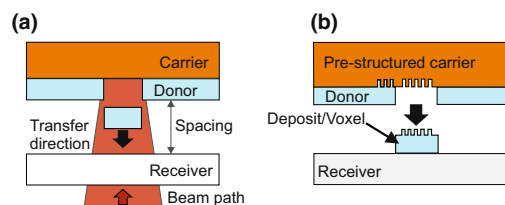
Fig. 1 Schematic of laser-induced backward transfer with **a** unstructured carrier during LIBT and **b** structured carrier after transfer

the difficulties to fabricate a compliant absorbing layer with constant thickness. Compared with LIFT, LIBT also has the benefit that the absorbing layer can be a bulk substrate, of arbitrary thickness and physical properties, provided it possesses the requisite characteristics to support high absorption of the laser pulse and transfer of the donor.

3 Experimental

Experiments used a Ti:sapphire laser oscillator and amplifier chain with a central wavelength of 800 nm and a pulse duration of $\sim$150 fs (Coherent, Legend) as shown in Fig. 2. The spatial intensity profile of the laser output was homogenized via a refractive top-hat beam shaper (Adloptica, Pi-Shaper) to uniformly illuminate the surface of the DMD array. An object mask displayed on the DMD was then imaged with the combination of a collimating tube lens and an infinity-corrected 20$\times$ or 50$\times$ microscope objective at the sample interface, which was translated on a computer-controlled mechanical stage. Pulse energies were adjusted to investigate the threshold for optimum LIBT, while the sample and image position were monitored with a CMOS camera, a white light source and a dichroic mirror. Further details of this setup can be found in a previous study [7].
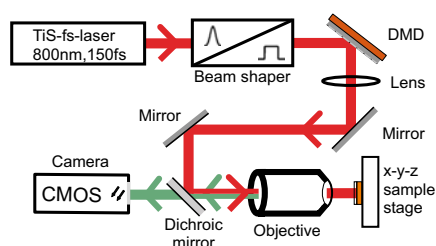
Donors were fabricated via spin coating of S1813 and SU-8 photoresists onto cleaned carrier substrates, and baked on a hotplate at 110 °C for 5 min. The donors were chosen to be materials conventionally used in lithography and served as ideal testbeds for observing achievable resolution via backward transfer. The carrier substrates were polished monocrystalline silicon wafers and silicon-on-insulator chips. The latter consisted of grating structures and slot/rib waveguides and had a layer structure from top to bottom consisting of $\sim$400-nm silicon, 2-μm silicon dioxide and $\sim$600-μm silicon. These structures were fabricated by e-beam lithography using ZEP e-beam resist for pattern definition and by subsequent transfer to the silicon

layer using inductively coupled plasma etching. The termination after the etching was native oxide. Receivers tried were bare 1-mm-thick microscope slides, microscope slides coated with $\sim$10-μm-thick polydimethylsiloxane (PDMS) or free-standing PDMS films, which were chosen as examples for hard, soft and mechanically flexible receivers. The free-standing films were obtained by peeling off the PDMS film from a glass slide.

4 Results and discussion

4.1 LIBT using an unstructured carrier

Donors (1.4, 1.5, 1.85 and 2.25 μm thick) and receivers were in close contact during the experiments, and typical lateral voxel dimensions were in the range of 20–50 μm. No spacer was used for establishing a defined donor–receiver distance. Due to material inhomogeneities, this spacing was estimated to be in the range of 0–5 μm, observed from white light thin film interference off the surfaces of donor and receiver. For a fluence just below threshold for transfer, bulging of the donor by some tens of nanometres was observed. The threshold fluence for S1813 for donor thicknesses of 1.4, 1.85 and 2.25 μm was measured to be $\sim$475, $\sim$580 and $\sim$765 mJ/cm^2, respectively. As expected, an increased donor thickness required a higher pulse fluence to achieve transfer, and complex shapes with a large ratio of sidewall area to donor–carrier interface (such as the numbers and letters shown in Fig. 3) also required a higher transfer fluence than simple shapes

Fig. 3 SEM images of DMD-shaped, $\sim$1.4-μm-thick S1813 printed via LIBT at a fluence of $\sim$475 mJ/cm^2 (**a**) and $\sim$510 mJ/cm^2 (**b**–**d**) onto PDMS-coated glass. The *scale bar* is 10 μm

Fig. 2 Setup used for our experiments. DMD, laser source and mechanical sample stage are controlled via computer (not shown)

such as circles or squares. We note that transfer threshold values were below the damage thresholds of the donors of ~ 1 J/cm^2 for both SU-8 and S1813.

The results shown in Fig. 3 demonstrate a few examples of the complexity of shapes that can be printed using LIBT via DMD-based image projection. The deposits (1.4-μm-thick S1813) in Fig. 3 had been printed at fluences of ~ 475 mJ/cm^2 (Fig. 3a) and ~ 510 mJ/cm^2 (Fig. 3b–d), respectively, onto a PDMS-coated glass receiver from an unstructured silicon carrier. For 1.5-μm-thick donors of SU-8, this transfer threshold of simple shapes was ~ 370 mJ/cm^2. We also successfully demonstrated transfer onto free-standing 10-μm-thick PDMS, which, as it is a flexible substrate, offers the promise of using LIBT to fabricate thin devices and electronic structures on non-planar surfaces such as optical fibres. The smallest feature size appeared to be limited by the creation of a tapered, angled border, seen quite clearly in Fig. 3d, for example, with a width of ~ 1 up to ~ 3 μm. Depending on the application, such a feature might limit the resolution or require the use of further donor preparation prior to transfer [11, 12].

The smallest features printed from these donors onto PDMS-coated glass were about 5.6-μm-wide rectangular structures. Successful transfer of simple shapes, such as squares and circles, was also demonstrated for uncoated glass receivers. However, more complex shapes were not transferred successfully due to the voxels breaking up as a consequence of using a glass receiver. Generally, transfer at a fluence just above threshold was accompanied with minimal debris further limiting the need for post-processing, e.g. the curing of laser-induced interface damage.

Most deposits (>90 %) on a PDMS-coated glass receiver remained adhered after submersion in an ultrasonic water bath for 30 min followed by a nitrogen blow dry, but could be removed completely via manual application of an adhesive tape. On uncoated glass, around 70 % of deposits remained intact after the described ultrasonic bath and nitrogen process.

4.2 LIBT using a structured carrier

Here, we demonstrate the use of a pre-structured carrier to achieve transfer of complementary features in the donor deposit. The carrier used was a silicon-on-insulator chip containing photonic structures originally used for mid-infrared wavelengths [22], while here they simply served as substrate with precisely defined surface features on the micro- and nanoscale and fabricated with a well-established lithographic technique. The chip layer structure consisted of a sequence of silicon and 2-μm-thick buried oxide layers where the chip surface facing the donor film was capped by a layer of 400-nm-thick silicon. Surface
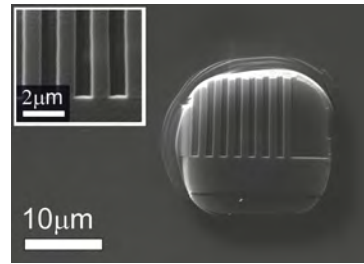
Fig. 4 SEM images of SU-8 LIBT-printed voxel with imprinted grating/waveguide structure on PDMS-coated glass receiver at a fluence of ~ 475 mJ/cm^2. The *inset* shows a magnified version of the grating surface with 50/50 mark to space ratio. The resulting finger width and height were ~ 900 and ~ 220 nm, respectively
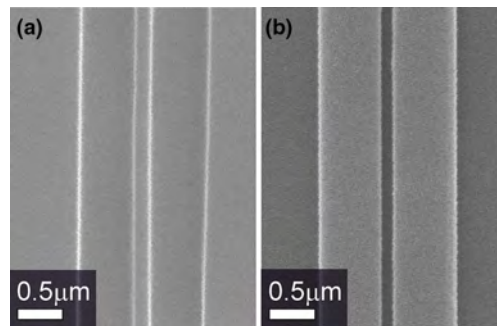
Fig. 5 SEM images of **a** deposit surface from an S1813 donor printed at ~ 475 mJ/cm^2 showing a rib within a trench structure and **b** a similar slot waveguide structure on a carrier used for the imprinting. The transferred smallest feature on the voxel in the centre of image (**a**) was ~ 140 nm wide and ~ 220 nm high

structures had been chemically etched into the top silicon layer prior to LIBT, forming waveguiding and grating relief structures with depths of ~ 220 nm. During spin coating, the photoresist donor conformed to the carrier in order to create a compliant donor–carrier interface, replicating these relief features with high fidelity, and at the same time forming a smooth and flat layer at the donor–air interface. Results for transfer of an imprint of a grating structure are shown in the SEM image in Fig. 4 for a voxel transferred at a fluence of ~ 475 mJ/cm^2.

The surface of the deposits on PDMS-coated glass did not show any signs of debris or damage from decomposed donor material, and the grating features are well resolved and have a period of 1.8 μm (with 50/50 mark to space ratio).

Results in Fig. 5a show an SEM image of a deposition of an imprinted slot waveguide structure at a surface of a

circular voxel, transferred at a fluence of $\sim$475 mJ/cm^2, where an SEM image of a similar waveguide structure on the carrier is shown in Fig. 5b. In the deposit, a slot was reproduced as a rib with a width of $\sim$140 nm for a height of $\sim$220 nm and centred in a trench of $\sim$1.4 µm width.

5 Conclusion

In conclusion, we have demonstrated the LIBT of solid photopolymers in an intact state using silicon substrates as absorbing carriers. Spatial voxel shaping was accomplished using a DMD-based image projection system resulting in lateral feature sizes as small as $\sim$6 µm for the materials studied. At fluences just above the transfer threshold, the volume of debris and damage to the donor was minimal with reduced edge quality as the interface area was not perfectly sheared from the donor. The limited damage occurring at the interface of carrier and donor and the possibility to use a structured carrier enabled the LIBT technique to be used to reproduce an interfacial carrier relief structure imprinted into the donor layer. This technique therefore enables the simultaneous patterning of the lateral extent and the surface structure of a deposit, with a smallest surface feature size of $\sim$140 nm enabling applications for electronic or photonic devices.

References

1. R.S. Braudy, Proc. IEEE **57**, 1771 (1969)
2. M.L. Levene, R.D. Scott, B.W. Siryj, Appl. Opt. **9**, 2260 (1970)
3. J. Bohandy, B.F. Kim, F.J. Adrian, J. Appl. Phys. **60**, 1538 (1986)
4. C.B. Arnold, P. Serra, A. Piqué, MRS Bull. **32**, 23 (2007)
5. M. Zenou, A. Sa'ar, Z. Kotler, Sci. Rep. **5**, 17265 (2015)
6. R.C.Y. Auyeung, H. Kim, N.A. Charipar, A.J. Birnbaum, S.A. Mathews, A. Piqué, Appl. Phys. A **102**, 21 (2011)
7. D.J. Heath, M. Feinaeugle, J.A. Grant-Jacob, B. Mills, R.W. Eason, Opt. Mater. Express **5**, 1129 (2015)
8. L. Rapp, C. Constantinescu, Y. Larmande, A.P. Alloncle, P. Delaporte, Appl. Phys. A **117**, 333 (2014)
9. M. Feinaeugle, P. Horak, C.L. Sones, T. Lippert, R.W. Eason, Appl. Phys. A **116**, 1939 (2014)
10. V. Sametoglu, V. Sauer, Y.Y. Tsui, Appl. Phys. A **110**, 823 (2012)
11. K.S. Kaur, M. Feinaeugle, D.P. Banks, J.Y. Ou, F. Di Pietrantonio, E. Verona, C.L. Sones, R.W. Eason, Appl. Surf. Sci. **257**, 6650 (2011)
12. R. Pohl, M. Jansink, G.R.B.E. Römer, A.J. Huis in 't Veld, Appl. Phys. A **120**, 427 (2015)
13. A.I. Kuznetsov, A.B. Evlyukhin, C. Reinhardt, A. Seidel, R. Kiyan, W. Cheng, A. Ovsianikov, B.N. Chichkov, J. Opt. Soc. Am. B **26**, B130 (2009)
14. S.Y. Chou, P.R. Krauss, P.J. Renstrom, Appl. Phys. Lett. **67**, 3114 (1995)
15. H. Sakata, S. Chakraborty, M. Wakaki, Microelectron. Eng. **96**, 56 (2012)
16. P. Papakonstantinou, N.A. Vainos, C. Fotakis, Appl. Surf. Sci. **151**, 159 (1999)
17. A. Patrascioiu, M. Duocastella, J.M. Fernández-Pradas, J.L. Morenza, P. Serra, Appl. Surf. Sci. **257**, 5190 (2011)
18. Y.P. Meshcheryakov, M.V. Shugaev, T. Mattle, T. Lippert, N.M. Bulgakova, Appl. Phys. A **113**, 521 (2013)
19. S.G. Koulikov, D.D. Dlott, J. Photochem. Photobiol. A. Chem. **145**, 183 (2001)
20. N.T. Kattamis, M.S. Brown, C.B. Arnold, J. Mater. Res. **26**, 2438 (2011)
21. J. Sotrop, A. Kersch, M. Domke, G. Heise, H.P. Huber, Appl. Phys. A **113**, 397 (2013)
22. M. Nedeljkovic, A.Z. Khokhar, Y. Hu, X. Chen, J.S. Penades, S. Stankovic, H.M.H. Chong, D.J. Thomson, F.Y. Gardes, G.T. Reed, G.Z. Mashanovich, Opt. Mater. Express **3**, 1205 (2013)

Full Length Article

Time-resolved imaging of flyer dynamics for femtosecond laser-induced backward transfer of solid polymer thin films

M. Feinaeugle [a],[*], P. Gregorčič [b], D.J. Heath [a], B. Mills [a], R.W. Eason [a]

[a] Optoelectronics Research Centre, University of Southampton, Southampton, SO17 1BJ, UK
[b] Faculty of Mechanical Engineering, University of Ljubljana, Aškerčeva 6, 1000, Ljubljana, Slovenia

ARTICLE INFO

ABSTRACT

We have studied the transfer regimes and dynamics of polymer flyers from laser-induced backward transfer (LIBT) via time-resolved shadowgraphy. Imaging of the flyer ejection phase of LIBT of 3.8 μm and 6.4 μm thick SU-8 polymer films on germanium and silicon carrier substrates was performed over a time delay range of 1.4–16.4 μs after arrival of the laser pulse. The experiments were carried out with 150 fs, 800 nm pulses spatially shaped using a digital micromirror device, and laser fluences of up to 3.5 J/cm^2 while images were recorded via a CCD camera and a spark discharge lamp. Velocities of flyers found in the range of 6–20 m/s, and the intact and fragmented ejection regimes, were a function of donor thickness, carrier and laser fluence. The crater profile of the donor after transfer and the resulting flyer profile indicated different flyer ejection modes for Si carriers and high fluences. The results contribute to better understanding of the LIBT process, and help to determine experimental parameters for successful LIBT of intact deposits.

© 2016 The Authors. Published by Elsevier B.V. This is an open access article under the CC BY license (http://creativecommons.org/licenses/by/4.0/).

1. Introduction

Additive methods for the microfabrication of devices have recently gained interest over conventional techniques due to their versatility, simplicity and resulting high speed of fabrication [1–3]. Among these, laser-based techniques are a promising way to enable device printing in a contactless fashion with demonstrated micronscale resolution. A unique advantage is that these methods allow the deposition of materials that not only have a specific structural role, but also have electronic, photonic or even biomedical functionality.

In particular, laser-induced forward transfer (LIFT) has proven its capability to allow manufacturing of a wide range of materials, such as metals [4], ceramics, semiconductors, superconductors [5], 2D materials and structures for e.g. MEMS [6], waveguides [7], biomedical sensors [8] or thermoelectric generators [9]. More recently, the transfer of silver pastes [10,11], 3-dimensional microobjects [12,13] and metal vias [14] has shown the potential of LIFT for microfabrication. During LIFT (e.g. with a transparent donor), shown schematically in Fig. 1a, a pulsed laser beam is focussed or imaged at the interface between a transparent carrier substrate and a sandwich of thin films, consisting of an absorbing material and the donor. As a consequence of the absorbed laser energy, a small volume of the donor is ejected and transferred onto a receiver substrate which is located parallel to the donor surface. In some cases, the donor itself acts as an absorber and no additional interfacial layer is required. The spacing between the donor and receiver is typically in the few to tens of micrometres range.

The minimum feature sizes of structures fabricated via LIFT is mainly limited to optical resolutions for congruent transfer of devices [15,16]. However, for molten transfer, structures that are smaller than the diffraction-limited size of the incident laser pulse have been demonstrated [17,18]. Specifically for the fabrication of those structures, laser-induced backward transfer (LIBT) [19] has produced submicron-structures with high repeatability which may prove to be an advantageous alternative to LIFT for specific applications [20,21]. During LIBT, shown schematically in Fig. 1b, the receiver whose absorption is low in comparison with the carrier is situated in the path of the laser, while the donor is coated on a (bulk) carrier substrate. The incident laser pulse energy that is either absorbed in the donor or- for partially transparent donors- the carrier leads to the transfer of a volume of the donor in a direction opposite to that of the laser beam path, hence the term 'backward'.

* Corresponding author. Current address: Chair of Applied Laser Technology, Laboratory of Mechanical Automation and Mechatronics, Faculty of Engineering Technology, University of Twente, Enschede, The Netherlands.
E-mail addresses: m.feinaeugle@utwente.nl (M. Feinaeugle), bm602@orc.soton.ac.uk (B. Mills).
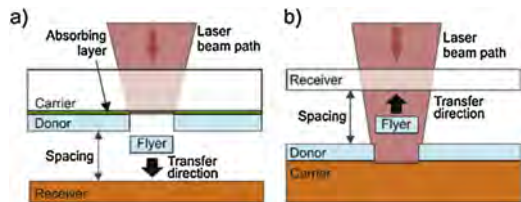
Fig. 1. Schematic side-view of (a) laser-induced forward transfer (LIFT) and (b) laser-induced backward transfer (LIBT) for a transparent donor.

In comparison with LIFT, LIBT has different requirements and restrictions concerning the transparency of the receiver and the donor, but the possibility to use a bulk carrier substrate might prove advantageous for certain applications. These advantages can also be used for transfer of other materials as demonstrated in previous work, where metals [22–25], oxides [25,26], CrSi2 [27], TiN [24] and corroded surfaces [28] have been the subject of studies of LIBT methods.

Recently, we have demonstrated that the use of a bulk substrate facilitates the imprint-based laser-induced fabrication of sub-micron-size structures via LIBT of solid polymers [29].

While LIFT has been the object of many studies to date, much less effort has been put into fully understanding and exploiting the process of LIBT. To help in predicting the outcome of an experiment via LIBT e.g. with a new material, imaging [24] and simulation [30] of the process can be useful tools. Also, as LIBT is closely related to the processes of laser lift-off [31], laser cleaning, laser scribing, or even ablation [32], studying LIBT could also aid in understanding these processes. The main difference with respect to previous work is that for our experiments, we are interested in the ejected material being in an intact state, and that its shape is geometrically similar to the incoming spatial shape of the laser pulse.

To improve the effectiveness of LIBT, factors such as low flyer velocity and reduced shock generation play a major role in transferring a flyer in an intact state [33]. An experimental time-resolved imaging study could therefore support future efforts to model the LIBT process to optimise experimental conditions, and to understand the advantages and limitations of this technique. Previously, the femtosecond laser ablation of silica grown on top of silicon was investigated in the first ∼10 ns after the arrival of the laser pulse [34]. In a different study, a simple model of silica on a Ag substrate was simulated on a picosecond timescale [30].

While the focus of those studies was on the observation of shock and film dynamics in the first nanoseconds after the arrival of the laser pulse, here, we have examined the dynamics of the emerging flyer and fragments on a microsecond scale to obtain experimental parameters for LIBT of intact deposits.

In this study, we have imaged the LIBT process from an epoxy-based SU-8 polymer donor film from planar silicon and germanium carriers via a femtosecond pulsed laser source. SU-8 is an example of a transparent donor material that can be used for e.g. photonic or microfluidic devices. This polymer, once developed, has a relatively high chemical resistance, and has been previously used in micro-opto-electro-mechanical systems (MOEMS). It is routinely used for lithographic patterning on the micro- and nanoscale, and hence beneficial for the creation of small structures. Silicon and Germanium carriers were used as readily available bulk substrates that are widely used in microfabrication of electronic and photonic devices, thus for which a large number of microfabrication processes are known.

When using polymers as donor material, photophysical effects as damage mechanisms need to be considered during transfer, and these mechanisms include photochemical decomposition, thermal
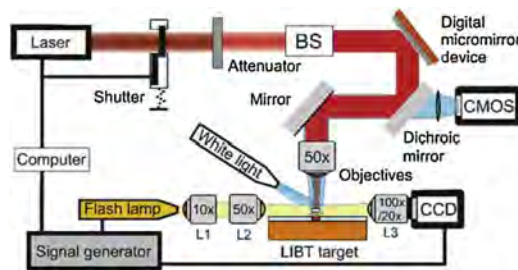

Fig. 2. Setup for time-resolved imaging of LIBT. The laser pulses with Gaussian beam profile are homogenised to a top hat profile via a refractive beam shaper (BS). Laser triggering, time-resolved imaging, DMD mask display and beam attenuation are controlled by a computer.

ablation, spallation and photopolymerisation of monomer chains [35,36]. The use of short pulses and infrared wavelength decrease the likelihood of damage via thermal effects or direct rupture of polymeric bonds respectively, while multiphoton effects would only be expected for the highest fluences used. At the same time, thermal effects to the semiconductor carriers are expected to be reduced with short laser pulses when compared to longer pulsed laser sources, and this has further motivated our choice of laser source for these experiments [37].

With the help of a time-resolved shadowgraphy setup, we have recorded the position of the emerging flyer as a function of pulse energy, donor thickness, carrier material, delay time after laser pulse arrival, and beam intensity distribution. Shadowgraphy can be used to determine the existence and position of particles and flyer ejected from the donor surface and is also sensitive to changes in the refractive index of the surrounding atmosphere, e.g. through gradients in pressure or gaseous elements. Generally, shadowgraphy can be most readily performed with the presence of a receiver to study impact and landing of the flyer, and the receiver's interaction with pressure waves. Instead we have chosen to study the dynamics of the flyer ejection without receiver which is a case relevant to the LIBT process as the velocity, integrity and orientation of the flyer, and the possible creation of debris or shock can be observed over a larger range than possible with a receiver in place. In the following we refer to 'transfer' for the dynamics of flyer ejection and propagation for targets in a LIBT configuration as used here. To allow a more direct comparison with the LIBT process, we have briefly contrasted the results from shadowgraphy with those of standard transfer experiments, where we have measured the ratio of intact flyers found on a receiver to flyers imaged in an intact state.

We will first introduce the experimental details and methods of the time-resolved studies of LIBT. Then we present experimental results from varying time delay, laser fluence, donor thickness and carrier. Further, we will discuss the different observed transfer regimes and the effects of experimental parameters on LIBT of SU-8.

2. Experimental

The imaging of the LIBT process was carried out using the setup shown in Fig. 2. It consisted of three different optical beam lines, one for live imaging of the sample surface, one for laser-induced transfer and the third one for time-resolved shadowgraph imaging. Transfer was induced via pulses from a Ti:sapphire laser oscillator-amplifier system (Mira/Legend, Coherent) with a central wavelength of 800 nm, and pulse lengths of 150 fs. The maximum pulse energy of 2 mJ was attenuated with a continuously variable

neutral density filter. The Gaussian intensity profile from the laser was transformed into a top-hat intensity profile via a refractive beam shaper (Pi-Shaper, AdlOptica). These laser pulses with top-hat profile then illuminated the surface of a 608×684 element digital micromirror device (DLP3000, Texas Instruments) whose mirrors were actuated to form a dynamic intensity mask. To do so, mirrors in the 'on' position directed light into the beam path shown in Fig. 2, while mirrors in 'off' position steered the laser pulses into a beam stop (not shown). The surface of the digital micromirror device (DMD) displaying a user-specified mask was imaged and de-magnified at the interface between the donor and carrier in the LIBT target with a $50\times$ de-magnification microscope objective (Mitutoyo).

For sample positioning and focussing, the sample, illuminated with a white light source, is imaged continuously on a CMOS camera, whose image path is collinear to the laser beam path. More details on the setup and on the configuration of the DMD for image projection can be found in previous work [38].

The laser-induced events above the sample surface were recorded via illumination from a white light spark discharge flash lamp (Nanolite KL-K, HSPS) with a pulse duration of 8 ns [39]. The flash lamp was placed at the focus of microscope objective L1 ($10\times$ magnification, Leitz Wetzlar) used as a collimator. A second microscope objective L2 ($50\times$ magnification, Nikon) was used to concentrate the illuminating light at the interaction area. The interaction of the illuminating beams and the laser-induced objects or differences in refractive indices were then observed as intensity gradients [40] on a CCD camera (scA1400–17 fm, 1.4 Mpx, Basler AG) equipped with a microscope objective L3. Depending on the resolution required and the field of view, we used one of two different ($20\times$ and $100\times$ magnification, Nikon) microscope objectives L3. Our setup therefore provided the following theoretical resolutions: 90 nm/pixel and 420 nm/pixel, while the field of view in the direction of flyer movement equalled approximately 120 μm and 400 μm respectively. The excitation laser, flash lamp, shutter and the CCD camera were synchronised by a signal generator (Tektronix, AFG 3102) while the display of the DMD image mask, laser triggering and attenuation level were controlled by a computer.

Following laser triggering, the signal generator caused the CCD camera to be active for ~20 ms and at the same time actuated the flash lamp at a chosen delay time with a minimum value of 1.4 μs. A snapshot was therefore taken after the chosen delay with an exposure time of ~8 ns. We varied this delay during experiments over the range between 1.4 μs and 16.4 μs with an estimated uncertainty of 100 ns. For each delay a new area of the donor was selected, so the data presented below consists of sequential flyers imaged at different delays but otherwise similar conditions. To reduce errors due to natural fluctuations in flyer behaviour, each set of similar conditions was repeated at least five times. The delay was chosen to show flyers travelling the full extent of the image frame visible to the camera.

Fig. 3a shows a schematic of the imaging setup and the image shown in Fig. 3b is a typical shadowgram recorded with the CCD
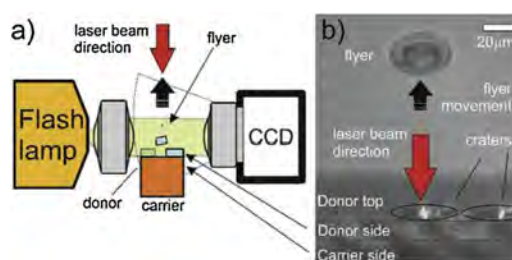
Fig. 3. (a) Schematic side-view of shadowgraphy imaging setup and (b) image frame as recorded by CCD camera and a $100\times$ microscope objective.

camera where flyer and donor surface orientation appear at an angle relative to each other as a result of camera perspective. The contrast, brightness and gamma values of the captured images were modified to optimise visibility of the laser-induced events.

The LIBT targets (i.e. the donor-coated carrier) were fabricated via spin-coating of SU-8 photoresist (Microchem) onto silicon and germanium carrier substrates (300–600 μm thick). The germanium carriers consisted of a 3 μm thick layer of Ge grown on a Si substrate. Before spin-coating, the carriers were ultrasonically cleaned in sequential baths of acetone, isopropanol and water for 30 min and subsequently dried by pressurised nitrogen. After coating, the LIBT targets were baked on a hotplate for 3 min ramping from 60 to 90 °C, and the sample was held at 90 °C for a further minute to solidify the polymer and to remove any residual gamma-butyrolactone solvent [41]. Final donor thicknesses were 3.8 μm (referred to later as 'thin') and 6.4 μm (referred to as 'thick'), measured with a mechanical profiler. The variation of donor thickness measurement was in the range of ±100 nm while the measurement error by the mechanical profiler used was estimated to be smaller than this variation. The films were coated at spin speeds of 2000 rpm and 4000 rpm for maximum accelerations of 300 rpm/s and a spin duration of 30 s. The film thickness of a few microns was a typical thickness used in SU-8 based MEOMS and around the standard thickness for SU-8 5 used in lithography.

The targets were then cleaved in the centre for better imaging of the central part of the donor to avoid shading by the thick donor bead found at the perimeter of a spin-coated sample and experiments were performed at least 100 μm away from the sample (donor) edges to avoid variation of material properties, such as a reduced donor-carrier adhesion.

3. Results and discussion

3.1. Velocity of the flyer

In the first experiments we varied the delay between values of 1.4–10 μs between incidence of the laser pulse and recording of the position of the flyer above the substrate. A sequence of images

Fig. 4. Time sequence of shadowgrams of flyers from a thick SU-8 donor on a Si carrier imaged with a $100\times$ microscope objective. The scale bar is 20 μm in all figures.

Fig. 5. Distance travelled by flyers for varying delay times from (a) Si carriers and (b) Ge carriers with thick and thin SU-8 donors. The error bar is the standard deviation at a certain delay time.
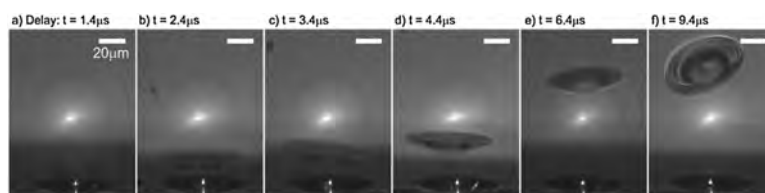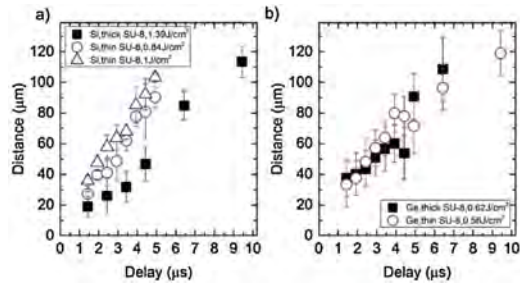
Table 1
Intact flyer velocities for different carrier/donor combinations extracted from distance vs. delay data. The fluence values for the samples are shown in Fig. 5. The temporal mean of the velocity is shown for different fluences and combinations of donor and carrier.

Carrier/Donor (Fluence)	Mean velocity [m/s]
Si/Thin SU-8 (0.84 J/cm^2)	18.1 ± 2.1
Si/Thin SU-8 (1 J/cm^2)	19.8 ± 2.3
Si/Thick SU-8	9.3 ± 2.8
Ge/Thin SU-8	13.5 ± 1.5
Ge/Thick SU-8	9.1 ± 5.4

Fig. 6. Velocity as a function of delay time for (a) silicon and (b) germanium carriers with thin (3.8 μm) and thick (6.4 μm) SU-8 donors.

taken for different delays at a fluence of 1.39 J/cm^2 for flyers from a thick SU-8 on silicon target are shown in Fig. 4.

A flyer emerges from the surface not as a cylindrical disc which could be the circular shape with top-hat spatial intensity projected at the interface, but is slightly tapered and additionally features a thin peripheral rim ripped out of the donor to result in a 'saucer-like' structure. Most of the shadowgraph images show two bright areas, one in the centre of the image and a second one in the crater on the donor. The first spot originates from direct imaging of the spark gap illumination, and while the presence of this bright spot in the image was undesired, this geometry was used to maximise flyer illumination. The second spot is a consequence of scattering of the laser pulse visible due to the long exposure time of the CCD camera.

The image also reveals that the bottom side of the tilted flyer carries some damage appearing in the central region of the flyer. This damage, seen as dark spots within a flyer, occurred to some of the flyers and was most likely caused by imperfections of the donor or fluctuations of the laser pulse intensity due to imperfect optics or laser output. As flyers were not collected, further evaluation of this damage was not possible. The particles shown in Fig. 4b–d is debris which likely has its origin in the central damaged spot of the flyer.

Experiments were carried out just above flyer removal fluence thresholds for the 3.8 μm and 6.4 μm thick films. For donors on silicon these threshold fluences were between 0.80 J/cm^2 and 1.35 J/cm^2 as a function of donor thickness. Germanium carriers had threshold fluences between 0.55 J/cm^2 and 0.60 J/cm^2. The differences in threshold fluences observed between experiments with the different carrier substrates could be reduced to both the different physical properties of the carrier or to the different adhesion of donor on carrier, and further measurements of adhesion would be required to determine the effect of these properties.

The distance d travelled by the resulting intact flyers for an image taken after a specific delay is shown in Fig. 5.

Experiments for thin SU-8 on silicon were performed at fluences just above and at 20% higher than threshold for comparison to see if there is a measurable influence of fluence on velocity. The higher value was chosen to be between the threshold and the fluence at which the likelihood of breaking up would increase dramatically. The velocity $v(t)$ of a flyer as a function of delay t as shown in Table 1 and Fig. 6 was defined as:
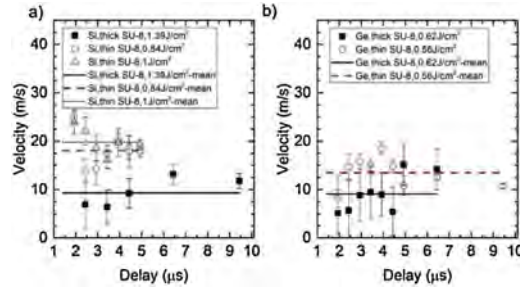
$$v(t) = \frac{d(t) - d(t_1)}{t - t_1} \qquad (1)$$

with t_1 the minimum delay (1.4 μs). From previous experiments, it is expected that flyer ejection (occurring at time t_0) is initiated on the timescale of hundreds of nanoseconds after laser pulse arrival and is a function of fluence [42,43]. Generally, using short pulses

and higher fluences can decrease t_0. However, the influence of dynamic release layers (DRL) such as Au [44] is inconclusive, while for a Triazene DRL [45], a thicker film can decrease t_0 significantly as compared to a thin DRL [43]. While the pressure of the surrounding atmosphere does have a large effect on propagation velocity, no major influence on ejection time could be observed in literature [33].

Resulting mean velocities for flyers were in the range of 9–20 m/s, and the lowest velocity recorded was 6 m/s. For both carriers, the thicker flyers had a lower velocity than the thin flyers. The comparison of a thin flyer from a Si carrier in Table 1 shows slightly higher velocities for a flyer ejected at 20% higher fluence but otherwise similar conditions for the mean velocity. Fig. 5 also shows that flyers ejected at higher fluence have always travelled further at comparable delay times, hinting at a smaller flyer release time t_0 for higher fluences. The velocities as a function of delay are plotted in Fig. 6.

No indication of any deceleration, e.g. by drag, could be seen in the velocity over the time delays studied. The flyer propagation was assumed to be influenced by the deceleration through the surrounding atmosphere as well as by the flyer rotation induced during flyer ejection. Gravity acting in the opposite direction of travel was neglected being several orders of magnitude smaller than drag from the surrounding air at atmospheric pressure. The different flyer velocities observed are crucial to estimate the outcome of a LIBT experiment as a higher velocity increases the impact when landing on a receiver.

3.2. Influence of laser fluence on flyer propagation

As observed in Fig. 5 for the thin donor films, distance travelled in a specific time period increased for higher laser pulse energies incident on the targets as seen earlier [46]. This relation was investigated in more detail by recording flyer propagation for a fixed delay time but varying laser fluence for Ge and Si carriers. Fig. 7 shows the resulting behaviour for flyers from a thick SU-8 donor and a Ge carrier.
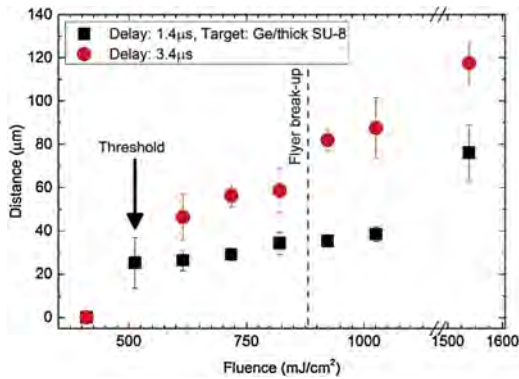
Fig. 7. Distance travelled by flyer for two delay times when varying incident pulse fluence for a Ge carrier and a thick SU-8 donor film. The first data points at ~400 mJ/cm² show that no flyer had emerged from the donor.

Fig. 9. Crater diameter for varying fluence measured on two Si and Ge donors after LIBT experiments for a thick SU-8 donor. The insets shows microscope images of craters in the donor after transfer (for Si carrier). The scale bar of the insets is 25 μm.
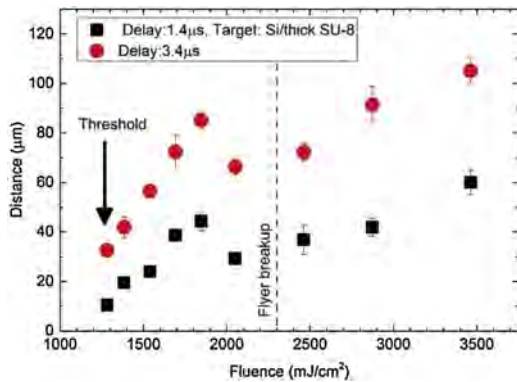

Fig. 8. Distance travelled as a function of incident laser fluence for a flyer from a thick SU-8 donor on Si carrier.

During this experiment only flyers up to a fluence of 0.9 J/cm² and 2.3 J/cm² for Ge and Si carriers respectively were observed to be in an intact state. For higher fluences, more than 90% of flyers were found to have fragmented. The distances plotted at larger fluences show the distance travelled by the main fragments ejected from the donor surface. Before breakup, the measured average velocities of the fastest flyers were 12.2 ± 7.7 m/s. The error found for these fastest flyers was relatively large and we assumed that the tilt of some of the recorded flyers may have contributed to their deceleration. For a germanium carrier, all flyers ejected at a high fluence travel further, thus at a higher average velocity, than flyers ejected at a lower fluence close to threshold. The resulting linear increase of velocity as a function of fluence was in the range of 0.023 ± 0.01 m/s mJ^{-1} cm² for flyers in an intact state.

A similar plot of distance over delay time from an experiment with silicon carriers is shown in Fig. 8. Here, the distance curves are split at a fluence value of ~1.8 J/cm² into a 'sawtooth' function with positive gradients. The first part of the fitted sawtooth function (1.25–1.8 J/cm²), showing the distances of intact flyers, has a gradient of velocity of 0.014 ± 0.01 m/s mJ^{-1} cm². The velocity of the fastest flyers here was 16.8 ± 4.6 m/s.

In the first part of the curve, distance increases monotonically. However, around 2.0–2.5 J/cm², propagation is much lower than expected. Only for values of 3.5 J/cm² is propagation again larger

than for flyers ejected at 1.8 J/cm². Such behaviour would seem to indicate a deceleration or a change of transfer regime for those higher fluences. To further investigate this behaviour, we have measured the diameter of the ablation craters in the donor films left behind by the ejected flyer as shown in Fig. 9.

For a fixed image mask as used throughout this experiment, it was expected that crater size would remain constant or increase only slightly for increasing fluence due to areas in the perimeter of the imaged mask feature, where intensity, decaying in an exponential fashion due to imperfect imaging, exceeded the transfer threshold, resulting in a larger flyer being ejected. However, Fig. 9 shows a local minimum in crater size for SU-8/Si targets at around 2.5 J/cm² confirming that craters, and as a consequence flyers, do not have a constant or linear increasing diameter.

The beam diameter at the donor-carrier interface was ~20 μm, estimated from microscope images of the donor damage at low fluences. From Fig. 9 and previous experiments we can see that the flyer shape is much larger. During flyer release, the flyer shears off additional neighbouring donor areas and thus results in an increase in flyer diameter. Although an exact cause of the observed variation in flyer diameter is difficult to confirm, we assumed that different factors could contribute to the observed flyers shape distribution. It had been observed earlier in polymers that higher impact velocities on polymer can lead to different failure modes [47]. Slow donor loading would induce brittle fracture (tensile failure mode) while fast loads would induce a transition to a ductile (failure) regime where shear crack growth is preferred. Thus a fast 'push' could lead to a different transfer regime preferring straight edges in crater and resulting flyer. This different failure mechanism would then cause a different amount of kinetic energy to be delivered to the flyer during flyer ejection or on the other hand the donor accelerated at different rates would suffer from these different failure regimes. The effect of varying crater size and velocity was not seen in the experiments with Ge carrier and hence could be a consequence of the relatively high fluences required for the Si carriers. In general, the failure mode determines the resulting flyer edge quality and shape. Additionally, the increased fluence could increase the likelihood of non-linear multiphoton absorption, shock-induced changes [48] or even heating of the flyer and hence its change in global or local mechanical properties explaining the observed changes in flyer and crater shape.

From our experiments here, we can also estimate the influence of the receiver by determining the fluence window *FW*, in which flyers are either seen intact for shadowgraphy experiments,
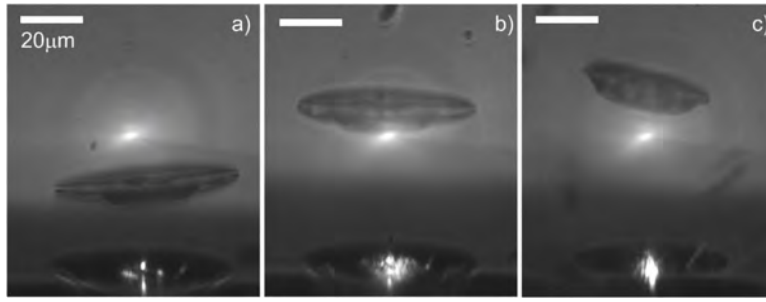
Fig. 10. Shadowgraph image of flyers ejected from a thick SU-8 film on a silicon carrier ejected at (a) 1.39 J/cm², (b) 1.69 J/cm², and (c) 2.05 J/cm² respectively. Delay times were 3.4 μs. Images were taken via a 100× objective. The scale bar is 20 μm in all figures.
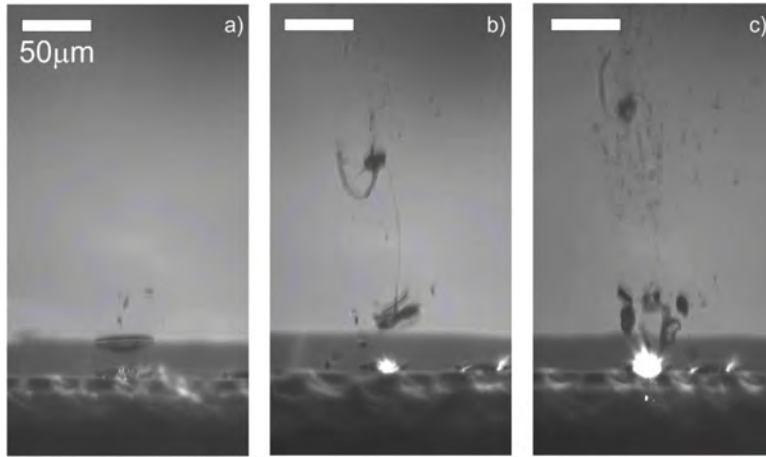
Fig. 11. Shadowgraph images from LIBT events of a thick SU-8 donor on silicon carrier. Fluences were (a) 1.39 J/cm2, (b) 2.05 J/cm2, and (c) 3.46 J/cm2. Images were taken with a CCD mounted 20x objective and delay was 2.4 μs. The scale bar is 50 μm in all figures.

or intact for LIBT experiments printing onto a receiver. This results in a transfer window defined as:

$$FW = \frac{F_u - F_{th}}{F_{th}} \tag{2}$$

with F_u and F_{th} the respective maximum and minimum fluence for which flyers are ejected or deposited in intact state. *FW* for thick flyers on Ge and Si was approximately 60%. For comparison, in an experiment using a polydimethylsiloxane-coated glass receiver and a thin SU-8 donor from a Si carrier (flyers in transfer were not imaged), *FW* was ∼16%, compared to ∼38% for shadowgraphy experiments, for flyers ejected from the donor. This indicates that the influence of the receiver contributes to a reduction of this transfer window by approximately a factor of two (≈38%/16%). As shown previously for LIFT, the reduction of transfer window can be explained by shock waves reflecting off the surface of the receiver [33] or destruction due to impact on the receiver [49]. Further, it may as well be possible that the receiver might cause aberrations leading to imperfect imaging of the object at the image plane which in turn would increase the likelihood of fractured flyer ejection.

3.3. Transfer regimes of flyers

The influence of laser pulse energy, and thus fluence delivered to the LIBT target, on the velocity and shape of a flyer, is further shown in images of flyer ejection events. Fig. 10 shows shadowgraphs taken with a 100× objective from a thin SU-8 on silicon target at delays of 3.4 μs. For the selected fluences of 1.39 J/cm², 1.69 J/cm² and 2.05 J/cm² propagation distance is described approximately by the data presented in Fig. 8.

The flyers with the same conditions as for the one shown in Fig. 10c have a different profile compared to the other flyers confirming the data of crater diameter shown in Fig. 9. They have a smaller diameter and appear to miss the thin rim seen in the other flyers of Fig. 10. However, they only propagate to a distance similar to a flyer ejected at a fluence of 1.69 J/cm², hence not all the excess energy deposited into the target is used for acceleration of the flyer in a direction away from the donor.

When using an objective with 20× magnification with a thick SU-8/Si target, debris distribution and fast particles can be better detected due to the larger field of view. Fig. 11 shows transfer events for low (1.39 J/cm²), medium (2.05 J/cm²) and high (3.46 J/cm²) fluences. Note that for these medium fluences, intact flyers only occurred in ∼50% of transfer events and were never seen for high fluences.
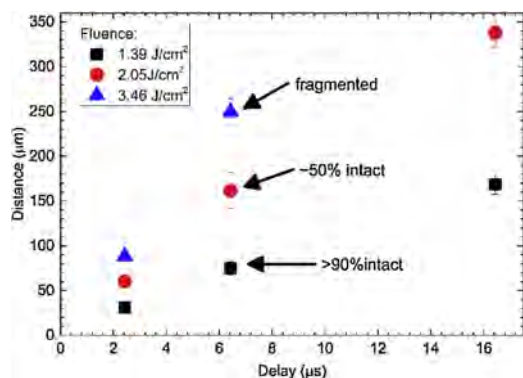
Fig. 12. Distance versus delay for thick SU-8/Si and different transfer regimes. Note that for the two higher fluences, distance values are shown for the main fragments, while for the lowest fluence, only intact flyers are shown.

For low fluences in more than 90% of the cases, the flyer was intact. As shown in Fig. 11, small amounts of debris presumably from the perimeter of the sheared flyer are visible. As the flyer appears to be slightly smaller than shown in Fig. 9, we assumed that one of the sources of such debris is the perimeter of the flyer. For medium fluences as for the flyer in Fig. 11b, disintegration of the main flyer is apparent at a distance of around 50 μm, the number of small particles or debris has increased, and at the centre of the image, an additional compact and relatively large feature can be seen which is connected with a long string of material to the lower, main flyer. Such a string or jet is an indicator of molten material and could explain the saturation of the main flyer velocity caused by a change in donor material phase and hence different mechanical properties [50]. Also, melting of the carrier at these relatively large fluences is likely to occur.

For high fluences, the molten features are still visible in the upper part of the image together with a large quantity of small particles. The main flyer is seen to have broken up in several pieces in a typical fashion for non-intact transfer. For the two higher fluences, seen near the crater, residual light emission is visible, originating from the incident laser pulse as the relatively long camera exposure time includes both laser pulse and flash lamp pulse events.

Fig. 12 emphasises further the different transfer regimes by showing propagation distances of intact flyers and large fragments of the main flyer. The largest extracted velocities for fragments seen at high fluences was ~40 m/s.

4. Conclusions

We have demonstrated the time-resolved shadowgraph imaging of thin transparent epoxy-based polymer SU-8 films via femtosecond laser-induced backward transfer. Flyer velocity, transfer regimes and intact transfer window were determined for different thicknesses (3.4 μm and 6.8 μm), delay times (1.4–16.4 μs) and carrier substrates of silicon and germanium for fluences of 0.5–3.5 J/cm². Observed velocities were in the range of 6–20 m/s for different donor thicknesses, carriers and laser fluences. We have seen that flyer velocity is a function of laser fluence with a gradient of 0.023 ± 0.01 m/s mJ^{-1} cm^2 for Ge and 0.014 ± 0.01 m/s mJ^{-1} cm^2 for Si carriers in intact state and flyers removed around threshold fluence. However, for Si carriers and large fluences, the crater found in the donor, the flyer shape and reduced flyer propagation velocity indicate a different flyer failure regime than for low fluences. Also, we have not detected any shock

waves which are known to compromise flyer integrity during LIFT experiments. The receiver has shown to be responsible for a reduction of the fluence transfer window by approximately a factor of two. Among the tested carriers, due to their relatively low ejection threshold a germanium carrier is preferred over the silicon one. These findings are helpful for better understanding of the LIBT process, for e.g. future modelling, and to determine experimental parameters for LIBT printing intact deposits.

References

[1] M. Vaezi, H. Seitz, S. Yang, A review on 3D micro-additive manufacturing technologies, Int. J. Adv. Manuf. Technol. 67 (2013) 1721–1754, http://dx.doi.org/10.1007/s00170-012-4605-2.
[2] Y. Zhang, C. Liu, D. Whalley, Direct-write techniques for maskless production of microelectronics: A review of current state-of-the-art technologies, in: 2009 Int. Conf. Electron. Packag. Technol. High Density Packag., IEEE, 2009, pp. 497–503, http://dx.doi.org/10.1109/ICEPT.2009.5270702.
[3] A. del Campo, E. Arzt, Fabrication approaches for generating complex micro- and nanopatterns on polymeric surfaces, Chem. Rev. 108 (2008) 911–945, http://dx.doi.org/10.1021/cr050018y.
[4] J.A. Grant-Jacob, B. Mills, M. Feinaeugle, C.L. Sones, G. Oosterhuis, M.B. Hoppenbrouwers, R.W. Eason, Micron-scale copper wires printed using femtosecond laser-induced forward transfer with automated donor replenishment, Opt. Mater. Express 3 (2013) 747, http://dx.doi.org/10.1364/OME.3.000747.
[5] C.B. Arnold, P. Serra, A. Piqué, Laser direct-write techniques for printing of complex materials, MRS Bull. 32 (2007) 23–32, http://dx.doi.org/10.1557/mrs2007.11.
[6] A.J. Birnbaum, H. Kim, N.A. Charipar, A. Pique, Laser printing of multi-layered polymer/metal heterostructures for electronic and MEMS devices, Appl. Phys. A: Mater. Sci. Process. 99 (2010) 711–716, http://dx.doi.org/10.1007/s00339-010-5743-8.
[7] C.L. Sones, K.S. Kaur, P. Ganguly, D.P. Banks, Y.J. Ying, R.W. Eason, S. Mailis, Laser-induced-forward-transfer: a rapid prototyping tool for fabrication of photonic devices, Appl. Phys. A 101 (2010) 333–338, http://dx.doi.org/10.1007/s00339-010-5827-5.
[8] P. Serra, M. Colina, J.M. Fernandez-Pradas, L. Sevilla, J.L. Morenza, Preparation of functional DNA microarrays through laser-induced forward transfer, Appl. Phys. Lett. 85 (2004) 1639–1641, http://dx.doi.org/10.1063/1.1787614.
[9] M. Feinaeugle, C.L. Sones, E. Koukharenko, B. Gholipour, D.W. Hewak, R.W. Eason, Laser-induced forward transfer of intact chalcogenide thin films: resultant morphology and thermoelectric properties, Appl. Phys. A 112 (2013) 1073–1079, http://dx.doi.org/10.1007/s00339-012-7491-4.
[10] D. Munoz-Martin, C.F. Brasz, Y. Chen, M. Morales, C.B. Arnold, C. Molpeceres, Laser-induced forward transfer of high-viscosity silver pastes, Appl. Surf. Sci. 366 (2016) 389–396, http://dx.doi.org/10.1016/j.apsusc.2016.01.029.
[11] E. Breckenfeld, H. Kim, R.C.Y. Auyeung, N. Charipar, P. Serra, A. Pique, Laser-induced forward transfer of silver nanopaste for microwave interconnects, Appl. Surf. Sci. 331 (2015) 254–261, http://dx.doi.org/10.1016/j.apsusc.2015.01.079.
[12] M. Zenou, Z. Kotler, Printing of metallic 3D micro-objects by laser induced forward transfer, Opt. Express 24 (2016) 1431, http://dx.doi.org/10.1364/OE.24.001431.
[13] C.W. Visser, R. Pohl, C. Sun, G.-W. Römer, B. Huis in 't Veld, D. Lohse, Toward 3D printing of pure metals by laser-induced forward transfer, Adv. Mater. 27 (2015) 4087–4092, http://dx.doi.org/10.1002/adma.201501058.
[14] Bert Huis in 't Veld, L. Overmeyer, M. Schmidt, K. Wegener, A. Malshe, P. Bartolo, Micro additive manufacturing using ultra short laser pulses, CIRP Ann. – Manuf. Technol. 64 (2015) 701–724, http://dx.doi.org/10.1016/j.cirp.2015.05.007.
[15] D.J. Heath, M. Feinaeugle, J.A. Grant-Jacob, B. Mills, R.W. Eason, Dynamic spatial pulse shaping via a digital micromirror device for patterned laser-induced forward transfer of solid polymer films, Opt. Mater. Express 5 (2015) 1129, http://dx.doi.org/10.1364/OME.5.001129.
[16] J. Ihlemann, R. Weichenhain-Schriever, Patterned deposition of thin SiOX-films by laser induced forward transfer, Thin Solid Films 550 (2014) 521–524, http://dx.doi.org/10.1016/j.tsf.2013.10.128.

[17] A.I. Kuznetsov, A.B. Evlyukhin, C. Reinhardt, A. Seidel, R. Kiyan, W. Cheng, A. Ovsianikov, B.N. Chichkov, Laser-induced transfer of metallic nanodroplets for plasmonics and metamaterial applications, J. Opt. Soc. Am. B 26 (2009) B130, http://dx.doi.org/10.1364/josab.26.00b130.

[18] D.P. Banks, C. Grivas, J.D. Mills, R.W. Eason, I. Zergioti, Nanodroplets deposited in microarrays by femtosecond Ti:sapphire laser-induced forward transfer, Appl Phys. Lett. 89 (2006) 193107, http://dx.doi.org/10.1063/1.2386921.

[19] M.L. Levene, R.D. Scott, B.W. Siryj, Material transfer recording, Appl. Opt. 9 (1970) 2260, http://dx.doi.org/10.1364/AO.9.002260.

[20] U. Zywietz, A.B. Evlyukhin, C. Reinhardt, B.N. Chichkov, Laser printing of silicon nanoparticles with resonant optical electric and magnetic responses, Nat. Commun. 5 (2014) 3402, http://dx.doi.org/10.1038/ncomms4402.

[21] A.I. Kuznetsov, J. Koch, B.N. Chichkov, Laser-induced backward transfer of gold nanodroplets, Opt. Express 17 (2009) 18820, http://dx.doi.org/10.1364/OE.17.018820.

[22] A.I. Kuznetsov, C. Unger, J. Koch, B.N. Chichkov, Laser-induced jet formation and droplet ejection from thin metal films, Appl. Phys. A 106 (2012) 479–487, http://dx.doi.org/10.1007/s00339-011-6747-8.

[23] B. Liu, Z. Hu, Y. Che, Ultrafast pulsed laser micro-deposition printing on transparent media, in: Micromach, Micromachining and Microfabrication Process Technology XV (2010) 759002–759006, http://dx.doi.org/10.1117/12.842806.

[24] S.G. Koulikov, D.D. Dlott, Ultrafast microscopy of laser ablation of refractory materials: ultra low threshold stress-induced ablation, J. Photochem. Photobiol. A Chem. 145 (2001) 183–194, http://dx.doi.org/10.1016/S1010-6030(01)00581-0.

[25] P. Papakonstantinou, N.A. Vainos, C. Fotakis, Microfabrication by UV femtosecond laser ablation of Pt, Cr and indium oxide thin films, Appl. Surf. Sci. 151 (1999) 159–170, http://dx.doi.org/10.1016/S0169-4332(99)00299-8.

[26] H. Sakata, S. Chakraborty, M. Wakaki, Patterning of Bi2O3 films using laser-induced forward and backward transfer techniques, Microelectron. Eng. 96 (2012) 56–60, http://dx.doi.org/10.1016/j.mee.2012.02.002.

[27] A. Luches, S.A. Mulenko, V.P. Veiko, A.P. Caricato, V. Chuiko, Y.V. Kudryavtsev, A.V. Lopato, A.A. Petrov, F. Romano, D. Valerini, Laser-assisted synthesis of semiconductor chromium disilicide films, Appl. Surf. Sci. 253 (2007) 6512–6516, http://dx.doi.org/10.1016/j.apsusc.2007.01.023.

[28] V.P. Veiko, E. a. Shakhno, V.N. Smirnov, G.D. Nikishin, S.P. Rho, Laser ablation and local deposition: physical mechanisms and application for decontamination of radioactive surfaces, J. Korean Phys. Soc. 51 (2007) 345, http://dx.doi.org/10.3938/jkps.51.345.

[29] M. Feinaeugle, D.J. Heath, B. Mills, J.A. Grant-Jacob, G.Z. Mashanovich, R.W. Eason, Laser-induced backward transfer of nanoimprinted polymer elements, Appl. Phys. A. 122 (2016) 398, http://dx.doi.org/10.1007/s00339-016-9953-6.

[30] E.T. Karim, M. Shugaev, C. Wu, Z. Lin, R.F. Hainsey, L.V. Zhigilei, Atomistic simulation study of short pulse laser interactions with a metal target under conditions of spatial confinement by a transparent overlayer, J. Appl. Phys. 115 (2014) 183501, http://dx.doi.org/10.1063/1.4872245.

[31] D.A. Zayarnyi, A.A. Ionin, S.I. Kudryashov, S.V. Makarov, A.A. Rudenko, E.A. Drozdova, S.B. Odinokov, Specific features of single-pulse femtosecond laser micron and submicron ablation of a thin silver film coated with a micron-thick photoresist layer, Quantum. Electron. 45 (2015) 462–466, http://dx.doi.org/10.1070/QE2015v045n05ABEH015788.

[32] C. Zhang, J. Yao, S. Lan, V.A. Trofimov, T.M. Lysak, Effects of plasma confinement on the femtosecond laser ablation of silicon, Opt. Commun. 308 (2013) 54–63, http://dx.doi.org/10.1016/j.optcom.2013.06.052.

[33] R. Fardel, M. Nagel, F. Nuesch, T. Lippert, A. Wokaun, Laser-induced forward transfer of organic LED building blocks studied by time-resolved shadowgraphy, J. Phys. Chem. C. 114 (2010) 5617–5636, http://dx.doi.org/10.1021/jp907387q.

[34] J.P. McDonald, J.A. Nees, S.M. Yalisove, Pump-probe imaging of femtosecond pulsed laser ablation of silicon with thermally grown oxide films, J. Appl. Phys. 102 (2007), http://dx.doi.org/10.1063/1.2778740.

[35] P.E. Dyer, Excimer laser polymer ablation: twenty years on, Appl. Phys. A: Mater. Sci. Process. 77 (2003) 167–173, http://dx.doi.org/10.1007/s00339-003-2137-1.

[36] M. Malinauskas, M. Farsari, A. Piskarskas, S. Juodkazis, Ultrafast laser nanostructuring of photopolymers: a decade of advances, Phys. Rep. 533 (2013) 1–31, http://dx.doi.org/10.1016/j.physrep.2013.07.005.

[37] B.N. Chichkov, C. Momma, S. Nolte, F. vonAlvensleben, A. Tunnermann, Femtosecond, picosecond and nanosecond laser ablation of solids, Appl. Phys. A: Materi. Sci. Process. 63 (1996) 109–115.

[38] B. Mills, M. Feinaeugle, C.L. Sones, N. Rizvi, R.W. Eason, Sub-micron-scale femtosecond laser ablation using a digital micromirror device, J. Micromech. Microeng. 23 (2013) 35005, http://dx.doi.org/10.1088/0960-1317/23/3/035005.

[39] M.S. Rabasović, D. Šević, N. Lukać, M. Jezeršek, J. Možina, P. Gregorčić, Evaluation of laser-induced thin-layer removal by using shadowgraphy and laser-induced breakdown spectroscopy, Appl. Phys. A 122 (2016) 186, http://dx.doi.org/10.1007/s00339-016-9697-3.

[40] G.S. Settles, Schlieren and Shadowgraph Techniques: Visualizing Phenomena in Transparent Media, Springer-Verlag, Berlin, 2006.

[41] Microchem, SU-8 Data Sheets, 2016 http://www.microchem.com/Prod-SU8.htm.

[42] M. Feinaeugle, A.P. Alloncle, P. Delaporte, C.L. Sones, R.W. Eason, Time-resolved shadowgraph imaging of femtosecond laser-induced forward transfer of solid materials, Appl. Surf. Sci. 258 (2012) 8475–8483, http://dx.doi.org/10.1016/j.apsusc.2012.04.101.

[43] K.S. Kaur, R. Fardel, T.C. May-Smith, M. Nagel, D.P. Banks, C. Grivas, T. Lippert, R.W. Eason, Shadowgraphic studies of triazene assisted laser-induced forward transfer of ceramic thin films, J. Appl. Phys. 105 (2009) 113118–113119 http://link.aip.org/link/?JAP/105/113119/1.

[44] L. Rapp, C. Cibert, A.P. Alloncle, P. Delaporte, S. Nenon, C. Videlot-Ackermann, F. Fages, Comparative time resolved shadowgraphic imaging studies of nanosecond and picosecond laser transfer of organic materials, Xvii Int Symp. Gas Flow, Chem. Lasers, High-Power Lasers 7131 (2009) 71311L, http://dx.doi.org/10.1117/12.817481.

[45] R. Fardel, M. Nagel, F. Nuesch, T. Lippert, A. Wokaun, Shadowgraphy investigation of laser-induced forward transfer: front side and back side ablation of the triazene polymer sacrificial layer, Appl. Surf. Sci. 255 (2009) 5430–5434 http://www.sciencedirect.com/science/article/pii/S0169433208018035.

[46] T. Mattle, J. Shaw-Stewart, A. Hintennach, C.W. Schneider, T. Lippert, A. Wokaun, Shadowgraphic investigations into the laser-induced forward transfer of different SnO2 precursor films, in: Appl. Surf. Sci. Elsevier B.V., 2013 pp. 77–81 10.1016/j.apsusc.2012.11.146.

[47] K. Ravi-Chandar, J. Lu, B. Yang, Z. Zhu, Failure mode transitions in polymers under high strain rate loading, Int. J. Fract. 101 (2000) 33–72, http://dx.doi.org/10.1023/A:1007581101315.

[48] K. Brown, R. Conner, Y. Fu, H. Fujiwara, D. Dlott, Microscopic states of shocked polymers, AIP Conf Proc. (2012) 1593–1596, http://dx.doi.org/10.1063/1.3686589.

[49] M. Feinaeugle, P. Horak, C.L. Sones, T. Lippert, R.W. Eason, Polymer-coated compliant receivers for intact laser-induced forward transfer of thin films: experimental results and modelling, Appl. Phys. A 116 (2014) 1939–1950, http://dx.doi.org/10.1007/s00339-014-8360-0.

[50] T. Kumada, H. Akagi, R. Itakura, T. Otobe, M. Nishikino, A. Yokoyama, Non-thermal effects on femtosecond laser ablation of polymers extracted from the oscillation of time-resolved reflectivity, Appl Phys. Lett. 106 (2015) 221605, http://dx.doi.org/10.1063/1.4921854.

Appendix B

LIBT code

In this section, the MATLAB code detailing the differential equation used to generate the results in section 4.3 is shown. Simple wrapper functions used to define starting parameters, as well as to save and graph results are excluded; instead input parameters are stated in commented code at the start. The development of this modelling work is ongoing, and has been included to demonstrate the level of agreement between experimental and simulated fluence vs. velocity curves for LIBT flyers achieved thus far.

```
% Dan Heath 20160601
%
% t is time, required input for ode45 solver
% q is matrix defining all x,y,z positions and velocities in known order,
% decomposed into relevant parts within function
% N is 2x1 vector of number of carrier layers, number of donor layers
% m is 2x1 vector of masses of carrier and donor volume elements
% EAz is 3D matrix of young's modulus for springs in z-direction multiplied
% by cross sectional area, E carrier = 170e9, E donor = 2e9 for silicon and
% SU-8
% xyStep is lattice spacing in x and y, 6.66 microns
% carrZStep is lattice spacing in z for carrier, 5 microns
% numXSteps is number of lattice points in x direction, 9
% numYSteps is number of lattice points in y direction, 9
% numZSteps is total z steps in lattice, 15
% donZStep is lattice spacing in z for donor, either 3.8/5 or 6.4/5 microns
% totSprings is total number of springs = 15*9*9
% specHeats are specific heats of carrier and donor in SI units, [710,1500];
% thermConds are thermal conductances of carrier and donor in SI units,
[130,0.2]
% thermExps are thermal expansions in SI units [2.6e-6,1e-4];
% poissRats are poisson ratios [0.27,0.22];
% restTemp is rest temperature, 300C
% carrTensStre is upper tensile strength of carrier, 7e9;
% donTensStre is donor tensile strength, 34e6;
% interTensStre is maximum adhesion force between donor and carrier, 2.3e6;
% rigEdgeCheck checks whether you want bottom and sides of simulation
% fixed, always set to true for final rounds of simulations




function dq =
LIBT2DThermalODE20160817_thesis(t,q,N,m,EAz,EAxy,xyStep,carrZStep,numXSteps,n
umYSteps,numZSteps,donZStep,...

totSprings,specHeats,thermConds,thermExps,poissRats,restTemp,carrTensStre,don
TensStre,interTensStre,rigEdgeCheck)




carrLatIntfac = carrZStep*xyStep;% get size of lateral interface for
F=EA/L*dx in carrier
donLatIntfac = donZStep*xyStep;
vertIntfac = xyStep^2;% get size of vertical interface

xPos = reshape(q(1:totSprings),numYSteps,numXSteps,numZSteps);
yPos = reshape(q(totSprings+1:2*totSprings),numYSteps,numXSteps,numZSteps);
zPos = reshape(q(2*totSprings+1:3*totSprings),numYSteps,numXSteps,numZSteps);
vx = reshape(q(3*totSprings+1:4*totSprings),numYSteps,numXSteps,numZSteps);
vy = reshape(q(4*totSprings+1:5*totSprings),numYSteps,numXSteps,numZSteps);
vz = reshape(q(5*totSprings+1:6*totSprings),numYSteps,numXSteps,numZSteps);
temps =
reshape(q(6*totSprings+1:7*totSprings),numYSteps,numXSteps,numZSteps);

% keep track of whether springs have snapped. Each mass will be connected
% to 6 springs, with the 3 defined below as the springs going 'into' the
```

```matlab
% mass, the 3 'outgoing' springs will be defined as broken by whether the
% adjacent 'ingoing' springs into adjacent masses have snapped (i.e. only
% have to keep track of 3 more big arrays...)
snapX =
reshape(q(7*totSprings+1:8*totSprings),numYSteps,numXSteps,numZSteps);
snapY =
reshape(q(8*totSprings+1:9*totSprings),numYSteps,numXSteps,numZSteps);
snapZ =
reshape(q(9*totSprings+1:10*totSprings),numYSteps,numXSteps,numZSteps);
interSnapX = snapX(:,1:numXSteps-1,:);% snaps used with tensions and heat
flows, which work better with the 'inbetween' springs values (end elements of
snap arrays only exist for concatenation at end, are constant)
interSnapY = snapY(1:numYSteps-1,:,:);
interSnapZ = snapZ(:,:,1:numZSteps-1);

% keep track of absolute distance between point masses, to be used for
% absolute tension and defining whether snapped this iteration, as well as
% then going on to work out interface of springs from each point mass
% before finally working out tensions
% Note: these are the absolute separations for springs that 'should' be
% adjacent in x, y, z, not their xyz components. Need to apply these to get
% components of force later
absSepsX = sqrt((xPos(:,2:numXSteps,:) - xPos(:,1:numXSteps-1,:)).^2 +
(yPos(:,2:numXSteps,:) - yPos(:,1:numXSteps-1,:)).^2 + (zPos(:,2:numXSteps,:)
- zPos(:,1:numXSteps-1,:)).^2);% get separations for springs adjacent in X
sepsX = abs(xPos(:,2:numXSteps,:) - xPos(:,1:numXSteps-1,:));% major
difference in 0803 version, never really made sense to define equilibrium
positions based on slightly weird forces – this version uses tensions based
on adjacent separations, applies cantilever forces separately
absSepsY = sqrt((xPos(2:numYSteps,:,:) - xPos(1:numYSteps-1,:,:)).^2 +
(yPos(2:numYSteps,:,:) - yPos(1:numYSteps-1,:,:)).^2 + (zPos(2:numYSteps,:,:)
- zPos(1:numYSteps-1,:,:)).^2);% in Y direction
sepsY = abs(yPos(2:numYSteps,:,:) - yPos(1:numYSteps-1,:,:));
absSepsZ = sqrt((xPos(:,:,2:numZSteps) - xPos(:,:,1:numZSteps-1)).^2 +
(yPos(:,:,2:numZSteps) - yPos(:,:,1:numZSteps-1)).^2 + (zPos(:,:,2:numZSteps)
- zPos(:,:,1:numZSteps-1)).^2);% in Z direction
sepsZ = abs(zPos(:,:,2:numZSteps) - zPos(:,:,1:numZSteps-1));

restLengthsX = temps - restTemp;
restLengthsY = restLengthsX;
restLengthsZ = restLengthsX;

% get rest lengths while at particular temperature
restLengthsZ(:,:,1:N(1)) =
(thermExps(1)*restLengthsZ(:,:,1:N(1))+1)*carrZStep;% generate current 'rest'
lengths for carrier in z
restLengthsZ(:,:,N(1)+1:N(1)+N(2)) =
(thermExps(2)*restLengthsZ(:,:,N(1)+1:N(1)+N(2))+1)*donZStep;% generate
current 'rest' lengths for donor in z

restLengthsX(:,:,1:N(1)) =
((thermExps(1)*restLengthsX(:,:,1:N(1))+1)*xyStep);
restLengthsX(:,:,N(1)+1:N(1)+N(2)) =
((thermExps(2)*restLengthsX(:,:,N(1)+1:N(1)+N(2))+1)*xyStep);

restLengthsY(:,:,1:N(1)) =
((thermExps(1)*restLengthsY(:,:,1:N(1))+1)*xyStep);
```

```matlab
restLengthsY(:,:,N(1)+1:N(1)+N(2)) =
((thermExps(2)*restLengthsY(:,:,N(1)+1:N(1)+N(2))+1)*xyStep);

% % in order to work out compressions properly, need to know whether some
% % springs have snapped. Work out how long they would be at snapping point,
% % use this in compression if snapped, use intPos if not

% start dealing with poisson ratio. First go through and get interface
% positions between springs with regular rest lengths, then apply
% compressions from the two orthogonal directions to each xyz direction for
% new rest lengths, redefine rest lengths, kxyz, interface positions for
% all directions
kZ = 2*EAz./restLengthsZ;
intPosZ = (kZ(:,:,2:numZSteps).*sepsZ + kZ(:,:,1:numZSteps-
1).*restLengthsZ(:,:,1:numZSteps-1)/2 -
kZ(:,:,2:numZSteps).*restLengthsZ(:,:,2:numZSteps)/2)./(kZ(:,:,2:numZSteps) +
kZ(:,:,1:numZSteps-1));
currZAbove = restLengthsZ/2;
currZBelow = restLengthsZ/2;
currZAbove(:,:,1:numZSteps-1) = intPosZ.*(interSnapZ == 0) +
currZAbove(:,:,1:numZSteps-1).*(interSnapZ ~= 0);% distance to end of spring
above is interface position if not snapped, rest length if snapped (not
actually rest length, but this will contribute zero compression as required
for a snapped spring)
currZBelow(:,:,2:numZSteps) = (sepsZ - intPosZ).*(interSnapZ == 0) +
currZBelow(:,:,2:numZSteps).*(interSnapZ ~= 0);
compressZ = (currZAbove+currZBelow)./restLengthsZ;

kX = 2*EAxy./restLengthsX;
intPosX = (kX(:,2:numXSteps,:).*sepsX + kX(:,1:numXSteps-
1,:).*restLengthsX(:,1:numXSteps-1,:)/2 -
kX(:,2:numXSteps,:).*restLengthsX(:,2:numXSteps,:)/2)./(kX(:,2:numXSteps,:) +
kX(:,1:numXSteps-1,:));
currXAbove = restLengthsX/2;
currXBelow = restLengthsX/2;
currXAbove(:,1:numXSteps-1,:) = intPosX.*(interSnapX == 0) +
currXAbove(:,1:numXSteps-1,:).*(interSnapX ~= 0);% distance to end of spring
above is interface position if not snapped, rest length if snapped (not
actually rest length, but this will contribute zero compression as required
for a snapped spring)
currXBelow(:,2:numXSteps,:) = (sepsX - intPosX).*(interSnapX == 0) +
currXBelow(:,2:numXSteps,:).*(interSnapX ~= 0);
compressX = (currXAbove+currXBelow)./restLengthsX;

kY = 2*EAxy./restLengthsY;
intPosY = (kY(2:numYSteps,:,:).*sepsY + kY(1:numYSteps-
1,:,:).*restLengthsY(1:numYSteps-1,:,:)/2 -
kY(2:numYSteps,:,:).*restLengthsY(2:numYSteps,:,:)/2)./(kY(2:numYSteps,:,:) +
kY(1:numYSteps-1,:,:));
currYAbove = restLengthsY/2;
currYBelow = restLengthsY/2;
currYAbove(1:numYSteps-1,:,:) = intPosY.*(interSnapY == 0) +
currYAbove(1:numYSteps-1,:,:).*(interSnapY ~= 0);% distance to end of spring
above is interface position if not snapped, rest length if snapped (not
actually rest length, but this will contribute zero compression as required
for a snapped spring)
```

```matlab
currYBelow(2:numYSteps,:,:) = (sepsY - intPosY).*(interSnapY == 0) +
currYBelow(2:numYSteps,:,:).*(interSnapY ~= 0);
compressY = (currYAbove+currYBelow)./restLengthsY;

restLengthsZ(:,:,1:N(1)) = restLengthsZ(:,:,1:N(1)).*(1-
poissRats(1)*(compressX(:,:,1:N(1))-1)).*(1-
poissRats(1)*(compressY(:,:,1:N(1))-1));
restLengthsZ(:,:,N(1)+1:numZSteps) = restLengthsZ(:,:,N(1)+1:numZSteps).*(1-
poissRats(2)*(compressX(:,:,N(1)+1:numZSteps)-1)).*(1-
poissRats(2)*(compressY(:,:,N(1)+1:numZSteps)-1));

restLengthsX(:,:,1:N(1)) = restLengthsX(:,:,1:N(1)).*(1-
poissRats(1)*(compressZ(:,:,1:N(1))-1)).*(1-
poissRats(1)*(compressY(:,:,1:N(1))-1));
restLengthsX(:,:,N(1)+1:numZSteps) = restLengthsX(:,:,N(1)+1:numZSteps).*(1-
poissRats(2)*(compressZ(:,:,N(1)+1:numZSteps)-1)).*(1-
poissRats(2)*(compressY(:,:,N(1)+1:numZSteps)-1));

restLengthsY(:,:,1:N(1)) = restLengthsY(:,:,1:N(1)).*(1-
poissRats(1)*(compressZ(:,:,1:N(1))-1)).*(1-
poissRats(1)*(compressX(:,:,1:N(1))-1));
restLengthsY(:,:,N(1)+1:numZSteps) = restLengthsY(:,:,N(1)+1:numZSteps).*(1-
poissRats(2)*(compressZ(:,:,N(1)+1:numZSteps)-1)).*(1-
poissRats(2)*(compressX(:,:,N(1)+1:numZSteps)-1));

kZ = 2*EAz./restLengthsZ;
intPosZ = (kZ(:,:,2:numZSteps).*sepsZ + kZ(:,:,1:numZSteps-
1).*restLengthsZ(:,:,1:numZSteps-1)/2 -
kZ(:,:,2:numZSteps).*restLengthsZ(:,:,2:numZSteps)/2)./(kZ(:,:,2:numZSteps) +
kZ(:,:,1:numZSteps-1));
currZAbove = restLengthsZ/2;
currZBelow = restLengthsZ/2;
currZAbove(:,:,1:numZSteps-1) = intPosZ.*(interSnapZ == 0) +
currZAbove(:,:,1:numZSteps-1).*(interSnapZ ~= 0);% distance to end of spring
above is interface position if not snapped, rest length if snapped (not
actually rest length, but this will contribute zero compression as required
for a snapped spring)
currZBelow(:,:,2:numZSteps) = (sepsZ - intPosZ).*(interSnapZ == 0) +
currZBelow(:,:,2:numZSteps).*(interSnapZ ~= 0);

kX = 2*EAxy./restLengthsX;
intPosX = (kX(:,2:numXSteps,:).*sepsX + kX(:,1:numXSteps-
1,:).*restLengthsX(:,1:numXSteps-1,:)/2 -
kX(:,2:numXSteps,:).*restLengthsX(:,2:numXSteps,:)/2)./(kX(:,2:numXSteps,:) +
kX(:,1:numXSteps-1,:));
currXAbove = restLengthsX/2;
currXBelow = restLengthsX/2;
currXAbove(:,1:numXSteps-1,:) = intPosX.*(interSnapX == 0) +
currXAbove(:,1:numXSteps-1,:).*(interSnapX ~= 0);% distance to end of spring
above is interface position if not snapped, rest length if snapped (not
actually rest length, but this will contribute zero compression as required
for a snapped spring)
currXBelow(:,2:numXSteps,:) = (sepsX - intPosX).*(interSnapX == 0) +
currXBelow(:,2:numXSteps,:).*(interSnapX ~= 0);

kY = 2*EAxy./restLengthsY;
```

```matlab
intPosY = (kY(2:numYSteps,:,:).*sepsY + kY(1:numYSteps-
1,:,:).*restLengthsY(1:numYSteps-1,:,:)/2 -
kY(2:numYSteps,:,:).*restLengthsY(2:numYSteps,:,:)/2)./(kY(2:numYSteps,:,:) +
kY(1:numYSteps-1,:,:));
currYAbove = restLengthsY/2;
currYBelow = restLengthsY/2;
currYAbove(1:numYSteps-1,:,:) = intPosY.*(interSnapY == 0) +
currYAbove(1:numYSteps-1,:,:).*(interSnapY ~= 0);% distance to end of spring
above is interface position if not snapped, rest length if snapped (not
actually rest length, but this will contribute zero compression as required
for a snapped spring)
currYBelow(2:numYSteps,:,:) = (sepsY - intPosY).*(interSnapY == 0) +
currYBelow(2:numYSteps,:,:).*(interSnapY ~= 0);

% % define cantilever spring constants
kCZy = EAz(:,:,1:numZSteps-1).*(currXAbove(:,:,1:numZSteps-1) +
currXBelow(:,:,1:numZSteps-1)).*(currYAbove(:,:,1:numZSteps-1) +
currYBelow(:,:,1:numZSteps-1)).^3./(4*intPosZ.^3*xyStep^2);% for y
deflections in z rest springs, x thickness
kCZx = EAz(:,:,1:numZSteps-1).*(currYAbove(:,:,1:numZSteps-1) +
currYBelow(:,:,1:numZSteps-1)).*(currXAbove(:,:,1:numZSteps-1) +
currXBelow(:,:,1:numZSteps-1)).^3./(4*intPosZ.^3*xyStep^2);% for x
deflections in z rest springs, y thickness

kCXy = EAxy(:,1:numXSteps-1,:).*(currZAbove(:,1:numXSteps-1,:) +
currZBelow(:,1:numXSteps-1,:)).*(currYAbove(:,1:numXSteps-1,:) +
currYBelow(:,1:numXSteps-1,:)).^3./(4*intPosX.^3);
kCXy(:,:,1:N(1)) = kCXy(:,:,1:N(1))./carrLatIntfac;
kCXy(:,:,N(1)+1:numZSteps) = kCXy(:,:,N(1)+1:numZSteps)./donLatIntfac;
kCXz = EAxy(:,1:numXSteps-1,:).*(currYAbove(:,1:numXSteps-1,:) +
currYBelow(:,1:numXSteps-1,:)).*(currZAbove(:,1:numXSteps-1,:) +
currZBelow(:,1:numXSteps-1,:)).^3./(4*intPosX.^3);
kCXz(:,:,1:N(1)) = kCXz(:,:,1:N(1))./carrLatIntfac;
kCXz(:,:,N(1)+1:numZSteps) = kCXz(:,:,N(1)+1:numZSteps)./donLatIntfac;

kCYx = EAxy(1:numYSteps-1,:,:).*(currZAbove(1:numYSteps-1,:,:) +
currZBelow(1:numYSteps-1,:,:)).*(currXAbove(1:numYSteps-1,:,:) +
currXBelow(1:numYSteps-1,:,:)).^3./(4*intPosY.^3);
kCYx(:,:,1:N(1)) = kCYx(:,:,1:N(1))./carrLatIntfac;
kCYx(:,:,N(1)+1:numZSteps) = kCYx(:,:,N(1)+1:numZSteps)./donLatIntfac;
kCYz = EAxy(1:numYSteps-1,:,:).*(currXAbove(1:numYSteps-1,:,:) +
currXBelow(1:numYSteps-1,:,:)).*(currZAbove(1:numYSteps-1,:,:) +
currZBelow(1:numYSteps-1,:,:)).^3./(4*intPosY.^3);
kCYz(:,:,1:N(1)) = kCYz(:,:,1:N(1))./carrLatIntfac;
kCYz(:,:,N(1)+1:numZSteps) = kCYz(:,:,N(1)+1:numZSteps)./donLatIntfac;

% define cantilever deflections and forces
defXy = (yPos(:,2:numXSteps,:) - yPos(:,1:numXSteps-1,:)).*intPosX./sepsX;%
need to multiply this by intPos/sep
defXz = (zPos(:,2:numXSteps,:) - zPos(:,1:numXSteps-1,:)).*intPosX./sepsX;
defYx = (xPos(2:numYSteps,:,:) - xPos(1:numYSteps-1,:,:)).*intPosY./sepsY;
defYz = (zPos(2:numYSteps,:,:) - zPos(1:numYSteps-1,:,:)).*intPosY./sepsY;
defZx = (xPos(:,:,2:numZSteps) - xPos(:,:,1:numZSteps-1)).*intPosZ./sepsZ;
defZy = (yPos(:,:,2:numZSteps) - yPos(:,:,1:numZSteps-1)).*intPosZ./sepsZ;

% Find values of tensions in springs - labels are based on x,y,z adjacence in
array
```

```matlab
tensX = -kX(:,1:numXSteps-1,:).*(intPosX - restLengthsX(:,1:numXSteps-
1,:)/2);% define positive as when spring is shorter than rest, last spring is
attached to nothing
tensY = -kY(1:numYSteps-1,:,:).*(intPosY - restLengthsY(1:numYSteps-
1,:,:)/2);
tensZ = -kZ(:,:,1:numZSteps-1).*(intPosZ - restLengthsZ(:,:,1:numZSteps-
1)/2);

% need some way to stop springs moving through each other, exponential
% increase in tension if they get too close?
nonLinFrac = 0.4;
xOverComp = intPosX < nonLinFrac*restLengthsX(:,1:numXSteps-1,:);
tensX = tensX.*(~xOverComp) +
xOverComp.*tensX.*nonLinFrac.*restLengthsX(:,1:numXSteps-1,:)./abs(intPosX);
yOverComp = intPosY < nonLinFrac*restLengthsY(1:numYSteps-1,:,:);
tensY = tensY.*(~yOverComp) +
yOverComp.*tensY.*nonLinFrac.*restLengthsY(1:numYSteps-1,:,:)./abs(intPosY);
zOverComp = intPosZ < nonLinFrac*restLengthsZ(:,:,1:numZSteps-1);
tensZ = tensZ.*(~zOverComp) +
zOverComp.*tensZ.*nonLinFrac.*restLengthsZ(:,:,1:numZSteps-1)./abs(intPosZ);

% find cantilever tensions in springs
cantXy = -kCXy.*defXy;
cantXz = -kCXz.*defXz;

cantYx = -kCYx.*defYx;
cantYz = -kCYz.*defYz;

cantZx = -kCZx.*defZx;
cantZy = -kCZy.*defZy;

% set broken springs to zero cantilever tension
cantXy(interSnapX ~= 0) = 0;
cantXz(interSnapX ~= 0) = 0;

cantYx(interSnapY ~= 0) = 0;
cantYz(interSnapY ~= 0) = 0;

cantZx(interSnapZ ~= 0) = 0;
cantZy(interSnapZ ~= 0) = 0;

stressXx = tensX./((currZAbove(:,1:numXSteps-1,:) + currZBelow(:,1:numXSteps-
1,:)).*(currYAbove(:,1:numXSteps-1,:) + currYBelow(:,1:numXSteps-1,:)));
stressXy = 6*cantXy.*intPosX./((currZAbove(:,1:numXSteps-1,:) +
currZBelow(:,1:numXSteps-1,:)).*(currYAbove(:,1:numXSteps-1,:) +
currYBelow(:,1:numXSteps-1,:)).^2);
stressXz = 6*cantXz.*intPosX./((currYAbove(:,1:numXSteps-1,:) +
currYBelow(:,1:numXSteps-1,:)).*(currZAbove(:,1:numXSteps-1,:) +
currZBelow(:,1:numXSteps-1,:)).^2);
% apply correction factor to cantilever stress
stressXy(:,:,N(1)+1:numZSteps) =
stressXy(:,:,N(1)+1:numZSteps).*(1+(xyStep/(N(2)*donZStep) -
1).*(abs(vy(:,2:numXSteps,N(1)+1:numZSteps)-vy(:,1:numXSteps-
1,N(1)+1:numZSteps))./max(abs(vy(:,2:numXSteps,N(1)+1:numZSteps)),abs(vy(:,1:
numXSteps-1,N(1)+1:numZSteps)))));
stressXy(isnan(stressXy)|isinf(stressXy)) = 0;
```

```
stressXz(:,:,N(1)+1:numZSteps) =
stressXz(:,:,N(1)+1:numZSteps).*(1+(xyStep/(N(2)*donZStep) -
1).*(abs(vz(:,2:numXSteps,N(1)+1:numZSteps)-vz(:,1:numXSteps-
1,N(1)+1:numZSteps))./max(abs(vz(:,2:numXSteps,N(1)+1:numZSteps)),abs(vz(:,1:
numXSteps-1,N(1)+1:numZSteps))))));
stressXz(isnan(stressXz)|isinf(stressXz)) = 0;

stressYy = tensY./((currZAbove(1:numYSteps-1,:,:) + currZBelow(1:numYSteps-
1,:,:)).*(currXAbove(1:numYSteps-1,:,:) + currXBelow(1:numYSteps-1,:,:)));
stressYx = 6*cantYx.*intPosY./((currZAbove(1:numYSteps-1,:,:) +
currZBelow(1:numYSteps-1,:,:)).*(currXAbove(1:numYSteps-1,:,:) +
currXBelow(1:numYSteps-1,:,:)).^2);
stressYz = 6*cantYz.*intPosY./((currXAbove(1:numYSteps-1,:,:) +
currXBelow(1:numYSteps-1,:,:)).*(currZAbove(1:numYSteps-1,:,:) +
currZBelow(1:numYSteps-1,:,:)).^2);
% apply correction factor to cantilever stress
stressYx(:,:,N(1)+1:numZSteps) =
stressYx(:,:,N(1)+1:numZSteps).*(1+(xyStep/(N(2)*donZStep) -
1).*(abs(vx(2:numYSteps,:,N(1)+1:numZSteps)-vx(1:numYSteps-
1,:,N(1)+1:numZSteps))./max(abs(vx(2:numYSteps,:,N(1)+1:numZSteps)),abs(vx(1:
numYSteps-1,:,N(1)+1:numZSteps))))));
stressYx(isnan(stressYx)|isinf(stressYx)) = 0;
stressYz(:,:,N(1)+1:numZSteps) =
stressYz(:,:,N(1)+1:numZSteps).*(1+(xyStep/(N(2)*donZStep) -
1).*(abs(vz(2:numYSteps,:,N(1)+1:numZSteps)-vz(1:numYSteps-
1,:,N(1)+1:numZSteps))./max(abs(vz(2:numYSteps,:,N(1)+1:numZSteps)),abs(vz(1:
numYSteps-1,:,N(1)+1:numZSteps))))));
stressYz(isnan(stressYz)|isinf(stressYz)) = 0;

stressZz = tensZ./((currYAbove(:,:,1:numZSteps-1) +
currYBelow(:,:,1:numZSteps-1)).*(currXAbove(:,:,1:numZSteps-1) +
currXBelow(:,:,1:numZSteps-1)));
stressZx = 6*cantZx.*intPosZ./((currYAbove(:,:,1:numZSteps-1) +
currYBelow(:,:,1:numZSteps-1)).*(currXAbove(:,:,1:numZSteps-1) +
currXBelow(:,:,1:numZSteps-1)).^2);
stressZy = 6*cantZy.*intPosZ./((currXAbove(:,:,1:numZSteps-1) +
currXBelow(:,:,1:numZSteps-1)).*(currYAbove(:,:,1:numZSteps-1) +
currYBelow(:,:,1:numZSteps-1)).^2);

% define von Mises stress in each direction
vMx = sqrt(((stressXx - stressXy).^2 + (stressXx - stressXz).^2 + (stressXy -
stressXz).^2)/2);
vMy = sqrt(((stressYx - stressYy).^2 + (stressYx - stressYz).^2 + (stressYy -
stressYz).^2)/2);
vMz = sqrt(((stressZx - stressZy).^2 + (stressZx - stressZz).^2 + (stressZy -
stressZz).^2)/2);

% set whether any snaps occur this time instant - ugly way of doing it, but
% step functions within ode are really awkward
reducFac = 1e15;
dSnapX = zeros(numYSteps,numXSteps,numZSteps);
dSnapY = dSnapX;
dSnapZ = dSnapX;

dSnapX(:,1:numXSteps-1,1:N(1)) = dSnapX(:,1:numXSteps-1,1:N(1)) +
reducFac*(((vMx(:,:,1:N(1)) > carrTensStre) & restLengthsX(:,1:numXSteps-
1,1:N(1))/2 < absSepsX(:,:,1:N(1)).*intPosX(:,:,1:N(1))./sepsX(:,:,1:N(1))) |
```

```
abs(stressXy(:,:,1:N(1))) > carrTensStre/sqrt(3) | abs(stressXz(:,:,1:N(1)))
> carrTensStre/sqrt(3));
dSnapX(:,1:numXSteps-1,N(1)+1:numZSteps) = dSnapX(:,1:numXSteps-
1,N(1)+1:numZSteps) + reducFac*(((vMx(:,:,N(1)+1:numZSteps) > donTensStre) &
restLengthsX(:,1:numXSteps-1,N(1)+1:numZSteps)/2 <
absSepsX(:,:,N(1)+1:numZSteps).*intPosX(:,:,N(1)+1:numZSteps)./sepsX(:,:,N(1)
+1:numZSteps)) | abs(stressXy(:,:,N(1)+1:numZSteps)) > donTensStre/sqrt(3) |
abs(stressXz(:,:,N(1)+1:numZSteps)) > donTensStre/sqrt(3));
dSnapY(1:numYSteps-1,:,1:N(1)) = dSnapY(1:numYSteps-1,:,1:N(1)) +
reducFac*(((vMy(:,:,1:N(1)) > carrTensStre) & restLengthsY(1:numYSteps-
1,:,1:N(1))/2 < absSepsY(:,:,1:N(1)).*intPosY(:,:,1:N(1))./sepsY(:,:,1:N(1)))
| abs(stressYx(:,:,1:N(1))) > carrTensStre/sqrt(3) |
abs(stressYz(:,:,1:N(1))) > carrTensStre/sqrt(3));
dSnapY(1:numYSteps-1,:,N(1)+1:numZSteps) = dSnapY(1:numYSteps-
1,:,N(1)+1:numZSteps) + reducFac*(((vMy(:,:,N(1)+1:numZSteps) > donTensStre)
& restLengthsY(1:numYSteps-1,:,N(1)+1:numZSteps)/2 <
absSepsY(:,:,N(1)+1:numZSteps).*intPosY(:,:,N(1)+1:numZSteps)./sepsY(:,:,N(1)
+1:numZSteps)) | abs(stressYx(:,:,N(1)+1:numZSteps)) > donTensStre/sqrt(3) |
abs(stressYz(:,:,N(1)+1:numZSteps)) > donTensStre/sqrt(3));
dSnapZ(:,:,1:N(1)-1) = dSnapZ(:,:,1:N(1)-1) + reducFac*(((vMz(:,:,1:N(1)-1) >
carrTensStre) & restLengthsZ(:,:,1:N(1)-1)/2 < absSepsZ(:,:,1:N(1)-
1).*intPosZ(:,:,1:N(1)-1)./sepsZ(:,:,1:N(1)-1)) | abs(stressZx(:,:,1:N(1)-1))
> carrTensStre/sqrt(3) | abs(stressZy(:,:,1:N(1)-1)) > carrTensStre/sqrt(3));
dSnapZ(:,:,N(1)) = dSnapZ(:,:,N(1)) + reducFac*(((vMz(:,:,N(1)) >
interTensStre) & restLengthsZ(:,:,N(1))/2 <
absSepsZ(:,:,N(1)).*intPosZ(:,:,N(1))./sepsZ(:,:,N(1))) |
abs(stressZx(:,:,N(1))) > interTensStre/sqrt(3) | abs(stressZy(:,:,N(1))) >
interTensStre/sqrt(3));
dSnapZ(:,:,N(1)+1:numZSteps-1) = dSnapZ(:,:,N(1)+1:numZSteps-1) +
reducFac*(((vMz(:,:,N(1)+1:numZSteps-1) > donTensStre) &
restLengthsZ(:,:,N(1)+1:numZSteps-1)/2 < absSepsZ(:,:,N(1)+1:numZSteps-
1).*intPosZ(:,:,N(1)+1:numZSteps-1)./sepsZ(:,:,N(1)+1:numZSteps-1)) |
abs(stressZx(:,:,N(1)+1:numZSteps-1)) > donTensStre/sqrt(3) |
abs(stressZy(:,:,N(1)+1:numZSteps-1)) > donTensStre/sqrt(3));

tensX(tensX < 0 & interSnapX~=0) = 0;% try just setting snapped springs to 0
tension if under extension
tensY(tensY < 0 & interSnapY~=0) = 0;
tensZ(tensZ < 0 & interSnapZ~=0) = 0;
cantXy(interSnapX~=0) = 0;
cantXz(interSnapX~=0) = 0;
cantYx(interSnapY~=0) = 0;
cantYz(interSnapY~=0) = 0;
cantZx(interSnapZ~=0) = 0;
cantZy(interSnapZ~=0) = 0;

% define total forces acting on each mass in each direction
forceX = zeros(numYSteps,numXSteps,numZSteps);
forceX(:,2:numXSteps,:) = tensX;
forceX(:,1:numXSteps-1,:) = forceX(:,1:numXSteps-1,:) - tensX;
forceX(2:numYSteps,:,:) = forceX(2:numYSteps,:,:) + cantYx;
forceX(1:numYSteps-1,:,:) = forceX(1:numYSteps-1,:,:) - cantYx;
forceX(:,:,2:numZSteps) = forceX(:,:,2:numZSteps) + cantZx;
forceX(:,:,1:numZSteps-1) = forceX(:,:,1:numZSteps-1) - cantZx;

forceY = zeros(numYSteps,numXSteps,numZSteps);
forceY(:,2:numXSteps,:) = cantXy;
```

```matlab
forceY(:,1:numXSteps-1,:) = forceY(:,1:numXSteps-1,:) - cantXy;
forceY(2:numYSteps,:,:) = forceY(2:numYSteps,:,:) + tensY;
forceY(1:numYSteps-1,:,:) = forceY(1:numYSteps-1,:,:) - tensY;
forceY(:,:,2:numZSteps) = forceY(:,:,2:numZSteps) + cantZy;
forceY(:,:,1:numZSteps-1) = forceY(:,:,1:numZSteps-1) - cantZy;

forceZ = zeros(numYSteps,numXSteps,numZSteps);
forceZ(:,2:numXSteps,:) = cantXz;
forceZ(:,1:numXSteps-1,:) = forceZ(:,1:numXSteps-1,:) - cantXz;
forceZ(2:numYSteps,:,:) = forceZ(2:numYSteps,:,:) + cantYz;
forceZ(1:numYSteps-1,:,:) = forceZ(1:numYSteps-1,:,:) - cantYz;
forceZ(:,:,2:numZSteps) = forceZ(:,:,2:numZSteps) + tensZ;
forceZ(:,:,1:numZSteps-1) = forceZ(:,:,1:numZSteps-1) - tensZ;

% change forces to accelerations
forceX(:,:,1:N(1)) = forceX(:,:,1:N(1))./m(1);
forceX(:,:,N(1)+1:N(1)+N(2)) = forceX(:,:,N(1)+1:N(1)+N(2))./m(2);
forceY(:,:,1:N(1)) = forceY(:,:,1:N(1))./m(1);
forceY(:,:,N(1)+1:N(1)+N(2)) = forceY(:,:,N(1)+1:N(1)+N(2))./m(2);
forceZ(:,:,1:N(1)) = forceZ(:,:,1:N(1))./m(1);
forceZ(:,:,N(1)+1:N(1)+N(2)) = forceZ(:,:,N(1)+1:N(1)+N(2))./m(2);

% look into thermal boundary conductance - massive headache, but may be
% necessary.
dTdX = diff(temps,1,2)/xyStep;% think thermal conductivity changes inversely
with stretch, so the 'step length' interested in should be kind of static
with expansion
dTdY = diff(temps,1,1)/xyStep;
dTdZ = diff(temps,1,3);
dTdZ(:,:,1:N(1)-1) = dTdZ(:,:,1:N(1)-1)/carrZStep;
dTdZ(:,:,N(1)) = 2*dTdZ(:,:,N(1))/(carrZStep+donZStep);% special case at
interface, this should really be based on thermal boundary conductance, but
can't find any useful values
dTdZ(:,:,N(1)+1:numZSteps-1) = dTdZ(:,:,N(1)+1:numZSteps-1)/donZStep;

% negligible heat flow between broken springs
dTdX(interSnapX~=0) = 0;% reduce heat flow between any springs currently
beyond UTS
dTdY(interSnapY~=0) = 0;
dTdZ(interSnapZ~=0) = 0;

heatFlow = zeros(numYSteps,numXSteps,numZSteps);
% calc total heat entering each point mass via x transmission
heatFlow(:,2:numXSteps,1:N(1)) = -
thermConds(1)*carrLatIntfac*dTdX(:,:,1:N(1));% heat gained from below (-ve x,
not 'below', but whatever)
heatFlow(:,1:numXSteps-1,1:N(1)) = heatFlow(:,1:numXSteps-1,1:N(1)) +
thermConds(1)*carrLatIntfac*dTdX(:,:,1:N(1));% heat lost to above,
+thermConds this time because adding heat flow in opposite direction to +ve
temp gradient direction
heatFlow(:,2:numXSteps,N(1)+1:numZSteps) =
heatFlow(:,2:numXSteps,N(1)+1:numZSteps) -
thermConds(2)*donLatIntfac*dTdX(:,:,N(1)+1:numZSteps);
heatFlow(:,1:numXSteps-1,N(1)+1:numZSteps) = heatFlow(:,1:numXSteps-
1,N(1)+1:numZSteps) + thermConds(2)*donLatIntfac*dTdX(:,:,N(1)+1:numZSteps);%
-thermConds this time because adding heat flow in opposite direction to +ve
temp gradient direction
```

```matlab
% calc total heat entering each point mass via y transmission
heatFlow(2:numYSteps,:,1:N(1)) = heatFlow(2:numYSteps,:,1:N(1)) -
thermConds(1)*carrLatIntfac*dTdY(:,:,1:N(1));
heatFlow(1:numYSteps-1,:,1:N(1)) = heatFlow(1:numYSteps-1,:,1:N(1)) +
thermConds(1)*carrLatIntfac*dTdY(:,:,1:N(1));% -thermConds this time because
adding heat flow in opposite direction to +ve temp gradient direction
heatFlow(2:numYSteps,:,N(1)+1:numZSteps) =
heatFlow(2:numYSteps,:,N(1)+1:numZSteps) -
thermConds(2)*donLatIntfac*dTdY(:,:,N(1)+1:numZSteps);
heatFlow(1:numYSteps-1,:,N(1)+1:numZSteps) = heatFlow(1:numYSteps-
1,:,N(1)+1:numZSteps) +
thermConds(2)*donLatIntfac*dTdY(:,:,N(1)+1:numZSteps);% +thermConds this time
because adding heat flow in opposite direction to +ve temp gradient direction
% calc total heat entering each point mass via z transmission
heatFlow(:,:,2:N(1)) = heatFlow(:,:,2:N(1)) -
thermConds(1)*vertIntfac*dTdZ(:,:,1:N(1)-1);% special case here of only going
up to N(1)-1 because I'm fudging thermal boundary conductance by saying it's
only the lower conductance that matters at the interface
heatFlow(:,:,1:N(1)-1) = heatFlow(:,:,1:N(1)-1) +
thermConds(1)*vertIntfac*dTdZ(:,:,1:N(1)-1);% might start to get non-energy
conservation here...
heatFlow(:,:,N(1)) = heatFlow(:,:,N(1)) +
thermConds(2)*vertIntfac*dTdZ(:,:,N(1));% special case where carrier loses
energy to above at max rate that donor can accept, hopefully irons out energy
conservation
heatFlow(:,:,N(1)+1:numZSteps) = heatFlow(:,:,N(1)+1:numZSteps) -
thermConds(2)*vertIntfac*dTdZ(:,:,N(1):numZSteps-1);% gain heat from below
heatFlow(:,:,N(1)+1:numZSteps-1) = heatFlow(:,:,N(1)+1:numZSteps-1) +
thermConds(2)*vertIntfac*dTdZ(:,:,N(1)+1:numZSteps-1);% lose heat to above

dT = heatFlow;
dT(:,:,1:N(1)) = dT(:,:,1:N(1))./(specHeats(1)*m(1));
dT(:,:,N(1)+1:numZSteps) = dT(:,:,N(1)+1:numZSteps)./(specHeats(2)*m(2));

if rigEdgeCheck % set base and sides (not top) to zeros for velocity, force
    setZero = false(numYSteps,numXSteps,numZSteps);
    setZero(:,[1,numXSteps],:) = true;
    setZero([1,numYSteps],:,:) = true;
    setZero(:,:,1) = true;

    vx(setZero) = 0;
    vy(setZero) = 0;
    vz(setZero) = 0;
    forceX(setZero) = 0;
    forceY(setZero) = 0;
    forceZ(setZero) = 0;

end

dq =
reshape(cat(4,vx,vy,vz,forceX,forceY,forceZ,dT,dSnapX,dSnapY,dSnapZ),totSprin
gs*10,1);

end
```

Appendix C

OPC automation description

In this appendix, a more detailed explanation of the algorithm used to generate automated Optical Proximity Corrections is given. The information follows on from the example figures and values used in section 6.4, and refers initially to the field in Figure 6.11(b) as the 'resultant field' after a DMD mask have been imaged through an aperture.

Suppose the resultant field acts on a sample whose ablation threshold is some arbitrary value (in this case the mean of the absolute resultant field value less 0.1 times the standard deviation of points within the intended ideal field positions, a value chosen purely for example, and not deliberately reflecting a real physical threshold). Above this threshold, make the approximation that the ablation depth is linear with field amplitude (a very simple model to demonstrate the effect of an ablation threshold). The depth profile would then appear similar to that shown in Figure C.1; almost unrecognisable from the original intensity mask in Figure 6.11(a).
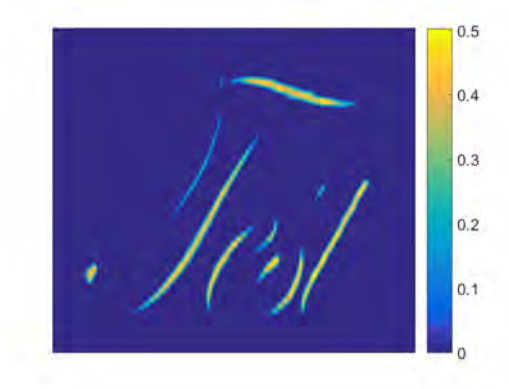
Figure C.1: The theoretical depth profile of a material, in arbitrary units, after exposure to a field imaged through an aperture.

The inherent thresholding in material responses allows intuitive pre-processing of the resultant field in Figure 6.11(b) before back-propagation to the mask position. Rather than attempting to bring the resultant field to an exact recreation of the intensity mask, it may be satisfactory to bring the field amplitude within the ideal field point positions

within a certain range of the mean, while any extraneous intensity may be tolerable below a certain threshold outside of the ideal field point positions. With this in mind, the resultant field in Figure 6.11(b) was thresholded to give three corrective terms. Figure C.2(a) shows the field associated with 'cold spots', namely points within the ideal field position whose amplitude is below threshold, with amplitude given by the difference between threshold and current value; their phase is given by the phase of the resultant field . Figure C.2(b) shows 'hot external spots', any points outside the ideal field positions whose amplitude is above threshold (0.1 times the standard deviation below the mean, very few points visible reached this value in the example); amplitude given by difference between current value and threshold, phase given by resultant field at each point. Finally, Figure C.2(c) shows 'hot internal spots', points within the ideal image field whose value is above an arbitrary maximum; value given by amplitude above this maximum compared to the resultant field, phase given by the phase of the resultant at each point (in this case set as the 0.1 times the standard deviation above mean of the resultant field values at intended ideal image points).

(a) 'Cold spots' in the resultant field

(b) 'Hot external spots' in the resultant field

(c) 'Hot internal spots' in the resultant field
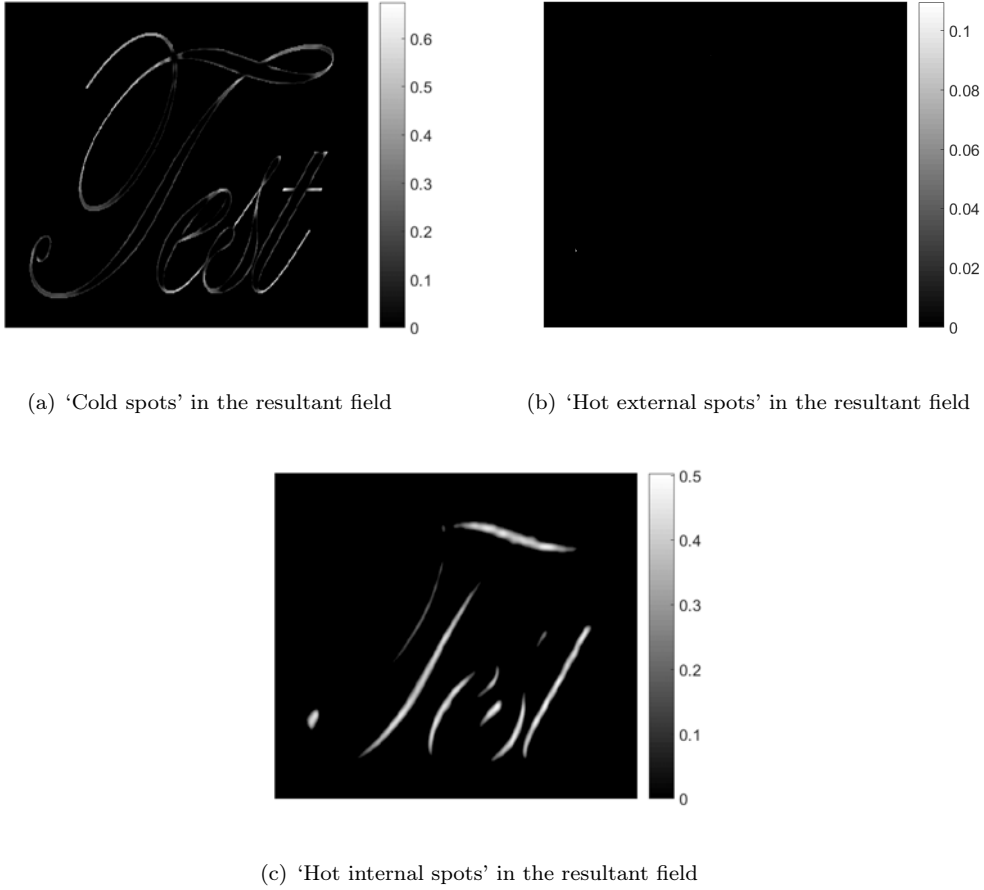
Figure C.2: The absolute values of the various corrective fields generated by thresholding the resultant field in Figure 6.11(b), in arbitrary units.
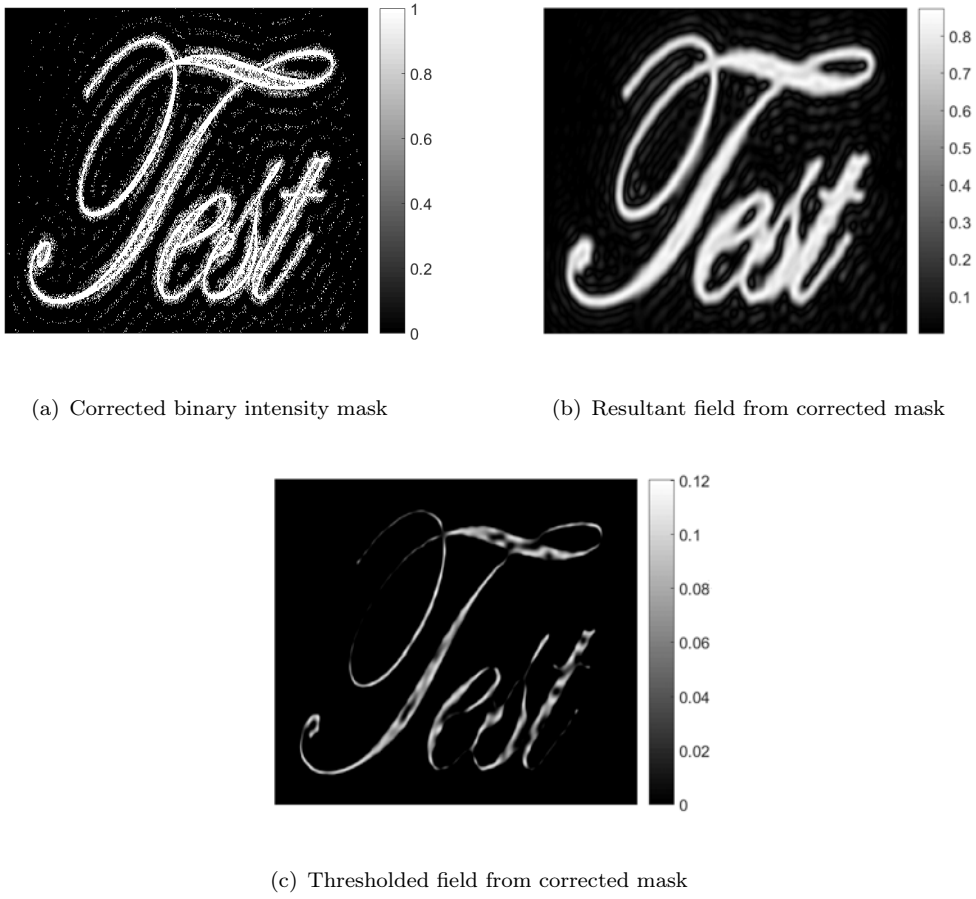
By back-propagating a linear combination of these fields (in practice the cold spots minus both hot spots), and adding it to the field at the mask plane (which on the first iteration is binary valued and purely real), a new, complex field at the mask position

is simulated. The problem then arises of how to represent a complex field on a binary intensity mask. One approach, used in the generation of so-called 'binary holograms' [162], is to set any pixels at the mask plane whose phase, ϕ, falls within the range $-\pi/2 \leq \phi \leq \pi/2$ to 'on', while those outside the range are set to 'off'. While this approach may be worth exploring, an alternate approach depending upon both phase and amplitude has been developed, and will be referred to as Random Complex Summation (RCS). A two-dimensional matrix M of the same size as the array of complex field values is defined on the interval [0,1]. Complex field values are reduced to real values by simply summing the real with imaginary parts, i.e. $0.5 + 0.5i \rightarrow 1$, $0.6 - 0.2i \rightarrow 0.4$, and compared to the corresponding value in M. If the reduced real value of the field exceeds the value given in M, the value in the binary mask is set to 1, while it is set to 0 otherwise.

Although no formal derivation for the success of the RCS algorithm has been made, it is likely based on similar principles to binary-rounding. In binary-rounding, switching on pixels which are in phase will reflect coherent light such that it will constructively interfere to form a hologram image. In RCS, field values where both real and imaginary parts are positive are most likely to exceed the random threshold between 0 and 1 set in M. Positive values only result from the reduction method in RCS from complex values with phases in the interval $-\pi/4 \leq \phi \leq 3\pi/4$, effectively the same range of phase values as in binary-rounding. The fundamental difference between binary-rounding and RCS then, is that in binary-rounding any field value in the desired phase range will *certainly* be set to 1, while in RCS the probability of being set to 1 varies with phase and amplitude, even within the phase range where a positive reduced value is certain.

The RCS algorithm then allows for small perturbations to an intensity mask by reducing a complex field to binary values, effectively confining changes to regions where large field changes were made – such as those generated by the back-propagation of the corrective fields here. A final piece of the OPC automation to consider, is that the flat-top illuminated area of a DMD may be limited, as in section 6.2. For this example, only pixels within a circle of radius 320 pixels at the centre of the DMD were allowed to be switched on for successive iterations of the algorithm, which corresponded approximately to the illuminated region of the DMD seen in Figure 2.11.

The algorithm proceeds by generating updated corrective fields, as in Figure C.2, back-propagating to the mask plane and generating a binary intensity mask through RCS, before forward propagating in the next iteration. Simulated results are shown in Figure C.3, using 100 iterations and thresholds as stated previously.

(a) Corrected binary intensity mask

(b) Resultant field from corrected mask

(c) Thresholded field from corrected mask

Figure C.3: The resulting binary mask, apertured field and material response.

The resultant field in Figure C.3(b) appears to contain significant intensity outside the intended region, however this is misleading for the success of the technique when a threshold is applied, as in Figure C.3(c). Comparing this thresholded response to that shown as a result from an uncorrected mask, as in Figure C.1, there has been a marked improvement in the fidelity of simulated material response. The corrected binary mask shown in Figure C.3(a) was used displayed under a continuous train of ultrafast pulses and imaged through a near-closed aperture onto a CMOS camera to produce the resulting corrected image seen in Figure 6.12(d).

Appendix D

Binary hologram discussion

In this appendix, a more detailed comparison of the RCSH and GSBR algorithms used to produce binary holograms and introduced in section 6.5 is given. Additional modes of functionality are shown, as well as an expanded level of consideration given to some aspects of the technique. The work was not included in the main body of the thesis as it has yet to produce experimental laser machining results, but has formed the basis of a successful application for a Doctoral Prize Award, which will provide 1 year of funding for its development and application to laser machining.

In the ordinary Gerchberg-Saxton algorithm, an intensity distribution is known at the image plane, but not at the object plane, while phase distribution is free to vary at both planes. For the generation of a binary hologram, however, it is required that all points at the object plane are in phase (or varying only due to the beam illuminating the DMD), while amplitude is zero or one (up to a uniform multiplier). Approximation of the complex field via binary-rounding at the object plane sets this condition, while the known intensity at the image plane is set by a target hologram field distribution. Otherwise, the basic steps of the Gerchberg-Saxton algorithm remain; a field is propagated back and forth between image and object plane (in this case by ASM), imposing the phase of the currently achieved field on the amplitude of the target field at the image plane after each iteration. Unlike the steps in Figure 6.2, HIO and shrink-wrap steps are not applied. HIO is the technique of averaging a previous field at the object plane with a current field, which would clearly be problematic when binary values are required at the object plane. Shrink-wrapping is unnecessary, as the only restraint at the object plane on the extent of the 'object' is the available region of the DMD illuminated by top-hat intensity, which will be known from the outset.

The RCSH method more closely follows the example of section 6.4, in that a corrective perturbation field is calculated at the image plane by comparing a currently achieved field to an ideal field, and back-propagating to the object plane. The perturbations are added after each iteration to a complex field at the object plane, and then converted to a binary mask via RCS. The initial guess for a mask at the object plane is made by back-propagating the ideal field, and generating a mask via RCS. A key advantage of

the RCSH method over GSBR is that in GSBR the phase of the field at the image plane *must* be allowed to vary – a property fundamental to the Gerchberg-Saxton algorithm – and so phase control at the image plane is impossible with GSBR. In RCSH, one may choose to apply the phase of the current image iteration to the corrective perturbation as in section 6.4, allowing phase at the image plane to vary in order to achieve an ideal amplitude distribution, *or* one may choose to generate the corrective perturbation by comparing the current complex field at the image plane to a target complex field. In practice, there is some tradeoff between amplitude and phase reproduction made here, though the quantitative impact has not been well investigated. Note that thresholding as in section 6.4 is not applied for RCSH, as no aperturing is assumed to occur here.

The simulated results presented here continue on from the end of section 6.5.1, where it was shown that the GSBR and RCSH methods produce different field amplitudes at the image plane. This was a result of the GSBR algorithm generating a binary hologram based purely on phase, while RCSH allows dependence on the amplitude of an intended field.

D.1 Peak intensity control

To show the change in recreated amplitude with intended amplitude, the same square of amplitude 2au was used as a target image. The produced mask and image via RCSH are shown in Figure D.1; a peak amplitude of around 1.1 is reached, almost corresponding to the intended doubling of the target field.

(a) Binary hologram after 100 iterations

(b) Image at 10cm of final hologram
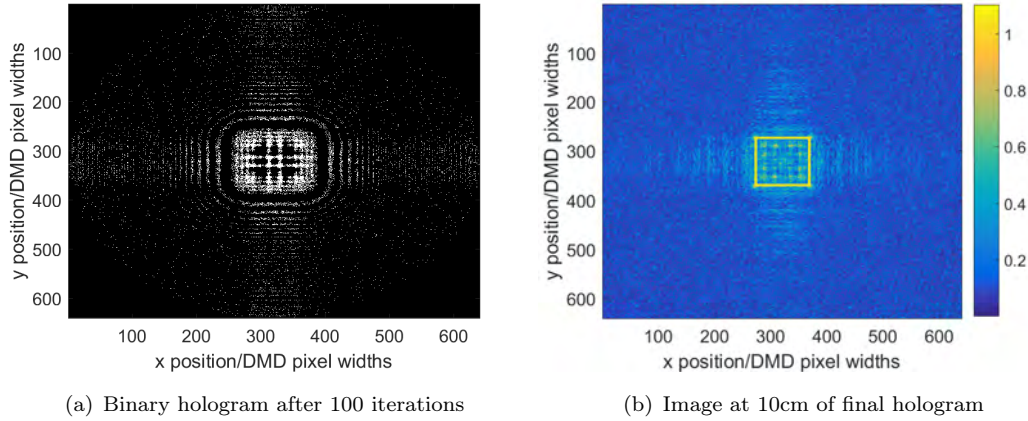
Figure D.1: Binary hologram and resulting image of a hollow square with intended amplitude of 2au as simulated with the RCSH algorithm.

This control over the absolute intensity of a recreated image is an advantage of the RCSH method. The GSBR algorithm, however, achieves the highest possible peak intensity with a binary hologram approach, as all available DMD pixels which would reflect light to constructively interfere at the image position are turned on. by taking

a probabilistic approach to turning on pixels which would constructively interfere, the RCSH approach would, at maximum intensity, turn on the same pixels as the GSBR algorithm, in accordance with the random complex summation method described in section 6.4.

While only the RCSH method controls absolute intensity in an intended image, both methods are capable of producing near-continuous *relative* intensities within an image. This functionality is explored in the next section.

D.2 Greyscale control

The ability to holographically represent continuous intensity distributions with a binary hologram would allow for the same machining advantages as seen in section 6.3. In order to test the algorithms' aptitude for reconstructing multi-level, complex intensity distributions, a similar test image to the stylised 'test' mask from Figure 6.11(a) will be used – the only difference being all features on the right hand side of the image are intended to be at $1/\sqrt{(2)}$ of those on the left, with a sharp step change at the midpoint, as shown in Figure D.2 highlighted by a dashed red line. The factor of $1/\sqrt{(2)}$ in the intended field is used so that the step change in the intensity distribution would be a factor of $1/2$.
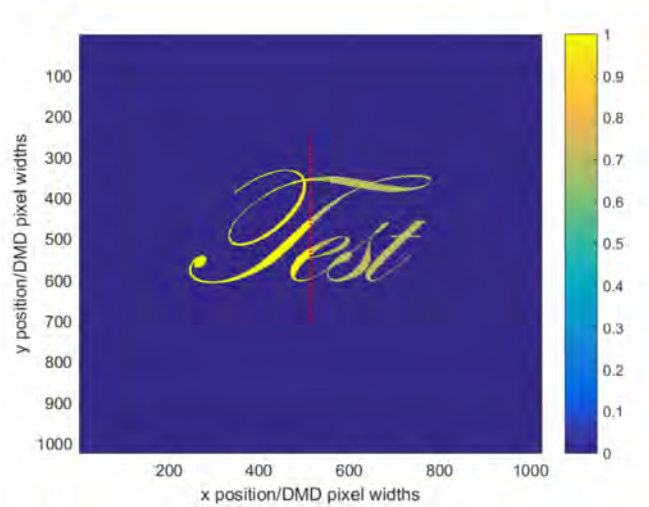
Figure D.2: The intended field amplitude distribution to be used in binary hologram generation, all points in the right half of the image have value $1/\sqrt{(2)}$, while those on the left have value 1. The dashed red line shows the position of the step change.

The resulting masks and final field distributions are shown in Figure D.3. While both techniques result in a successful reproduction of the target image with a step change, the contrast appears more stark in the RCSH image. By taking the mean of absolute field values at all points within the intended image on left and right sides for both the RCSH and GSBR results, it was found that the step change seen in the RCSH image

192

corresponded to a factor of 0.7089, and the step change in the GSBR image to a factor of 0.7887. As $1/\sqrt{(2)} \approx 0.7071$, the RCSH produces a step change error of only 0.25%, while the GSBR gives an error of over 11.5%.

(a) Binary hologram produced by GSBR

(b) Absolute field value from GSBR hologram at 10cm from object plane

(c) Binary hologram produced by RCSH

(d) Absolute field value from RCSH hologram at 10cm from object plane
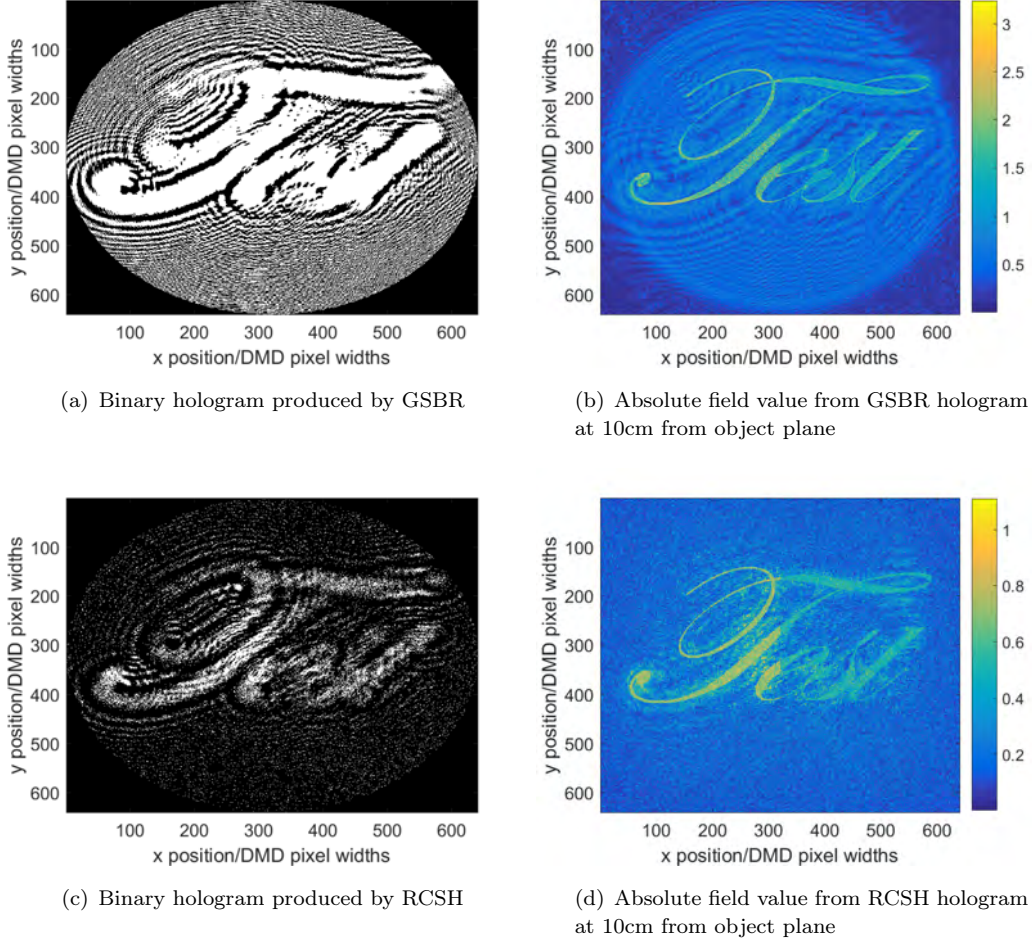
Figure D.3: Binary holograms and resulting images of a greyscale field.

The greyscale control offered by these binary hologram approaches would allow the laser ablation of '2.5D' structures in the surface of materials, similar to those in section 6.3. However, the images from these holograms are still confined to a single plane. In order to machine at multiple depths simultaneously, for instance over a non-flat surface or throughout the volume of a multi-photon resist, the projection of fully 3D intensity distributions is desirable. Additionally, digital control of the image plane depth would mean that the maintenance of focal depth could be removed from the ≈micron accurate translation stages, and instead performed via a combination of interferometric sample depth measurement and hologram generation. The production of such 3D intensity control will be shown in the next section.

D.3   3D field control

Holograms are a natural choice for representing 3D information on a 2D surface, and so the extension of binary holograms to the production of 3D images is a fairly straightforward one. In both algorithms until now, fields have been propagated back and forth between an object and image plane, with some modifications made at each plane (binary rounding or random complex summation at the object plane, imposing updated phase to a set amplitude distribution or calculating a corrective field at the image plane). To extend to multiple depths, or 3D images, a 3D field distribution is simply broken down into 2D slices, representing multiple image planes to be used at each iteration of the algorithm.

Figure D.4 shows the binary holograms and images produced with both methods for the same intended 3D field distributions. The intended field takes a simple form: two hollow squares of equal dimensions to those in section 6.5.1, laterally separated such that the bottom right corner of one is at the top left corner of the other, separated in depth. The first square is intended to be imaged at 7.5cm from the DMD surface, while the second is to be imaged at 12.5cm away from the DMD.
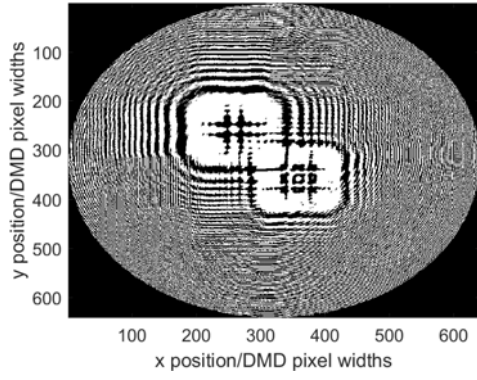
(a) Binary hologram from GSBR
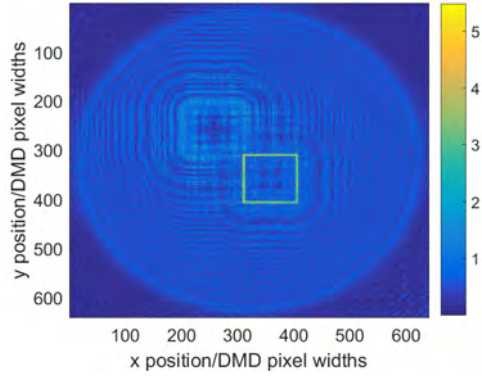
(b) Image at 7.5cm from GSBR
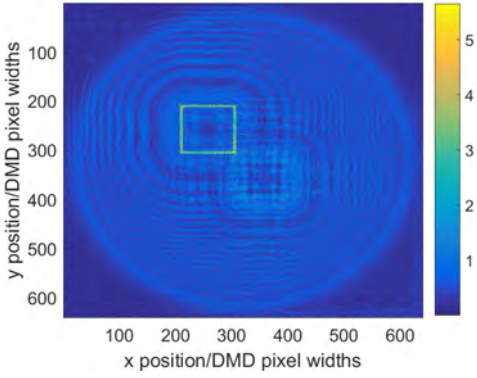
(c) Image at 12.5cm from GSBR
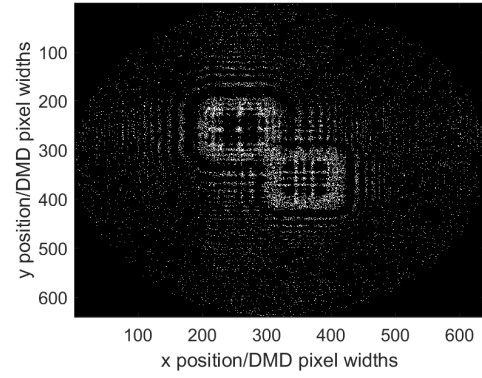
(d) Binary hologram from RCSH
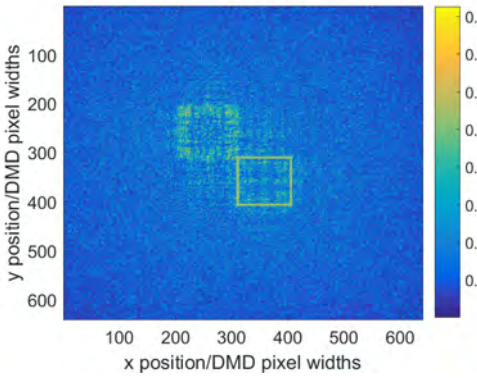
(e) Image at 7.5cm from RCSH
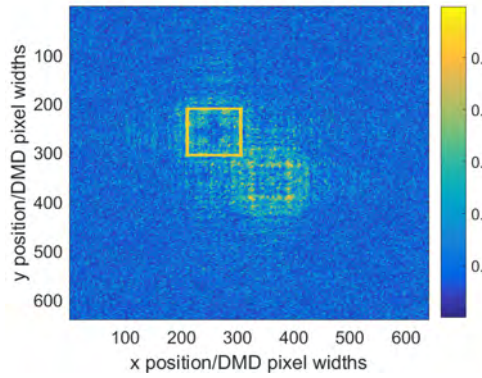
(f) Image at 12.5cm from RCSH

Figure D.4: Binary holograms and resulting images of hollow squares at two depths separated by 5cm from both methods.

Again, both methods reliably succeed at producing the intended distributions. However, interference fringes are apparent in the intended flat hollow square regions from the GSBR hologram in Figures D.4(b) and D.4(c), and 'bright spots' of diffracted high intensity are evident outside the intended flat square regions from the RCSH hologram in Figures D.4(e) and D.4(f). These bright spots appear in the lateral regions occupied by the 'currently out of focus' square, i.e. at the 12.5cm plane there are bright spots in the lateral positions of the square which is imaged at 7.5cm, and vice versa. Though

195

the diffracted fields from the 'out of focus' squares is visible in the GSBR images, they are distributed such that they are low intensity compared to the currently 'in focus' square. Why these particular drawbacks and advantages occur is not yet determined.

The squares at each depth were intended to be of equal intensity; once more measuring the mean absolute field and standard deviations gives a measure of the success of the techniques. The mean intensities for the squares at 7.5cm and 12.5cm were, respectively, for the GSBR method: 3.220 and 3.047, and for the RCSH: 0.5242 and 0.5251. The normalised standard deviations then were, in the same order, 0.1681, 0.2490, 0.0733 and 0.0478. Both algorithms perform more poorly in these measures than for a single-plane image, but the RCSH continues to show significantly smaller errors. Figure D.5 shows the resulting images for a smaller separation in depth, with images intended to form at 9.5cm and 10.5cm.

(a) Image at 9.5cm from GSBR

(b) Image at 10.5cm from GSBR

(c) Image at 9.5cm from RCSH
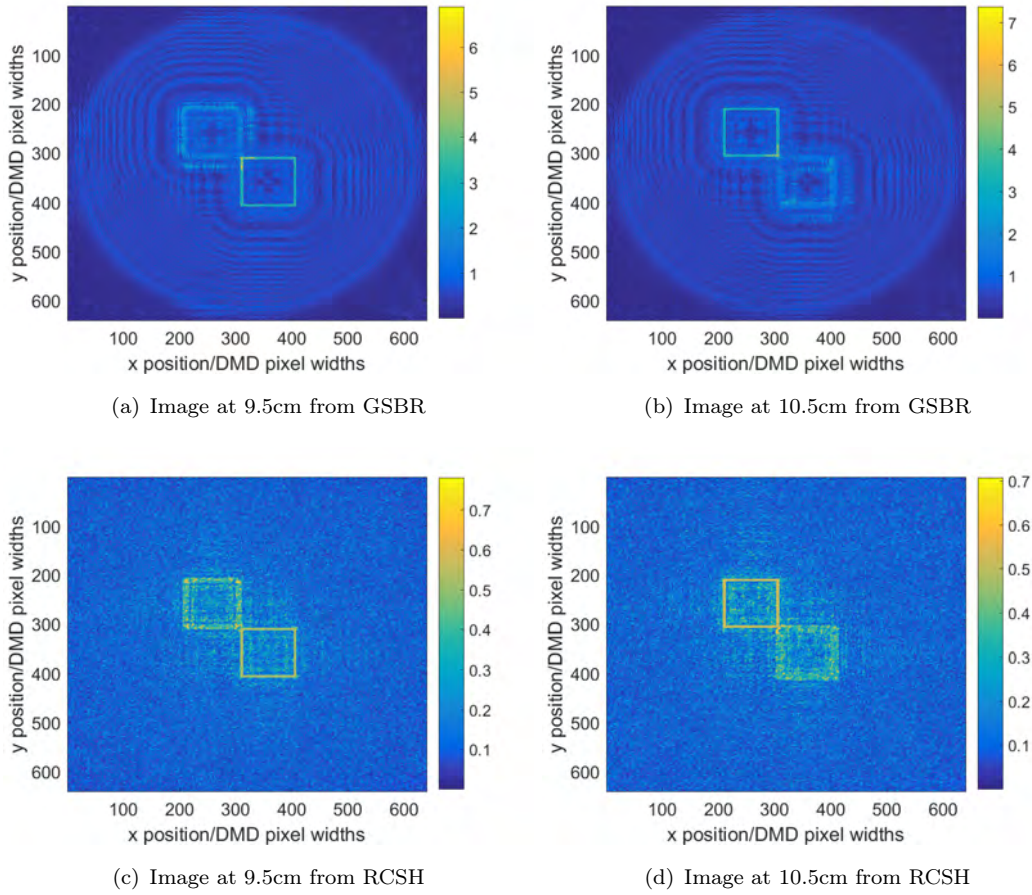
(d) Image at 10.5cm from RCSH

Figure D.5: Resulting images of hollow squares at two depths separated by 1cm from both methods.

The interference effects seen from the GSBR method are exacerbated; though similar average intensities are achieved, the normalised standard deviations have risen to 0.2356 and 0.2334. The mean intensity from the RCSH remain similar also, however the level

of normalised standard deviation has remained almost unchanged at 0.0621 and 0.0547.

D.4 Phase control

As stated at the beginning of this section, the RCSH method allows phase control. A simple demonstration of this is shown in Figure D.6; hollow squares laterally separated similarly to those in section D.2, but $\pi/2$ out of phase with each other are set as the target image.

(a) Binary hologram for hollow squares $\pi/2$ out of phase

(b) Real part of the field at the image plane

(c) Imaginary part of the field at the image plane

(d) Absolute value of the field at the image plane
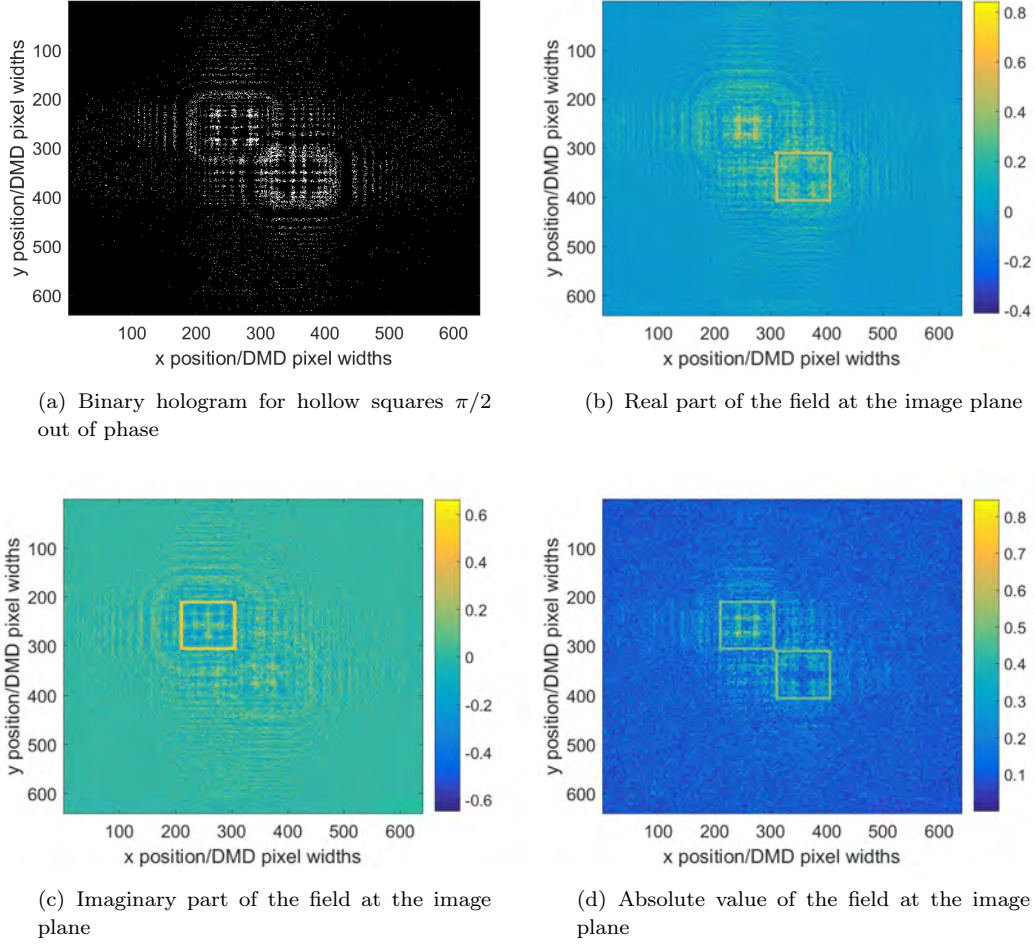
Figure D.6: Resulting images of hollow squares $\pi/2$ out of phase with each other at 10cm from the object plane.

The real part of the resultant image in Figure D.6(b) shows a near-uniform amplitude distribution, and the corresponding imaginary part of the field at this square's position in Figure D.6(c) is almost zero. Similarly, a purely imaginary square is clear in Figure D.6(c), whose corresponding real part in Figure D.6(b) is near zero. This shows that the technique has successfully controlled the phase across the target image. The absolute value of the field in Figure D.6(d) shows that the amplitude in both squares is close to

197

uniform. By requiring phase control, there is some tradeoff in the amplitude control; compared to the image in section 6.5.1, there is a greater degree of intensity outside the intended region.

D.5   Sub-pixel image shifting

Until now, both DMD mask and projected images have been represented on grids of identical size; this is a natural choice when simulating beam propagation with the ordinary ASM, as FFT algorithms typically return arrays equal to the input size. In section 6.2, the minimum lateral translation of an image with pure DMD control corresponded to shifting the entire mask by one pixel. Typically any DMD mask used in this thesis for imaging through an objective lens for micro-machining would be minified to the point that resolving even single pixels would be impossible under the diffraction limit. For these reasons, it has not been attempted to produce binary holograms to produce images of features below single-pixel widths, and beam simulation techniques for sub-pixel resolution has not been necessary. However, sub-pixel translation capabilities, moving below the limit seen in section 6.2, would be of great interest.

Consider attempting to produce a binary hologram of a single-pixel wide spot at some distance from the DMD, an example hologram and output intensity are shown in the diagram in Figure D.7. A grid of squares is laid out to represent the pixel positions of the DMD in the (x,y)-plane, with white mirrors representing 'on' pixels and black representing 'off'. The grid is retained in Figure D.7(b) to show the intensity distribution's relative position to the DMD grid. The binary hologram takes the form of simple concentric rings, and at the image plane a central spot of high intensity forms.

(a) Binary hologram   (b) Central small spot of high intensity
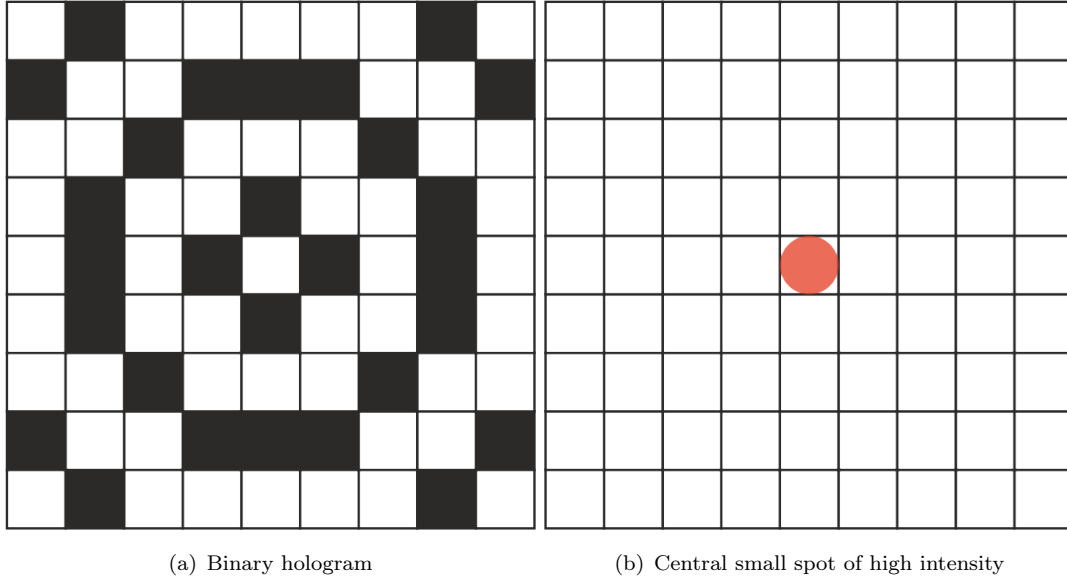
Figure D.7: Diagram of binary hologram and intensity at image plane for a focused spot.

198

Now suppose that one wishes to translate the central spot in Figure D.7(b) by a sub-pixel lateral distance to the left. Each white 'on' pixel in the hologram in Figure D.7(a) makes only a small contribution to the overall intensity distribution at the image plane, and so switching a single mirror between 'on' and 'off' states would likely shift the central lobe of intensity by a sub-pixel amount – a possible choice of a few mirror switches and resulting output intensity is shown in Figure D.8.

(a) Binary hologram

(b) Shifted, warped small spot of high intensity
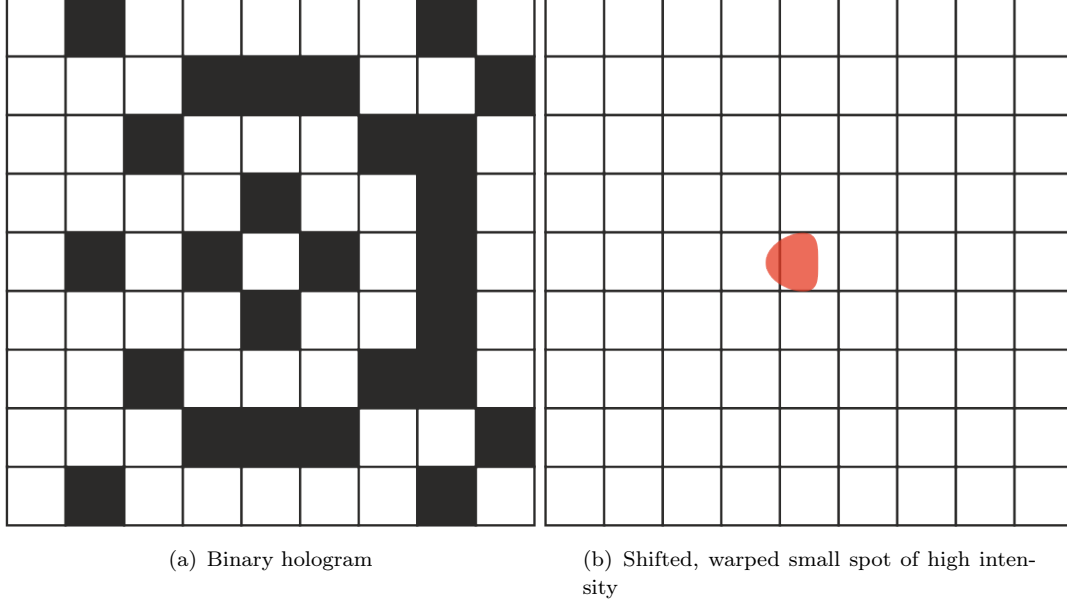
Figure D.8: Diagram of binary hologram and intensity at image plane for a focused spot with sub-pixel shift.

The central intensity position has been shifted left, as intended, in Figure D.8(b), by a sub-pixel amount. However, there was no prior knowledge of how much the chosen switched pixels would shift the image, and there has been a distortion to the shape of the intensity output. For binary hologram sub-pixel translations, a direct way of targeting a particular translation, without additional field distortion, is desirable. The Fourier Shift Theorem, given in equation 6.7, provides a rapid solution to this problem. Whereas in section 6.2 whole number solutions for Δx and Δy were sought (corresponding to whole number pixel shifts of an image), here *fractional* Δx and Δy values are inserted, and applied in Fourier space during ASM propagation steps. This effectively allows the ASM to output a display window of a propagated field offset in lateral directions by arbitrarily small amounts, while still using input and producing outputs of the same grid size, which is efficient computationally.

In steps of the RCSH and GSBR methods wherein the current field is compared to a target field, the output field from the DMD surface is shifted laterally by sub-pixel amounts such that it aligns with a well-defined pattern on a grid of the same size as the DMD itself. This is explained in Figure D.9; it is difficult to determine a set of values on the same size grid that would make an appropriate target image after BH propagation under ASM for an image which is not defined explicitly at the same lateral

positions as the DMD, but with a Fourier shift it becomes simple to define appropriate target images for the BH generation algorithms.
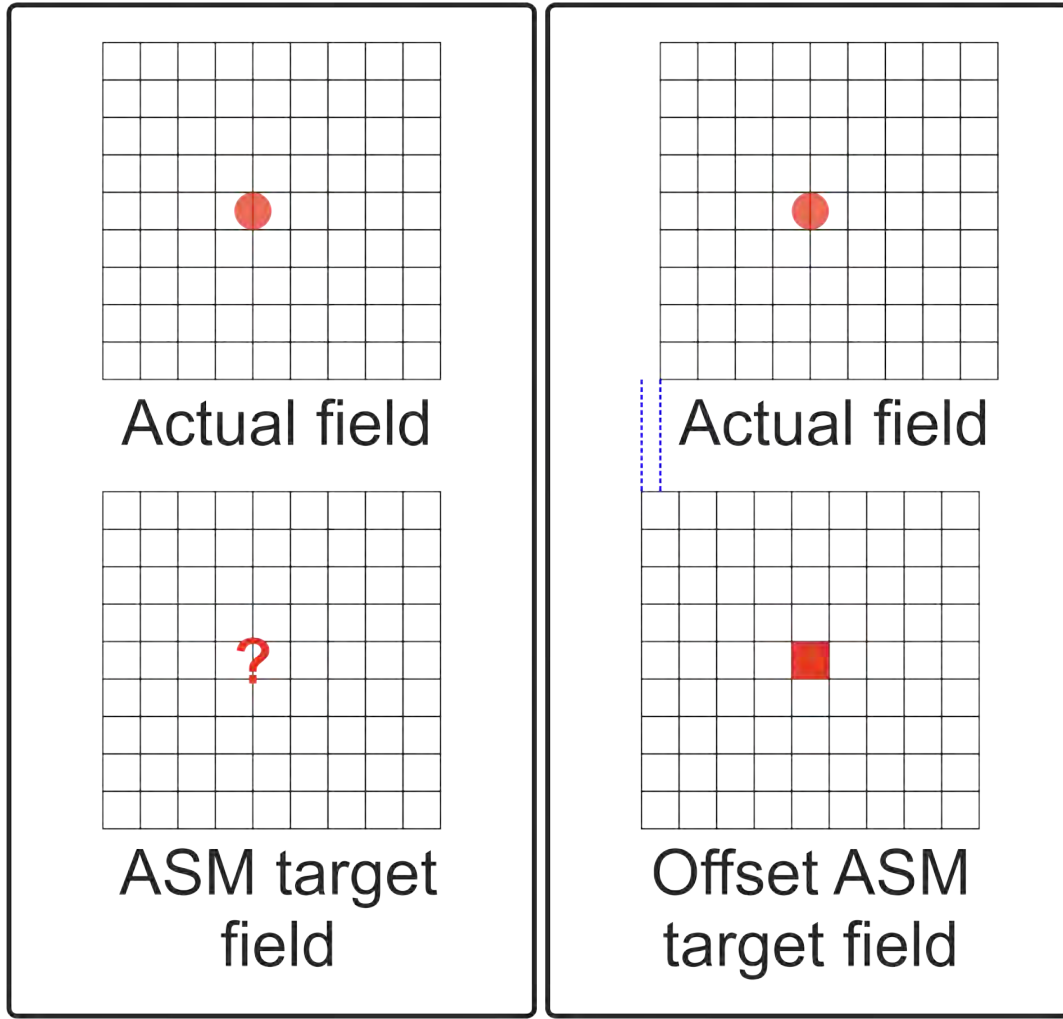
(a) For a focused spot located laterally between two DMD pixel positions, it is difficult to define field values for a target image

(b) By shifting the output window of the ASM, it becomes simple to define a target image for such a spot location

Figure D.9: Diagram of target image versus real image with and without a Fourier shift step in the ASM.

With this technique applied for both BH generation techniques, holograms designed to produce images of single-pixel wide spots at a set distance (10cm) from the DMD surface were generated, with sub-pixel relative shifts between the spot positions. A straightforward, but computationally expensive, method to simulate whether the holograms recreated spots at the intended locations was to interpolate each binary hologram to a larger grid, and use the ASM to propagate the field with an appropriately reduced pixel measurement. For instance, after generating a mask to be displayed on a 1024 by 1024 DMD of 10μm wide pixels which would produce a spot shifted by 1/2 a pixel width, a new array of 2048 by 2048 points would be defined, where each 'on' pixel in the original mask would correspond to a block of 2 by 2 'on' pixels in the new array, and the pixel width would be reduced to 5μm. The central region of interest in the image

plane is shown for four focused spot images, each intended to be shifted relatively by 1/4 of a DMD pixel, with the RCSH method, in Figure D.10.

(a) First image

(b) Shifted by 1/4 DMD pixel

(c) Shifted by 1/4 DMD pixel

(d) Shifted by 1/4 DMD pixel
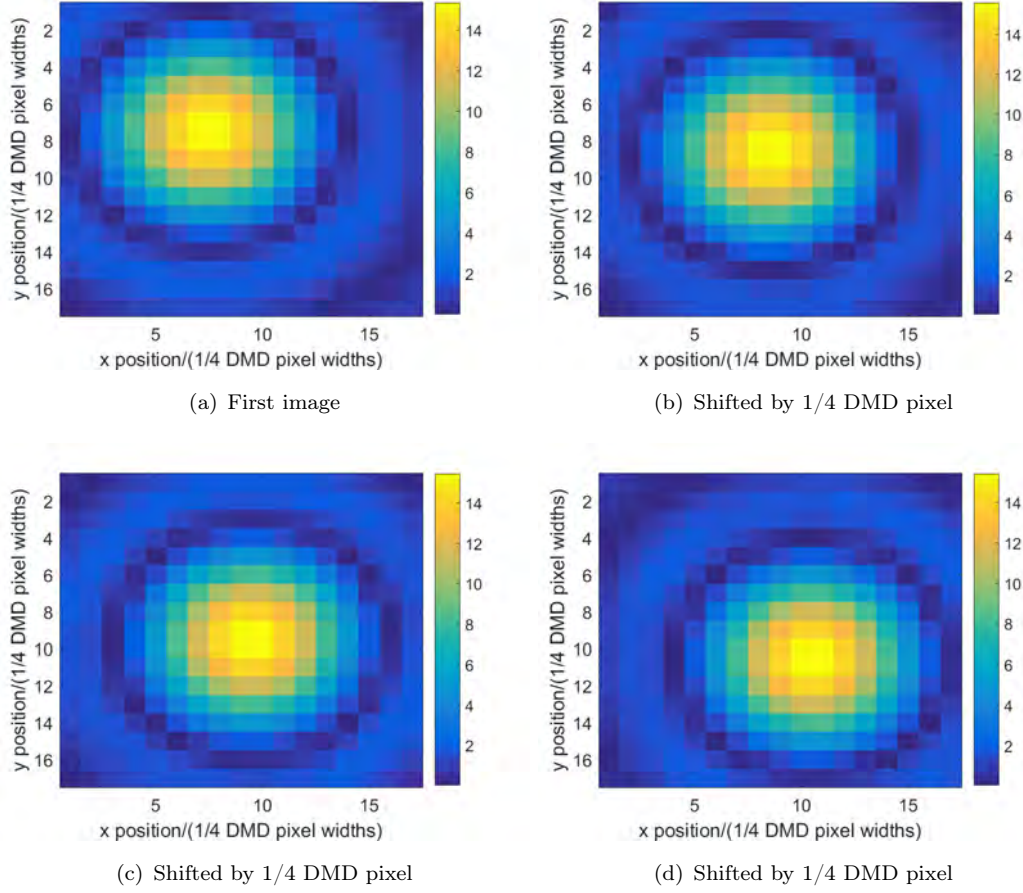
Figure D.10: Images of pixel-wide spots shifted by quarters of a DMD pixel via the RCSH method.

The method appears to work well. Between each image, the 1 DMD-pixel wide spot (equal to four pixels in the displayed images, as the holograms were expanded before ASM propagation) appears to maintain the same shape, while translating 1/4 of a DMD pixel width between images. The GSBR method produces similar fidelity in Figure D.11.

(a) First image

(b) Shifted by 1/4 DMD pixel

(c) Shifted by 1/4 DMD pixel

(d) Shifted by 1/4 DMD pixel
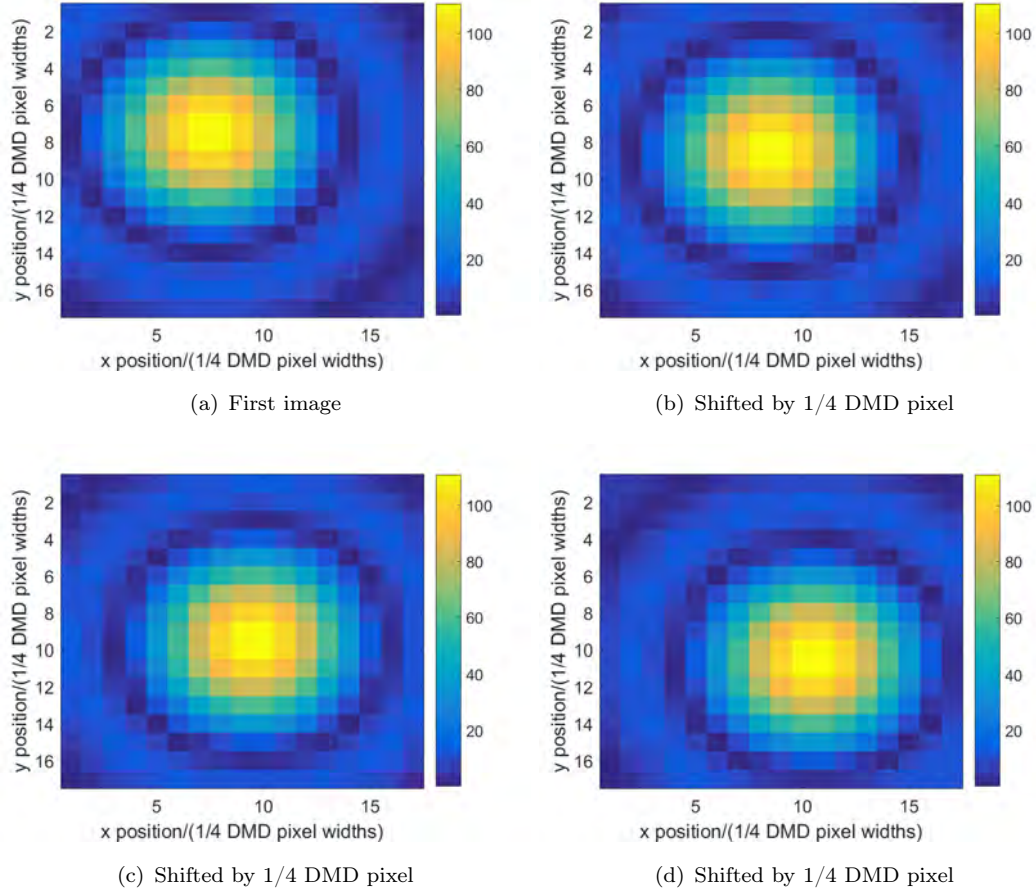
Figure D.11: Images of pixel-wide spots shifted by quarters of a DMD pixel via the GSBR method.

In order to more accurately measure the centre of intensity, a centre-of-mass style calculation is used. The fields are thresholded above half their maximal values (to remove aliasing effects at the edges of the arrays), before multiplying the absolute field value by its x and y position in the output image, summing, and dividing by the total absolute field value. Plots of the deviation from the intended positions of output x and y positions versus the intended x and y positions for the quarter-pixel shifting are shown in Figure D.12.
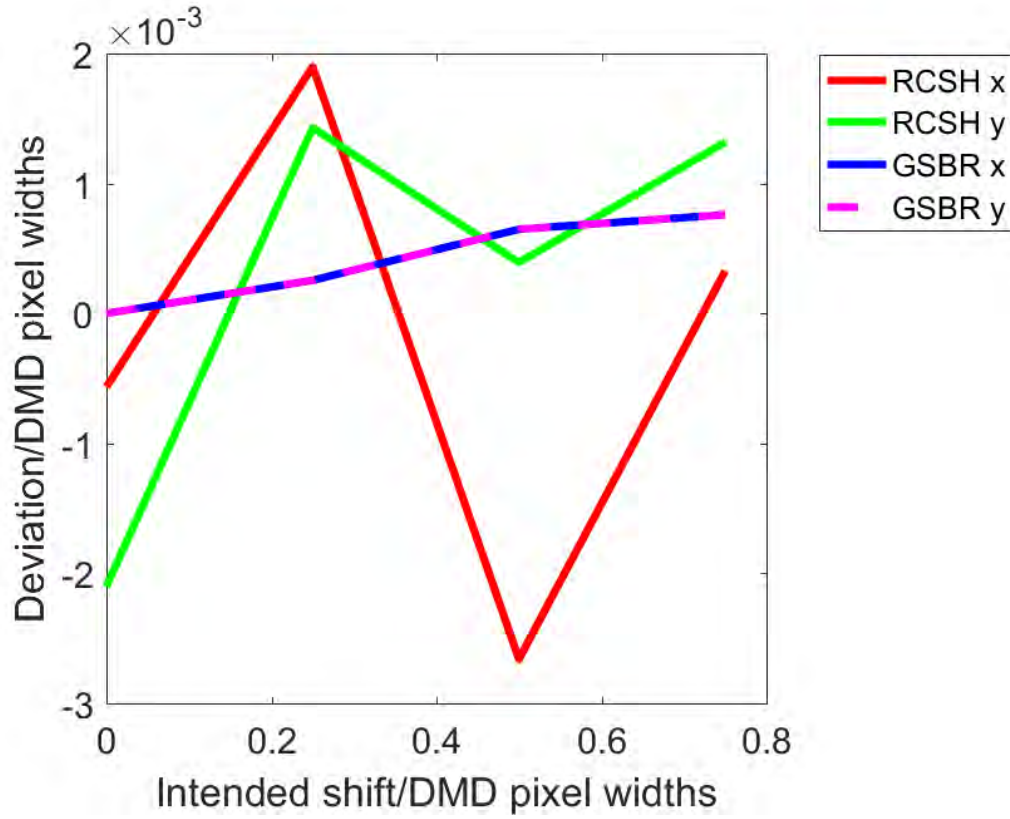
Figure D.12: The intended relative x and y shifts versus calculated centre of intensity x and y positions, for both hologram generation methods

In this case, there is almost perfect agreement between intended and calculated centre of intensity; the RCSH method achieves positional errors on the order of 0.002 DMD pixel widths, while the GSBR method is even more accurate at an error of below 0.001 DMD pixel widths. The method cannot be expected to succeed at arbitrarily small relative shifts, however. A small enough shift may not result in a large enough change in the phase distribution (or phase and amplitude, for RCSH) at the object plane to switch a single pixel, at which point the sub-pixel shifting method would reach its ultimate limit. As a further test, 32 pixel-wide spot holograms were produced with both methods, with intended 1/32 pixel shifts between each image. In order to reliably measure the centre of intensity position in this case, expanding up the 1024 by 1024 grid by 32 times for ASM propagation required more memory than available on the used computer system, and so a smaller array of 128 by 128 pixels was used to produce the hologram. In-keeping with only the central region of the DMD being illuminated (320 pixel radius when using the 1024 by 1024 grid), only pixels from within a central radius of 30 pixels in the hologram were allowed to contribute. The resulting centre of intensity plots are shown in Figure D.13; plotted on separate accuracies, to reflect the two methods' different magnitude of accuracy in this test.

(a) RCSH x accuracy   (b) RCSH y accuracy

(c) GSBR x accuracy   (d) GSBR y accuracy
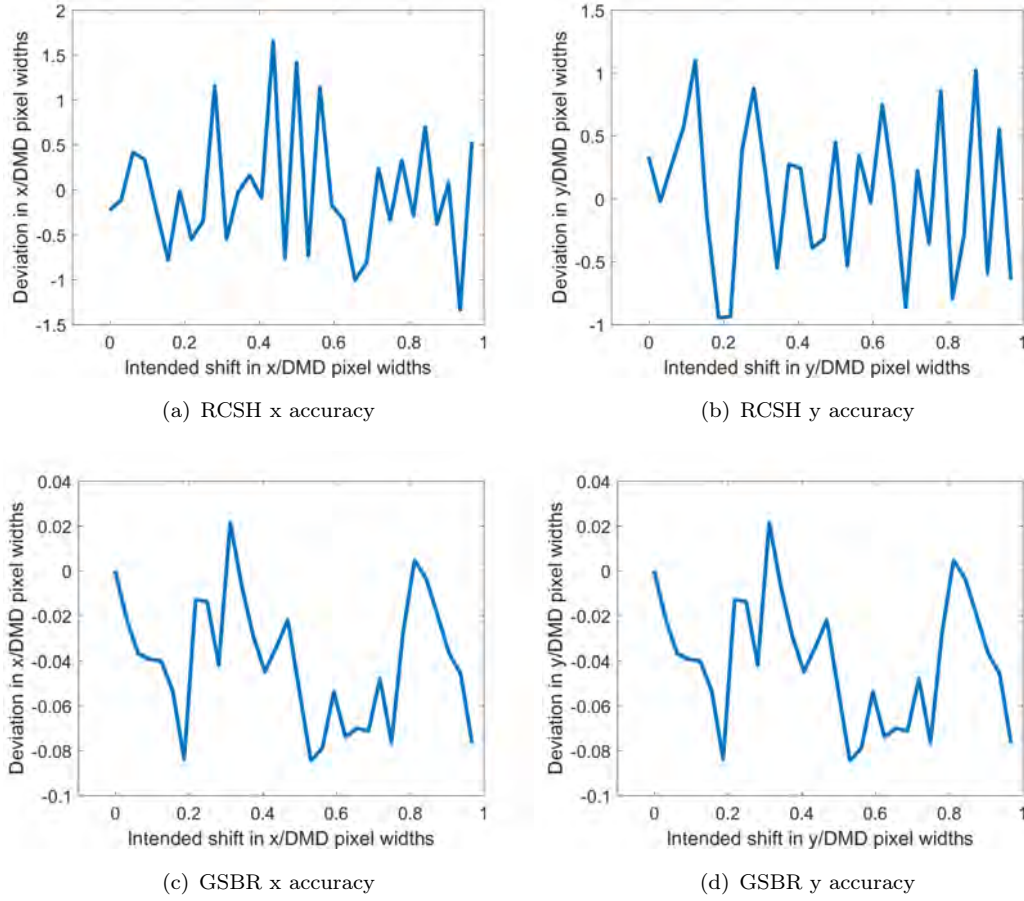
Figure D.13: The intended relative x and y positions versus calculated deviation from these positions of central intensity for 1/32 DMD pixel width shifts between successive images.

The GSBR results in Figures D.14(c) and D.14(d) still show reasonable agreement between calculated and intended positions, at below 0.1 DMD pixel width error. This means that the error exceeds the intended relative shift, however, and so the technique at the current parameters has reached its limit. The RCSH results are little better than random for 1/32 shifts, with errors on the order of a DMD pixel width. It must be noted though, that these results were achieved with only a circular region of radius 30 pixels available on the DMD. While not as rigorous as expanding the arrays for ASM propagation, a similar centre of intensity calculation can be made from images whose scales are identical to the input images; i.e. a binary hologram made with 1024 by 1024 DMD pixels propagated to an image plane on a 1024 by 1024 array. Now that the method is proven to produce sub-pixel shifts in images, and retain the shape distribution of the field, the centre of intensity calculation method is used to show the intended versus calculated image position for 1/32 DMD pixel width shifts when the 320 pixel radius region on a 1024 by 1024 array is once more made available. The resulting plots are shown in Figure D.14.

(a) RCSH x accuracy   (b) RCSH y accuracy

(c) GSBR x accuracy   (d) GSBR y accuracy
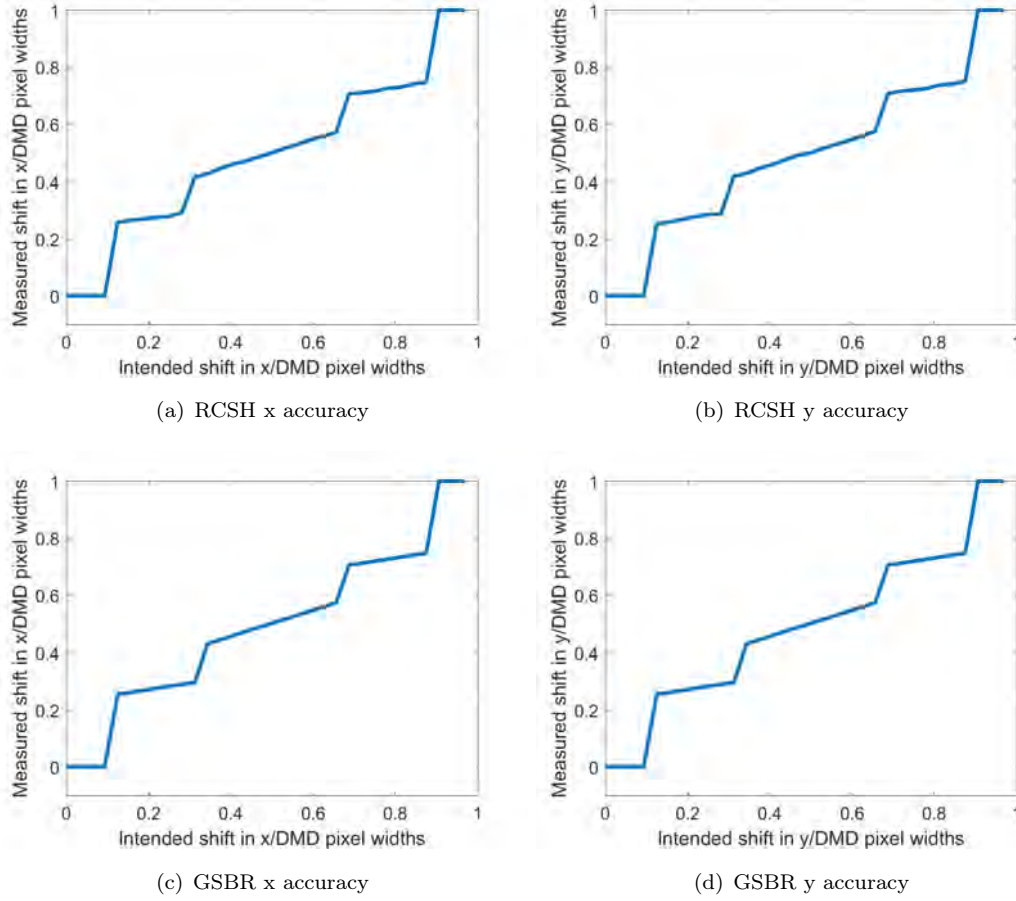
Figure D.14: The intended relative x and y versus calculated centre of intensity x and y positions for 1/32 DMD pixel width shifts between successive images, when a 320 pixel radius region of the DMD is available for hologram display.

Both methods now show agreement between calculated and intended positions, albeit with an apparent stepped structure in all plots. It is undetermined whether this step structure is an artefact of the coarse pixellation necessary when not expanding the array size before ASM propagation, or a genuine result under the stated conditions. However the latter seems unlikely, as making more pixels available to represent a complex field should not make the result less accurate, which would be the case when comparing GSBR results in Figures D.13 and D.14.

Though the sub-pixel shifting has been demonstrated here with a small spot, this was for ease of demonstrating the relative shifts between images; it would not be computationally or optically more difficult to generate sub-pixel relative shifts for more complex images. An extension to this technique would be to make sub-pixel shifts of only certain parts within a 3D image, for instance to project two hollow squares separated laterally by only half a DMD pixel width. In section 6.2, it was shown that a single DMD pixel corresponded to 100nm at the sample when projecting through the 100x objective on the DLP3000 line. If the 1/32 image shifts shown here were successfully applied, this would mean image translations of only 3nm would be achievable.

Bibliography

[1] G. E. Moore. Cramming more components onto integrated circuits (Reprinted from Electronics, pg 114-117, April 19, 1965). *Proceedings Of The Ieee*, 86(1): 82–85, 1965. ISSN 1098-4232. doi: 10.1109/N-SSC.2006.4785860. URL papers3://publication/uuid/8E5EB7C8-681C-447D-9361-E68D1932997D.

[2] V. Manfrinato, L. Zhang, D. Su, and H. Duan. Resolution limits of electron-beam lithography toward the atomic scale. *Nano letters*, 13(4):1555–1558, 2013. URL http://pubs.acs.org/doi/abs/10.1021/nl304715p.

[3] H. J. Booth. Recent applications of pulsed lasers in advanced materials processing. *Thin Solid Films*, 453:450–457, 2004.

[4] E. G. Gamaly, A. V. Rode, B. Luther-Davies, and V. T. Tikhonchuk. Ablation of solids by femtosecond lasers: Ablation mechanism and ablation thresholds for metals and dielectrics. *Physics of Plasmas*, 9(3):949, 2002. ISSN 1070664X. doi: 10.1063/1.1447555.

[5] A. Yariv and P. Yeh. *Photonics: Optical Electronics in Modern Communications (The Oxford Series in Electrical and Computer Engineering)*. Oxford University Press, Inc., 2006.

[6] T. Brabec, C. Spielmann, P. F. Curley, and F. Krausz. Kerr lens mode locking. *Optics Letters*, 17(18):1292, 1992. ISSN 0146-9592. doi: 10.1364/OL.17.001292. URL https://www.osapublishing.org/abstract.cfm?URI=ol-17-18-1292.

[7] C. Inc. MIRA900 - Modelocked Ti:Sapphire Lasers, 2002. URL http://www.upc.edu/sct/documents{_}equipament/d{_}122{_}id-627.pdf.

[8] C. Inc. Legend Elite Femtosecond. URL http://www.coherent.it/fileadmin/data/pdf/LegendEliteF{_}DataSheet.pdf.

[9] R. Srinivasan. Kinetics of the ablative photodecomposition of organic polymers in the far ultraviolet (193 nm). *Journal of Vacuum Science & Technology B*, 1(4): 923–926, 1983.

[10] B. N. Chichkov, C. Momma, S. Nolte, F. von Alvensleben, and A. Tünnermann. Femtosecond, picosecond and nanosecond laser ablation of solids. *Applied Physics A: Materials Science & Processing*, 63(2):109–115, 1996. ISSN 0947-8396. doi: 10.1007/s003390050359. URL http://www.springerlink.com/openurl.asp?genre=article{&}id=doi:10.1007/s003390050359.

[11] M. Moll, M. Schlanges, T. Bornath, and V. P. Krainov. Inverse bremsstrahlung heating beyond the first Born approximation for dense plasmas in laser fields. *New Journal of Physics*, 14, 2012. ISSN 13672630. doi: 10.1088/1367-2630/14/6/065010.

[12] P. Pronko, P. V. Rompay, C. Horvath, X. Liu, T. Juhasz, and G. Mourou. Avalanche ionization and dielectric breakdown in silicon with\nultrafast laser pulses. *Physical Review B*, 58(5):2387–2390, 1998. ISSN 0163-1829. doi: 10.1109/CLEO.1998.676562.

[13] B. C. Stuart, M. D. Feit, S. Herman, A. M. Rubenchik, B. W. Shore, and M. D. Perry. Nanosecond-to-femtosecond laser-induced breakdown in dielectrics. *Physical Review B*, 53(4):1749–1761, 1996. ISSN 0163-1829. doi: 10.1103/PhysRevB.53.1749. URL http://link.aps.org/doi/10.1103/PhysRevB.53.1749.

[14] R. R. Gattass and E. Mazur. Femtosecond laser micromachining in transparent materials. *Nature Photonics*, 2(4):219–225, 2008. ISSN 1749-4885. doi: 10.1038/nphoton.2008.47.

[15] N. Bulgakova, R. Stoian, a. Rosenfeld, I. Hertel, and E. Campbell. Electronic transport and consequences for material removal in ultrafast pulsed laser ablation of materials. *Physical Review B*, 69(5):054102, feb 2004. ISSN 1098-0121. doi: 10.1103/PhysRevB.69.054102. URL http://link.aps.org/doi/10.1103/PhysRevB.69.054102.

[16] L. Jiang and H. L. Tsai. Femtosecond Lasers Ablation : Challenges and Opportunities. *Aerospace Engineering*, 1(1):51–53, 2003. URL http://galilei.chem.psu.edu/{~}tatiana/PUBLIS/My{_}papers/prlpaper/femtosecond{_}rev{_}NSFWorkshop.pdf.

[17] M. Göppert-Mayer. Über elementarakte mit zwei quantensprüngen. *Annalen der Physik*, 401(3):273–294, 1931.

[18] J. Fischer and M. Wegener. Three-dimensional optical laser lithography beyond the diffraction limit. *Laser & Photonics Reviews*, 7(1):22–44, jan 2013. ISSN 18638880. doi: 10.1002/lpor.201100046. URL http://doi.wiley.com/10.1002/lpor.201100046.

[19] A. P. Joglekar, H. Liu, G. J. Spooner, E. Meyhöfer, G. Mourou, and A. J. Hunt. A study of the deterministic character of optical damage by femtosecond laser pulses and applications to nanomachining. *Applied Physics B: Lasers and Optics*, 77(1):25–30, 2003. ISSN 09462171. doi: 10.1007/s00340-003-1246-z.

[20] Clark-MXR, Inc. Ultrafast Laser Micromachining Handbook, apr 2014. URL http://www.cmxr.com/Education/Introduction.html.

[21] Texas Instruments. DLP 3000, . URL http://www.ti.com/product/dlp3000{#}parametrics.

[22] J. Sperling Reich. Texas Instruments On Track With 4K, 2010. URL https://celluloidjunkie.com/2010/03/26/texas-instruments-on-track-with-4k/.

[23] T. Instruments. DLP3000 DLP ® 0 . 3 WVGA Series 220 DMD, 2015. URL http://www.ti.com/lit/ds/symlink/dlp3000.pdf.

[24] Texas Instruments. DLP7000UV DLP® 0.7 UV XGA 2x LVDS Type A DMD, 2015. URL http://www.ti.com/lit/ds/symlink/dlp7000.pdf.

[25] Texas Instruments. Wavelength Transmittance Considerations for DLP ® DMD Window, . URL http://www.ti.com/lit/an/dlpa031c/dlpa031c.pdf.

[26] Texas Instruments. Laser Power Handling for DMDs, 2012. URL http://www.ti.com/lit/wp/dlpa027/dlpa027.pdf.

[27] B. Mills, M. Feinaeugle, C. L. Sones, N. Rizvi, and R. W. Eason. Sub-micron-scale femtosecond laser ablation using a digital micromirror device. *Journal of Micromechanics and Microengineering*, 23(3):35005, mar 2013. ISSN 0960-1317. doi: 10.1088/0960-1317/23/3/035005. URL http://stacks.iop.org/0960-1317/23/i=3/a=035005?key=crossref.99cfa14153f13e89ec061ec09defc146.

[28] D. Dudley, W. M. Duncan, and J. Slaughter. Emerging digital micromirror device (DMD) applications. In *Micromachining and Microfabrication*, pages 14–25. International Society for Optics and Photonics, 2003.

[29] A. Piqué, H. Kim, R. C. Y. Auyeung, and A. T. Smith. Laser Forward Transfer of Functional Materials for Digital Fabrication of Microelectronics. *Journal of Imaging Science and Technology*, 57(4):40401–40404, 2013.

[30] Y. Lu, G. Mapili, G. Suhali, S. Chen, and K. Roy. A digital micro-mirror device-based system for the microfabrication of complex, spatially patterned tissue engineering scaffolds. *Journal of Biomedical Materials Research Part A*, 77(2):396–405, 2006.

[31] J. Cheng, C. Gu, D. Zhang, and S.-C. Chen. High-speed femtosecond laser beam shaping based on binary holography using a digital micromirror device. *Optics letters*, 40(21):4875–8, 2015. ISSN 1539-4794. doi: 10.1364/OL.40.004875. URL http://www.osapublishing.org/viewmedia.cfm?uri=ol-40-21-4875{&}seq=0{&}html=true.

[32] Product Technical Description Gauß-to-Top-Hat beam shaper lens, 2011. URL http://www.topag.de/images/stories/PDF{_}Neu/Strahlformung/TOPAGGTH-5-250-4.pdf.

[33] Thorlabs. LNR50SE / M, 2013. URL https://www.thorlabs.com/newgrouppage9.cfm?objectgroup{_}id=2297.

[34] Coherent. Regenerative Amplifier Electro-Optics, 2003. URL http://www.coherent.com/downloads/ACF86A.pdf{#}page=1.

[35] M. A. Dugan, J. X. Tull, and W. S. Warren. High-resolution acousto-optic shaping of unamplified and amplified femtosecond laser pulses. *Journal of the Optical Society of America B-Optical Physics*, 14(9):2348–2358, 1997. ISSN 0740-3224. doi: 10.1364/JOSAB.14.002348.

[36] S.-H. Shim, D. B. Strasfeld, E. C. Fulmer, and M. T. Zanni. Femtosecond pulse shaping directly in the mid-IR using acousto-optic modulation. *Optics Letters*, 31(6):838–840, 2006. ISSN 0146-9592. doi: 10.1364/OL.31.000838. URL http://ol.osa.org/abstract.cfm?URI= ol-31-6-838{%}5Cnhttp://www.opticsinfobase.org/DirectPDFAccess/ DB9C79D5-9BEB-3337-90CA4794AD8287D7{_}88440.pdf?da=1{&}id= 88440{&}seq=0{&}mobile=no{%}5Cnhttp://www.opticsinfobase.org/ol/ abstract.cfm?URI=ol-31-6-838.

[37] a. M. A. Weiner. Femtosecond pulse shaping using spatial light modulators. *Review of scientific instruments*, 71(5):1929, 2000. ISSN 00346748. doi: 10.1063/ 1.1150614. URL http://link.aip.org/link/?RSINAK/71/1929/1{%}5Cnhttp: //link.aip.org/link/RSINAK/v71/i5/p1929/s1{&}Agg=doi.

[38] Z. Zhang, Z. You, and D. Chu. Fundamentals of phase-only liquid crystal on silicon (LCOS) devices. *Light: Science & Applications*, 3(10):e213, 2014. ISSN 2047-7538. doi: 10.1038/lsa.2014.94. URL http://www.nature.com/doifinder/ 10.1038/lsa.2014.94.

[39] J. L. de Bougrenet de la Tocnaye and L. Dupont. Complex amplitude modulation by use of liquid-crystal spatial light modulators. *Applied Optics*, 36(8):1730, 1997. ISSN 0003-6935. doi: 10.1364/AO.36. 001730. URL http://www.ncbi.nlm.nih.gov/pubmed/18250859{%}5Cnhttps: //www.osapublishing.org/abstract.cfm?URI=ao-36-8-1730.

[40] D. Cai, K. Wang, A. Zhai, and H. Wei. Light efficiency of liquid crystal spatial light modulator using, for wavefront corrector in AO. *Optik*, 125(15):4177–4180, 2014. ISSN 00304026. doi: 10.1016/j.ijleo.2014.01.023. URL http://dx.doi. org/10.1016/j.ijleo.2014.01.023.

[41] E. Ronzitti, M. Guillon, V. de Sars, and V. Emiliani. LCoS nematic SLM characterization and modeling for diffraction efficiency optimization, zero and ghost orders suppression. *Optics Express*, 20(16):17843, 2012. ISSN 1094-4087. doi: 10.1364/OE.20.017843.

[42] Thorlabs. Exulus Spatial Light Modulator, . URL https://www.thorlabs.com/ newgrouppage9.cfm?objectgroup{_}id=10378.

[43] Z. Kuang, W. Perrie, J. Leach, M. Sharp, S. P. Edwardson, M. Padgett, G. Dearden, and K. G. Watkins. High throughput diffractive multi-beam femtosecond laser processing using a spatial light modulator. *Applied Surface Science*, 255(5 PART 1):2284–2289, 2008. ISSN 01694332. doi: 10.1016/j.apsusc.2008.07.091.

[44] Thorlabs. Exulus Spatial Light Modulator, . URL https://www.thorlabs.com/ newgrouppage9.cfm?objectgroup{_}id=10378.

[45] C. D. Liao and J. C. Tsai. The evolution of MEMS displays. *IEEE Transactions on Industrial Electronics*, 56(4):1057–1065, 2009. ISSN 02780046. doi: 10.1109/ TIE.2008.2005684.

[46] M. Shaw, S. Hall, S. Knox, R. Stevens, and C. Paterson. Characterization of deformable mirrors for spherical aberration correction in optical sectioning microscopy. *Optics Express*, 18(7):6900–6913, 2010. ISSN 1094-4087. doi: 10.1364/OE.18.006900.

[47] Y. Taii, A. Higo, H. Fujita, and H. Toshiyoshi. Transparent color pixels using plastic MEMS technology for electronic papers. *IEICE Electronics Express*, 3(6): 97–101, 2006. ISSN 13492543. doi: 10.1587/elex.3.97.

[48] D. M. Bloom. Grating Light Valve: revolutionizing display technology. *Projection Displays III*, 3013:165–171, 1997. ISSN 0277786X. doi: 10.1117/12.273868. URL http://link.aip.org/link/?PSI/3013/165/1{&}Agg=doi.

[49] J. I. Trisnadi, C. B. Carlisle, and R. Monteverde. Overview and applications of Grating-Light-Valve-based optical write engines for high-speed digital imaging. *MOEMS Display and Imaging Systems II*, 5348(January):52–64, 2004. ISSN 0277786X. doi: 10.1117/12.525898. URL http://www.siliconlight.com/wp-content/themes/siliconlight/pdf/spie-jan04-slmwrteng-5348-5.pdf{%}5Cnhttp://link.aip.org/link/?PSI/5348/52/1{&}Agg=doi.

[50] D. T. Amm and R. W. Corrigan. 5.2: Grating Light Valve^TM Technology: Update and Novel Applications. *SID Symposium Digest of Technical Papers*, 29(1):29–32, 1998. ISSN 0097-966X. doi: 10.1889/1.1833752. URL http://www.siliconlight.com/wp-content/themes/siliconlight/pdf/sid98.pdf{%}5Cnhttp://link.aip.org/link/DTPSDS/v29/i1/p29/s1{&}Agg=doi.

[51] K. R. Kim, J. Yi, S. H. Cho, N. H. Kang, M. W. Cho, B. S. Shin, and B. Choi. SLM-based maskless lithography for TFT-LCD. *Applied Surface Science*, 255(18): 7835–7840, 2009. ISSN 01694332. doi: 10.1016/j.apsusc.2009.05.022.

[52] M. Wagner. Micro Mirror Arrays (Mma) From Duv To Nir, 2008. URL http://www.ipms.fraunhofer.de/content/dam/ipms/common/products/SLM/memi-e.pdf.

[53] M. Scholles. Fraunhofer Institute for Photonic Microsystems Ipms, 2013. URL http://www.ipms.fraunhofer.de/content/dam/ipms/common/mems-reports/m2014-q1-e.pdf.

[54] J. Gierak. Focused Ion Beam nano-patterning from traditional applications to single ion implantation perspectives. *Nanofabrication*, 1(1):35–52, 2014. ISSN 2299-680X. doi: 10.2478/nanofab-2014-0004. URL http://www.degruyter.com/view/j/nanofab.2014.1.issue-1/nanofab-2014-0004/nanofab-2014-0004.xml.

[55] H. Niino, Y. Kawaguchi, T. Sato, A. Narazaki, T. Gumpenberger, and R. Kurosaki. Laser ablation of toluene liquid for surface micro-structuring of silica glass. *Applied Surface Science*, 252(13 SPEC. ISS.):4387–4391, 2006. ISSN 01694332. doi: 10.1016/j.apsusc.2005.07.084.

[56] L. Kelemen, S. Valkai, and P. Ormos. Parallel photopolymerisation with complex light patterns generated by diffractive optical elements. *Optics express*, 15:14488–14497, 2007. ISSN 1094-4087. doi: 10.1364/OE.15.014488.

[57] S. Matsuo, S. Juodkazis, and H. Misawa. Femtosecond laser microfabrication of periodic structures using a microlens array. *Applied Physics A: Materials Science and Processing*, 80(4):683–685, 2005. ISSN 09478396. doi: 10.1007/s00339-004-3108-x.

[58] S. Juodkazis, T. Kondo, H. Misawa, a. Rode, M. Samoc, and B. Luther-Davies. Photo-structuring of {As_2S}_3 glass by femtosecond irradiation. *Opt. Express*, 14(17):7751–7756, 2006.

[59] B. Mills, D. J. Heath, M. Feinaeugle, J. a. Grant-Jacob, and R. W. Eason. Laser ablation via programmable image projection for submicron dimension machining in diamond. *Journal of Laser Applications*, 26(4):041501, 2014. ISSN 1938-1387. doi: 10.2351/1.4893749. URL http://scitation.aip.org/content/lia/journal/jla/26/4/10.2351/1.4893749.

[60] I. Aharonovich, A. D. Greentree, and S. Prawer. Diamond photonics. *Nature Photonics*, 5(7):397–405, 2011. ISSN 1749-4885. doi: 10.1038/nphoton.2011.54. URL http://dx.doi.org/10.1038/nphoton.2011.54.

[61] G. Zhang, B. Zhang, Z. Deng, and J. Chen. An Experimental Study on Laser Cutting Mechanisms of Polycrystalline Diamond Compacts. *CIRP Annals - Manufacturing Technology*, 56(1):201–204, 2007. ISSN 00078506. doi: 10.1016/j.cirp.2007.05.049.

[62] O. H. Y. Zalloum, M. Parrish, A. Terekhov, and W. Hofmeister. On femtosecond micromachining of HPHT single-crystal diamond with direct laser writing using tight focusing. *Optics express*, 18(1996):13122–13135, 2010. ISSN 1094-4087. doi: 10.1364/OE.18.013122.

[63] A. Mathis, F. Courvoisier, L. Froehly, L. Furfaro, M. Jacquot, P. A. Lacourt, and J. M. Dudley. Micromachining along a curve: Femtosecond laser micromachining of curved profiles in diamond and silicon using accelerating beams. *Applied Physics Letters*, 101(7):99–102, 2012. ISSN 00036951. doi: 10.1063/1.4745925.

[64] R. D. Simmonds, P. S. Salter, A. Jesacher, and M. J. Booth. Three dimensional laser microfabrication in diamond using a dual adaptive optics system. *Optics Express*, 19(24):24122, 2011. ISSN 1094-4087. doi: 10.1364/OE.19.024122.

[65] G. Dumitru, V. Romano, H. P. Weber, M. Sentis, and W. Marine. Femtosecond ablation of ultrahard materials. *Applied Physics A: Materials Science and Processing*, 74(6):729–739, 2002. ISSN 09478396. doi: 10.1007/s003390101183.

[66] R. Buividas, M. Mikutis, and S. Juodkazis. Surface and bulk structuring of materials by ripples with long and short laser pulses: Recent advances. *Progress in Quantum Electronics*, 38(3):119–156, 2014. ISSN 00796727. doi: 10.1016/j.pquantelec.2014.03.002.

[67] K. Venkatakrishnan, B. Tan, and B. K. A. Ngoi. Femtosecond pulsed laser ablation of thin gold film. *SPIE*, 2403(437):199–202, 1995.

[68] M. Lenner, A. Kaplan, and R. E. Palmer. Ultrafast laser ablation of graphite. *Physical Review B*, 79:1–11, 2009. doi: 10.1103/PhysRevB.79.184105.

[69] P. Gay-Balmaz and O. J. F. Martin. Electromagnetic resonances in individual and coupled split-ring resonators. *Journal of Applied Physics*, 92(5):2929–2936, 2002. ISSN 00218979. doi: 10.1063/1.1497452.

[70] J. Bonache, I. Gil, J. García-García, and F. Martín. Complementary split rings resonators (CSRRs): Towards the miniaturization of microwave device design. *Journal of Computational Electronics*, 5(2-3):193–197, 2006. ISSN 1569-8025. doi: 10.1007/s10825-006-8843-0. URL http://link.springer.com/10.1007/s10825-006-8843-0.

[71] R. Burgess, M. Coleman, and J. Keil. A Cr-Ag-Au metalization system. *IEEE Transactions on Electron Devices*, 16(4):356–360, 1969. ISSN 0018-9383. doi: 10.1109/T-ED.1969.16757. URL http://ieeexplore.ieee.org/lpdocs/epic03/wrapper.htm?arnumber=1475799.

[72] A. J. Pedraza, R. A. Kumar, and D. H. Lowndes. Greatly improved adhesion of gold films sputter-deposited on laser-treated and thermally annealed alumina. *Applied Physics Letters*, 66(9):1065–1067, 1995. ISSN 10773118. doi: 10.1063/1.114231.

[73] S. J. Mihailov, C. W. Smelser, P. Lu, R. B. Walker, D. Grobnic, H. Ding, and J. Unruh. Fiber Bragg gratings (FBG) made with a phase mask and 800 nm femtosecond radiation. *Conference on Optical Fiber Communication, Technical Digest Series*, 2003-Janua:PD30.1–PD30.3, 2003. ISSN 0146-9592. doi: 10.1109/OFC.2003.316135.

[74] C. W. Smelser, S. J. Mihailov, and D. Grobnic. Formation of Type I-IR and Type II-IR gratings with an ultrafast IR laser and a phase mask. *Optics Express*, 13(14):5377, 2005. ISSN 1094-4087. doi: 10.1364/OPEX.13.005377. URL http://www.osapublishing.org/viewmedia.cfm?uri=oe-13-14-5377{&}seq=0{&}html=true.

[75] J. Thomas, E. Wikszak, T. Clausnitzer, U. Fuchs, U. Zeitner, S. Nolte, and a. Tünnermann. Inscription of fiber Bragg gratings with femtosecond pulses using a phase mask scanning technique. *Applied Physics A*, 86(2): 153–157, nov 2006. ISSN 0947-8396. doi: 10.1007/s00339-006-3754-2. URL http://www.springerlink.com/index/10.1007/s00339-006-3754-2http://link.springer.com/10.1007/s00339-006-3754-2.

[76] G. D. Valle, R. Osellame, and P. Laporta. Micromachining of photonic devices by femtosecond laser pulses, 2009. ISSN 1464-4258.

[77] G. D. Marshall, M. Ams, and M. J. Withford. Direct laser written waveguide-Bragg gratings in bulk fused silica. *Optics Letters*, 31(18):2690, 2006. ISSN 0146-9592. doi: 10.1364/OL.31.002690. URL http://www.opticsinfobase.org/abstract.cfm?URI=ol-31-18-2690.

[78] T. L. Chang, S. W. Luo, H. P. Yang, and C. H. Lee. Fabrication of diffraction grating in polydimethylsiloxane using femtosecond-pulsed laser micromachining. *Microelectronic Engineering*, 87(5-8):1344–1347, 2010. ISSN 01679317. doi: 10.1016/j.mee.2009.12.037. URL http://dx.doi.org/10.1016/j.mee.2009.12.037.

[79] Y. Li, W. Watanabe, K. Yamada, T. Shinagawa, K. Itoh, J. Nishii, and Y. Jiang. Holographic fabrication of multiple layers of grating inside soda-lime glass with femtosecond laser pulses. *Applied Physics Letters*, 80(9):1508–1510, 2002. ISSN 00036951. doi: 10.1063/1.1457524.

[80] S. Sakabe, M. Hashida, S. Tokita, S. Namba, and K. Okamuro. Mechanism for self-formation of periodic grating structures on a metal surface by a femtosecond laser pulse. *Physical Review B*, 79(3):033409, jan 2009. ISSN 1098-0121. doi: 10.1103/PhysRevB.79.033409. URL http://link.aps.org/doi/10.1103/PhysRevB.79.033409.

[81] S. Kinoshita, S. Yoshioka, and K. Kawagoe. Mechanisms of structural colour in the Morpho butterfly: cooperation of regularity and irregularity in an iridescent scale. *Proceedings. Biological sciences / The Royal Society*, 269(1499):1417–21, jul 2002. ISSN 0962-8452. doi: 10.1098/rspb.2002.2019. URL http://www.pubmedcentral.nih.gov/articlerender.fcgi?artid=1691047{&}tool=pmcentrez{&}rendertype=abstract.

[82] M. Shaik and I. A. Motaleb. Effect of growth temperature on the material properties of PLD-grown Bi2Te3 and Sb2Te3. *IEEE International Conference on Electro Information Technology*, 2013. ISSN 21540357. doi: 10.1109/EIT.2013.6632706.

[83] M. F. Pittenger, A. M. Mackay, S. Beck, R. K. Jaiswal, R. Douglas, J. D. Mosca, M. a. Moorman, D. W. Simonetti, S. Craig, and D. Marshak. Multilineage Potential of Adult Human Mesenchymal Stem Cells. *Science*, 284(April):143–147, 1999. ISSN 00368075. doi: 10.1126/science.284.5411.143.

[84] M. J. Dalby, N. Gadegaard, R. Tare, A. Andar, M. O. Riehle, P. Herzyk, C. D. Wilkinson, and R. O. Oreffo. The control of human mesenchymal cell differentiation using nanoscale symmetry and disorder. *Nature Materials*, 6(5):407–413, 2007. ISSN 1476-1122. doi: 10.1038/nmat2013.

[85] P. M. Tsimbouri, R. J. McMurray, K. V. Burgess, E. V. Alakpa, P. M. Reynolds, K. Murawski, E. Kingham, R. O. C. Oreffo, N. Gadegaard, and M. J. Dalby. Using nanotopography and metabolomics to identify biochemical effectors of multipotency. *ACS Nano*, 6(11):10239–10249, 2012. ISSN 19360851. doi: 10.1021/nn304046m.

[86] R. J. McMurray, N. Gadegaard, P. M. Tsimbouri, K. V. Burgess, L. E. McNamara, R. Tare, K. Murawski, E. Kingham, R. O. C. Oreffo, and M. J. Dalby. Nanoscale surfaces for the long-term maintenance of mesenchymal stem cell phenotype and multipotency. *Nature Materials*, 10(8):637–644, 2011. ISSN 1476-1122. doi: 10.1038/nmat3058. URL http://www.ncbi.nlm.nih.gov/pubmed/21765399{%}5Cnhttp://www.nature.com/doifinder/10.1038/nmat3058.

[87] M. J. Dalby, N. Gadegaard, and R. O. C. Oreffo. Harnessing nanotopography and integrin-matrix interactions to influence stem cell fate. *Nature materials*, 13(6):558–69, 2014. ISSN 1476-1122. doi: 10.1038/nmat3980. URL http://www.ncbi.nlm.nih.gov/pubmed/24845995.

[88] S. K. Sia and G. M. Whitesides. Microfluidic devices fabricated in poly(dimethylsiloxane) for biological studies. *Electrophoresis*, 24(21):3563–3576, 2003. ISSN 01730835. doi: 10.1002/elps.200305584.

[89] J. A. Grant-Jacob, B. Mills, and R. W. Eason. Parametric study of the rapid fabrication of glass nanofoam via femtosecond laser irradiation. *Journal of Physics D: Applied Physics*, 47(5):055105, 2014. ISSN 0022-3727. doi: 10.1088/0022-3727/47/5/055105. URL http://stacks.iop.org/0022-3727/47/i=5/a=055105?key=crossref.2378b61c63f732fa336c34be2c4d7af4.

[90] J. N. Lee, C. Park, and G. M. Whitesides. Solvent compatibility of poly (dimethylsiloxane)-based microfluidic devices. *Analytical Chemistry-Washington Dc-*, 75(23):6544–6554, 2003. ISSN 0003-2700. doi: 10.1021/ac0346712. URL http://www.ncbi.nlm.nih.gov/entrez/query.fcgi?db=pubmed{&}cmd=Retrieve{&}dopt=AbstractPlus{&}list{_}uids=3530600456095646107related:m8FprWg2{_}zAJ{%}5Cnpapers://a76c0a6f-2dfa-4447-9b59-289496d5a5e4/Paper/p873.

[91] N. Guo and M. C. Leu. Additive manufacturing: Technology, applications and research needs. *Frontiers of Mechanical Engineering*, 8(3):215–243, 2013. ISSN 20950233. doi: 10.1007/s11465-013-0248-8.

[92] S. Pochon and D. Pearson. Ion Beam Deposition. *Oxford Instruments*, i:463–500, 2010. ISSN 0912-0289. doi: 10.1016/B978-0-08-096532-1.00410-6.

[93] M. Vaezi, H. Seitz, and S. Yang. A review on 3D micro-additive manufacturing technologies. *International Journal of Advanced Manufacturing Technology*, 67 (5-8):1721–1754, 2013. ISSN 02683768. doi: 10.1007/s00170-012-4605-2.

[94] Y. Zhang, C. Liu, and D. Whalley. Direct-write techniques for maskless production of microelectronics: A review of current state-of-the-art technologies. *2009 International Conference on Electronic Packaging Technology and High Density Packaging, ICEPT-HDP 2009*, pages 497–503, 2009. doi: 10.1109/ICEPT.2009.5270702.

[95] M. L. Levene, R. D. Scott, and B. W. Siryj. Material Transfer Recording. *Applied Optics*, 9(10):2260, oct 1970. ISSN 0003-6935. doi: 10.1364/AO.9.002260.

[96] J. Bohandy, B. F. Kim, and F. J. Adrian. Metal deposition from a supported metal film using an excimer laser. *Journal of Applied Physics*, 60(4):1538–1539, 1986. ISSN 00218979. doi: 10.1063/1.337287. URL http://scitation.aip.org/content/aip/journal/jap/60/4/10.1063/1.337287.

[97] J. A. Grant-Jacob, B. Mills, M. Feinaeugle, C. L. Sones, G. Oosterhuis, M. B. Hoppenbrouwers, and R. W. Eason. Micron-scale copper wires printed using femtosecond laser-induced forward transfer with automated donor replenishment. *Optical Materials Express*, 3(6):747–754, may 2013. ISSN 2159-3930. doi: 10.1364/OME.3.000747. URL http://www.opticsinfobase.org/abstract.cfm?URI=ome-3-6-747.

[98] M. Feinaeugle, P. Horak, C. L. Sones, T. Lippert, and R. W. Eason. Polymer-coated compliant receivers for intact laser-induced forward transfer of thin films: experimental results and modelling. *Applied Physics A*, 116(4):1–12, 2014.

[99] B. Hopp, T. Smausz, Z. Antal, N. Kresz, Z. Bor, and D. Chrisey. Absorbing film assisted laser induced forward transfer of fungi (Trichoderma conidia). *Journal of applied physics*, 96(6):3478–3481, 2004. ISSN 00218979. doi: 10.1063/1.1782275. URL http://scitation.aip.org/content/aip/journal/jap/96/6/10.1063/1.1782275.

[100] N. T. Kattamis, P. E. Purnick, R. Weiss, and C. B. Arnold. Thick film laser induced forward transfer for deposition of thermally and mechanically sensitive materials. *Applied Physics Letters*, 91(17):171120, 2007.

[101] M. Nagel, R. Hany, T. Lippert, M. Molberg, F. a. Nüesch, and D. Rentsch. Aryltriazene Photopolymers for UV-Laser Applications: Improved Synthesis and Photodecomposition Study. *Macromolecular Chemistry and Physics*, 208 (3):277–286, feb 2007. ISSN 10221352. doi: 10.1002/macp.200600492. URL http://doi.wiley.com/10.1002/macp.200600492.

[102] D. P. Banks, K. Kaur, R. Gazia, R. Fardel, M. Nagel, T. Lippert, and R. W. Eason. Triazene photopolymer dynamic release layer-assisted femtosecond laser-induced forward transfer with an active carrier substrate. *EPL (Europhysics Letters)*, 83 (3):38003, 2008.

[103] M. Feinaeugle, A. P. Alloncle, P. Delaporte, C. L. Sones, and R. W. Eason. Time-resolved shadowgraph imaging of femtosecond laser-induced forward transfer of solid materials. *Applied Surface Science*, 258(22):8475–8483, 2012.

[104] R. Fardel, M. Nagel, F. Nüesch, T. Lippert, and A. Wokaun. Laser-Induced Forward Transfer of Organic LED Building Blocks Studied by Timed-Resolved Shadowgraphy. *Journal of Physical Chemistry C*, (114):5617–5636, 2010. ISSN 1932-7447. doi: 10.1021/jp907387q.

[105] L. Rapp, C. Cibert, A. P. Alloncle, P. Delaporte, S. Nenon, C. Videlot-Ackermann, and F. Fages. Comparative time resolved shadowgraphic imaging studies of nanosecond and picosecond laser transfer of organic materials. *Proceedings of SPIE*, 33(0):71311L–71311L–7, 2008. ISSN 0277786X. doi: 10.1117/12.817481. URL http://link.aip.org/link/PSISDG/v7131/i1/p71311L/s1{&}Agg=doi.

[106] M. Feinaeugle, C. L. Sones, E. Koukharenko, B. Gholipour, D. W. Hewak, and R. W. Eason. Laser-induced forward transfer of intact chalcogenide thin films: resultant morphology and thermoelectric properties. *Applied Physics A*, 112(4): 1073–1079, 2013.

[107] M. L. Tseng, P. C. Wu, S. Sun, C. M. Chang, W. T. Chen, C. H. Chu, P. L. Chen, L. Zhou, D. W. Huang, T. J. Yen, and D. P. Tsai. Fabrication of multilayer metamaterials by femtosecond laser-induced forward-transfer technique. *Laser and Photonics Reviews*, 6(5):702–707, 2012. ISSN 18638880. doi: 10.1002/lpor. 201200029.

[108] J. Xu, J. Liu, D. Cui, M. Gerhold, A. Y. Wang, M. Nagel, and T. K. Lippert. Laser-assisted forward transfer of multi-spectral nanocrystal quantum dot emitters. *Nanotechnology*, 18(2):025403, 2007. ISSN 0957-4484. doi: 10.1088/0957-4484/18/2/025403. URL http://www.iop.org/EJ/abstract/0957-4484/18/2/025403.

[109] J. Shaw Stewart, T. Lippert, M. Nagel, F. Nüesch, and A. Wokaun. Red-green-blue polymer light-emitting diode pixels printed by optimized laser-induced forward transfer. *Applied Physics Letters*, 100(20):203303, 2012. ISSN 00036951. doi: 10.1063/1.4717463.

[110] S. H. Ko, H. Pan, S. G. Ryu, N. Misra, C. P. Grigoropoulos, and H. K. Park. Nanomaterial enabled laser transfer for organic light emitting material direct writing. *Applied Physics Letters*, 93(2008):91–94, 2008. ISSN 00036951. doi: 10.1063/1.3001803.

[111] A. I. Kuznetsov, A. B. Evlyukhin, M. R. Goņalves, C. Reinhardt, A. Koroleva, M. L. Arnedillo, R. Kiyan, O. Marti, and B. N. Chichkov. Laser fabrication of large-scale nanoparticle arrays for sensing applications. *ACS Nano*, 5:4843–4849, 2011. ISSN 19360851. doi: 10.1021/nn2009112.

[112] M. Feinaeugle, C. L. Sones, E. Koukharenko, and R. W. Eason. Fabrication of a thermoelectric generator on a polymer-coated substrate via laser-induced forward transfer of chalcogenide thin films. *Smart Materials and Structures*, 22(11):115023, 2013.

[113] L. Rapp, C. Constantinescu, Y. Larmande, A. P. Alloncle, and P. Delaporte. Smart beam shaping for the deposition of solid polymeric material by laser forward transfer. *Applied Physics A*, 117:1–7, feb 2014. ISSN 0947-8396. doi: 10.1007/s00339-014-8305-7. URL http://link.springer.com/10.1007/s00339-014-8305-7.

[114] R. C. Y. Auyeung, H. Kim, N. A. Charipar, A. J. Birnbaum, S. A. Mathews, and A. Piqué. Laser forward transfer based on a spatial light modulator. *Applied Physics A*, 102:21–26, 2010. ISSN 0947-8396. doi: 10.1007/s00339-010-6054-9. URL http://link.springer.com/10.1007/s00339-010-6054-9.

[115] A. I. Kuznetsov, A. B. Evlyukhin, C. Reinhardt, A. Seidel, R. Kiyan, W. Cheng, A. Ovsianikov, and B. N. Chichkov. Laser-induced transfer of metallic nanodroplets for plasmonics and metamaterial applications. *Journal of the Optical Society of America B*, 26(12):B130, nov 2009. ISSN 0740-3224. doi: 10.1364/JOSAB.26.00B130.

[116] H. Sakata, S. Chakraborty, and M. Wakaki. Patterning of Bi 2O 3 films using laser-induced forward and backward transfer techniques. *Microelectronic Engineering*, 96:56–60, 2012. ISSN 01679317. doi: 10.1016/j.mee.2012.02.002. URL http://dx.doi.org/10.1016/j.mee.2012.02.002.

[117] A. Patrascioiu, M. Duocastella, J. M. Fernández-Pradas, J. L. Morenza, and P. Serra. Liquids microprinting through a novel film-free femtosecond laser based technique. *Applied Surface Science*, 257(12):5190–5194, 2011. ISSN

01694332. doi: 10.1016/j.apsusc.2010.11.093. URL http://dx.doi.org/10.1016/j.apsusc.2010.11.093.

[118] D. A. Zayarnyi, A. A. Ionin, S. I. Kudryashov, S. V. Makarov, A. A. Rudenko, E. A. Drozdova, and S. B. Odinokov. Specific features of single-pulse femtosecond laser micron and submicron ablation of a thin silver film coated with a micron-thick photoresist layer. *Quantum Electronics*, 45(5):462–466, 2015. ISSN 1063-7818. doi: 10.1070/QE2015v045n05ABEH015788. URL http://stacks.iop.org/1063-7818/45/i=5/a=462?key=crossref.fe52a117f6895f7b3cbd8fb5b2641261.

[119] N. T. Kattamis, M. S. Brown, and C. B. Arnold. Finite element analysis of blister formation in laser-induced forward transfer. *Journal of Materials Research*, 26 (18):2438–2449, aug 2011. ISSN 0884-2914. doi: 10.1557/jmr.2011.215.

[120] J. Sotrop, A. Kersch, M. Domke, G. Heise, and H. P. Huber. Numerical simulation of ultrafast expansion as the driving mechanism for confined laser ablation with ultra-short laser pulses. *Applied Physics A: Materials Science and Processing*, 113 (2):397–411, aug 2013. ISSN 09478396. doi: 10.1007/s00339-013-7849-2.

[121] Y. P. Meshcheryakov, M. V. Shugaev, T. Mattle, T. Lippert, and N. M. Bulgakova. Role of thermal stresses on pulsed laser irradiation of thin films under conditions of microbump formation and nonvaporization forward transfer. *Applied Physics A*, 113(2):521–529, jan 2013. ISSN 0947-8396. doi: 10.1007/s00339-013-7563-0.

[122] S. G. Koulikov and D. D. Dlott. Ultrafast microscopy of laser ablation of refractory materials: ultra low threshold stress-induced ablation. *Journal of Photochemistry and Photobiology A: Chemistry*, 145(3):183–194, dec 2001. ISSN 10106030. doi: 10.1016/S1010-6030(01)00581-0.

[123] M. Feinaeugle. *Laser-induced forward transfer of intact, solid-phase inorganic materials*. PhD thesis, Optoelectronics Research Centre, University of Southampton, 2013, 2013.

[124] E. Sollier, C. Murray, P. Maoddi, and D. Di Carlo. Rapid prototyping polymers for microfluidic devices and high pressure injections. *Lab on a Chip*, 11:3752, 2011. ISSN 1473-0197. doi: 10.1039/c1lc20514e.

[125] C. Liu. Recent developments in polymer MEMS. *Advanced Materials*, 19:3783–3790, 2007. ISSN 09359648. doi: 10.1002/adma.200701709.

[126] S. Satyanarayana, R. N. Karnik, and A. Majumdar. Stamp-and-stick room-temperature bonding technique for microdevices. *Journal of Microelectromechanical Systems*, 14(2):392–399, 2005. ISSN 10577157. doi: 10.1109/JMEMS.2004.839334.

[127] Y. Qi, N. T. Jafferis, K. Lyons, C. M. Lee, H. Ahmad, and M. C. McAlpine. Piezoelectric ribbons printed onto rubber for flexible energy conversion. *Nano Letters*, 10:524–525, 2010. ISSN 15306984. doi: 10.1021/nl903377u.

[128] D. H. Kim, Y. S. Kim, J. Wu, Z. Liu, J. Song, H. S. Kim, Y. Y. Huang, K. C. Hwang, and J. a. Rogers. Ultrathin silicon circuits with strain-isolation layers and mesh layouts for high-performance electronics on fabric, vinyl, leather, and paper. *Advanced Materials*, 21:3703–3707, 2009. ISSN 09359648. doi: 10.1002/adma.200900405.

[129] S. M. Pimenov, G. A. Shafeev, A. A. Smolin, V. I. Konov, and B. K. Vodolaga. Laser-induced forward transfer of ultra-fine diamond particles for selective deposition of diamond films. *Applied Surface Science*, 86:208–212, 1995.

[130] S. A. Mathews, R. C. Y. Auyeung, H. Kim, N. a. Charipar, and A. Piqué. High-speed video study of laser-induced forward transfer of silver nano-suspensions. *Journal of Applied Physics*, 114(6):064910, 2013. ISSN 00218979. doi: 10.1063/1.4817494.

[131] R. C. Y. Auyeung, H. Kim, S. Mathews, and A. Piqué. Laser forward transfer using structured light. *Optics Express*, 23(1):422–430, 2015. ISSN 1094-4087. doi: 10.1364/OE.23.000422.

[132] M. Feinaeugle, D. J. Heath, B. Mills, J. A. Grant-Jacob, G. Z. Mashanovich, and R. W. Eason. Laser-induced backward transfer of nanoimprinted polymer elements. *Applied Physics A*, 122(4):398, apr 2016. ISSN 0947-8396. doi: 10.1007/s00339-016-9953-6.

[133] J. Bonse, S. Baudach, J. Krüger, W. Kautek, and M. Lenzner. Femtosecond laser ablation of silicon-modification thresholds and morphology. *Applied Physics A: Materials Science and Processing*, 74(1):19–25, 2002. ISSN 09478396. doi: 10.1007/s003390100893.

[134] R. Fardel, M. Nagel, F. Nüesch, T. Lippert, and A. Wokaun. Laser-induced forward transfer of organic LED building blocks studied by time-resolved shadowgraphy. *Journal of Physical Chemistry C*, 114:5617–5636, 2010. ISSN 19327447. doi: 10.1021/jp907387q.

[135] M. Feinaeugle, P. Gregorčič, D. Heath, B. Mills, and R. Eason. Time-resolved imaging of flyer dynamics for femtosecond laser-induced backward transfer of solid polymer thin films. *Applied Surface Science*, 396:1231–1238, 2017. ISSN 01694332. doi: 10.1016/j.apsusc.2016.11.120. URL http://linkinghub.elsevier.com/retrieve/pii/S0169433216324886.

[136] K. Ravi-Chandar, J. Lu, B. Yang, and Z. Zhu. Failure mode transitions in polymers under high strain rate loading. *International Journal of Fracture*, 101(1/2):33–72, 2000. ISSN 03769429. doi: 10.1023/A:1007581101315. URL http://link.springer.com/10.1023/A:1007581101315.

[137] E. T. Karim, M. Shugaev, C. Wu, Z. Lin, R. F. Hainsey, and L. V. Zhigilei. Atomistic simulation study of short pulse laser interactions with a metal target under conditions of spatial confinement by a transparent overlayer. *Journal of Applied Physics*, 115(18):183501, may 2014. ISSN 0021-8979. doi: 10.1063/1.4872245.

[138] K. Na, I. I. I. Kim, E. Lee, H. C. Kim, Y.-h. Lee, and K. Chun. Thick SU-8 Photoresist. In *MEMS, NANO and Smart Systems*, pages 31–34, 2006. ISBN 1424408997.

[139] R. Peeters, S. Lok, J. Mallman, M. van Noordenburg, N. Harned, P. Kuerz, M. Lowisch, E. van Setten, G. Schiffelers, A. Pirati, J. Stoeldraijer, D. Brandt, N. Farrar, I. Fomenkov, H. Boom, H. Meiling, and R. Kool. EUV lithography: NXE platform performance overview. *SPIE Advanced Lithography*, 9048(February 2013):90481J, 2014. ISSN 1996756X. doi: 10.1117/12. 2046909. URL http://proceedings.spiedigitallibrary.org/proceeding. aspx?doi=10.1117/12.2046909.

[140] T. Ito and S. Okazaki. Pushing the limits of lithography. *Nature*, 406(6799): 1027–31, 2000. ISSN 1476-4687. doi: 10.1038/35023233. URL http://www.ncbi. nlm.nih.gov/pubmed/10984061.

[141] D. T. Elg, J. R. Sporre, G. A. Panici, S. N. Srivastava, and D. N. Ruzic. In situ collector cleaning and extreme ultraviolet reflectivity restoration by hydrogen plasma for extreme ultraviolet sources. *Journal of Vacuum Science & Technology A: Vacuum, Surfaces, and Films*, 34(2):021305, 2016. ISSN 0734-2101. doi: 10.1116/1.4942456. URL http://dx.doi.org/10.1116/1.4942456http:// scitation.aip.org/content/avs/journal/jvsta/34/2/10.1116/1.4942456.

[142] K. G. Kemp. Lithographic method using double exposure techniques, mask position shifting and light phase shifting, US Patent No 5308741, 1994.

[143] A. J. Hazelton, S. Wakamoto, S. Hirukawa, M. McCallum, N. Magome, J. Ishikawa, C. Lapeyre, I. Guilmeau, S. Barnola, and S. Gaugiran. Double-patterning requirements for optical lithography and prospects for optical extension without double patterning. *Journal of Micro/Nanolithography, MEMS and MOEMS*, 8(1):011003, 2009. ISSN 19325150. doi: 10.1117/1.3023077.

[144] H. Ooki, K. Masaya, and S. Masato. A Novel Super-Resolution Technique for Optical Lithography–Nonlinear Multiple Exposure Method. *Japanese journal of applied physics*, 33.2A:L177–L179, 1994.

[145] H. Ooki, D. P. Coon, S. Owa, T. Sei, and K. Okamoto. Experimental study on nonlinear multiple-exposure method. In G. E. Fuller, editor, *Microlithography'97*, pages 85–93, jul 1997. doi: 10.1117/12.276012. URL http://proceedings. spiedigitallibrary.org/proceeding.aspx?articleid=924003.

[146] B. Mills, J. A. Grant-Jacob, M. Feinaeugle, and R. W. Eason. Single-pulse multiphoton polymerization of complex structures using a digital multimirror device. *Optics express*, 21(12):14853–14858, 2013.

[147] Y.-C. Li, L.-C. Cheng, C.-Y. Chang, C.-H. Lien, P. J. Campagnola, and S.-J. Chen. Fast multiphoton microfabrication of freeform polymer microstructures by spatiotemporal focusing and patterned excitation. *Optics express*, 20(17):19030–8, aug 2012. ISSN 1094-4087. URL http://www.ncbi.nlm.nih.gov/pubmed/ 23038543.

[148] P. T. Mannion, J. Magee, E. Coyne, G. M. O'Connor, and T. J. Glynn. The effect of damage accumulation behaviour on ablation thresholds and damage morphology in ultrafast laser micro-machining of common metals in air. *Applied Surface Science*, 233(1-4):275–287, 2004. ISSN 01694332. doi: 10.1016/j.apsusc.2004.03. 229.

[149] M. D. Shirk and P. A. Molian. A review of ultrashort pulsed laser ablation of materials A review of ultrashort pulsed laser ablation of materials. *Journal of Laser Applications*, 10(1):18–28, 1998. doi: 10.2351/1.521827.

[150] E. L. Gurevich and S. V. Gurevich. Laser Induced Periodic Surface Structures induced by surface plasmons coupled via roughness. *Applied Surface Science*, 302:118–123, 2014. ISSN 01694332. doi: 10.1016/j.apsusc.2013.10.141. URL http://dx.doi.org/10.1016/j.apsusc.2013.10.141.

[151] J. Li, J. Mu, B. Wang, W. Ding, J. Liu, H. Guo, W. Li, C. Gu, and Z. Y. Li. Direct laser writing of symmetry-broken spiral tapers for polarization-insensitive three-dimensional plasmonic focusing. *Laser and Photonics Reviews*, 8(4):602–609, 2014. ISSN 18638899. doi: 10.1002/lpor.201300206.

[152] M. Malinauskas, A. Žukauskas, G. Bičkauskaitė, R. Gadonas, and S. Juodkazis. Mechanisms of three-dimensional structuring of photo-polymers by tightly focussed femtosecond laser pulses. *Optics Express*, 18(10):10209, 2010. ISSN 1094-4087. doi: 10.1364/OE.18.010209. URL https://www.osapublishing.org/oe/abstract.cfm?uri=oe-18-10-10209.

[153] S. Shioiri and H. Tanabe. Fast optical proximity correction: analytical method, 1995. ISSN 0277786X.

[154] O. W. Otto, J. G. Garofalo, K. K. Low, C.-M. Yuan, R. C. Henderson, C. Pierrat, R. L. Kostelak, S. Vaidya, and P. K. Vasudev. Automated optical proximity correction: a rules-based approach. *Proc. SPIE*, 2197:278–293, 1994. ISSN 0277786X. doi: 10.1117/12.175422. URL http://dx.doi.org/10.1117/12.175422.

[155] K. Matsushima and T. Shimobaba. Band-limited angular spectrum method for numerical simulation of free-space propagation in far and near fields. *Optics express*, 17(22):19662–19673, oct 2009. ISSN 1094-4087. URL http://www.ncbi.nlm.nih.gov/pubmed/19997186.

[156] R. Hild. Angular spectrum description of light propagation in planar diffractive optical elements. In *Proceedings of SPIE*, volume 5456, pages 364–373, 2004. doi: 10.1117/12.544471. URL http://www.imn.htwk-leipzig.de/{~}hild/publikationen/ASTR.pdf.

[157] Y. Shechtman, Y. C. Eldar, O. Cohen, H. N. Chapman, J. Miao, and M. Segev. Phase Retrieval with Application to Optical Imaging. *arXiv preprint arXiv:1402.7350*, pages 1–25, feb 2014. URL http://arxiv.org/abs/1402.7350.

[158] S. Marchesini. Invited article: A unified evaluation of iterative projection algorithms for phase retrieval. *Review of Scientific Instruments*, 78(1):11301, mar 2007. doi: 10.1063/1.2403783. URL http://arxiv.org/abs/physics/0603201.

[159] J. R. Fienup. Phase retrieval algorithms: a comparison. *Applied optics*, 21 (15):2758–69, aug 1982. ISSN 0003-6935. URL http://www.ncbi.nlm.nih.gov/pubmed/20396114.

[160] R. W. Gerchberg. A practical algorithm for the determination of phase from image and diffraction plane pictures. *Optik*, 35:237, 1972.

[161] J. Miao, T. Ishikawa, E. Anderson, and K. Hodgson. Phase retrieval of diffraction patterns from noncrystalline samples using the oversampling method. *Physical Review B*, 67(17):174104, may 2003. ISSN 0163-1829. doi: 10.1103/PhysRevB. 67.174104. URL http://link.aps.org/doi/10.1103/PhysRevB.67.174104.

[162] D. Stuart, O. Barter, and A. Kuhn. Fast algorithms for generating binary holograms. *Optics express*, 211001(2008):10, sep 2014. URL http://arxiv.org/abs/1409.1841.

[163] C. Zhang, Y. Hu, W. Du, P. Wu, S. Rao, and Z. Cai. Optimized holographic femtosecond laser patterning method towards rapid integration of high-quality functional devices in microchannels. *Nature Publishing Group*, (August):1–9, 2016. ISSN 20452322. doi: 10.1038/srep33281. URL http://dx.doi.org/10.1038/srep33281.